

HU ISSN 1586–2070

JOURNAL OF COMPUTATIONAL AND APPLIED MECHANICS

A Publication of the University of Miskolc

VOLUME 5, NUMBER 2 (2004)



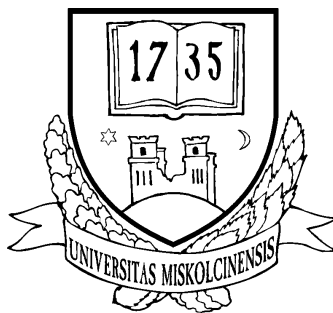
MISKOLC UNIVERSITY PRESS

HU ISSN 1586–2070

JOURNAL OF COMPUTATIONAL AND APPLIED MECHANICS

A Publication of the University of Miskolc

VOLUME 5, NUMBER 2 (2004)



MISKOLC UNIVERSITY PRESS

EDITORIAL BOARD

- István PÁCZELT, Editor in Chief, Department of Mechanics, University of Miskolc, 3515 MISKOLC, Hungary, mechpacz@gold.uni-miskolc.hu
- Vladimir KOMPIŠ, Department of Mechanics, Faculty of Mechanical Engineering, University of Žilina, ŽILINA, Slovakia, kompis@fstroj.utc.sk
- László BARANYI, Department of Fluid and Heat Engineering, University of Miskolc, 3515 MISKOLC, Hungary, arambl@gold.uni-miskolc.hu
- Imre KOZÁK, Department of Mechanics, University of Miskolc, 3515 MISKOLC, Hungary, mechkoz@gold.uni-miskolc.hu
- Edgár BERTÓTI, Department of Mechanics, University of Miskolc, 3515 MISKOLC, Hungary, mechber@gold.uni-miskolc.hu
- Márta KURUTZ, Department of Structural Mechanics, Budapest University of Technology and Economics, Műegyetem rkp. 3, 1111 BUDAPEST, Hungary, kurutzm@eik.bme.hu
- Tibor CZIBERE, Department of Fluid and Heat Engineering, University of Miskolc, 3515 MISKOLC, Hungary, aramct@gold.uni-miskolc.hu
- R. Ivan LEWIS, Room 2-16 Bruce Building, Newcastle University, NEWCASTLE UPON TYNE, NE1 7RU, UK, R.I.Lewis@NCL.AC.UK
- Wolfram FRANK, Institut für Fluid- und Thermodynamik, Universität Siegen, Paul-Bonatz-Strasse 9-11, 57076 SIEGEN, Germany, frank@ift.mb.uni-siegen.de
- Gennadij LVOV, Department of Mechanics, Kharkov Polytechnical Institute, 2 Frunze Str., 310002 KHARKOV, Ukraine, lvovgi@kpi.kharkov.ua
- Ulrich GABBERT, Institut für Mechanik, Otto-von-Guericke-Universität Magdeburg, Universitätsplatz 2, 39106 MAGDEBURG, Germany, ulrich.gabbert@mb.uni-magdeburg.de
- Herbert MANG, Institute for Strength of Materials, University of Technology, Karlsplatz 13, 1040 VIENNA, Austria, Herbert.Mang@tuwien.ac.at
- Zsolt GÁSPÁR, Department of Structural Mechanics, Budapest University of Technology and Economics, Műegyetem rkp. 3, 1111 BUDAPEST, Hungary, gaspar@ep-mech.me.bme.hu
- Zenon MROZ, Polish Academy of Sciences, Institute of Fundamental Technological Research, Swietokrzyska 21, WARSAW, Poland, zmroz@ippt.gov.pl
- Robert HABER, Department of Theoretical and Applied Mechanics, University of Illinois at Urbana-Champaign, 216 Talbot Lab., 104 S. Wright Str., URBANA, IL 61801, USA, r-haber@uiuc.edu
- Tibor NAGY, Department of Physics, University of Miskolc, 3515 MISKOLC, Hungary, fiznagyt@uni-miskolc.hu
- Gyula PATKÓ, Department of Machine Tools, University of Miskolc, 3515 MISKOLC, Hungary, mechpgy@uni-miskolc.hu
- Gábor HALÁSZ, Department of Hydraulic Machines, Budapest University of Technology and Economics, Műegyetem rkp. 3, 1111 BUDAPEST, Hungary, HALASZ@vizgep.bme.hu
- Gyula PATKÓ, Department of Machine Tools, University of Miskolc, 3515 MISKOLC, Hungary, mechpgy@uni-miskolc.hu
- Ji Huan HE, Department of Mathematics, College of Basic Science, Shanghai Donghua University, No. 1882 Yan'anxilu Road, 200051 Shanghai, China, jhhe@dhu.edu.cn
- Jan SLADEK, Ústav stavbenictva a architektúry, Slovenskej akadémie vied, Dubróvska cesta 9, 842 20 BRATISLAVA, Slovakia, usarslad@savba.sk
- Károly JÁRMAI, Department of Materials Handling and Logistics, University of Miskolc, 3515 MISKOLC, Hungary, altjar@gold.uni-miskolc.hu
- Gábor STÉPÁN, Department of Mechanics, Budapest University of Technology and Economics, Műegyetem rkp. 3, 1111 BUDAPEST, Hungary, stepan@mm.bme.hu
- László KOLLÁR, Department of Strength of Materials and Structures, Budapest University of Technology and Economics, Műegyetem rkp. 1-3. K.II.42., 1521 BUDAPEST, Hungary, lkollar@goliat.eik.bme.hu
- Barna SZABÓ, Center for Computational Mechanics, Washington University, Campus Box 1129, St. LOUIS, MO63130, USA, szabo@ccm.wustl.edu
- Szilárd SZABÓ, Department of Fluid and Heat Engineering, University of Miskolc, 3515 MISKOLC, Hungary, aram2xs@uni-miskolc.hu
- György SZEIDL, Department of Mechanics, University of Miskolc, 3515 MISKOLC, Hungary, Gyorgy.SZEIDL@uni-miskolc.hu

LOCAL EDITORIAL COUNCIL

T. CZIBERE, I. KOZÁK, I. PÁCZELT, G. PATKÓ, G. SZEIDL

PREFACE

A Conference on Modelling Fluid Flow

We are pleased to bring to you this special issue of the Journal of Computational and Applied Mechanics, which contains, among others, twelve selected papers from the Conference on Modelling Fluid Flow (CMFF'03). This event, the 12th International Conference on Fluid Flow Technologies, was held September 4-6, 2003 in Budapest, Hungary. It was the most recent in a series of events that make up the International Conference on Fluid Machinery, which has been held every fourth year in Budapest since 1959.

The CMFF'03 conference program included over 170 presentations by authors from 30 countries. The papers included here were chosen from among them based on the recommendations of referees for journal publication. These referees were members of the International Scientific and Program Committee, and we are grateful for the time given and the care with which they read and commented upon the papers.

In this issue we bring to you twelve CMFF'03 conference papers from authors around the world. Their papers are on varied topics within the fields of fluids engineering. Many of them are focused on fluid machinery, while the others address a wide range of topics within heat and fluids engineering. This reflects the topics covered in the conference itself, which is moving towards a broader focus on computational and experimental studies in fluids engineering, while still retaining its original focus upon fluid machinery.

In this issue, we offer several papers from the conference on various topics related to turbomachinery. Experimental studies in turbomachinery were performed by Canepa et al. and Hergt et al.; while computational methods were used by Lampart and in the study of Lewis. Gabi and Klemm, and Vad employed both computational and experimental methods in their studies. The other papers cover a wide range of topics: a mathematical approach to turbulence modelling by Corsini et al.; an experimental study in the area of combustion by Trimis and Wawrzinek; a paper on flow visualization by Rusch et al.; a computational study related to process engineering and heat transfer by Nikrityuk et al.; and two papers on external flow, one experimental by Koide et al., and one computational by Baranyi.

The scope of the conference included both the theoretical and practical aspects of numerical simulation of flows and physical modelling of flow processes using advanced measurement methods. The sessions were on Axial Flow Turbomachinery;

Complex Flows with Chemical Reactions; Multiphase Flow; Turbulence Modelling and Numerical Methods; Chemical and Process Engineering; Combustion and Heat Transfer; Optical Flow Diagnostics; Turbines; Fluid Machinery; Internal Flows; Radial Flow Turbomachinery; External Fluid Dynamics; and Environment. Workshops were offered in the following areas: Particle Image Velocimetry with High Temporal Resolution; Numerical Modelling of Turbomachinery Fluid Dynamics; Recent State and Future Trends in Pump Design and Development; Challenges in Optimization of Axial Flow Turbomachinery Blades for 3D Flow; Including Sweep and Dihedral Effects; and What Do Users/Developers of CFD-Codes Expect from Advanced Experiments on Turbomachinery, while a popular poster session was also available.

Special thanks go to the invited lecturers who addressed the conference: Professor Rudolf Shilling (*Application of CFD-Techniques in Fluid Machinery*); Professor Michael Leschziner (*Modelling Separation from Curved Surfaces with Anisotropy-Resolving Turbulence: Closures and Related Supplementary Observations on LES*); Professor Franz Durst (*Development of Fluid Mechanics Methods in the 20th Century and the Application to Laminar and Turbulent Flow Investigations*); and Professor Tibor Frank (*Theodore von Kármán: A Global Life*).

The following cooperating organizations are most gratefully thanked for their help in organizing, advertising, and supporting CMFF'03: Budapest University of Technology and Economics (Department of Fluid Mechanics & the Department of Hydraulic Machines); FLUENT Europe Ltd.; the Hungarian Academy of Sciences (Committee of Fluid Mechanics and Thermodynamics); the Japan Society of Mechanical Engineers; the Scientific Society of Mechanical Engineers (Flow Technology Section); the University of Miskolc (Department of Heat and Fluid Engineering); and the Visualization Society of Japan (in alphabetical order).

The next Conference of Modelling Fluid Flow (CMFF'06), the 13th in the International Conference on Fluid Flow Technologies series, is scheduled to be held in Budapest, Hungary in September 2006. We await the participation of those engaged in experimental and computational research in fluid and heat engineering. Please watch for announcements of CMFF'06 in conference lists and journals as the conference approaches, including the Calendar of Events to be found on the homepage of this journal.

We hope that you will find many articles of interest to you in this special issue.

Miskolc, July 1, 2004

László Baranyi
Editor of the special issue
János Vad
Guest editor

NUMERICAL SIMULATION OF FLOW PAST A CYLINDER IN ORBITAL MOTION

LÁSZLÓ BARANYI

Department of Fluid and Heat Engineering, University of Miskolc
H-3515 Miskolc-Egyetemváros, Hungary
arambl@uni-miskolc.hu

[Received: January 19, 2004]

Abstract. A finite difference solution is presented for 2D laminar unsteady flow around a circular cylinder in orbital motion placed in a uniform flow for $Re = 130, 160$, and 180 . Four cases displaying full lock-in are presented. The variation of time-mean and root-mean-square (rms) values of lift and drag coefficients were investigated against the amplitude of vibration in transverse direction. Abrupt jumps were found in the time-mean and rms values of lift and rms values of drag. These jumps seem to be caused by a change in the vortex structure.

Mathematical Subject Classification: 76B47, 76D25, 76M20

Keywords: circular cylinder, lock-in, orbital motion, vortex shedding, unsteady flow

Nomenclature

a_0	[-]	cylinder acceleration, nondimensionalized by U^2/d
A	[-]	amplitude of oscillation, nondimensionalized by d
C_D	[-]	drag coefficient
C_L	[-]	lift coefficient
d	[m]	cylinder diameter
D	[-]	dilation
f	[-]	oscillation frequency, nondimensionalized by U/d
p	[-]	pressure, nondimensionalized by ρU^2
Re	[-]	Reynolds number, Ud/ν
t	[-]	time, nondimensionalized by d/U
U	[m/s]	free stream velocity, velocity scale
u, v	[-]	velocities in x, y directions, nondimensionalized by U
x, y	[-]	Cartesian coordinates, nondimensionalized by d
ν	[m ² /s]	kinematic viscosity
ρ	[kg/m ³]	fluid density

Subscripts

L	lift
D	drag
rms	root-mean-square value
x, y	components in x and y directions

1. Introduction

Flow-induced vibration of structures is encountered in various fields of engineering such as civil engineering, power generation and transmission, ocean engineering and offshore industry, aero-space industry, wind engineering. These motions are often not limited to one direction, i.e. they oscillate in both transverse and in-line directions. Oscillation in two directions can result in an orbital motion of the body, in which it follows an elliptical path.

Oscillatory flow has been fairly widely researched (e.g. [1]-[4]), as have oscillating cylinders in uniform flow (e.g. [5]-[9]). Also in fluid at rest, an orbiting cylinder has been investigated numerically by Teschauer et al. [10], while Stansby and Rainey [11] investigated a cylinder which was orbiting and rotating. However, research on an orbiting cylinder in uniform flow seems to have been neglected.

Earlier the author carried out computational investigations on a cylinder in orbital motion in a uniform stream at $Re = 180$ [12]. The orbital path resulted from the superposition of in-line and transverse oscillations, with frequencies of 85% that of the vortex shedding frequency from a stationary cylinders at that Reynolds number. The non-dimensional amplitude of oscillation in the in-line direction A_x was kept constant, while that of the transverse oscillation A_y was varied. At about A_y equals one-third of A_x , sudden jumps were observed in the time-mean value of the lift coefficient and in the root-mean-square (rms) values of lift and drag coefficients.

These unexpected results led the author to investigate this phenomenon further. It was thought that the jumps may be related to three-dimensional instability, called Mode A instability, occurring at around $Re = 188.5$ for a stationary cylinder as proven theoretically by Barkley and Henderson [13] and Posdziech and Grundmann [14], and experimentally by Williamson [15], although Norberg's results showed a somewhat lower value [16]. In this study, lower Reynolds numbers were also investigated ($Re = 130, 160$).

2. Governing equations

The governing equations are the two components of the Navier-Stokes equations, the continuity equation and the pressure Poisson equation written in dimensionless form in the non-inertial system fixed to the orbiting cylinder. The Navier-Stokes equations can be written as

$$\frac{\partial u}{\partial t} + u \frac{\partial u}{\partial x} + v \frac{\partial u}{\partial y} = -\frac{\partial p}{\partial x} + \frac{1}{Re} \nabla^2 u - a_{0x} , \quad (2.1)$$

$$\frac{\partial v}{\partial t} + u \frac{\partial v}{\partial x} + v \frac{\partial v}{\partial y} = -\frac{\partial p}{\partial y} + \frac{1}{Re} \nabla^2 v - a_{0y} , \quad (2.2)$$

where ∇^2 is the 2D Laplacian operator, a_{0x} and a_{0y} are the x and y components of the cylinder acceleration. In these equations the body force is included in the pressure terms. The equation of continuity has the form

$$D = \frac{\partial u}{\partial x} + \frac{\partial v}{\partial y} = 0 , \quad (2.3)$$

where D is the dilation. Taking the divergence of the Navier-Stokes equations yields the Poisson equation for pressure

$$\nabla^2 p = 2 \left[\frac{\partial u}{\partial x} \frac{\partial v}{\partial y} - \frac{\partial u}{\partial y} \frac{\partial v}{\partial x} \right] - \frac{\partial D}{\partial t} . \quad (2.4)$$

No-slip boundary condition (BC) is used on the cylinder surface for the velocity and a Neumann-type condition is used for pressure p . A potential flow distribution is assumed far from the cylinder. We do not go into further details here (see [7, 17]).

3. Transformation of domain

Boundary conditions can be imposed accurately by using boundary fitted coordinates. In this way interpolation, often leading to poor solutions, can be omitted. By using unique, single-valued functions $g(\xi)$, $f(\eta)$, the physical domain (x, y, t) can be mapped into a computational domain (ξ, η, τ) (see Figure 1):

$$x(\xi, \eta) = R(\eta) \cos[g(\xi)] , \quad (3.1)$$

$$y(\xi, \eta) = -R(\eta) \sin[g(\xi)] , \quad (3.2)$$

$$t = \tau , \quad (3.3)$$

where the dimensionless radius is

$$R(\eta) = R_1 \exp[f(\eta)] . \quad (3.4)$$

In this study the following linear mapping functions are used:

$$g(\xi) = 2\pi \frac{\xi}{\xi_{\max}}; \quad f(\eta) = \frac{\eta}{\eta_{\max}} \log\left(\frac{R_2}{R_1}\right) , \quad (3.5)$$

where subscript *max* refers to maximum value, R_1 is the dimensionless radius of the cylinder, and R_2 is that of the outer boundary of the computational domain (see Figure 1). Using equations (3.1) to (3.5) cylindrical coordinates with logarithmically spaced radial cells are obtained on the physical plane, providing a fine grid scale near the cylinder wall and a coarse grid in the far field.

Using equations (3.1) to (3.5), the governing equations and BCs (not shown here) can also be transformed into the computational plane. The transformed equations are solved by using the finite difference method, see e.g. [7, 17].

4. Computational results

The motion of the center of the cylinder is specified as follows

$$x_0(t) = A_x \cos(2\pi f_x t); \quad y_0(t) = A_y \sin(2\pi f_y t), \quad (4.1)$$

where A_x , A_y and f_x , f_y are the dimensionless amplitudes and frequencies of oscillations in x and y directions, respectively. Here $f_x = f_y$ which for nonzero A_x , A_y amplitudes gives an ellipse, the orbital path of which will become a circle when the two amplitudes are equal to each other. If one of the amplitudes is zero, in-line or transverse oscillation is obtained. When both amplitudes are zero, the cylinder becomes stationary.

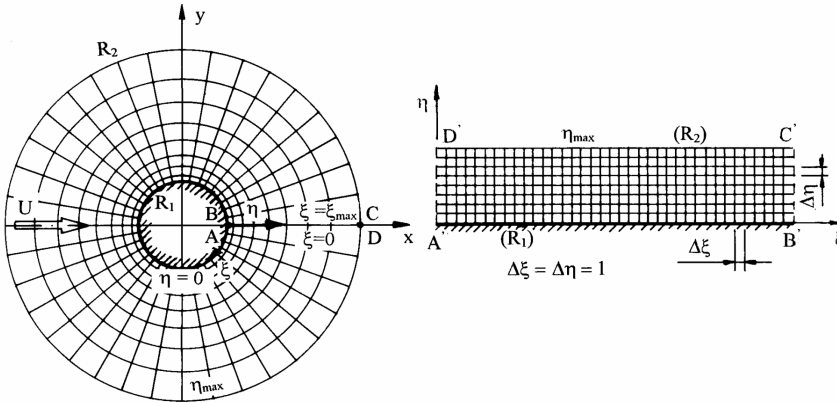


Figure 1. Physical and computational domains

Computations were carried out for Reynolds numbers 130, 160 and 180. The dimensionless frequencies f_x and f_y were kept constant at 85% of the frequency of vortex shedding from a stationary cylinder at that Reynolds number. This value was chosen because we wanted to reach lock-in without very large amplitudes of A_x and A_y .

Here, A_x was kept constant for a given Reynolds number while increasing the value of A_y . Various A_x values were used in computations; only those cases in which lock-in was reached at zero A_y value are shown in this paper. These were $Re = 130$ ($A_x = 0.3$), $Re = 160$ ($A_x = 0.3$), and $Re = 180$ ($A_x = 0.3$, $A_x = 0.26$). Lock-in is a phenomenon typical of oscillating structures. When the body is vibrating, either in forced or natural motion, a nonlinear interaction occurs as the frequency of the vibration approaches that of the vortex shedding. In this case vortex shedding occurs at the vibration frequency of the body, a phenomenon called lock-in.

In an earlier paper [12] computational results were shown for a cylinder in orbital motion at $Re = 180$ and $A_x = 0.3$. C_{Lrms} , C_{Drms} and \bar{C}_D , (the overbar denotes

time-mean value of the quantity) were shown against different A_y values. In that paper the time-mean and *rms* values were approximated based on the maximum and minimum values of the lift and drag coefficients. In the current study a more refined approach was applied to take into account the non-sinusoidal nature of the functions by following the integral definition of mean and *rms* values of a function f

$$\bar{f} = \frac{1}{nT} \int_{t_1}^{t_1+nT} f(t) dt, \quad (4.2)$$

$$f_{rms} = \sqrt{\frac{1}{nT} \int_{t_1}^{t_1+nT} [f(t) - \bar{f}]^2 dt}, \quad (4.3)$$

where t_1 is the starting time value for integration, T is the length of one cycle and n is the number of cycles. The *rms* and time-mean values were evaluated for a few n values in order to find the most precise fit. The original approach showed a sudden jump at $A_y = 0.1$ in all three values shown (C_{Drms} , C_{Lrms} , \bar{C}_D). The more precise current approach showed that, although the *rms* values are essentially the same, there is now only a small shift in \bar{C}_D at $A_y = 0.1$. This indicates that signals should not be assumed to be sinusoidal in case of oscillating cylinders or those in orbital motion. While for a stationary cylinder, the simple original approach worked very well (showing that those signals are extremely near to sinusoidal shape), for oscillating cylinders Equations (4.2) and (4.3) should be used for evaluating time-mean and *rms* values.

Actually, C_L signals are rather distinctly asymmetric. Figures 2 and 3 show the time history of the lift coefficient at $Re = 160$, $A_x = 0.3$. In Figure 2, A_y is at 0.068 and the upper peaks are quite rounded and somewhat asymmetric, while the lower peaks are relatively sharp and more symmetric. In Figure 3, where A_y is just a little higher at 0.07, the pattern has reversed itself, with sharper upper peaks and more rounded lower peaks. In addition, the minimum value of C_L dropped substantially. The calculated mean value of the lift coefficient at $A_y = 0.068$ is 0.2432, and at $A_y = 0.07$ it is -0.3685 as seen in Table 2 in the Appendix. This rather drastic change is not limited to the lift coefficient.

Figures 4 to 6 (and their corresponding Tables, given in the Appendix) show the variations of time-mean and *rms* values of lift and drag coefficients C_L and C_D at $A_x = 0.3$ against A_y . As mentioned earlier, the frequency of oscillation in x and y directions (resulting in an elliptical path) was taken to be 85% of the vortex shedding frequency of a stationary cylinder at the same Reynolds number.

In Figure 4 (and Table 1), where $Re = 130$ and $f_x = f_y = 0.1521$, two sudden jumps were found in \bar{C}_L . Other values are just slightly affected at these critical A_y values. The time-mean value of \bar{C}_D has practically no jump, and it slightly increases with increasing A_y values. Although it seems that \bar{C}_D is hardly affected by the phenomenon that causes jumps in \bar{C}_L values, C_{Drms} is influenced at the second critical point, though to a much lesser extent than \bar{C}_L . While passing through the

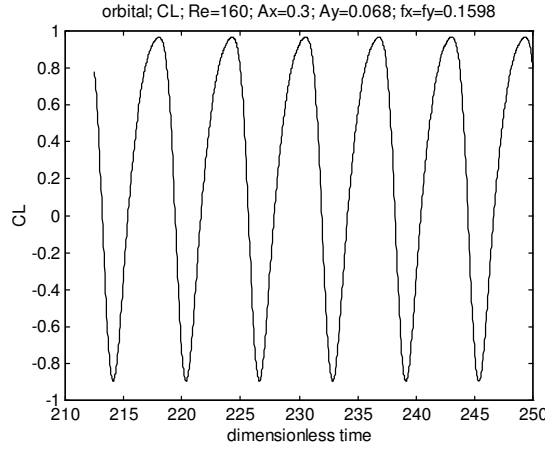


Figure 2. Time history of the lift coefficient for flow around a cylinder in orbital motion at $Re = 160$, $A_x = 0.3$, $A_y = 0.068$

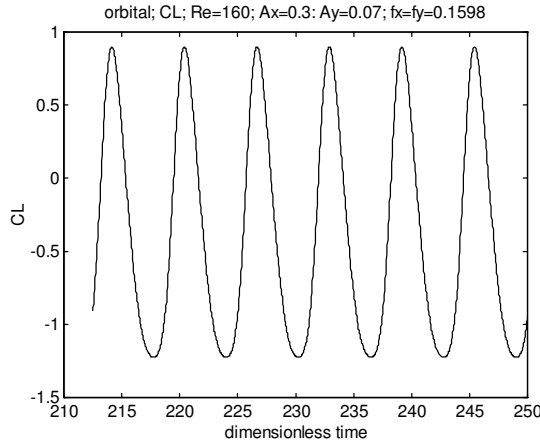


Figure 3. Time history of the lift coefficient for flow around a cylinder in orbital motion at $Re = 160$, $A_x = 0.3$, $A_y = 0.07$

critical values in A_y , there are also sudden changes in the shape of the time history curve of C_L , similar to those shown in Figures 2 and 3.

Time history signals for C_D also exhibited a change in amplitude after passing through the critical A_y values, although their shape was quite similar before and after. Before, between and after the jumps the slope of \bar{C}_L is roughly identical and \bar{C}_L decreases with increasing A_y approaching zero when A_y tends to A_x . After the second jump C_{Lrms} decreases and C_{Drms} increases with A_y .

In Figure 5 (and Table 2), where $Re = 160$ and $f_x = f_y = 0.1598$, only one sudden jump was found in \bar{C}_L . Here \bar{C}_D seems to be insensitive to the phenomenon causing the jump in \bar{C}_L . The change in the shape of the C_L signal before and after the critical value A_y can be seen in Figures 2 and 3. Again, before and after the jump the slope of \bar{C}_L is roughly identical. The *rms* values tend in opposite directions with A_y from those in Figure 4.

In Figure 6 (and Table 3), where $Re = 180$ and $f_x = f_y = 0.165665$, there are three sudden jumps in \bar{C}_L . Here \bar{C}_D seems to be almost completely unaffected by the phenomenon that causes the jumps in \bar{C}_L . The change in the shape of the C_L signal while passing through the three critical A_y values is very similar to the changes shown in Figures 2 and 3. The slope of \bar{C}_L between and after the jumps is again roughly identical. The variation of the *rms* values with A_y is very similar to that shown in Figure 5. Here \bar{C}_L tends to about -0.5 as A_y tends to A_x . The *rms* curves are very similar to those shown in Figure 4.

Figure 7 (and Table 4) show the variations of time-mean and *rms* values of lift and drag coefficients at $A_x = 0.26$ against A_y for $Re = 180$. Just a small change (compared to Figure 6) in A_x resulted in a drastic change in the variation of \bar{C}_L with A_y , while the other signals shown in Figures 6 and 7 are very similar to each other. All four variables are very similar to those in Figures 5 and 7.

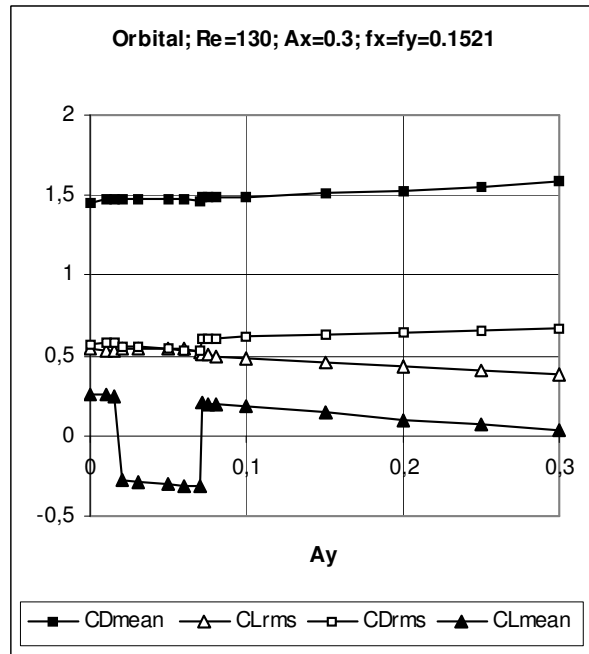


Figure 4. Time-mean and *rms* values of lift and drag coefficients versus A_y for $Re = 130$ and $A_x = 0.3$

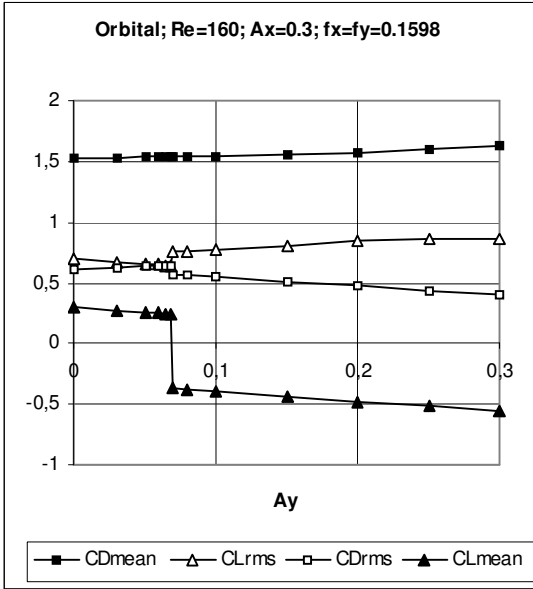


Figure 5. Time-mean and *rms* values of lift and drag coefficients versus A_y for $Re = 160$ and $A_x = 0.3$

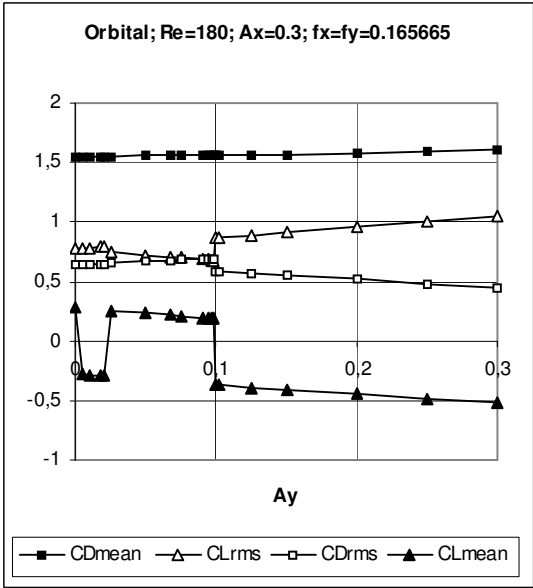


Figure 6. Time-mean and *rms* values of lift and drag coefficients versus A_y for $Re = 180$ and $A_x = 0.3$

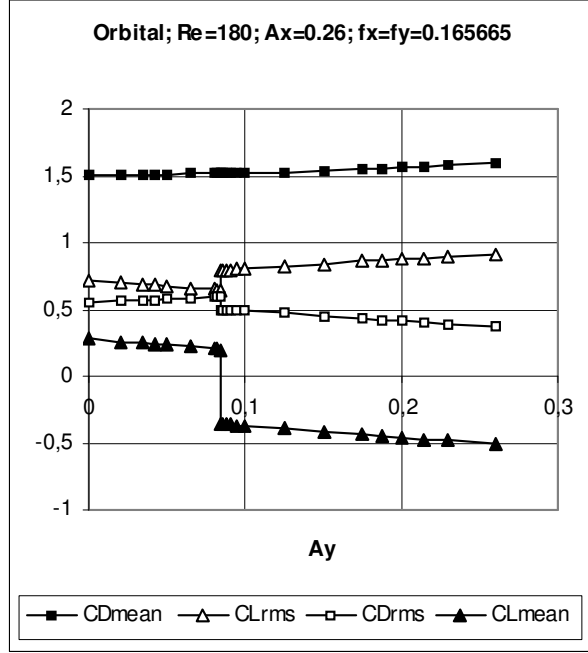


Figure 7. Time-mean and *rms* values of lift and drag coefficients versus A_y for $Re = 180$ and $A_x = 0.26$

To sum up, four cases were reported here. Reynolds numbers and the dimensionless amplitude of oscillation in the in-line direction A_x were kept fixed and the dimensionless amplitude of oscillation in transverse direction A_y was varied. One, two or three sudden jumps can be observed in the time-mean values of the lift coefficient \bar{C}_L in each of the cases shown in Figures 4 to 7. The shape of the C_L signal changes abruptly while passing through the critical values of A_y values where the jumps take place. Interestingly, the slope of curve \bar{C}_L is roughly identical before and after the jump(s). For all cases \bar{C}_D seems to be almost completely unaffected by the phenomenon causing the jumps in \bar{C}_L and it increases slightly with A_y . The *rms* values of the lift and drag coefficients have their most discernable jumps only at the highest critical A_y values. In case of $Re = 180$, these upper critical A_y values are practically equal to one third of A_x . This is not true for $Re = 130$ and 160 . Somewhat unexpectedly, the direction in which *rms* values jump at the last critical A_y value differed: for $Re = 130$, where C_{Drms} jumped upwards and increased thereafter and C_{Lrms} jumped downwards and decreased, and for the other three cases, in which the directions were reversed.

While not shown here, base pressure coefficients were also calculated for $Re = 130$ and 160 , and their time-mean and *rms* values also exhibit the same number of jumps as \bar{C}_L at the same A_y values.

Our original possible explanation was that the jump(s) might have been caused by the 3D instability that occurs at around $Re = 188.5$ for a stationary cylinder. However, here we found that these jumps occurred at lower Reynolds number ($Re = 130$ and 160) as well, so the instability explanation seems unlikely, unless instability zones are very different for oscillating cylinders compared to stationary cylinders. Experimental evidence (see e.g. [18, 19]) for oscillating cylinders shows that lock-in increases the span-wise correlation of signals and the two-dimensionality of the flow compared to flow around stationary cylinders. In [19] the increase in the cross correlation coefficient for velocity is actually used to identify lock-in. Poncet [20] shows how the 3D wake behind a circular cylinder can be made 2D by using lock-in triggered by rotary oscillation of the cylinder. These results suggest that the jumps are probably not caused by 3D instabilities. The only explanation we can offer at present is that the structure of vortices changes while going through the critical A_y values, which is represented by the change in lift coefficient signals as shown in Figures 2 and 3. There is a possibility that bifurcation occurs at these critical values. This phenomenon needs further investigation.

5. Summary

Flow around a circular cylinder in orbital motion placed in an otherwise uniform flow was investigated numerically using the computational method developed by the author, based on a finite difference solution. Four cases are shown in the paper: (a) $Re = 130$, $A_x = 0.3$; (b) $Re = 160$, $A_x = 0.3$; (c) $Re = 180$, $A_x = 0.3$; (d) $Re = 180$, $A_x = 0.26$. Reynolds numbers and the dimensionless amplitude of oscillation in the in-line direction A_x were kept fixed and the dimensionless amplitude of oscillation in transverse direction A_y was varied. Lock-in was observed at all A_y values. One, two or three sudden jumps can be observed in the time-mean values of the lift coefficient \bar{C}_L for (a)-(d). The shape of the C_L signal changes abruptly while going through the critical values of A_y where the jumps take place. The slope of curve \bar{C}_L is roughly identical before and after the jump(s). For all cases \bar{C}_D seems to be almost completely unaffected by the phenomenon that caused the jumps in \bar{C}_L , unlike C_{Drms} . The *rms* values of the lift and drag coefficients have their most discernible jumps exactly at the highest critical A_y value.

The jumps were originally thought to have been possibly caused by the 3D instability that occurs at around $Re = 188.5$ for a stationary cylinder. However, the fact that jumps occurred at lower Reynolds numbers make this explanation unlikely. Furthermore, other researchers have found that lock-in states for oscillating cylinders strengthen the 2D effects, when compared to flow around stationary cylinders. The only explanation we can offer at present is that the vortex structure must change while passing through the critical A_y values. Further plans include further investigation of the phenomenon of the jumps and trying to find a physical explanation, beginning with the possibility of bifurcation effects.

Acknowledgement. The support provided by the Hungarian Research Foundation (OTKA, Project No. T 042961) is gratefully acknowledged.

References

1. BEARMAN, P.W., DOWNIE, M.J., GRAHAM, J.M.R. AND OBASAJU, E.D.: Forces on cylinders in viscous oscillatory flow at low Keulegan-Carpenter numbers. *Journal of Fluid Mechanics*, **154**, (1985), 337-356.
2. SARPKEYA, T.: Force on a circular cylinder in viscous oscillatory flow at low Keulegan-Carpenter numbers. *Journal of Fluid Mechanics*, **165**, (1986), 61-71.
3. YAN, B.: Oscillatory flow beneath a free surface. *Fluid Dynamics Research*, **22**, (1998), 1-23.
4. HU, P., WU, G.X. AND MA, Q.W.: Numerical simulation of nonlinear wave radiation by a moving vertical cylinder. *Ocean Engineering*, **29**, (2002), 1733-1750.
5. OKAJIMA, A.: Numerical analysis of the flow around an oscillating cylinder. *Proceedings of the Sixth International Conference on Flow-Induced Vibration*, London, 1995, 159-166.
6. MITTAL, S. AND KUMAR, V.: Finite element study of vortex-induced cross-flow and in-line oscillations of a circular cylinder at low Reynolds numbers. *International Journal for Numerical Methods in Fluids*, **31**, (1999), 1087-1120.
7. BARANYI, L. AND SHIRAKASHI, M.: Numerical solution for laminar unsteady flow about fixed and oscillating cylinders. *Computer Assisted Mechanics and Engineering Sciences*, **6**, (1999), 263-277.
8. DENNIS, S.C.R., NGUYEN, P. AND KOCABIYIK, S.: The flow induced by a rotationally oscillating and translating circular cylinder. *Journal of Fluid Mechanics*, **407**, (2000), 123-144.
9. MAHFOUZ, I. AND BADR, H.M.: Flow structure in the wake of a rotationally oscillating cylinder. *Journal of Fluids Engineering*, **122**, (2000), 290-301.
10. TESCHAUER, I., SCHÄFER, M. AND KEMPF, A.: Numerical simulation of flow induced by a cylinder orbiting in a large vessel. *Journal of Fluids and Structures*, **16**, (2002), 435-451.
11. STANSBY, P.K., AND RAINEY, R.C.T.: On the orbital response of a rotating cylinder in a current. *Journal of Fluid Mechanics*, **439**, (2001), 87-108.
12. BARANYI, L. AND LAKATOS, K.: Computation of viscous flow around a circular cylinder in orbital motion in a uniform flow, *Proceedings of MicroCAD 2000, International Computer Science Conference*, Miskolc, 2000, 7-12.
13. BARKLEY, D. AND HENDERSON, R.D.: Three-dimensional Floquet stability analysis of the wake of a circular cylinder. *Journal of Fluid Mechanics*, **322**, (1996), 215-241.
14. POSDZIECH, O. AND GRUNDMANN, R.: Numerical simulation of the flow around an infinitely long circular cylinder in the transition regime. *Theoretical and Computational Fluid Dynamics*, **15**, (2001), 121-141.
15. WILLIAMSON, C.H.K.: Vortex dynamics in the cylinder wake. *Annual Review of Fluid Mechanics*, **28**, (1996), 477-539.
16. NORBERG, C.: Flow around a circular cylinder: Aspect of fluctuating lift. *Journal of Fluids and Structures*, **15**, (2001), 459-469.
17. BARANYI, L.: Computation of unsteady momentum and heat transfer from a fixed circular cylinder in laminar flow. *Journal of Computational and Applied Mechanics*, **4**(1), (2003), 13-25.

18. BEARMAN, P.W. AND OBASAJU, E.D.: An experimental study of pressure fluctuations on fixed and oscillating square-section cylinders, *Journal of Fluid Mechanics*, **119**, (1982), 297-321.
19. KOIDE, M., TOMIDA, S., TAKAHASHI, T., BARANYI, L. AND SHIRAKASHI, M.: Influence of cross-sectional configuration on the synchronization of Kármán vortex shedding with the cylinder oscillation. *JSME International Journal*, Series B, **45**(2), (2002), 249-258.
20. PONCET, P.: Vanishing of B mode in the wake behind a rotationally oscillating cylinder. *Physics of Fluids*, **14**(6), (2002), 2021-2023.

6. APPENDIX

Tables 1 to 4 are appended here, containing time-mean and *rms* values for lift and drag coefficients versus dimensionless amplitude of transverse oscillation for different Reynolds numbers. These Tables contain the data on which Figures 4 to 7 were based.

Table 1. Time-mean and *rms* values of lift and drag coefficients for $Re = 130$ and $A_x = 0.3$

A_y	\bar{C}_D	C_{Lrms}	C_{Drms}	\bar{C}_L
0	1.4571	0.5409	0.5715	0.2641
0.01	1.4752	0.5357	0.5763	0.2556
0.015	1.4757	0.5335	0.5789	0.2514
0.02	1.4736	0.5467	0.5598	-0.2805
0.03	1.4735	0.5489	0.5540	-0.2886
0.05	1.4730	0.5488	0.5414	-0.3035
0.06	1.4719	0.5439	0.5345	-0.3096
0.07	1.4666	0.5250	0.5265	-0.3109
0.072	1.4858	0.5042	0.6051	0.2043
0.075	1.4858	0.5017	0.6065	0.2012
0.08	1.4870	0.4988	0.6086	0.1970
0.1	1.4930	0.4878	0.6168	0.1806
0.15	1.5099	0.4586	0.6340	0.1409
0.2	1.5317	0.4315	0.6479	0.1028
0.25	1.5567	0.4072	0.6596	0.0662
0.3	1.5846	0.3875	0.6696	0.0307

Table 2. Time-mean and *rms* values of lift and drag coefficients for $Re = 160$ and $A_x = 0.3$

A_y	\bar{C}_D	C_{Lrms}	C_{Drms}	\bar{C}_L
0	1.5316	0.6979	0.6110	0.3053
0.03	1.5331	0.674	0.6266	0.2779
0.05	1.5353	0.6580	0.6364	0.2598
0.06	1.5367	0.6500	0.6409	0.2506
0.065	1.5375	0.6460	0.6432	0.2461
0.068	1.5380	0.6436	0.6445	0.2432
0.07	1.5367	0.7522	0.5693	-0.3685
0.08	1.5382	0.7599	0.5630	-0.3771
0.1	1.5421	0.7747	0.5496	-0.3947
0.15	1.5560	0.8098	0.5145	-0.4371
0.2	1.5746	0.8412	0.4772	-0.4779
0.25	1.5985	0.8649	0.4385	-0.5173
0.3	1.6306	0.8629	0.3994	-0.5585

Table 3. Time-mean and *rms* values of lift and drag coefficients for $Re = 180$ and $A_x = 0.3$

A_y	\bar{C}_D	C_{Lrms}	C_{Drms}	\bar{C}_L
0	1.5524	0.7719	0.6481	0.2766
0.005	1.5521	0.7770	0.6453	-0.2827
0.01	1.5519	0.7818	0.6425	-0.2874
0.0175	1.5520	0.7890	0.6384	-0.2945
0.021	1.5514	0.7918	0.6364	-0.2990
0.025	1.5551	0.7478	0.6606	0.2544
0.05	1.5590	0.7241	0.6720	0.2310
0.0675	1.5624	0.7075	0.6796	0.2142
0.075	1.5636	0.7006	0.6829	0.2066
0.09	1.5671	0.6867	0.6889	0.1925
0.095	1.5686	0.6818	0.6907	0.1872
0.0975	1.5696	0.6792	0.6913	0.1851
0.09875	1.5696	0.6792	0.6913	0.1851
0.1	1.5560	0.8674	0.5887	-0.3696
0.1025	1.5566	0.8694	0.5869	-0.3727
0.125	1.5600	0.8906	0.5718	-0.3913
0.15	1.5643	0.9139	0.5547	-0.4114
0.2	1.5769	0.9604	0.5185	-0.4494
0.25	1.5909	1.0067	0.4819	-0.4825
0.3	1.6076	1.0532	0.4455	-0.5115

Table 4. Time-mean and *rms* values of lift and drag coefficients for $Re = 180$ and $A_x = 0.26$

A_y	\bar{C}_D	C_{Lrms}	C_{Drms}	\bar{C}_L
0	1.5093	0.7208	0.5509	0.2788
0.02	1.5099	0.7024	0.5619	0.2606
0.035	1.5115	0.6891	0.5694	0.2468
0.042	1.5106	0.6816	0.5722	0.2397
0.05	1.5122	0.6748	0.5760	0.2323
0.065	1.5167	0.6630	0.5834	0.2188
0.08	1.5201	0.6499	0.5900	0.2046
0.082	1.5209	0.6481	0.5905	0.2033
0.084	1.5212	0.6464	0.5915	0.2009
0.0845	1.5165	0.7919	0.5000	-0.3574
0.085	1.5178	0.7917	0.4990	-0.3596
0.088	1.5176	0.7943	0.4974	-0.3614
0.09	1.5180	0.7962	0.4961	-0.3629
0.095	1.5191	0.8001	0.4927	-0.3675
0.1	1.5205	0.8042	0.4893	-0.3720
0.125	1.5281	0.8238	0.4716	-0.3946
0.15	1.5379	0.8420	0.4530	-0.4170
0.175	1.5479	0.8605	0.4345	-0.4378
0.188	1.5540	0.8695	0.4247	-0.4484
0.2	1.5602	0.8768	0.4152	-0.4587
0.215	1.5683	0.8857	0.4035	-0.4711
0.23	1.5772	0.8935	0.3917	-0.4835
0.26	1.5970	0.9054	0.3682	-0.5078

AN EXPERIMENTAL INVESTIGATION OF THE UNSTEADY FLOW IN A TWO-STAGE LOW-PRESSURE RESEARCH TURBINE

EDWARD CANEPA, ANDREA CATTANEI, MARINA UBALDI, PIETRO ZUNINO
Dipartimento di Macchine, Sistemi Energetici e Trasporti, University of Genova
Via Montallegro 1, I-16145 Genova, Italy
zunmp@unige.it

[Received: November 14, 2003]

Abstract. Results of an experimental investigation of the unsteady flow in a two-stage low-pressure large-scale research turbine are presented. Velocity and turbulence measurements were performed upstream and downstream each blade row at midspan by means of a two-sensor hot-wire probe. Results show a complex unsteady flow with remarkable wake generated and potential flow interaction effects.

Keywords: axial flow turbine, hot-wire measurements, rotor-stator aerodynamic interaction

Nomenclature

c	absolute velocity
g	stator pitch
r	radial coordinate
t	time
T	rotor blade passing period
w	relative velocity
x	axial coordinate
y	circumferential coordinate
α	absolute flow angle
β	relative flow angle
ω	rotational speed

Subscripts and superscripts

nom	nominal condition
x, y	in axial, tangential direction
l	fluctuating component
\sim	ensemble averaged
$\sim l$	ensemble averaged rms of fluctuating components

1. Introduction

Current design of axial turbines is carried out under the hypothesis of steady flow, regardless of whether the flow in bladed components is unsteady and blade boundary layer development and associated losses are strongly influenced by unsteady effects.

Aerodynamic rotor-stator interaction constitutes the major cause of unsteadiness in turbomachines working under nominal conditions. Each cascade produces a non-uniform flow field which is due to potential flow effects as well as viscous effects acting through blade wakes and secondary flows. Therefore a blade row in relative motion with respect to the preceding one is affected by strong periodic variations of all the thermofluid-dynamic quantities and operates under strongly unsteady flow conditions.

In general perturbation causes the stage loss to increase compared with the ideal condition of isolated blade row [1-2]. However, the interaction between blade rows in relative motion has sometimes also positive effects, as it happens when the periodic perturbation promotes the boundary layer transition before laminar separation takes place [3-4]. This is the case of the low pressure stages of aero-engine gas turbines operating at low Reynolds numbers (50000-200000) during high altitude cruise. To avoid severe boundary layer laminar separations, characteristic of such low Re conditions, the designer is forced to limit the blade loading and to reduce the boundary layer laminar extension, with a consequent increase of losses under the high Reynolds number operating conditions [5]. Therefore, only a deep knowledge of the phenomenon can allow the designer to remove the aerodynamic loading restriction obtaining a more compact and efficient turbine design.

Results from fundamental experiments on wake-boundary layer interaction on flat plates and in cascades operating with inlet flow perturbed by the wakes are available in the technical literature (among the most recent [6-8]). They provide detailed insights into the physics of the rotor-stator interaction phenomena, contributing to increase the understanding of the physics and stimulating ideas applicable to wake-induced transition modelling to be used for CFD calculations.

In order to extend these unsteady flow principles to a real machine environment and incorporate the appropriate physical models into the design procedures a further step is essential [9, 10], which consists in detailed experiments on realistic geometries representative of a multi-stage turbine environment. For this reason a large-scale research turbine has been conceived, designed and constructed in the framework of a National Research Program (PRIN 1998) and it is in operation in the Aerodynamics and Turbomachinery Laboratory of the University of Genova [11]. This facility is suitable for both basic and applied experiments focused on the exploitation of blade row interaction effects for low-pressure turbine performance improvement.

The present paper describes the large-scale low-pressure research turbine and presents the results of a preliminary investigation aiming at identifying and quantifying the aerodynamic interaction mechanisms in the two-stage turbine model.

2. Test Facility and Experimental Procedure

2.1. Axial flow turbine. The test facility, shown in Figure 1, is a large-scale low-speed two-stage axial flow research turbine representative of low-pressure gas turbine stages and its overall dimensions are $3766\text{ mm} \times 2170\text{ mm} \times 2269\text{ mm}$ (*length* \times *width* \times *height*). The working fluid is atmospheric air fed by a centrifugal fan mounted downstream of the turbine. The rig allows chord based Reynolds number variations from 50000 up to 500000. To obtain repetitive flow conditions on the two stages as well as to vary the operating point, the turbine is provided with a variable stagger centripetal distributor producing pre-swirled flow at the first stage inlet.

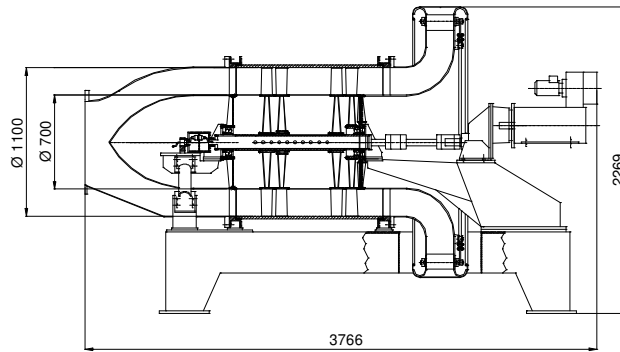


Figure 1. Meridional section of the turbine model

The turbine is braked by means of a 40 kW D.C. reversible electric motor and the fan is driven by a 60 kW electric motor, both of them equipped with a variable speed electronic controls. The desired operating point is obtained by acting simultaneously on the rotational speeds of the electric motors and on the guide vane stagger angle.

The turbine model has been especially designed to study unsteady flow phenomena in LP turbines. All four rows consist of unshrouded blades mounted on discs, whose circumferential and axial positioning may be varied, thus allowing both rows clocking and gapping. The Plexiglas casing is designed to allow independent rotation. A long longitudinal opening, where modular caps or an optical glass window may be fitted, allows for stationary probes insertion between the rows and for LDV measurements. A photograph of the research turbine is shown in Figure 2.

Axial and radial positioning of the probes is realised by means of a two-axis traversing system mounted on the casing, while angular positioning is obtained by means of the casing rotation system; all movements are computer controlled with minimum steps of $10\text{ }\mu\text{m}$.

2.2. Flow conditions and turbine geometry. The meridional channel mean diameter is 900 mm and the blade height and chord are 200 mm and 120 mm , respectively;

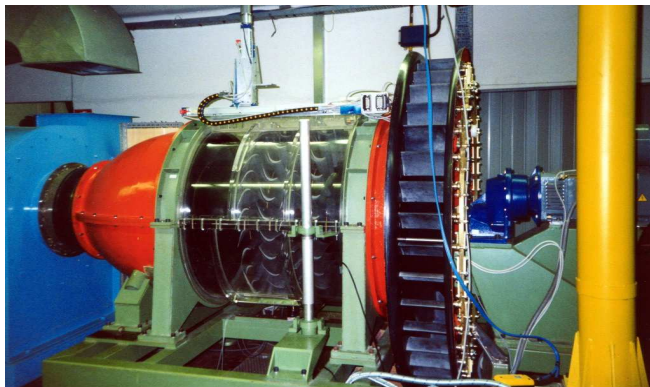


Figure 2. Two-stage low-pressure research turbine

the bladings may be axially moved within a maximum length of 925 mm. At the design operating condition the rotational speed is 450 rpm and the flow rate 11.8 kg/s, with a total pressure drop per stage of about 1200 Pa and an overall ideal power of about 24 kW.

In the present configuration the stage is symmetric at midspan and is provided with a MTU T106 blade profile ($\beta_1 = 37.7 \text{ deg}$, $\beta_2 = -63.2 \text{ deg}$, angles measured from axial direction) for which extensive cascade investigations exist (e.g. [12-13]); at nominal conditions the Zweifel coefficient is 1.055. However, the particular mechanical solutions allow for an easy substitution of the bladed disks and different geometries can be easily tested.

The two stages are repetitive and the stator has prismatic blades radially stacked on the trailing edge. The rotor has twisted blades, designed to obtain an outlet flow similar to the one generated by the centripetal distributor at the turbine inlet, so that nearly repetitive stages are obtained. Particular care has also been put in obtaining a highly loaded stage at midspan without extensive separations at both stator and rotor tips where solidity is lower.

2.3. Experimental procedure. Measurements of the unsteady velocity components were made using a two-component crossed hot-wire probe (Dantec P64) and a two-channel constant temperature anemometer (Dantec 55M10). Data were sampled by means of a Metrabyte DAS 58 Sample & Hold AD converter board and the instantaneous velocity components were determined by means of the directional calibration and non-iterative hot-wire analysis method of Schroeder [14].

In order to measure the velocity components on the blade-to-blade surfaces, the probe was traversed radially at 5 axial positions upstream and downstream each blade row. A scheme of the turbine blade rows with the measuring sections is shown in Figure 3. In the following only the results obtained at midspan surfaces are reported.

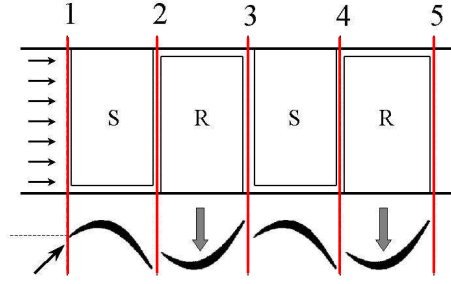


Figure 3. Scheme of measuring sections

In the present experiment the axial gap between blade rows at midspan was 0.35 of the axial chord.

A phase-locked ensemble average technique [15], with the reference signal obtained from the shaft encoder, has been applied to separate periodic velocity variations associated with the blade passing frequency from random fluctuations.

In order to investigate rotor-stator interaction flow effects, measurements at each axial position are repeated for several different relative circumferential positions between probe and stator vanes [16].

The instantaneous velocity is a function of time (t_j) or rotor circumferential coordinate, of the data record (n), of the stationary probe circumferential position with respect to the stator vane (θ_k) and of the axial coordinate (x).

Omitting for simplicity's case the axial coordinate, the equations defining the ensemble average procedure are as follows:

- instantaneous velocity

$$c(t_j, \theta_k, n) = \tilde{c}(t_j, \theta_k) + c'(t_j, \theta_k, n)$$

- ensemble averaged velocity

$$\tilde{c}(t_j, \theta_k) = \frac{1}{N} \sum_{n=1}^N c(t_j, \theta_k, n)$$

- root mean square of the random unsteady fluctuations

$$\sqrt{\widetilde{c'^2}(t_j, \theta_k)} = \sqrt{\frac{1}{(N-1)} \sum_{n=1}^N [c(t_j, \theta_k, n) - \tilde{c}(t_j, \theta_k)]^2}$$

where:

$n = 1 \dots N$ is the index of the sequence of records to be ensemble averaged or rotor revolutions considered,

$j = 1 \dots J$ is the index of the time coordinate t or order of the sampled signal in the record,
 $k = 1 \dots K$ is the index of the circumferential position of the probe.

Typical data acquisition parameters for the present investigation are as follows:

Rotational speed	$\omega = 20.94 \text{ rad/s}$
Sampling frequency	$f_s = 10 \text{ kHz}$
Number of data for each rotor blade passage	$I = 100$
Number of measured blade passages	$z = 5$
Dimension of each sampled record	$J = zI = 500$
Number of rotor revolutions or records to be ensemble averaged	$N = 500$
Number of circumferential measuring positions over 1.5 stator pitch	$N = 500$

From verification tests performed in a steady flow calibration wind tunnel the following experimental uncertainties have been estimated [14]:

$$\text{velocity magnitude} = \pm 1 \%, \quad \text{yaw angle} = \pm 1 \text{ deg.}$$

Statistical uncertainties of ensemble averaged quantities due to the finite number of samples with confidence level of 95%, turbulence intensity of 20% and 500 samples are as follows:

$$\varepsilon_c = \pm 1.75 \% \quad \varepsilon_{c'} = \pm 6.2 \% .$$

3. Results and Discussion

The test Reynolds number is based on the stator vane outlet velocity and, as a consequence, depends on the turbine expansion ratio, which is determined by the fan rotational speed. In the present experiment a Reynolds number of 230000 was prescribed. Once the Reynolds number is prescribed, the nominal turbine operating condition can be searched for by imposing null incidence condition on both stators 1 and 2 at midspan. While the incidence angle on stator 1 is easily achieved by adjusting the inlet guide vane stagger angle, the null incidence on stator 2 has to be sought by changing the turbine rotational speed.

Figure 4 shows the ensemble averaged relative velocity and absolute flow angle distributions downstream of rotor 1 at midspan, with the rotational speed as varying parameter. For $\omega/\omega_{nom} = 1$, the mean yaw angle results in 38 deg , i. e. the zero incidence condition on stator 2 is achieved. At this rotational speed the rotor wake velocity defect and the standard deviations of the random fluctuations (Figure 5) indicate a suitable non-separated rotor flow with a moderate tangential extension of the wake.

The pressure side is on the right of the rotor wakes. As expected, the wake defect is larger on the suction side, where the unresolved unsteadiness is also larger. The increase of unresolved unsteadiness in the mid-pitch region of the rotor passage is a

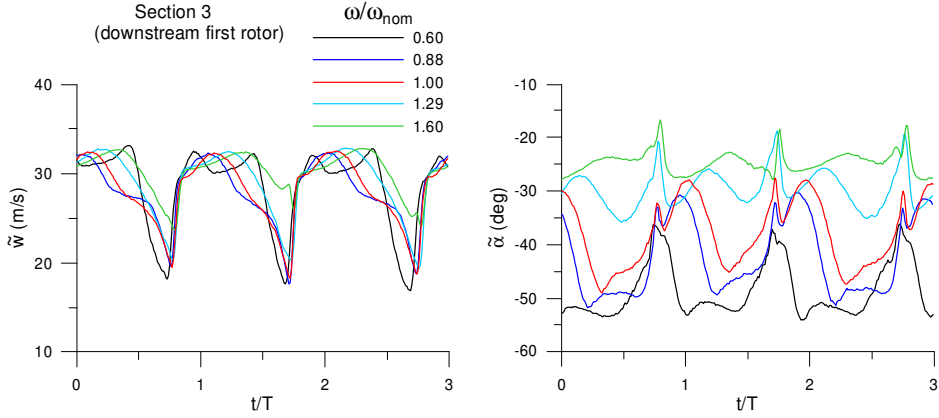


Figure 4. Ensemble averaged relative velocity and absolute flow angle for different turbine rotational speeds

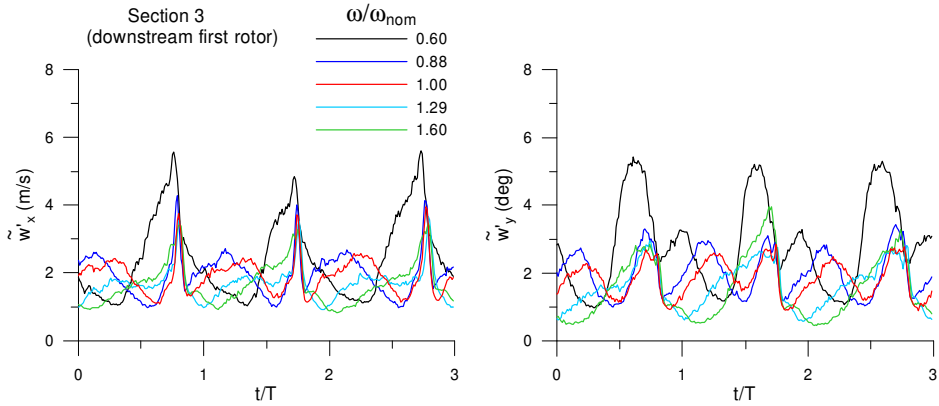


Figure 5. Ensemble averaged velocity fluctuations for different turbine rotational speeds

trace of the vane wake of stator 1. The chopped nozzle wake segments are conveyed through the rotor passages and distorted by the velocity gradients in the rotor passage.

In order to identify flow interaction effects between blade rows, ensemble averaged velocity components and random fluctuations rms are represented in space-time diagrams (Figures 6 to 11). Data for three blade passing periods are plotted on the vertical axis t/T . The normalized circumferential positions of the probe in the absolute frame of reference y/g are plotted on the horizontal axis. Data were measured over 1.5 times the stator pitch g . Stator vane wakes are represented in the plots by

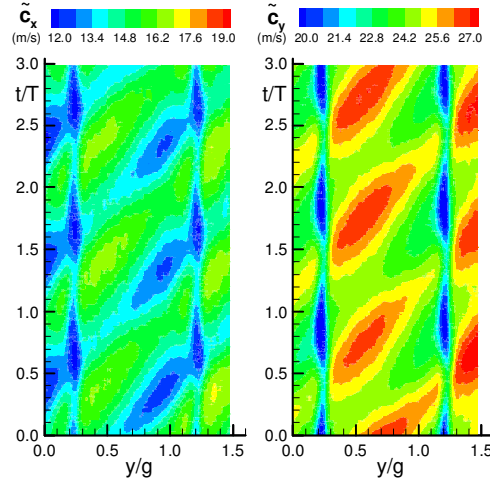


Figure 6. Space-time plots of absolute velocity components: section 2

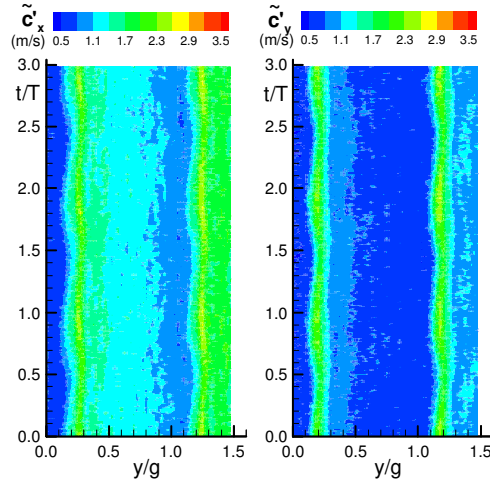


Figure 7. Space-time plots of rms of velocity fluctuations: section 2

vertical lines (fixed absolute circumferential positions), while rotor blade wakes appear as inclined lines since disturbances reach the probe in the absolute frame of reference with the peripheral velocity u . The probe is traversed circumferentially through the vane wake from the suction to the pressure side, therefore the vane suction side is on the left of the vane wakes. Rotor blade wakes hit the probe sensor with the suction

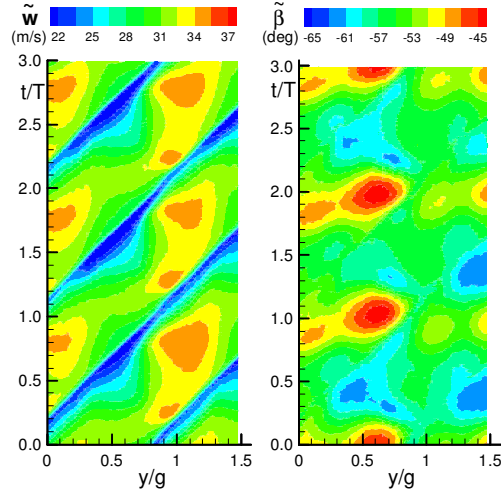


Figure 8. Space-time plots of relative velocity and flow angle: section 3

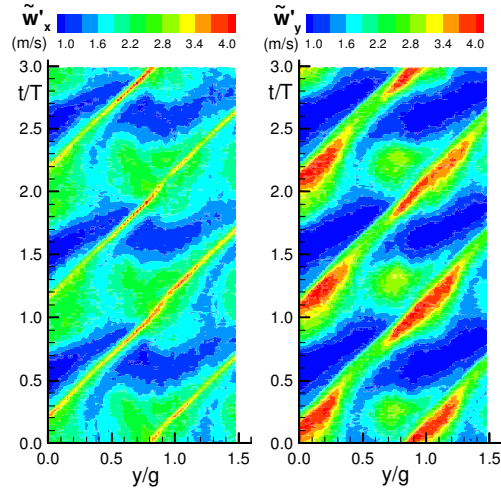


Figure 9. Space-time plots of rms of velocity fluctuations: section 3

side first and then leave the probe with the pressure side. Therefore the rotor blade suction side is on the lower side of the inclined strips.

At station 2 (downstream stator 1) vane wakes are clearly identified by vertical lines displaying the velocity defect (Figure 6) and the increase of random fluctuations (Figure 7). The turbulence level based on the rms of the random velocity fluctuations

and the averaged velocity varies between 2-3 per cent in the free-stream flow and 8-10 per cent in the vane wakes. As expected, the turbulence level is only weakly influenced by the downstream passing rotor blades.

On the contrary, the potential flow effect from the downstream rotor blades on the stator outflow is remarkable. The main effect of the passing rotor blades is to depress both components of the velocity on the suction side of the stator passage, inducing a strong periodic increase of the vane wake defect. The opposite happens on the vane pressure side where the outcoming flow is periodically accelerated.

At station 3 (between rotor 1 and stator 2) the flow pattern is dominated by the wakes shed from rotor blades, identified by the inclined lines showing the velocity defect and the random fluctuations increase (Figures 8 and 9).

In Figure 9 nuclei of relatively large values of rms of the velocity fluctuations are located at a fixed position around $y/g = 0.75$ in the absolute frame of reference. These high turbulence flow patches are the segments of the stator vane wakes chopped by the rotor blades, transported through the rotor and finally shed by each individual rotating channel. In the relative frame these vane wake segments are located between mid-pitch and blade pressure side. According to the analysis of Zaccaria and Lakshminarayana [17] in highly loaded rotor passages the nozzle wake segments are re-oriented near the rotor leading edge and become nearly parallel to the rotor pressure side.

This type of wake redistribution is further confirmed by the results of recent DNS and LES numerical simulations of the wake periodically perturbed flow in a linear cascade equipped with T106 profiles [18]. The numerical results show that high levels of turbulence kinetic energy occur at the passage exit near the vane pressure side where the simulations predict that the bow apex of the chopped wake segment is located.

A second important spatial non-uniformity of the turbulence distributions is the remarkable increase of turbulence around $y/g = 1$ on the suction side of the wake. Presently it is not clear if it is due to a viscous effect (stator 1 vane wakes) or to the potential flow effect of stator 2. Looking at the relative velocity plots of Figure 8, it turns out that these high turbulence wake regions correspond to zones with relatively weak velocity defect. The blade wake velocity defect, in fact, is non-uniform in the absolute frame of reference, and a region with large velocity defect and relatively low turbulence alternates in y/g with a region of relatively low velocity defect and large turbulence. Figure 8 shows the high non-uniformity of the relative flow angle both in time (through the rotor passage) and in space. In general the flow changes from a more tangential direction to a more axial one from suction to pressure side through the blade wake. However, the most striking feature of the flow angle distribution is the presence of nuclei of low absolute values (flow more axial) fixed in space at $y/g = 0.6$. The flow becomes more axial after the rotor blade pressure side has passed in front of the vane leading edge of stator 2 (located at $y/g = 0.3$).

A comparison between the distributions of relative yaw angle at station 3 (downstream rotor 1, Figure 8) and at station 5 (downstream rotor 2, without any other blade row downstream, Figure 10) confirms the significant upstream potential flow

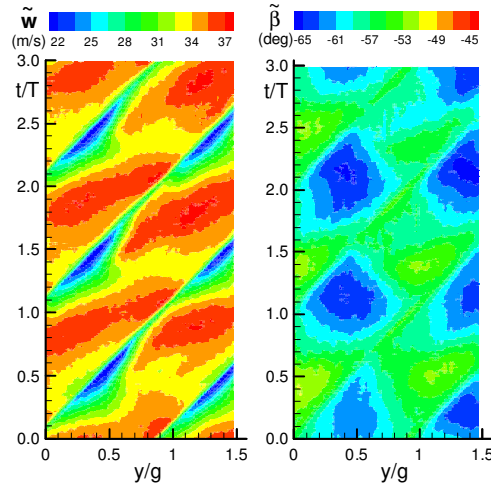


Figure 10. Space-time plots of relative velocity and flow angle: section 5

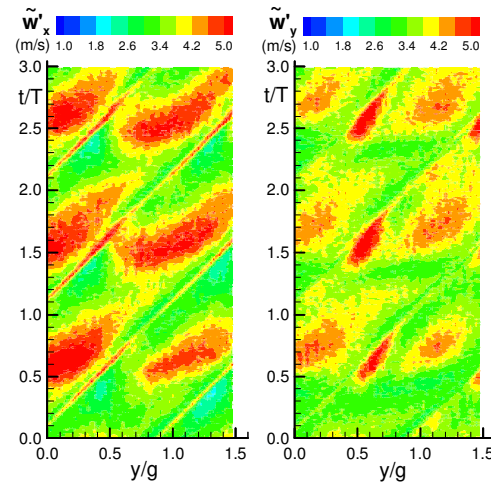


Figure 11. Space-time plots of rms of velocity fluctuations: section 5

effects generated by the downstream vanes of stator 2 on the flow coming out from rotor 1. However, at station 5 a certain circumferential non-uniformity resulting from the presence of the two stators upstream is still evident. Overall the flow leaving rotor 2 is more tangential than the flow leaving rotor 1. Since the geometry of the

two rotors is identical, the downstream stator seems to influence the outflow angle and consequently also the rotor work extraction.

Comparing the relative velocity distributions of Figure 8 and Figure 10 it can be shown that the kinematic fields downstream of the two rotors are very similar. The main difference is that at station 5 the relative velocity is moderately higher than at station 3. That is due to the combined effects of a larger endwall flow obstruction and higher absolute values of relative flow angle at station 5.

At station 5 the rms of random fluctuations (Figure 11) are increased compared with the distributions at station 3, because turbulence is continuously produced through the stages. Turbulence of the second stage nozzle wake segments is added to the diffused background turbulence. The mixing of increased turbulence has flurred the details of the remains of preceding blade row wakes and also the blade wakes of the second rotor are less distinguishable.

4. Conclusions

Results from an experimental investigation of the unsteady flow in a two-stage low-pressure large-scale research turbine were presented. The flow was surveyed upstream and downstream each blade row by means of hot-wire anemometry. In order to study rotor-stator aerodynamic interaction, the flow has been investigated at each measuring axial station moving the probe circumferentially over 1.5 pitches of the stators.

The potential flow unsteadiness generated by the downstream rows is remarkable and comparable to the wake generated unsteadiness. Rotor wakes present a significant spatial non-uniformity in terms of turbulence level and relative velocity defect due to the combined viscous and potential flow effects.

Segments of the wakes of the preceding stator vanes can be easily identified downstream each rotor. Due to the high aerodynamic loading of the blade profiles, the segments are distorted and shifted to mid-pitch and toward the pressure side of the rotor wake streets.

Random fluctuations increase continuously through turbine blade rows. Downstream of rotor 2 the inter-blade turbulence associated with the remains of wake segments of the preceding rows is comparable with rotor 2 blade wake turbulence.

In the near future investigations will be performed in order to separate the effects of wake generated and potential flow interaction mechanisms.

Acknowledgement. This work was supported by MURST (Italian Ministry of University and Scientific and Technological Research) through the PRIN 98 Research Programme.

References

1. HODSON, H.P.: Boundary layer and loss measurements on the rotor of an axial-flow turbine. *ASME Journal of Engineering for Gas Turbines and Power*, **106**, (1984), 391-399.

2. SCHULTE, V. AND HODSON, H.P.: Unsteady wake-induced boundary layer transition in high lift LP turbines. *ASME Journal of Turbomachinery*, **120**, (1998), 28-35.
3. SCHROEDER, TH.: Investigations of blade row interaction and boundary layer transition phenomena in a multistage aero engine low-pressure turbine by measurements with hot-film probes and surface-mounted hot-film gauges, in: *Boundary Layer in Turbomachines, Lecture Series 1991-06, VKI*, 1991.
4. HALSTEAD, D.E., WISLER, D.C., OKIISHI, T., WALKER, G.J., HODSON, H.P. AND SHIN, H.W.: Boundary layer development in axial compressors and turbines. *ASME Journal of Turbomachinery*, **119**, (1997), 225-237.
5. HOURMOUZADIS, J.: Aerodynamic design of low pressure turbines. *AGARD L. S.*, **167**, (1989), 8.1-40.
6. HOWELL, R.J., RAMESH, O.N., HODSON, H.P., HARVEY, N.W. AND SCHULTE, V.: High lift and aft loaded profiles for low pressure turbines. *ASME Paper, 2000-GT-0261*, 2000.
7. BRUNNER, S., FOTTNER, L. AND SCHIFFER, H.-P.: Comparison of two highly loaded low pressure turbine cascades under the influence of wake-induced transition. *ASME Paper, 2000-GT-268*, 2000.
8. STIEGER, R.D. AND HODSON, H.P.: Unsteady Dissipation Measurements on a Flat Plate Subject to Wake Passing, *Proc. 5th European Conference on Turbomachinery*, Praha, Czech Republic, 2003, 901-910.
9. SOLOMON, W.J.: Effects of turbulence and solidity on the boundary layer development in a low pressure turbine. *ASME Paper, 2000-GT-0273*, 2000.
10. SIEVERDING, C.H.: *Trends in Experimental Aero-Thermal Turbine Research*, Invited Lecture, 55^o Congresso ATI, Bari, Italy, 2000.
11. ARNONE, A., CATTANEI, A., NURZIA, F., PACCIANI, R. AND ZUNINO, P.: A two-stage low pressure gas-turbine model for rotor-stator aerodynamic interaction investigations, *Proc. 15th Symposium on Measuring Techniques in Transonic and Supersonic Flows in Cascades and Turbomachines*, Florence, Italy, 2000.
12. HOHEISEL, H., KIOCK, R., LICHTFUSS, H.J. AND FOTTNER, L.: Influence of free-stream turbulence and blade pressure gradient on boundary layer and loss behavior of turbine cascades. *ASME Journal of Turbomachinery*, **109**, (1987), 210-219.
13. ACTON, P.: *Untersuchung des Grenzschichtumschlages an einem hochbelasteten Turbinengitter unter inhomogenen und instationären Zuströmbedingungen*, PhD Thesis, Universität der Bundeswehr, München, Germany, 1998.
14. SCHRÖDER, TH. AND ZUNINO, P.: A new method for the calibration of the directional sensitivity of x-hot-wire probes, *Proc. XVth Bi-Annual Symposium on Measuring Techniques in Transonic and Supersonic Flows in Cascades and Turbomachines*, Florence, Italy, 2000.
15. LAKSHMINARAYANA, B.: Techniques for aerodynamic and turbulence measurements in turbomachinery rotors. *ASME Journal of Engineering for Power*, **103**, (1981), 374-392.
16. UBALDI, M., ZUNINO, P., BARIGOZZI, G. AND CATTANEI, A.: An experimental investigation of stator induced unsteadiness on centrifugal impeller outflow. *ASME Journal of Turbomachinery*, **118**, (1996), 41-54.

17. ZACCARIA, M. A. AND LAKSHMINARAYANA, B.: Unsteady flow field due to nozzle wake interaction with the rotor in an axial flow turbine: Part i - Rotor passage flow field. *ASME Paper, 95-GT-295*, 1995.
18. MICHELASSI, V., WISSINK, J.G. AND RODI, W.: DNS, LES and URANS of periodic unsteady flow in a LP turbine cascade: a comparison, *Proc. 5th European Conference on Turbomachinery Fluid Dynamics and Thermodynamics*, Praha, Czech Republic, 2003, 1185-1195.

A QUADRATIC PETROV-GALERKIN FORMULATION FOR ADVECTION-DIFFUSION-REACTION PROBLEMS IN TURBULENCE MODELLING

ALESSANDRO CORSINI, FRANCO RISPOLI AND ANDREA SANTORIELLO

Department of Mechanics and Aeronautics, University of Rome “La Sapienza”

I00184 Rome, Italy

`corsini@dma.ing.uniroma1.it`

[Received: November 12, 2003]

Abstract. A new stabilized FEM formulation for advective-diffusive-reactive problems is presented. The new method, called Spotted Petrov-Galerkin (SPG), combines two perturbations of quadratic Galerkin weight function: the first one is a generalized SUPG operator, the second one a nodal spot-like controlling operator designed for reactive instabilities. The formulation covers all the combinations of advective and reactive effects, associated with the dimensionless element Peclet and reaction numbers. After an introduction to the method, we assess the reliability of SPG in the control of reactivity related oscillations both in model problems and in turbomachinery turbulence modelling. In the numerical experiments the SPG performance has been compared to classical stabilization schemes, e.g. SUPG.

Mathematical Subject Classification: 76F99, 76M10

Keywords: reaction effects, stabilized finite element method, turbulence modelling

1. Introduction

In this work we focus on the numerical solution of advective-reactive-diffusive problems using the Finite Element Method (FEM) on quadratic space of approximation. Here, diffusion, advection and reaction refer to the terms in the partial differential equations (PDEs) involving second, first and zero order derivatives of the unknowns. This family of equations that governs several phenomena of industrial interest is discussed here because of its importance in the modelling of turbomachinery fluid dynamics.

Several sources of oscillations affect the solution of PDEs in fluid dynamics if standard schemes are used (e.g. central finite differences or Galerkin finite elements). In the finite element framework a number of stabilized formulations have been proposed during the last two decades as remedial strategies. Most of them were based on a Petrov-Galerkin (PG) approach, where the stabilization is achieved preserving the Euler-Lagrange condition's consistency by adding a perturbation to the Galerkin weights (such as SUPG [1-4], or PSPG [3], or Discontinuity Capturing [5] schemes).

An additional origin of instabilities stems from the reaction or zero order derivative terms. Local oscillations arise near boundaries or solution discontinuities and it is not possible to obtain a global stability estimate in the H^1 norm, though it could be evaluated in L^2 [6]. Moving towards the turbomachinery CFD, these terms are usually related to the rotation of turbomachinery frame of reference (e.g. in the modelling of Coriolis forces), but it is worth noting that they appear also in an absorption-like fashion in the turbulence modelling closure equations (e.g. two equations eddy viscosity models (EVM)).

To the best of the authors' knowledge, in the open literature only equal order PG formulations have been developed to control advective-diffusive-reactive flow problems, dealing with scalar equations (e.g. (SU+C)PG in [7]) or linear reactive operators [8]. Few studies are concerned with reactive problems pertinent to real turbomachinery fluid dynamics [6].

From this viewpoint, the present work addresses the definition of a new Petrov-Galerkin stabilization scheme for the reactive flow limit, formulated on a quadratic finite element space of approximation. The use of a higher order stabilized formulation, though its complexity is due to the non-negligibility of second order derivatives, guarantees the best compromise between solution stability and accuracy [9]. In particular, the authors propose a stabilized formulation that performs well both in the advection and in the reaction dominated case. The new method is called *Spotted Petrov-Galerkin* (SPG) and possesses some distinctive features. For advection-diffusion problems it behaves like a SUPG method, whereas in the reactive-diffusive limit the space invariant problem is controlled by a perturbation able to give rise to spot-like weight functions, symmetric and concentrated around each nodal position. In intermediate situations, the scheme combines the perturbation integrals using tuning or *upwind* coefficients that depend on element Peclet and reaction numbers.

The remainder of the paper is organized as follows. In Section 2 the SPG formulation is presented for linear scalar advective-diffusive-reactive equations. The extension of the formulation to multi-dimensional case is discussed, and the family of weights for Q2 element is shown. In Section 3 the reactivity features of general PDE that models the budget of turbulent determining-scale variables are commented on. Finally in Section 4 the performance of SPG is assessed in three test cases against solutions provided by SUPG, Streamline Upwind or Galerkin.

2. Finite element scalar advective-diffusive-reactive problem

2.1. Introductory remarks. Let us take the general linear scalar advective-reactive-diffusive problem statement on the closed domain Ω for the unknown ϕ :

$$\begin{aligned} u_j \phi_{,j} - k \phi_{,jj} + c \phi &= f, & (j = 1, nsd) \\ \phi(\Gamma_g) &= \phi_g, \\ \phi_{,n}(\Gamma_h) &= \theta_n, \end{aligned} \tag{2.1}$$

where nsd is the number of space dimensions, $k > 0$ is constant diffusivity, u_j are the velocity components, $c \geq 0$ is the reaction coefficient, and f is the source term. The

boundary conditions are specified along $\Gamma = \underline{\Gamma}_h \cup \underline{\Gamma}_g$ ($\underline{\Gamma}_h$ and $\underline{\Gamma}_g$ are closed, disjoint subsets of Γ), including Dirichlet (ϕ_g) and Neumann conditions (θ_n).

A finite element partition of the original closed domain $\underline{\Omega}$ into elements Ω_e , $e = 1, \dots, nel$ (nel number of elements) reads as

$$\cup_e \Omega_e = \Omega \quad \text{and} \quad \cap_e \Omega_e = \emptyset \quad (2.2)$$

with the definition of interior boundary as $\Gamma_{int} = \cup_e \Gamma_e - \Gamma$.

Let us define the finite dimensional spaces of trial and weight functions as:

$$S^h = \phi^h | \phi^h \in H^{1h}(\Omega), \phi^h = \phi_g \text{ on } \Gamma_g, \quad \phi_g \in H^{(1/2)h}(\Gamma_g) \quad (2.3)$$

$$W^h = \{w^h | w^h \in H_0^{1h}(\Omega), w^h = 0 \text{ on } \Gamma_g\} \quad (2.4)$$

where $H^{1h}(\Omega)$ and $H_0^{1h}(\Omega)$ are the Sobolev spaces for the continuous pair of finite element functions, $H^{(1/2)h}(\Gamma_g)$ is their restriction to the domain boundary, and the superscript h denotes the characteristic length scale of the domain discretization.

The Galerkin weak formulation of problem (2.1) reads as follows:

$$\begin{aligned} \sum_{e=1}^{nel} \int_{\Omega_e} w^h u_j \phi_{,j}^h d\Omega + \sum_{e=1}^{nel} \int_{\Omega_e} w_{,j}^h k \phi_{,j}^h d\Omega + \\ \sum_{e=1}^{nel} \int_{\Omega_e} w^h c \phi^h d\Omega = \sum_{e=1}^{nel} \int_{\Omega_e} w^h f d\Omega + \int_{\Gamma_h} w^h k \frac{\partial \phi^h}{\partial n} d\Gamma. \end{aligned} \quad (2.5)$$

2.2. Galerkin formulation in one dimension. Let us consider the ordinary differential equation obtained from (2.1) for $nsd = 1$ and source term $f = 0$. The problem statement reads as:

$$u \frac{d\phi}{dx} - k \frac{d^2\phi}{dx^2} + c\phi = 0, \quad (2.6)$$

The discretization of (2.6) by using the Galerkin method on a quadratic space of interpolation with uniform elements of length h , in case of constant coefficients leads to the following difference equations:

$$\phi_{i-1}[-4 - 2Pe + r/10] + \phi_i[8 + r4/5] + \phi_{i+1}[-4 + 2Pe + r/10] = 0 \quad (2.7)$$

if (i) is chosen as element central node and

$$\begin{aligned} \phi_{i-2}[1 + Pe - r/10] + \phi_{i-1}[-8 - 4Pe + r/5] + \\ \phi_i[14 + r4/5] + \phi_{i+1}[-8 + 4Pe + r/5] + \phi_{i+2}[1 - Pe - r/10] = 0 \end{aligned} \quad (2.8)$$

if $(i-2, i, i+2)$ are chosen as element extreme nodes.

In the above equations, the magnitudes of advection or reaction versus diffusion are, respectively, given by element Peclet number $Pe = ||u|| h/2k$, and element reaction number $r = ch^2/k$.

Let us now focus on the element central node (i) . Now the null advection limit equation (2.7) reads as:

$$\phi_{i-1}[-4 + r/10] + \phi_i[8 + r4/5] + \phi_{i+1}[-4 + r/10] = 0 . \quad (2.9)$$

The solutions of the characteristic equation associated with (2.9), which are the so-called Galerkin nodal amplification factors [8], purely depend on the magnitude of reaction:

$$\rho = \frac{-(8 + \frac{4}{5}r) \pm \sqrt{(8 + \frac{4}{5}r)^2 - 4(-4 + \frac{r}{10})^2}}{2(-4 + \frac{r}{10})} \quad (2.10)$$

where it could be easily seen that the exact solution exponential behavior is preserved only with $r < 40$. This circumstance confirms the need for a stabilized scheme with built-in component to preclude oscillatory behavior in reaction dominated cases.

2.3. SPG formulation. The stabilized SPG formulation is obtained by imposing nodal exactness on the numerical solution of problem (2.6). Provided that different equations have been obtained for the extreme and central nodes [4], it is possible to find two optimal perturbations, on the basis of the discrete equations (2.7) and (2.8) separately.

The PG weight functions now result from the addition to the Galerkin ones w_i of two perturbations P_{1i} and P_{2i} as:

$$\tilde{w}_i = w_i + \alpha P_{1i} + \gamma P_{2i} \quad (2.11)$$

with α and γ being the tuning coefficients for element central nodes, and

$$\tilde{w}_i = w_i + \beta P_{1i} + \eta P_{2i} \quad (2.12)$$

with β and η being the tuning coefficients for element extreme nodes.

The first perturbation is formally similar to a SUPG one and reads as:

$$P_{1i} = \frac{h}{2 \|u\|} u_k w_{,k} . \quad (2.13)$$

On the other hand, the design of P_{2i} is based on the following constraints. First, in *null advection* case the invariance of the equation under coordinate inversion suggests preserving the weight symmetry [7]. Moreover, in the *pure reaction* limit ($r \rightarrow \infty$), the optimal weight would be a Dirac's delta. On this basis, the expression of P_{2i} suggested by the authors is a polynomial of the sixth order, negative definite inside each element:

$$P_{2i} = -\frac{C_{SPG}}{h^6} [\xi^6 - \frac{h^2}{2} \xi^4 + \frac{h^4}{16} \xi^2], \quad (2.14)$$

where ξ represents the coordinate in the master or logic space, and the coefficient C_{SPG} sets the asymptotic values of reactive tuning functions γ and η , without affecting α and β .

Figure 1 shows the perturbation P_{2i} and the resulting weight functions for nodes of two neighboring elements, for one-dimensional quadratic elements in case of null advection with varying γ and η coefficients. The weights are plotted for $C_{SPG} = (2^{12}/3^2) \times 0.35$. This value stems from the fulfillment of seven constraints for P_{2i}

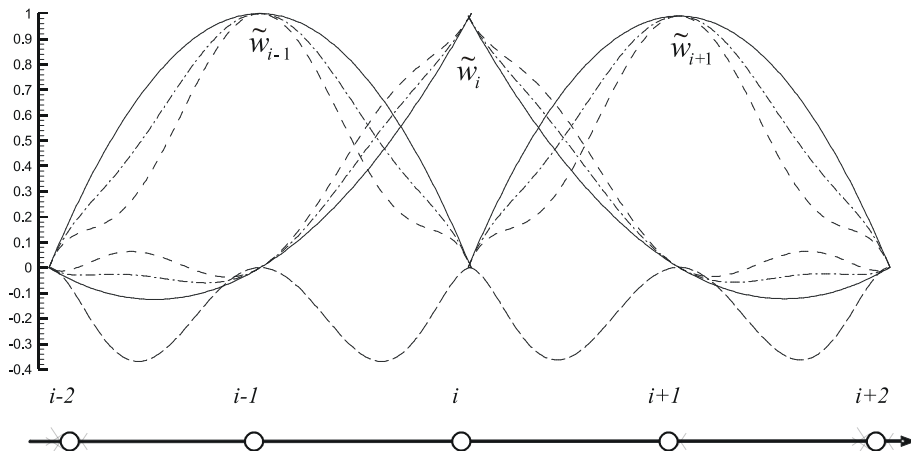


Figure 1. 1D null advection. Resulting nodal weights for neighboring elements (solid lines: $\gamma = -2\eta = 0$; dashdot lines: $\gamma = -2\eta = 0.5$; dashed lines: $\gamma = -2\eta = 1$; longdash lines: P_{2i} function)

perturbation on quadratic elements, including null nodal values and derivatives, and P_{2i} magnitude at $\xi = \pm h/4$.

The expression for the tuning functions α and γ , and β and η are consequent to the super-convergence condition. Figures 2.a and 2.b show the behaviors of α and γ for different combinations of Pe and r . Furthermore, Figures 3a and 3b show those of β and η tuning functions.

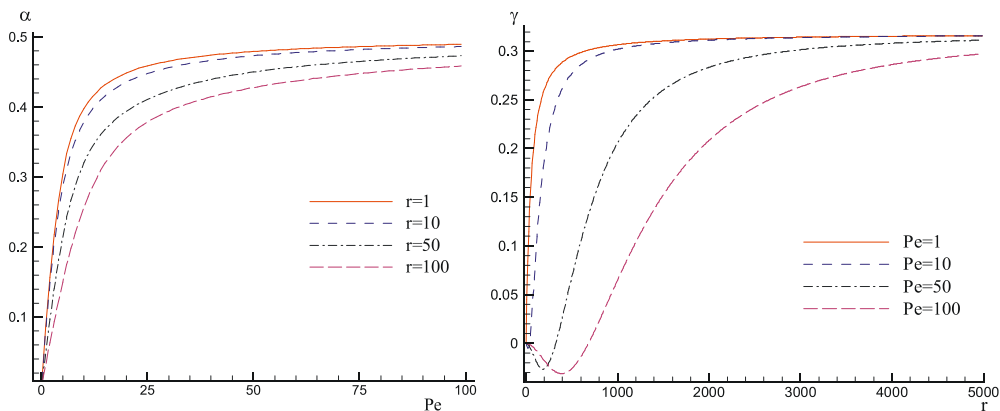


Figure 2. Tuning functions: a) α and b) γ

2.4. Extension of SPG formulation to multi-dimensional case. The 2D extension of the P_{2i} function has been designed to preserve its 1D requirement, that is the isotropic concentration of the perturbed weight around the nodal positions. To this end, we designed a Cartesian product between the 1D counterparts of the second

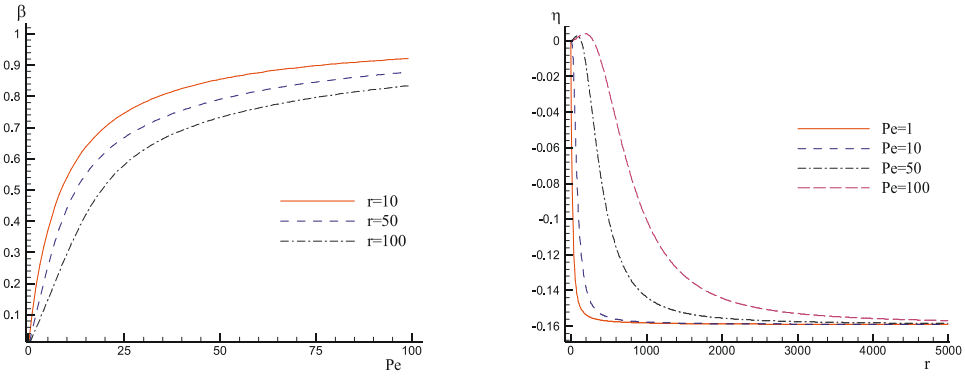


Figure 3. Tuning functions: a) β and b) η

perturbation function, where the P_{2i} spots are moved in the element portion closer to the corresponding nodes.

This concept is depicted in Figure 4, which shows the resulting geometries for the two-dimensional second perturbation functions on logic space.

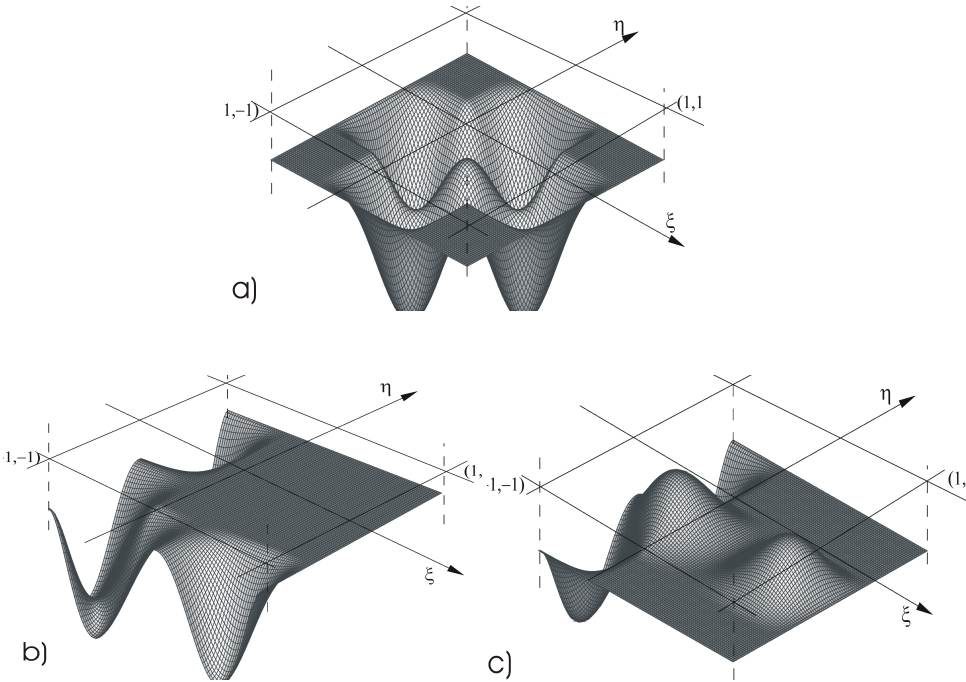


Figure 4. 2D P_{2i} functions in the logic space: a) central-central node (0,0), b) corner node (-1,-1), c) mid-side node (-1,0)

3. Problem statement for EVM

Let us now examine the determining-scale equations in a first moment turbulence closure. The general steady-state advective-diffusive-reactive equation used to model the budget of a turbulent variable ϕ (i.e. ϕ could represent the turbulent viscosity ν_t , the turbulent kinetic energy k , or the dissipation ε) reads as:

$$F_{\phi a} + F_{\phi d} = P_{\phi} + \varepsilon_{\phi} + S_{\phi} \quad (3.1)$$

here: $F_{\phi a}$ are the convective fluxes, $F_{\phi d}$ are the diffusive fluxes, P_{ϕ} is the production, ε_{ϕ} is the dissipation (or destruction) term, and S_{ϕ} is the term containing the near wall extra sources. When the standard $k - \varepsilon$ model proposed by Launder and Sharma (1974) [10] is used, the budget structure (3.1) gives rise to the terms sketched in Table 1.

Table 1. $k - \varepsilon$ turbulence model equations; budget

	k	ε
$F_{\phi a}$	$\rho u_j k_{,j}$	$\rho u_j \varepsilon_{,j}$
$F_{\phi d}$	$-[(v + \frac{v_t}{\sigma_k})k_{,j}]_{,j}$	$-[(v + \frac{v_t}{\sigma_k})\varepsilon_{,j}]_{,j}$
P_{ϕ}	$v_t[u_{i,j} + u_{j,i}]u_{i,j}$	$c_1 f_1 \frac{\varepsilon}{k} v_t[u_{i,j} + u_{j,i}]u_{i,j}$
ε_{ϕ}	$-\frac{\varepsilon}{k}k$	$-c_2 f_2 \frac{\varepsilon}{k}k$
S_{ϕ}	0	$E = 2 v v_t (\frac{\partial^2 u_i}{\partial x_j \partial x_k})^2$

In Table 1: $\nu_t = c_{\mu} f_{\mu} k^2 / \varepsilon$ is the scalar eddy viscosity; f_1, f_2, f_{μ} are damping functions; $c_1, c_2, c_{\mu}, \sigma_k, \sigma_{\varepsilon}$ are empirical constants. The extra term E is the buffer-layer source to correct the near wall dissipation behaviour.

It is worth mentioning that in the numerical approach developed, the dissipation integrals ε_{ϕ} explicitly contain the reaction terms and, for the EVM under study, they are made proportional to the inverse of turbulence time scale $\tau = k / \varepsilon$. These integrals are included as left-hand side (LHSV) contributions to the coefficient matrix. By that way a strong coupling is built between the $k - \varepsilon$ determining-scale equations in order to improve the solver convergence.

4. Numerical examples

4.1. The examples presented. In this section we assess the numerical performance of the proposed SPG formulation for model problems and for configurations pertinent to turbomachinery fluid dynamics. In these validation studies the improvement of the SPG are discussed with respect to the classical stabilization schemes, such as the SUPG or Streamline Upwind. It is remarkable that, since all the stabilization schemes usually share the optimum property in 1D, all the investigated test cases violate one of the super-convergence conditions (i.e. non-uniform mesh, multidimensional domain, non-linear equations and problems with source terms).

4.2. Scalar advective-diffusive-reactive equation on a square domain. The first test cases (labeled TC1 and TC2) concern the numerical solution of the linear scalar advective-diffusive-reactive model problem (2.1), in a unit square domain. The mesh is uniform with 10×10 quadratic elements, thus consisting of 441 nodes. For both TC1 and TC2 the known velocity field u is assumed to have a parabolic profile (e.g. $u(x, y) = 2y - y^2$, $v(x, y) = 0$), with maximum value equal to 1. The coefficients are: $k = 10^{-5}$, $c = 5 \times 10^2$. The maxima for dimensionless element numbers are: $Pe = o(10^3)$ and $r = o(10^5)$. As concerns the source term, TC1 has null f value, whereas in TC2 a non-uniform f has been adopted with a peak value equal to $50 \phi_{BC}$. For both the test cases the SPG solutions are compared to quadratic Galerkin (G Q2), and SUPG Q2 ones. Concerning TC1, the complete problem statement and the solution fields for Galerkin and SPG are shown in Figure 5.

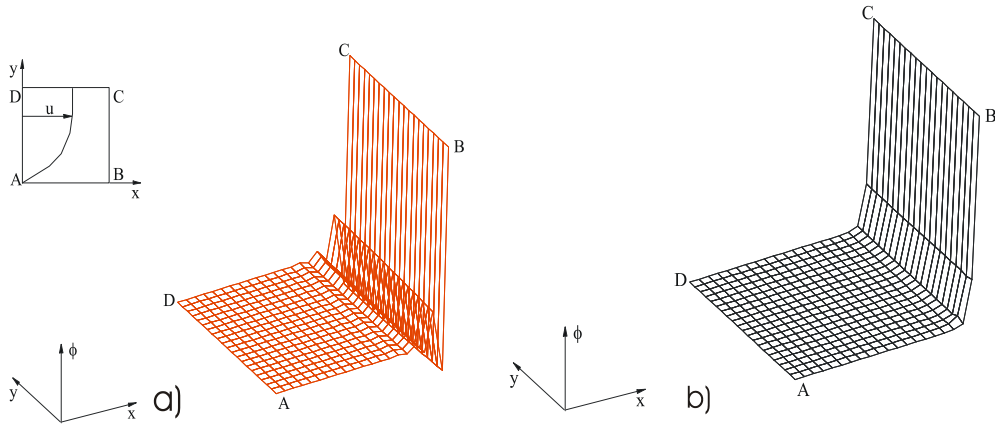


Figure 5. Scalar advective-diffusive-reactive problem statement TC1 ($f = 0$) and solution fields: a) G Q2 and b) SPG

As it clearly appears, the proposed SPG formulation is able of controlling completely the instability origins in the near- and far-wall regions. Figure 6 shows the ϕ streamwise profiles predicted by G Q2, SUPG Q2 and SPG schemes at $y = 0.05$ where reaction dominates. The PG-like solutions are both able to predict smooth ϕ profiles, thus improving the G Q2 oscillatory behaviour. Nonetheless, the SUPG Q2 returns an over-diffused layer close to the Dirichlet bound. This confirms its inability to control the reactive effects, with respect to SPG solution that predicts a sharp but continuous solution layer.

As far as the TC2 case is concerned, in Figure 7 the problem statement and the SUPG Q2 and SPG solutions are shown. It is worth noting that the source integral has been approximated linearly, according to Q2 element optimal conditions [4].

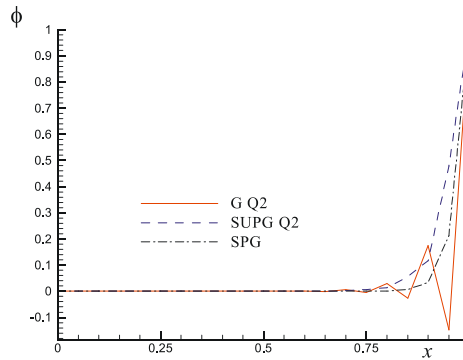


Figure 6. TC1 comparison of streamwise ϕ profiles at $y = 0.05$

Moreover, Figure 8 shows the ϕ streamwise profiles predicted by G Q2, SUPG Q2 and SPG schemes at $y = 0.05$, where the reactive effect is combined with a positive gradient of the source.

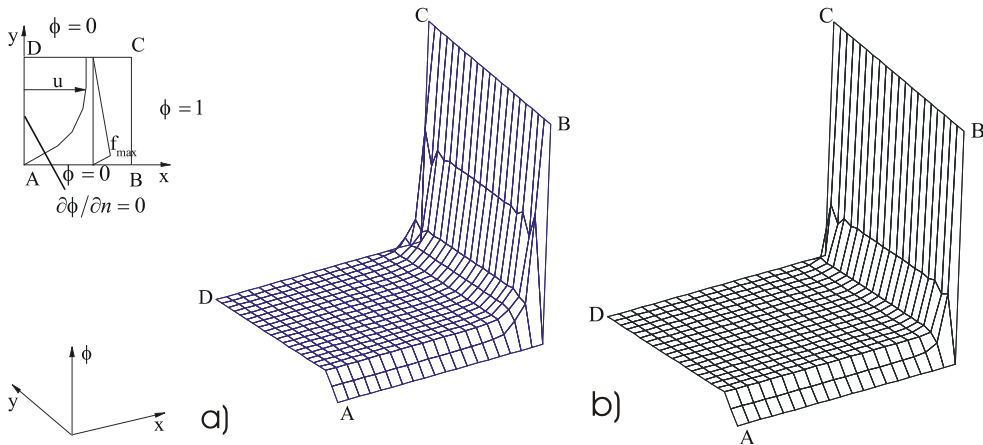


Figure 7. Scalar advective-diffusive-reactive problem statement TC2 ($f_{max(y=0.1)} = 50$) and solution fields: a) SUPG Q2 and b) SPG

The comparison between stabilized PG schemes confirms that the SPG is able to totally recover a non-oscillatory solution, also where the sharp streamwise solution layer develops under the effect of a non-uniform source.

4.3. Semi-circular leading edge. The last test case concerns the prediction of the turbulent boundary layer development on a flat plate, with a semi-circular leading edge. The leading edge configuration is that proposed by ERCOFTAC Special Interest Group on Transition in 1991 (labelled T3L). The experimental data have been provided by Palikaras et al. [11], for the zero pressure gradient configuration.

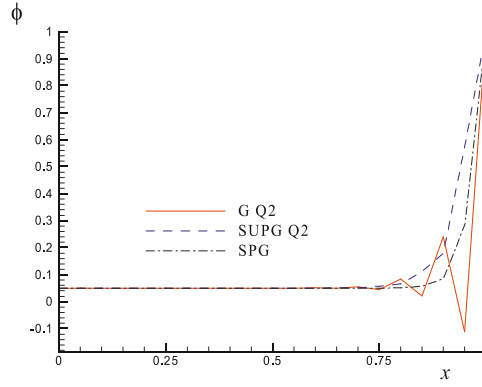


Figure 8. TC2 comparison of streamwise ϕ profiles at $y = 0.05$

The Reynolds number, based on inlet velocity and leading edge radius ($e_r = 5\text{ mm}$) is equal to 1660. The free stream turbulence intensity (TI) at the inlet is set to 7%, and the chosen dissipation length l_ε is 18 mm .

The flow is assumed two-dimensional with constant temperature and incompressible. A 12681 node block-structured (H-O) grid has been used. In the vicinity of the wall (O-connected region) the nearest node to the solid wall has a dimensionless distance $\delta^+ = 1.0$. At the inlet section of the computation domain, the experimental free-stream uniform profile is used for the mean velocity ($u = 5\text{ m/s}$). Uniform distributions are also imposed on the turbulent variables, computed on the basis of TI and l_ε . No-slip conditions are then applied on the solid surface, and homogeneous Neumann conditions are imposed at the outlet section.

The SUPG and SPG formulations have been used on Q2Q1 elements, with PSPG-like relaxation of incompressibility constraint. The turbulence closure is the standard $k - \varepsilon$ model [10], in its near wall extension. A GMRes(50) solver has been used with convergence thresholds for error R_{res} and solution R_{sol} residuals set to 10^{-6} . The convergence histories are first compared in Figure 9, clearly showing the faster convergence of SPG compared to the SUPG scheme. Figures 10 and 11 show the streamwise turbulence intensity and velocity profiles computed in two locations close to the leading edge stagnation point at $x/e_r = 2.4$ and $x/e_r = 3.2$, respectively. The predicted velocity and turbulence intensity profiles agree with published numerical studies using isotropic EVMs (e.g. [10]). To this end, the stabilized formulations are able to give a good prediction of the free-stream values. Notwithstanding, the near wall region is affected by an over-prediction of TI level and layer thickness related to the stagnation point anomaly [12]. With respect to the comparative performance between PG schemes, the solutions do not show appreciable differences, as shown in Figures 10 and 11.

This evidence confirms that in a flow region dominated by the effect of advection, such as the flat plate region downwind the leading edge, where the maximum reaction

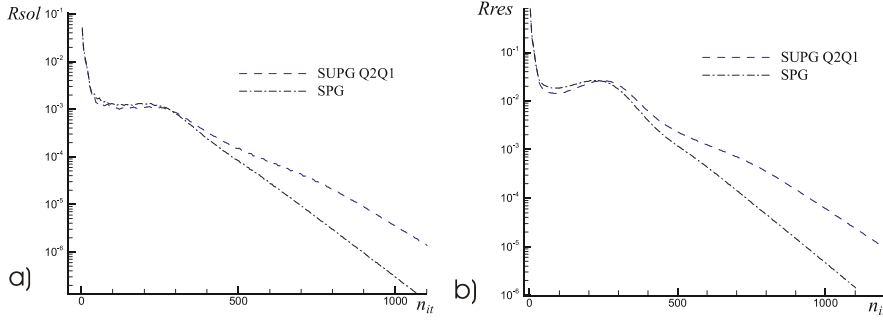


Figure 9. T3L convergence histories for PG formulations: a) R_{sol} and b) R_{res}

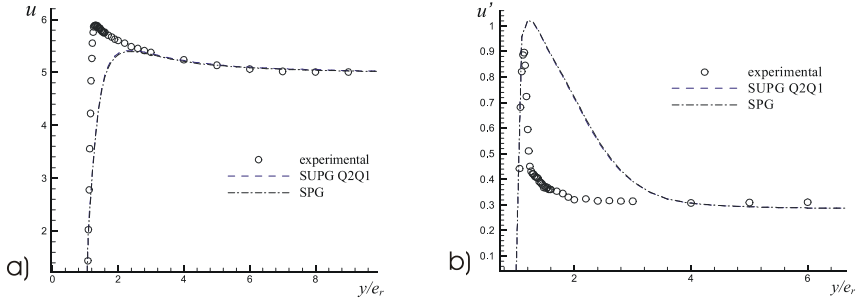


Figure 10. Comparison of streamwise: velocity $u(m/s)$ a) and turbulence intensity $u'(m/s)$ b) at $x/e_r = 2.4$

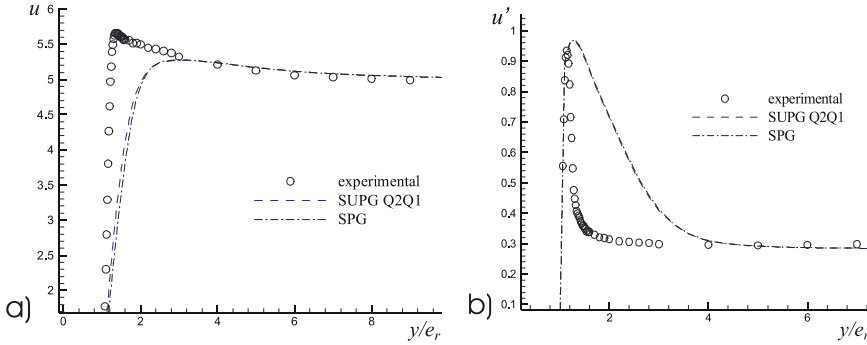


Figure 11. Comparison of streamwise: velocity $u(m/s)$ a) and turbulence intensity $u'(m/s)$ b) at $x/e_r = 3.2$

number is of $o(10^2)$, the SPG correctly annihilates its sensitivity to the equation reactivity recovering a SUPG-like behaviour. Moving upwind in the stagnating flow region, some distinguishing feature of the proposed SPG could be found. To this end

in Figures 12 and 13 are compared, respectively, the computed TI and turbulence time scale profiles along the stagnation streamline.

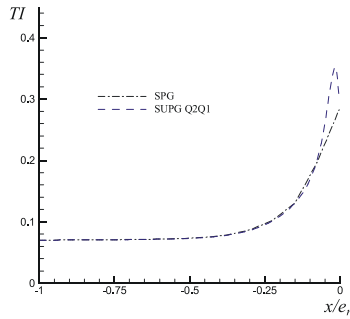


Figure 12. Comparison of TI profiles along the stagnation streamline

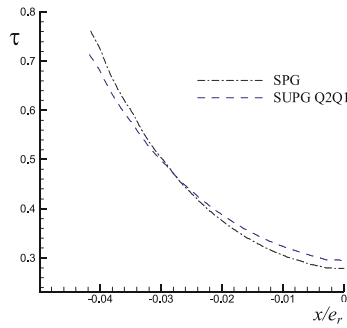


Figure 13. Comparison of τ profiles along the stagnation streamline

The comparison of turbulence intensity profiles, in Figure 12, demonstrates that the SPG is able to reduce the TI peak ($TI_{SPG} = 28\%$ instead $TI_{SUPG} = 36\%$). This suggests that approaching a null-advection region, the SPG partially corrects one of the well recognized drawbacks of linear two-equation EVMs, the so-called stagnation point anomaly. Figure 13 shows that this remarkable feature of SPG formulation is related to the capacity of controlling the over-prediction of turbulence time scale in the pure reactive-diffusive flow limit. In this condition, the SPG perturbation activates a dependence of weights from the predicted turbulence scale intensity able to affect the corresponding residual projection basis.

5. Conclusions

The paper investigated the prediction capabilities of a FEM stabilized formulation developed for the purpose of solving advective-diffusive-reactive problems. This scheme, called SPG, addresses the use of a perturbation to the weight function composed by

two contributions. The first is a SUPG-like operator and is used to overcome instabilities due to advective or skew-symmetric terms, whereas the second operator is a symmetric one aiming at precluding oscillations due to reactive terms. The FEM formulation has been obtained by means of one-dimensional nodal exactitude, but has been tested in several more complex examples that violate the super convergence conditions. In this respect, the SPG method demonstrates its suitability for solving the typical equations of turbulence EVMs used in turbomachinery CFD.

Acknowledgement. The authors acknowledge MIUR under the projects COFIN 2001, and MIUR-Ateneo 2001.

References

1. HUGHES, T.J.R. AND BROOKS, A.N.: Streamline Upwind/Petrov-Galerkin formulations for convection dominated flows with particular emphasis on the incompressible Navier-Stokes equations. *Comp. Meth. Appl. Mech. Eng.*, **32**, (1982), 199–259.
2. HUGHES, T.J.R. AND BROOKS, A.N.: A theoretical framework for Petrov-Galerkin methods with discontinuous weighting functions: application to the streamline-upwind procedure. *Finite Elements in Fluids*, **4**, (1982), 47–65.
3. TEZDUYAR, T.E., MITTAL, S., RAY, S.E. AND SHIH, R.: Incompressible flow computations with stabilized bilinear and linear equal-order-interpolation velocity-pressure elements. *Comp. Meth. Appl. Mech. Eng.*, **95**, (1992), 221–242.
4. CODINA, R., OÑATE, E. AND CERVERA, M.: The intrinsic time for the streamline upwind/Petrov-Galerkin formulation using quadratic elements. *Comp. Meth. Appl. Mech. Eng.*, **94**, (1992), 239–262.
5. HUGHES, T.J.R., MALLETT, M. AND MIZUKAMI, A.: A new finite element formulation for computational fluid dynamics: II. Beyond SUPG. *Comp. Meth. Appl. Mech. Eng.*, **54**, (1986), 341–355.
6. CODINA, R.: A stabilized finite element method for generalized stationary incompressible flows. *Comp. Meth. Appl. Mech. Eng.*, **190**, (2001), 2681–2706.
7. IDELSOHN, S., NIGRO, N., STORTI, M. AND BUSCAGLIA G.: A Petrov-Galerkin formulation for advection-reaction-diffusion problems. *Comp. Meth. Appl. Mech. Eng.*, **136**, (1996), 27–46.
8. HARARI, I., AND HUGHES, T.J.R.: Stabilized finite element methods for steady advection-diffusion with production. *Comp. Meth. Appl. Mech. Eng.*, **115**, (1994), 165–191.
9. BORELLO, D., CORSINI, A. AND RISPOLI, F.: A finite element overlapping scheme for turbomachinery flows on parallel platforms. *Computers & Fluids*, **32**(7), (2003), 1017–1047.
10. LAUNDER, B.E., AND SHARMA, B.I.: Application of the energy dissipation model of turbulence to the calculation of flow near a spinning disc. *Letter in Heat and Mass Transfer*, **1**, (1974), 131–138.
11. PALIKARAS, A., YAKINTHOS, K. AND GOULAS, A.: Transition on a flat plate with a semi-circular leading edge under uniform and positive shear free-stream flow. *Int. J. Heat Fluid Flow*, **23**, (2002), 455–470.
12. DURBIN, P.A.: On the $k-\varepsilon$ stagnation point anomaly. *Int. J. of Heat and Fluid Flow*, **17**, (1996), 89–90.

NUMERICAL AND EXPERIMENTAL INVESTIGATIONS OF CROSS-FLOW FANS

MARTIN GABI AND TONI KLEMM
Universität Karlsruhe (TH)
D-761289 Karlsruhe, Germany
martin.gabi@mach.uka.de

[Received: November 12, 2003]

Abstract. The prediction of performance characteristics and flow field data of cross-flow fans (CFF) is difficult due to the complex flow structure and working principle. Numerical methods will become more important in order to get a better knowledge of the complex flow-phenomena in CFF and will lead to a reduction of experimental work in the process of development and construction. CFD calculations are carried out to compute the flow field and the performance of CFF. For the validation of the numerical computations, experimental investigations are made to measure flow field and performance data. In the flow field measurements mainly Particle Image Velocimetry (PIV) is used.

Keywords: cross-flow fan, CFD, particle image velocimetry

1. Nomenclature

D_2	[m]	impeller outer diameter
D_1	[m]	impeller inner diameter
L	[m]	blade length
M	[Nm]	rotor torque
n	[s ⁻¹]	rotation speed
Δp	[Pa]	pressure difference
Q	[m ³ /s]	volume flow rate
Re	[-]	Reynolds number
S	[m]	blade chord length
U_2	[m/s]	peripheral speed
V	[m/s]	velocity (local or global)
φ	[-]	volume flow coefficient
ψ	[-]	pressure coefficient
ν	[m ² /s]	kinematic viscosity
ρ	[kg/m ³]	fluid density
ω	[s ⁻¹]	angular velocity

2. Introduction

Cross-flow fans (CFF), as per Figure 1, are used in cooling, heating, air conditioning systems, in automotive applications as well as in industrial applications e.g. for heating and drying purposes.

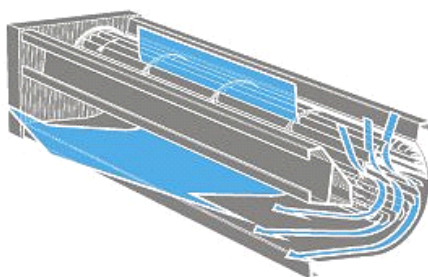


Figure 1. Typical construction of a CFF

They consist of a broad cylindrical rotor with many forward curved blades of a high ratio of diameter $D1/D2$. The air passes the blade grid twice, driven by a large vortex, the steering vortex, situated inside and outside of the impeller, near the so called stabilizer, see Figure 2 and 3.

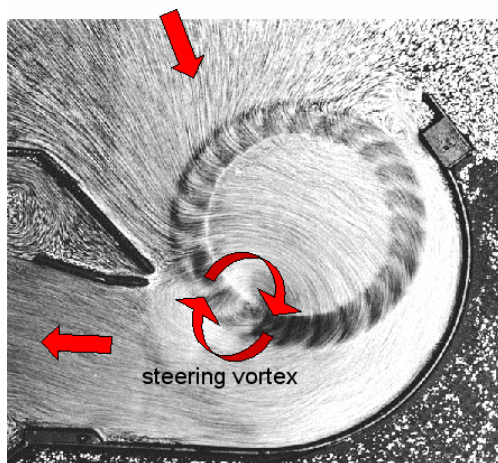


Figure 2. Flow field

Position, size and intensity of this vortex is strongly influenced by geometrical parameters of the casing and the point of operation (volume flow rate and pressure difference) of the CFF [1] .

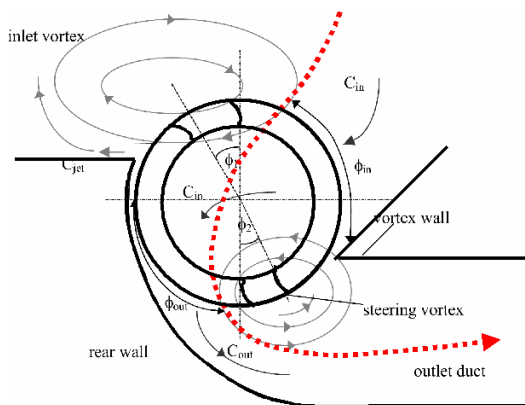


Figure 3. Global flow pattern

Depending on geometry and operating conditions also secondary vortices in the inlet and outlet zones may appear. The flow field and the performance characteristics of a CFF depend much more significantly on the shape of the surrounding casing than on the design of the rotor and the blade grid. Because of the principle of operation, the performance characteristics of a CFF is characterized by high volume flow and pressure coefficients, in comparison to other fan types, see Figure 4.

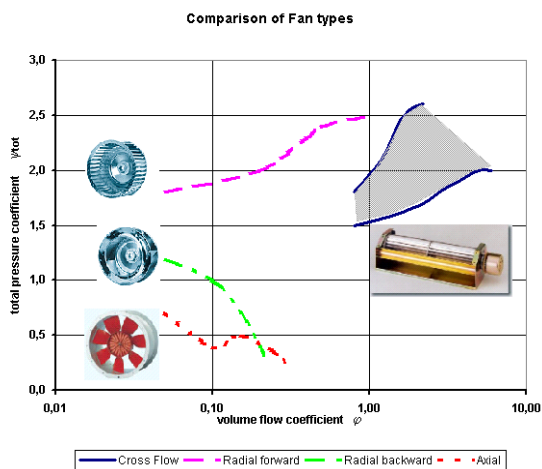


Figure 4. Comparison of fan types

Due to the complex flow structure, the design process is still mainly based on numerous experiments, because classical design methods are not applicable to a CFF in a satisfying way. It is helpful to use numerical methods for getting a better impression of the complex flow phenomena of a CFF and to reduce the number of experiments

in the process of design, development and construction. Therefore CFD calculations are used to compute the flow field and the performance characteristics of CFF [4].

In order to validate and prove the numerical computations, experimental investigations are made to measure the flow field and the performance characteristics. For the flow field measurements mainly the Particle Imaging Velocimetry (PIV) method is used [3, 5].

3. Numerical simulation

The object of the numerical simulations is to get a better impression of the flow field in a CFF, particularly inside the impeller. The results of these numerical investigations should be the basis to develop guidelines for the design and construction of efficient CFF. The main objective is to develop numerical procedures to obtain the flow variables determining the characteristics of CFF, such as pressure coefficient and efficiency vs. volume flow coefficient as well as velocity and pressure fields.

In the literature only few papers dealing with CFD calculation of the flow in CFF are published. Mainly the flow is considered to be two-dimensional, inviscid and steady. The impeller usually is modelled by an infinite number of thin blades. More recent studies try to take into account transient and viscous effects, but need the calibration of constants used in the mathematical modelling using experimental investigations. Today the development of hardware and calculation methods allows calculation of the complete flow inside the CFF. Most of the commercial CFD software packages are based on finite volume methods (FVM). The FVM is also implemented in the software package STAR-CD, which is used for the present investigations [6].

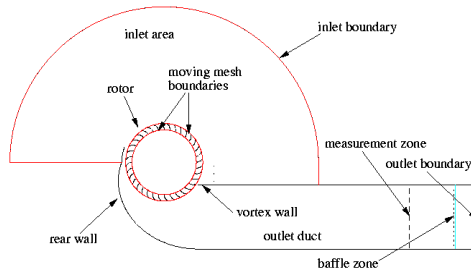


Figure 5. Computational domains and boundaries

Figures 5 and 6 show computational domains and boundaries. The model of Figure 5 shows a very simple configuration, which is very well documented in literature [2]. Figure 6 shows the typical configuration of a frequently used geometry with a 90 degree deflection. Because of the distinctive transient character of the flow through the impeller, it is necessary to use a transient method in the impeller domain. The

link between the rotating impeller domain and the casing domain is realised by a sliding interface.

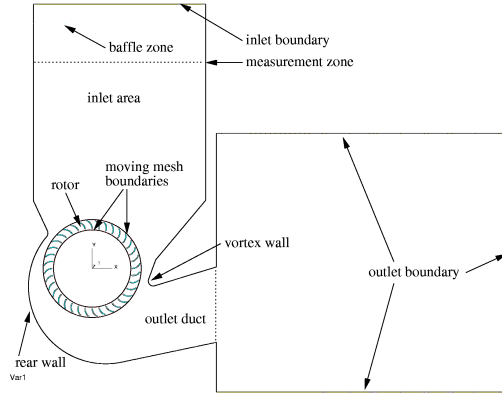


Figure 6. Computational domains and boundaries

An ‘arbitrary sliding mesh method’ (ASI), which is implemented in STAR-CD, is used to simulate the movement of the different mesh regions. The ‘sliding’ involves a continuous change in connectivity for cells on each side of the interface. Due to an indirect addressing method, the two sides of the interface remain coupled implicitly during this process. Appropriate interpolations in time and space preserve flux continuity across the interface and avoid the production of perturbations to the flow field. It is assumed, that in a broad CFF-impeller the flow can be taken as two-dimensional with negligible changes perpendicular to the main flow direction. The influences of the side walls of the casing and the end and intermediate discs of the impeller are neglected. The $k - \varepsilon$ turbulence model is used for turbulence modelling.

Flow characteristics and performance of CFF are usually described by the following dimensionless parameters:

$$Re_S = \frac{U_2 S}{\nu} \quad \text{Reynolds-number (chord length)}$$

$$Re_D = \frac{U_2 D_2}{\nu} \quad \text{Reynolds-number (global)}$$

$$\varphi_c = \frac{Q}{LD_2 U_2} \quad \text{volume flow coefficient (CFF)}$$

$$\varphi = \frac{4Q}{\pi D_2^2 U_2} \quad \text{volume flow coefficient (global)}$$

$$\psi_s = \frac{\Delta p_{stat}}{\frac{1}{2} \rho U_2^2} \quad \text{stat. pressure coefficient}$$

4. Experimental investigations

4.1. Test installation. Planning the experimental investigations, measurements of the global performance data pressure rise, volume rate and input torque, as well as velocity distributions have to be provided. A test rig was set up as a closed circuit channel, which contains all installations to control and measure the volume rate, the pressure rise and the input power of the test CFF. The principle of the channel is similar to a standard airway for fans [7]. Figure 7 shows the view of the complete test channel from the top.

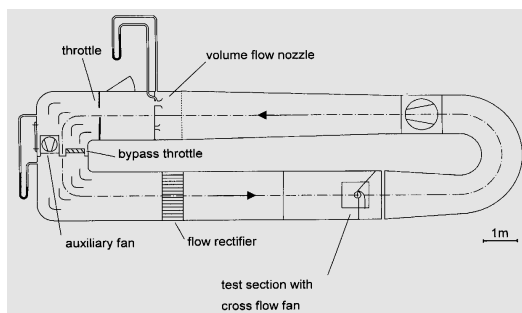


Figure 7. Test installation

4.2. PIV measurements. Figure 8 shows the details of the test installation for the CFF with the PIV system. Due to the complex geometry, several transparent wall sections are realized for the laser light sheets. The PIV measurements were carried out in the inlet and outlet zones, in a representative plane perpendicular to the axis of rotation. Inside the impeller, PIV measurements cannot be performed actually.

The global performance data are measured at positions which correspond to the analysis of the numerical data.

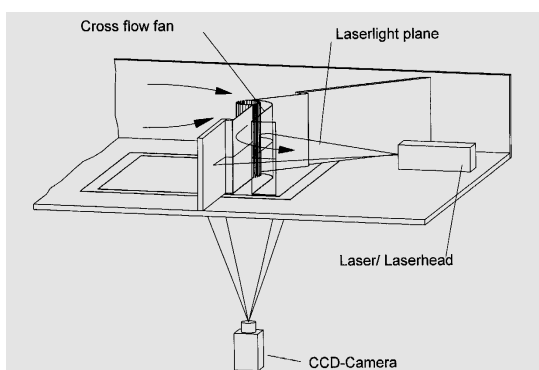


Figure 8. PIV measurements

5. Results

5.1. **Test case.** This geometry was investigated experimentally by Tuckey et al. [2]. The CFF is designed as the air supply for an open-circuit wind tunnel. The resulting rotor parameters and operating conditions are shown in Table 1, the geometrical values correspond to Figure 9. This table also shows the dimensions and the operational conditions of the model fan in the test installation. The geometrical scale factor is 0,16.

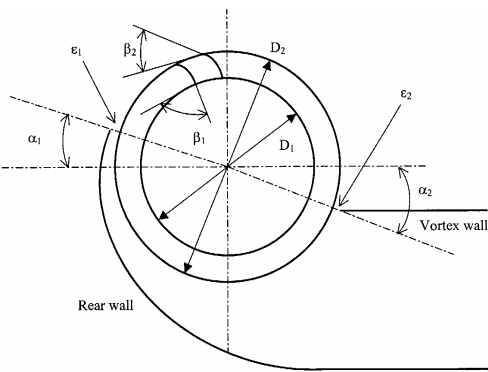


Figure 9. Test geometry [2]

Figure 10 represents the results of measurements of the static pressure coefficient vs. the volume rate coefficient of both fans.

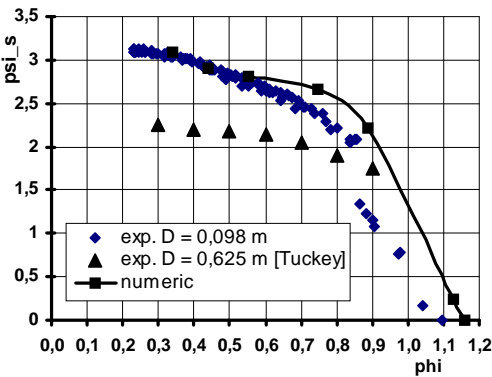


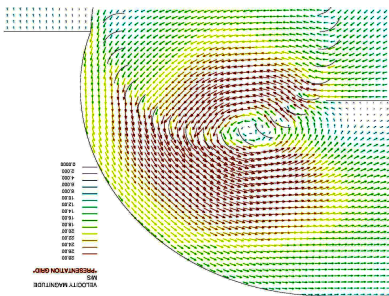
Figure 10. Comparison of experimental and numerical results

The fact that the pressure coefficient of the model is higher than that of the large fan in the left part of the characteristics may be caused by the higher number of blades.

Table 2. Geometric and operating data

Literature [2]:	
impeller diameter D_2	0.625 m
diameter ratio D_1/D_2	0.78
blade angles	$\beta_1 = 90^\circ, \beta_2 = 26^\circ$
number of blades	24
chord length S	0.084 m
blade profile	circular arc
rotating speed	$n = 6.67\text{ sec}^{-1}$
Re (chord length)	$Re_S = 70.000$
Re (global)	$Re_D = 550.000$
volume flow coefficient	$0.2 < \varphi < 0.9$
stat. pressure coefficient	$1,6 < \psi_s < 2,2$
Model:	
impeller diameter D_2	0.098 m
diameter ratio D_1/D_2	0.65
blade angles	$\beta_1 = 90^\circ, \beta_2 = 26^\circ$
number of blades	36
chord length S	0.01 m
blade profile	circular arc
rotating speed	$n = 25\text{ sec}^{-1}$
Re (chord length)	$Re_S = 5.000$
Re (global)	$Re_D = 50.000$
volume flow coefficient	$0,3 < \varphi < 1,1$
stat. pressure coefficient	$0 < \psi_s < 3$

The line marks the results of the numerical calculations. Corrections for 3D losses, caused by friction of the discs and volumetric losses in the lateral gaps are not taken into consideration during the numerical calculations.



Velocity field, numeric

Figure 11. Velocity field, numeric

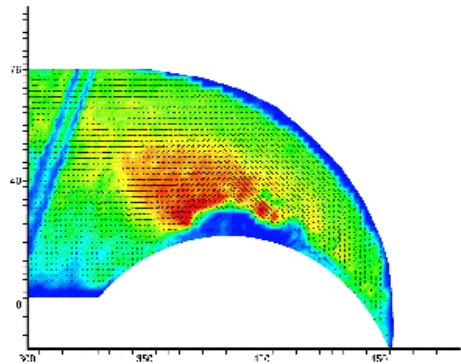


Figure 12. Velocity field, PIV

Figure 11 shows a calculated velocity field, which gives a good impression of the steering vortex. It corresponds with the PIV measurements in Figure 12 in a satisfactory way.

5.2. Variation of operational conditions. Within these investigations a variation of the point of operation is calculated and measured for a typical CFF configuration with a 90 degree deflection. Figures 13 and 14 show the CFD results for two different values of the volume flow coefficient. In Figures 15 and 16 the corresponding flow fields measured with PIV are shown. Calculated and measured flow fields, especially the formation of the steering vortex are in good agreement.

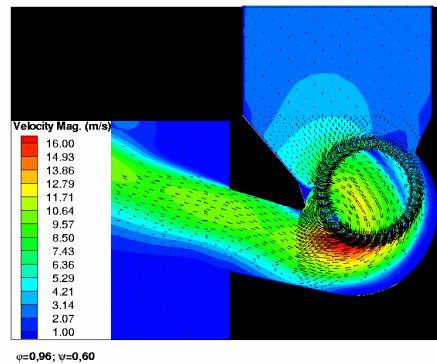


Figure 13. Velocity field, calculated, $\varphi = 0,96$

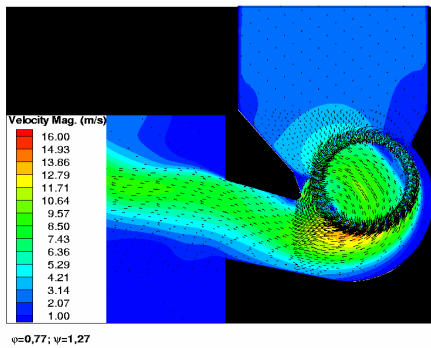


Figure 14. Velocity field, calculated, $\varphi = 0,77$

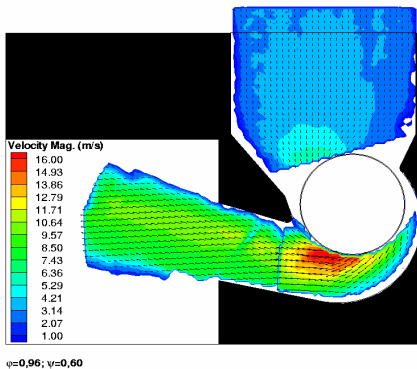


Figure 15. Velocity field, PIV, $\varphi = 0,96$

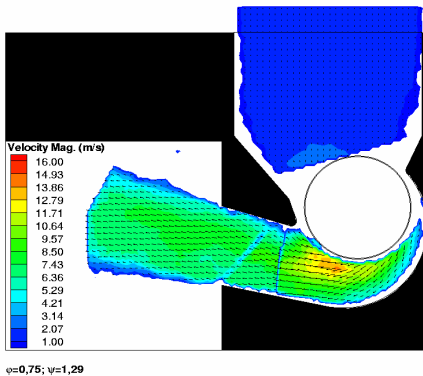


Figure 16. Velocity field, PIV, $\varphi = 0,75$

6. Summary

PIV measurement techniques in combination with CFD are useful tools to understand the flow fields in fluid machinery. Particularly with regard to CFF, whose functional principle cannot be described sufficiently with the common theories of fluid machinery, these techniques can help in the process of design and dimensioning. Further investigations will allow a better look into the zones more immediate to the impeller. It is also planned to arrange PIV measurements inside the impeller to detect vortices more exactly.

Acknowledgement. This project is initiated and promoted by the German Fan Manufacturer's Research Association (FLT).

References

1. ECK, B.: *Ventilatoren*. Auflage, Berlin: Springer-Verlag, 5, 1972.
2. TUCKEY, P.R., HOLGATE, M.J. AND CLAYTON, B.R.: *Performance and aerodynamics of a cross flow fan design & applications*. Guildford, England, 1982.
3. WILLERT, C.E., RAFFEL, M. AND KOMPENHANS, J.: *Particle image velocimetry, A practice guide*, Springer-Verlag, Germany, 1998.
4. DORNSTETTER, S.: *Numerische und experimentelle Untersuchungen an Querstromventilatoren*, Dissertation Universität Karlsruhe(TH), 2002.
5. GABI, M., DORNSTETTER, S. AND KLEMM, T.: Investigation of the flow field in cross-flow fans by particle imaging velocimetry, Proc. 10th Int. Symp. On Flow Visualisation, Kyoto, Japan, 2002.

RELATIONS FOR WATER-VAPOR TRANSPORT THROUGH FIBERS

AKBAR KHODAPARAST HAGHI

Guilan University

P.O. Box 3756, Rasht, Iran

Haghi@Guilan.ac.ir

[Received: November 8, 2002]

Abstract. The present work is devoted to the combined microwave and convective drying behavior of carpets. The mathematical relations developed may be used to describe the moisture sorption mechanisms of carpets. The effects of important parameters during the drying process are discussed and the mathematical relations are formulated to illustrate the range of their applications. According to the results presented in this work, it is shown that combined microwave and convective drying can provide higher drying rates and, consequently, faster drying times.

Mathematical Subject Classification: 80A20

Keywords: convective drying, drying behavior, heat and mass transfer, mathematical relations, microwave assisted drying

1. Introduction

The cost of drying carpets, which is done toward the end of the manufacturing process, is quite high. A very common method of removing water from carpets is convective drying. Hot air is used as the heat transfer medium and is exhausted to remove vaporized water. Considerable thermal energy, about 30% of the total energy used, is required to heat make-up air as the hot air is exhausted. Thus, reducing the amount of exhaust is clearly a way to conserve energy, but there is little in the literature that can be used as guidelines for optimizing dryer exhaust flow. In this case the effect of humidity on the drying rates of carpet tiles should be studied.

When the water is deep within the carpet, combined microwave and convective drying, which have faster heat and mass transfer, may be a better choice. To fully understand the heat and mass transfer phenomena occurring within the carpet during combined microwave and convective drying, it is required to analyze the moisture, temperature, and pressure distributions generated throughout the process. The water remaining in the carpet is 50-60% times the weight of the carpet and after mechanical removal is in its thermodynamically favorable position, largely because the low viscosity of the water and connectivity of the pores ensure rapid equilibration. The pores are approximated as essentially cylindrical, with their axis vertical to the carpet

backing. The amount of porosity, i.e., the volume fraction of voids within the carpet, determines the capacity of a carpet to hold water; the greater the porosity, the more water the carpet can hold. The carpet is able to absorb 6 times its weight in water. When the water content is reduced to roughly 50-60% by mechanical extraction, free water is probably situated in pores with an effective capillary diameter of up to 200 μm . The occupied pores are distributed throughout the carpet pile thickness and largely within the yarns.

The flow of air through carpet dryers is very complex, and neither simple concurrent or countercurrent flow of air and material takes place. Usually there are a set of well mixed zones, throughout which the drying conditions are effectively uniform. The commonest strategy for regulating a dryer's behavior is feedback control, in which the controlled variables (such as the moisture content of the material) are compared with the desired set point. The difference signal, suitably processed by the controller, is then used to modulate the input parameter being used as the control variable. An ideal three-term controller incorporates proportional, integral and derivative action. The proportional term gives a rapid response to an error signal, but the controlled variable is permanently offset from its desired value. The integral function compensates for the steady-state error. Derivative action is rarely used, except with well defined signals, because noise in the signal can confuse the controller, resulting in a hunting action about some mean value. The difficulties in obtaining online measures of a material's moisture content have led to the use of environmental control of the humidity or temperature within the drying chamber. This strategy, however, can lead to inadequate control, as the wet-bulb depression is the driving force for drying. Use of the dry-bulb temperature or relative humidity of the bulk air as the control variable will only be satisfactory as long as the surface conditions of the material remain constant. The difference in temperature between the surface and the bulk air will give a measure of the surface moisture content, provided the material is hygroscopic and all unbound moisture has been driven out.

2. Notational conventions

<i>Notations</i>	
C_P	Specific heat
D	Diffusivity (m^2s^{-1})
g	Gravitational constant (ms^{-2})
h	Intrinsic averaged enthalpy (Jkg^{-1})
h_{vap}	Latent heat of evaporation (Jkg^{-1})
Δh_W	Differential heat of sorption (Jkg^{-1})
K	Intrinsic permeability (m^2)
K'	Thermal conductivity ($\text{kW m}^{-1} \text{K}^{-1}$)
K_g	Relative permeability of gas
K_m	Mass transfer coefficient (ms^{-1})
K_W	Relative permeability of water
L	Thickness of the fabric (m)
M	Molar mass (kg mol^{-1})

P_{abs}	Power absorbed in the material per unit area (Wm^{-2})
Q	Heat transfer coefficient ($Wm^{-2}K^{-1}$)
R	Universal gas constant ($J\ mol^{-1}\ K^{-1}$)
S	Volume saturation
t	Time (s)
T	Temperature (K)
v	Averaged velocity (ms^{-1})
z	Distance (m)
θ	Non-dimensional temperature
ρ	Density of the fibers ($kg\ m^{-3}$)
σ	Surface tension (Nm^{-1})
τ	Non-dimensional time
ϕ	Porosity (m^3m^{-3})
χ	Surface porosity (m^2m^{-2})
Φ	Internal microwave power source (Wm^{-3})
Ψ	Relative humidity
μ_g	Dynamic viscosity of gas ($kg\ m^{-1}s^{-1}$)
μ_W	Dynamic viscosity of water ($kg\ m^{-1}s^{-1}$)
μ	Permeability of free space (Hm^{-1})

Subscripts

a	Air
c	Capacity
g	Gas
v	Vapor
W	Liquid
o	Atmospheric
1	Initial

3. Background

In general, drying means disposing of the liquid completely or partially. We define it more narrowly in this paper as the vaporization and removal of water from a material. The typical drying curve begins with a warm-up period, where the material is heated and the drying rate is usually low. The drying rate can be negative in the warm-up period if the gas stream is humid enough. As the material heats up, the rate of drying increases to peak rate that is maintained for a period of time known as the constant rate period. Eventually, the moisture content of the material drops to a level, known as the critical moisture content, where the high rate of evaporation cannot be maintained. This is the beginning of the falling rate period. During the falling rate period, the moisture flow to the surface is insufficient to maintain saturation at the surface. This period can be divided into the first and second falling rate periods. The first falling rate period is a transition between the constant rate period and the second falling rate period. In the constant rate period, external variables such as gas stream humidity, temperature, and flow rate dominate. In the second falling rate period, internal factors such as moisture and energy transport in the carpet dominate.

Although much of the water is removed in the constant rate period of drying, the time required to reduce the moisture in the product to the desired value can depend on the falling rate period. If the target moisture content is significantly lower than the critical moisture content, the drying rates in the falling rate period become important.

It has been recognized that microwave could perform a useful function in carpet drying in the leveling out of moisture profiles across a wet sample. This is not surprising because water is more reactive than any other material to dielectric heating so that water removal is accelerated.

Many investigators have attempted to explain the effect of humidity drying rates and the existence of inversion temperatures. The explanations are usually based on changes that occur in convective heat transfer, radiative heat transfer, and mass transfer as the humidity and temperature of the gas stream change. We will briefly discuss these explanations.

At a given gas stream temperature, convective heat transfer rate can change as the humidity in the gas stream is varied, because product temperature and fluid properties vary with humidity. These effects can be explained using the following relationship for the convective heat transfer rate:

$$\frac{q}{A} = h (T_{\infty} - T_S) = h \Delta T ,$$

where $\frac{q}{A}$ = convective heat transfer per unit surface area A , h = heat transfer coefficient, T_{∞} = free stream temperature of the drying medium, T_S = surface temperature of material being dried.

Since the product temperature is dependent on humidity, clearly ΔT is also dependent. Further, the heat transfer coefficient h is a function of both product temperature and fluid properties. Thus, the convective heat transfer rate changes with humidity, as does the drying rate of a material. However, drying in air will always have an advantage over drying in steam because ΔT is larger for drying in air; this is a consequence of T_S being very near the wet bulb temperature. The wet bulb temperature is lowest for dry air, increases with increasing humidity, and reaches the saturation temperature of water for a pure steam environment. Thus, ΔT_{AIR} will be larger than ΔT_{STEAM} , but $\Delta T_{AIR}/\Delta T_{STEAM}$ decreases with increasing T_{∞} . Further, the heat transfer coefficient increases with humidity. Apparently, the net effect of the changes in h and ΔT is that the convective heat transfer rate increases faster for steam than for air with increasing temperature.

King and Cassie [1] conducted an experimental study on the rate of absorption of water vapor by wool fibers. They observed that, if a textile is immersed in a humid atmosphere, the time required for the fibers to come to equilibrium with this atmosphere is negligible compared with the time required for the dissipation of heat generated or absorbed when the regain changes. McMahon and Watt [2] investigated the effects of heat of sorption in the wool-water sorption system. They observed that the equilibrium value of the water content was directly determined by the humidity but that the rate of absorption and desorption decreased as the heat-transfer efficiency decreased. Heat transfer was influenced by the mass of the sample, the packing density

of the fiber assembly, and the geometry of the constituent fibers. Crank [3] pointed out that the water-vapor-uptake rate of wool is reduced by a rise in temperature that is due to the heat of sorption.

The dynamic-water-vapor-sorption behavior of fabrics in the transient state will therefore not be the same as that of single fibers owing to the heat of sorption and the process to dissipate the heat released or absorbed.

Henry [4,5] was the first to start theoretical investigation of this phenomenon. He proposed a system of differential equations to describe the coupled heat and moisture diffusion into bales of cotton. Two of the equations involve the conservation of mass and energy, and the third relates fiber moisture content to moisture in the adjacent air. Since these equations are non-linear, Henry made a number of simplifying assumptions to derive an analytical solution.

In order to model the two-stage sorption process of wool fibers, David and Nordon [6] proposed three empirical expressions for a description of the dynamic relationship between fiber moisture content and the surrounding relative humidity. By incorporating several features omitted by Henry [4] into the three equations, David and Nordon [6] were able to solve the model numerically. Since their sorption mechanisms (i.e. sorption kinetics) of fibers were neglected, the constants in their sorption-rate equations had to be determined by comparing theoretical predictions with experimental results.

Farnworth [7] reported a numerical model describing the combined heat and water-vapor transport through fibers. The assumptions in the model did not allow for the complexity of the moisture-sorption isotherm and the sorption kinetics of fibers. Wehner *et al* [8] presented two mechanical models to simulate the interaction between moisture sorption by fibers and moisture flux through the void spaces of a fabric. In the first model, diffusion within the fiber was considered to be so rapid that the fiber moisture content was always in equilibrium with the adjacent air. In the second model, the sorption kinetics of the fiber were assumed to follow Fickian diffusion. In these models, the effect of heat of sorption and the complicated sorption behavior of the fibers were neglected.

Li and Holcombe [9] developed a two-stage model, which takes into account water-vapor-sorption kinetics of wool fibers and can be used to describe the coupled heat and moisture transfer in wool fabrics. The predictions from the model showed good agreement with experimental observations obtained from a sorption-cell experiment. More recently, Li and Luo [10] further improved the method of mathematical simulation of the coupled diffusion of the moisture and heat in wool fabric by using a direct numerical solution of the moisture-diffusion equation in the fibers with two sets of variable diffusion coefficients. These research publications were focused on fabrics made from one type of fiber. The features and differences in the physical mechanisms of coupled moisture and heat diffusion into fabrics made from different fibers have not been systematically investigated.

Downes and Mackay [11] found experimentally that the sorption of water vapor by wool is a two-stage process, the first stage obeys Fick's law of diffusion with

a concentration-dependent diffusion coefficient. The second stage, which involves structural changes within fibers, is much slower than the first. To simulate the two-stage-sorption process, David and Nordon [6] proposed an exponential function to describe the rate of change of fiber water content, which needed to be adjusted according to the measured fabric moisture content. Li and Holcombe [9] developed a two stage sorption-rate equation to describe the moisture sorption of wool. The first stage is represented by a Fickian diffusion with a constant coefficient. The diffusion equation was solved by using Crank's truncated solution [3]. The second stage is described by an exponential relationship, which also needs to be adjusted according to the experimental measurements. The relative contributions of the two stages to the total moisture sorption are functions of the sorption time and the initial regain of the fibers.

Before a carpet is conveyed into the drying oven, most of the water is typically vacuum extracted. After vacuum extraction, the moisture regain is about 50-60%, indicating that there is still a significant amount of water inside the carpet. This water is usually removed with heat in industrial manufacturing processes. As a general rule, the water is distributed in larger pores.

It seems reasonable to anticipate that many of these pores are formed within the pile yarns throughout the thickness of the carpet. The location of this water is of interest to people in the carpet industry.

4. Mathematical Formulation

It was shown by Ilic and Turner [12] that a theory based on a continuum approach led to the following equations of motion governing the drying of a slab of material:

Total mass:

$$\frac{\partial}{\partial t} (\phi S_g \rho_g + \phi S_W \rho_W) + \nabla \cdot (X_g \rho_g V_g + X_W \rho_W V_W) = 0 . \quad (4.1)$$

Total liquid:

$$\frac{\partial}{\partial t} (\phi S_g \rho_{gv} + \phi S_W \rho_W) + \nabla \cdot (x_g \rho_{gv} V_{gv} + X_W \rho_W V_W) = 0 \quad (4.2)$$

Total enthalpy:

$$\begin{aligned} \frac{\partial}{\partial t} \left[\phi S_g \rho_{gv} h_{gv} + \phi S_g \rho_{ga} h_{ga} + \phi S_g \rho_{ga} h_{ga} + \phi S_W \rho_W h_W + \right. \\ \left. + (1 - \phi) \rho_S h_S - \phi \rho_W \int_0^{S_W} \Delta h_W(S) dS \right] + \\ + \nabla \cdot (X_g \rho_{gv} V_{gv} h_{gv} + X_g \rho_{ga} V_{ga} h_{ga} + X_W \rho_W V_W h_W) = \\ = \nabla \cdot ((K_g X_g + K_W X_W + K_S (1 - X)) \nabla T) + \phi , \quad (4.3) \end{aligned}$$

where ϕ is the internal microwave power dissipated per unit volume. In equation (3) the effects of viscous dissipation and compressional work have been omitted.

Equations (1-3) are augmented with the usual thermodynamic relations and the following relations:

Flux expressions are given as follows:

- Gas flux:

$$X_g \rho_g V_g = -\frac{K K_g (S_W) \rho_g}{\mu_g(T)} [\nabla P_g - \rho_g g] , \quad (4.4a)$$

- Liquid flux:

$$X_W \rho_W V_W = -\frac{K K_W (S_W) \rho_W}{\mu_W(T)} [\nabla (P_g - P_C(S_W, T)) - \rho_W g] , \quad (4.4b)$$

- Vapor flux :

$$X_g \rho_{gv} V_{gv} = X_g \rho_g V_g - \frac{X_g \rho_g D(T, P_g) M_a M_v}{M^2} \nabla \left(\frac{P_{qv}}{P_g} \right) , \quad (4.4c)$$

- Air flux :

$$X_g \rho_{ga} V_{ga} = X_g \rho_g V_g - X_g \rho_g V_{gv} . \quad (4.4d)$$

Relative humidity (Kelvin effect):

$$\psi(S_W, T) = \frac{P_{gv}}{P_{gvs}(T)} = \exp \left(\frac{2\sigma(T) M_v}{r(S_W) \rho_W R T} \right) ,$$

where $P_{gvs}(T)$ is the saturated vapour pressure given by the 0Clausius-Clapeyron equation.

Differential heat of sorption:

$$\Delta h_W = R_v T^2 \frac{\partial (\ln \psi)}{\partial T} .$$

Enthalpy-Temperature relations:

$$\begin{aligned} h_{ga} &= C_{pa}(T - T_R) , \\ h_{gv} &= h_{vap}^0 + C_{pv}(T - T_R) , \\ h_W &= C_{pW}(T - T_R) , \\ h_s &= C_{ps}(T - T_R) . \end{aligned}$$

The expressions for K_g , K_W are those given by Turner and Ilic [12], and μ_g , μ_W have had functional fits according to the data by Holman [13]. The diffusivity

$$D(T, P_g)$$

is given by Quintard and Puiggali [14] and the latent heat of evaporation given by

$$h_{vap}(T) = h_{gv} - h_W .$$

After some mathematical manipulations, the one-dimensional system of three non-linear coupled partial differential equations which model the drying process in a thermal equilibrium environment are given by :

$$a_{s1} \frac{\partial S_W}{\partial t} + a_{s2} \frac{\partial T}{\partial t} = \frac{\partial}{\partial Z} \left[K_{S1} \frac{\partial S_W}{\partial Z} + K_{T1} \frac{\partial T}{\partial Z} + K_{T1} \frac{\partial T}{\partial Z} + K_{P1} \frac{\partial P_g}{\partial Z} + K_{gr1} \right] , \quad (4.5)$$

$$a_{T1} \frac{\partial S_W}{\partial t} + a_{T2} \frac{\partial T}{\partial t} = \frac{\partial}{\partial Z} \left(K_e \frac{\partial T}{\partial Z} \right) - \phi \rho_W h_{vap} \frac{\partial}{\partial Z} \left[K_S \frac{\partial S_W}{\partial Z} + K_T \frac{\partial T}{\partial Z} + K_P \frac{\partial P_g}{\partial Z} K_{gr} \right] \\ + \left[\phi \rho_W C_{pW} \left(K_{S2} \frac{\partial S_W}{\partial Z} + K_{T2} \frac{\partial T}{\partial Z} + K_{P2} \frac{\partial P_g}{\partial Z} + K_{gr2} \right) \right] \frac{\partial T}{\partial Z} + \Phi(S_W, T) , \quad (4.6)$$

$$a_{P1} \frac{\partial S_W}{\partial t} + a_{P2} \frac{\partial T}{\partial t} + a_{P3} \frac{\partial P_g}{\partial t} = \frac{\partial}{\partial Z} \left[K_S \frac{\partial S_W}{\partial Z} + K_T \frac{\partial T}{\partial Z} + K_{P3} \frac{\partial P_g}{\partial Z} + K_{gr3} \right] . \quad (4.7)$$

The capacity coefficients a_{S1} , a_{T1} , a_{p1} and the kinetic coefficients K_{S1} , K_{T1} , K_{P1} , K_{gr1} all depend on the independent variables : Saturation S_W , Temperature T and total pressure P_g . The boundary conditions are written in one dimension as:

At $z = 0$ (Drying surface) :

$$K_{S1} \frac{\partial S_W}{\partial Z} + K_{T1} \frac{\partial T}{\partial Z} + K_{P1} \frac{\partial P_g}{\partial Z} + K_{gr1} = \frac{K_m M_V}{R \phi \rho_W} \left(\frac{P_{gV}}{T} - \frac{P_{gV0}}{T_0} \right) , \quad (4.8a)$$

$$K_e \frac{\partial T}{\partial Z} - \phi \rho_W h_{vap} \left(K_S \frac{\partial S_W}{\partial Z} + K_T \frac{\partial T}{\partial Z} + K_P \frac{\partial P_g}{\partial Z} + K_{gr} \right) = Q(T - T_0) , \quad (4.8b)$$

$$P_g = P_o . \quad (4.8c)$$

At $z = L$ (Impermeable surface):

$$K_{S1} \frac{\partial S_W}{\partial Z} + K_{T1} \frac{\partial T}{\partial Z} + K_{P1} \frac{\partial P_g}{\partial Z} + K_{gr1} = 0 , \quad (4.9a)$$

$$K_e \frac{\partial T}{\partial Z} - \phi \rho_W h_{vap} \left(K_S \frac{\partial S_W}{\partial Z} + K_T \frac{\partial T}{\partial Z} + K_P \frac{\partial P_g}{\partial Z} + K_{gr} \right) = 0 , \quad (4.9b)$$

$$(K_{S1} - K_S) \frac{\partial S_W}{\partial Z} + (K_{T1} - K_T) \frac{\partial T}{\partial Z} + (K_{P1} - K_{P3}) \frac{\partial P_g}{\partial Z} + (K_{gr1} - K_{gr3}) = 0 . \quad (4.9c)$$

Initial conditions:

$$T(z, 0) = T_1 , \quad (4.10a)$$

$$P_g(z, 0) = P_0 , \quad (4.10b)$$

$$\frac{\partial P_c}{\partial Z} = -\rho_W g . \quad (4.10c)$$

The numerical solution technique employed to solve the resulting system over the control volume is discussed by Patankar [15].

5. Discussion

Figures 1 and 2 show a comparison of convective drying with and without microwave. Whilst for convective drying there are definite constant rate periods, when microwaves are added, the form of the curves change and the use of the words constant and falling rate may no longer apply. In hot air drying the constant rate period is the period of drying before the drying front recedes below the outer boundary. In our calculations the SMER (Figure 3) is defined as the energy required to extract a unit of water from the product. Figure 3 shows that the SMER for the microwave case is much lower than the convective case.

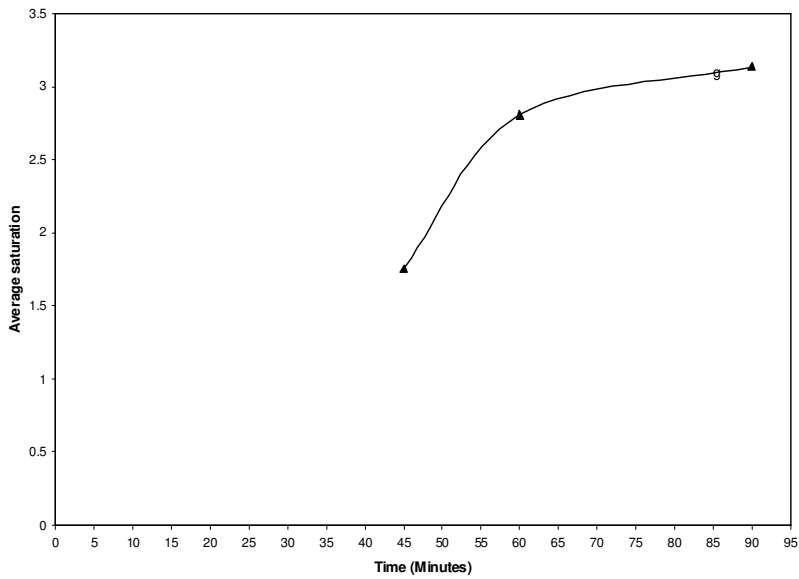


Figure 1. Average saturation profiles in time for drying

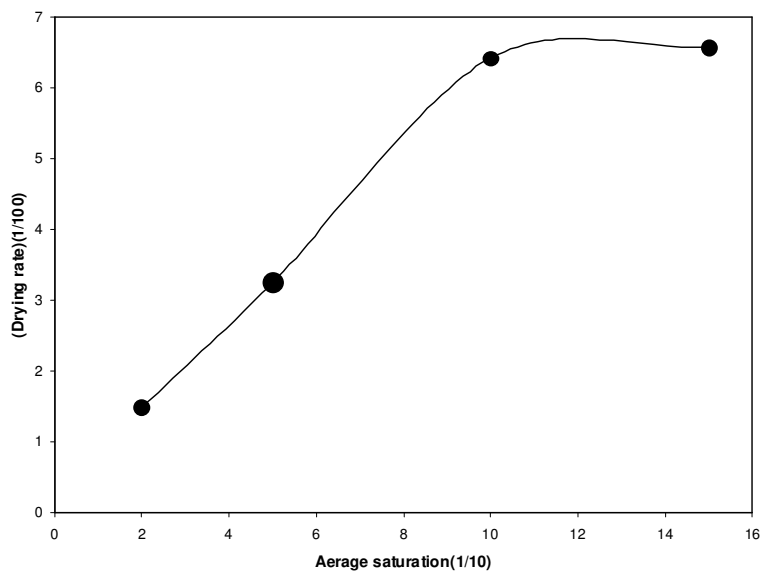


Figure 2. Drying rate curve corresponding to the profile plotted in Figure 1

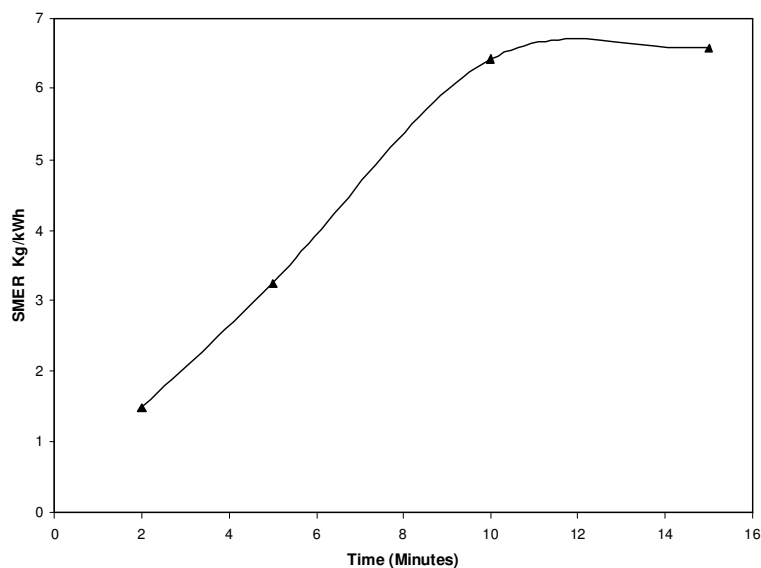


Figure 3. Specific moisture extraction rate time for drying

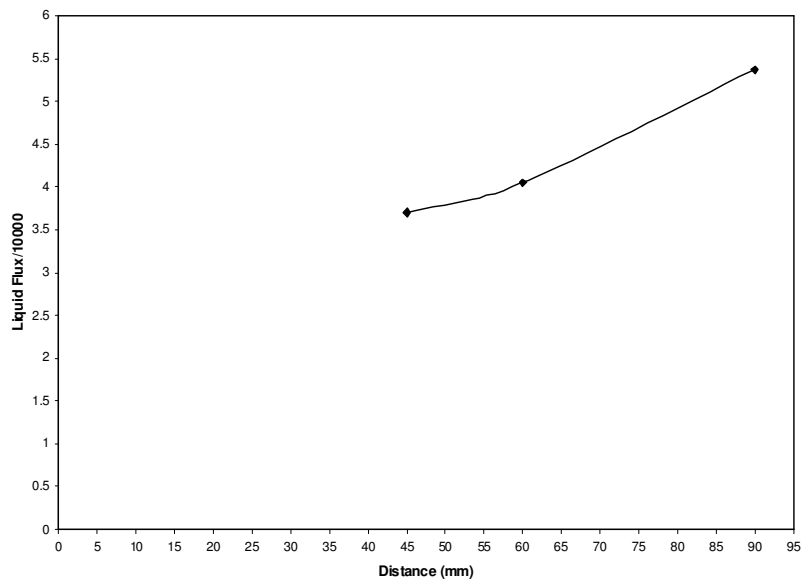


Figure 4. Liquid flux as function of distance

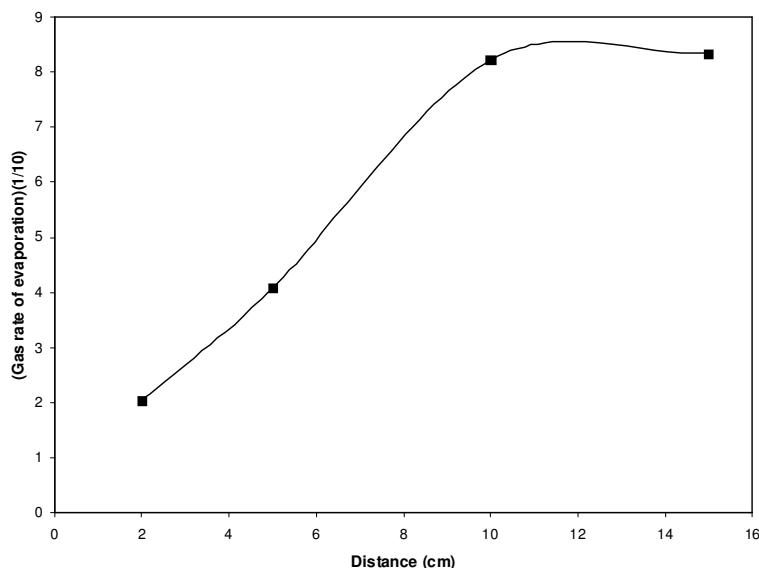


Figure 5. Rate of evaporation as function of distance

The analysis of liquid and gas flux as given by equations (4.4a)-(4.4d) has been exhibited in Figures 4 and 5, for both the combined microwave and convective and convective drying cases. During this period the convective heat transfer is used for evaporation only, resulting in a constant surface temperature and drying rate (see horizontal plateau in Figure 4). The liquid flows to the surface initially in a linear fashion. As the fibers begin to dry out, there is a liquid flux up to what can confidently be explained as the position of evaporation front and there is no movement of liquid from that point to the surface.

6. Conclusion

The primary parameter monitored during the drying tests was moisture content, which may be calculated as a ratio of wet weight minus the final dry weight over the final dry weight. The weights include the weight of the entire sample, tufts, and backing. Weight loss during drying is predominately due to water evaporation. Although other materials such as finish may be driven off during drying, the associated weight loss is insignificant compared to that of water. Thus, the determination of moisture content is simple yet accurate.

For most industrial carpet tile operations, the target moisture content is set so that the weight of moisture on the tiles is approximately 5% of the weight of the face yarns. Whilst for convective drying there are definite constant rate and falling rate periods, when microwaves are added, the use of the words constant and falling rate may no longer apply.

In hot air drying the constant rate period is the period of drying before the drying front recedes below the outer boundary. During this period the convective heat transfer can be used for evaporation only, resulting in a constant surface temperature and drying rate.

As the material begins to dry out, there is a liquid flux up to what can confidently be explained as the position of evaporation front and then there is no movement of liquid from that point to the surface.

According to the results presented in this work, it is concluded that combined microwave and convective drying can provide higher drying rates and consequently faster drying times. Moreover, there are higher fluxes of liquid to the drying surface from the interior of the carpet. A good dryer design should take advantage of this feature and optimize excess water removal from the drying surface.

References

1. KING, G. AND CASSIE, A.: Propagation of Temperature Changes through Textiles in Humid Atmospheres, Part I : Rate of Absorption of Water Vapor by Wool Fibers. *Trans Faraday Soc.*, **36**, (1940), 445–453.
2. MCMAHON, G. B. AND WATT, I. G.: Temperature changes in sorption systems due to heat of sorption, *Text. Res. J.*, **35**, (1965), 37–44.
3. CRANK, J.: *The Mathematics of Diffusion*, Clarendon Press, Oxford, UK, 1975.
4. HENRY, P.: Diffusion in absorbing media. *Proc. Roy. Soc.*, **171A**, (1939), 215–241.
5. HENRY, P.: The diffusion of moisture and heat through textiles. *Disc. Faraday Soc.*, **3**, (1948), 243–257.
6. DAVID, H. G. AND NORDON, P.: Case studies of coupled heat and moisture diffusion in wool beds. *Text. Res. J.*, **39**, (1969), 166–172.
7. FARNWORTH, B.: A numerical model of the combined diffusion of heat and water vapor through clothing, *Text. Res. J.*, **56**, (1986), 653–665.
8. WEHNER, J., MILLER, B. AND REBENFELD, L.: Dynamics of water vapor transmission through fabric barriers. *Text. Res. J.*, **58**, (1988), 581–592.
9. LI, Y. and HOLCOMBE, B.: A two-stage sorption model of the coupled diffusion of moisture and heat in wool fabrics. *Text. Res. J.*, **62**, (1992), 211–217.
10. LI, Y. AND LUO, Z.: An improved mathematical simulation of the coupled diffusion of moisture and heat in wool fabric. *Text. Res. J.*, **69**, (1999), 760–768.
11. DOWNES, J. G. AND MACKAY, B.: Sorption kinetics of water vapor in wool fibers. *J. Polym. Sci.*, **28**, (1958), 45–67.
12. ILIC, M. AND TURNER, I. W.: Convective drying of wet porous material. *Int. J. Heat Mass Transfer*, **32**(12), (1989), 2351–2362.
13. HOLMAN, J. P.: *Heat Transfer*. McGraw-Hill Book Company, 1989.
14. QUINTARD, M. AND PULGGALI, J. R.: Numerical modelling of transport process during drying of porous medium. *J. Heat and Technology*, **4**(2), (1986), 34–45.
15. PATANKAR, S.V.: *Numerical Heat Transfer and Fluid Flow*. Hemisphere/McGraw Hill, 1980.

THE FLOW AND HEAD DISTRIBUTION WITHIN THE VOLUTE OF A CENTRIFUGAL PUMP IN COMPARISON WITH THE CHARACTERISTICS OF THE IMPELLER WITHOUT CASING

PETER HERGT, STEPHAN MESCHKAT AND BERND STOFFEL
Chair of Turbomachinery and Fluid Power, Darmstadt University
67059 Ludwigshafen, Germany
`meschkat@tfa.maschinenbau.tu-darmstadt.de`

[Received: November 12, 2003]

Abstract. Measurements of the unsteady velocity, pressure and flow angle have been carried out at the impeller outlet of a centrifugal pump with and without volute casing at 5 operating points using the hotwire technology and a fast response single hole cylindrical probe. The test fluid was air. While the velocities and pressures depend only on the axial coordinate and are rotationally symmetrical, if there is no casing around the impeller, the influence of the volute on the circumferential distribution of these quantities increases with the deviation of the operating point from the design point. With respect to the local throughflow distribution, this influence is much more pronounced in comparison to the pressure distribution.

Keywords: spiral casing pump, rotor stator interaction, experimental investigation

Nomenclature

b	[mm]	width of the vaneless radial diffuser, inlet width of the volute (42 mm)
c_m	[m/s]	meridional velocity at, r_M
r_M	[mm]	radial position of the measuring section (208.5 mm)
u_2	[m/s]	peripheral velocity at the impeller outlet
x	[mm]	axial distance from the front shroud at, r_M
H	[m]	total head
Q	[m ³ /s]	flow rate
Q_{des}	[m ³ /s]	flow rate at design point
ε	[°]	circumferential angle from the tongue in the sense of rotation
φ	[-]	flow coefficient, c_m/u_2
φ_{des}	[-]	flow coefficient at design point
$\bar{\varphi}$	[-]	local mean value of $\varphi = \int_0^1 \varphi d\left(\frac{x}{b}\right)$
$\bar{\varphi}$	[-]	local mean value of $\varphi = \frac{1}{2\pi} \int_0^{2\pi} \bar{\varphi} d\varepsilon$
ψ	[-]	pressure coefficient, $\frac{2gH}{u_2^2}$

1. Introduction

Single stage centrifugal pumps are mostly designed and produced with a volute casing. It is well known that – in this case – the flow at the impeller outlet can only be nearly independent of the circumferential position in the volute if the volute geometry is well designed and the pump is operated at its design point. For off-design operation of volute casing pumps, the volute casing geometry does not ‘fit’ the outflow from the impeller. This leads to a non-uniform distribution of (time averaged) pressure and velocity along the circumference of the volute.

Different approaches exist for modelling this type of rotor-stator-interactions in turbomachines (mixing plane, frozen rotor, transient), see e.g. [2, 5]. To compare the capabilities of the respective modellings in taking into account and describing important features of off-design flow in volute casing pumps, detailed flow field measurements and evaluations are needed.

A research project was carried out at the Laboratory for Turbomachinery and Fluid Power of the Darmstadt University of Technology which aimed at gaining more insight into the aspects of rotor-stator interactions in volute casing pumps and – additionally – creating a data basis for the validation of CFD simulations. Likewise experimental investigations on rotor stator interactions can be found in [1, 2, 4-8].

2. Test rig

The test rig and its instrumentation which was described in more detail in [4] are suited for measurements of transient velocity and pressure distribution for different circumferential positions inside the volute near the impeller outlet. For this purpose and to enable a continuous variation of the measuring positions along the whole circumference of the volute, the volute casing of the test pump can be turned by an electrical motor around the pump axis while the mechanism for traversing the probes is mounted to a fixed inner part of the casing and remains at a constant location. Table 1 shows the technical data of the pump.

Table 2. Technical specifications

Impeller outlet diameter	: 405 mm
Impeller outlet width	: 38 mm
Impeller inlet diameter	: 240 mm
Blade number	: 7
Outlet angle, shroud	: 25°
Outlet angle, hub	: 29°
Specific speed	: 35 min ⁻¹
Rotational speed	: 3000 min ⁻¹
Design flow rate	: 1380 m ³ /h

As can be seen in Figure 1, the inner part of the casing is mounted on two vertical uprights on the front side and rear side while the turnable volute casing is supported on the inner parts (see Figure 2) by ball bearings. For the sealing between both parts of the casing, sheets of felt are used.

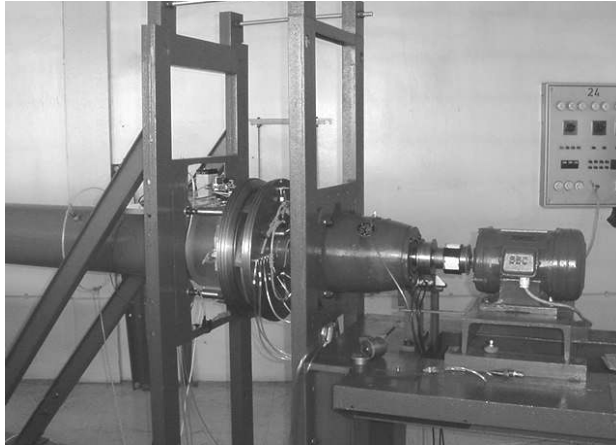


Figure 1. Test rig configuration without volute

The configuration with mounted volute is shown in Figure 2.

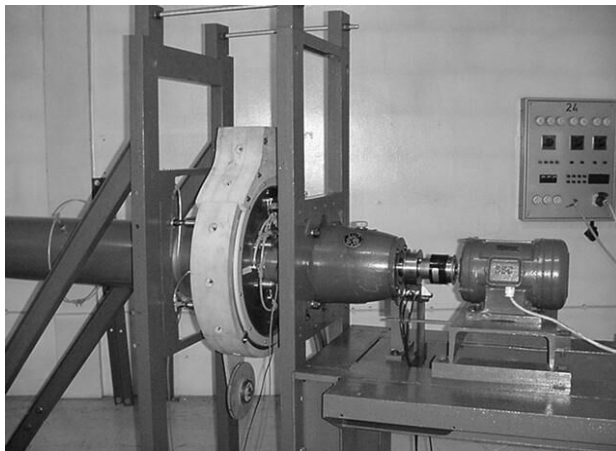


Figure 2. Test rig with mounted volute

In the case of the test rig configuration without the volute part of the casing (Figure 1), flow measurements are possible for free impeller discharge where the pressure at the impeller outlet is constant (= atmospheric pressure) along the impeller outlet.

The analysis of flow was performed by the use of hotwire anemometry and a fast response single hole cylindrical probe [4] which were located 6 mm radially outward of the impeller outlet. Using this single hole cylindrical probe with an integrated high frequency response pressure transducer gives information on the unsteady static and total pressure of the flow from which also the flow velocity can be calculated. But from the experience gained, more reliable information on the unsteady velocity and flow angle is found from a single-wired hotwire probe.

Both probes are traversed across the width of the impeller outlet (see Figure 3). As the probes are turned stepwise around their longitudinal axis at each axial position while the flow direction is nearly perpendicular to the longitudinal axis, the flow angle can be determined by calculating the position of the maximum of measurement data for all time steps (as an ensembled average value in dependence of the angular impeller position and as a time-averaged value, as well).

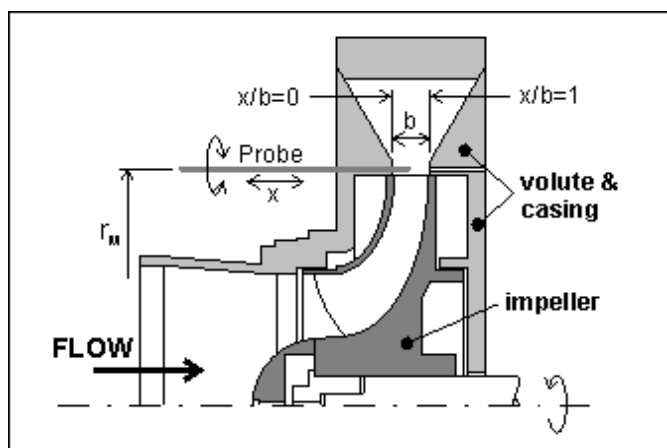


Figure 3. Meridional contour and position of probe

The circumferential distribution of pressure on the surface of the single hole cylindrical probe is detected through a 0.3 mm diameter hole. A calibration for different constant velocities allows one to find the exact maximum pressure position and to determine a circumferential position on the cylinder surface where the measured pressure equals the local static pressure in the flow. The angle of the position where the measured pressure indicates the static pressure of the flow remains constant for a wide range of velocities as described in Schlichting [3]. Because transient effects in unsteady flow influence the circumferential pressure distribution on the probe surface and thus especially the right position where the surface pressure equals the local static pressure of the flow, the determination of the flow direction and magnitude of velocity is done additionally by the hotwire technique.

3. Results and discussion

3.1. Impeller without casing, throughflow. The distribution of the throughflow component φ is plotted versus the dimensionless axial coordinate in Figure 4 for various values of the normalized flow rate Q/Q_{des} . The character of the curves is well known from other publications and shows that the main throughflow takes place near the rear shroud.

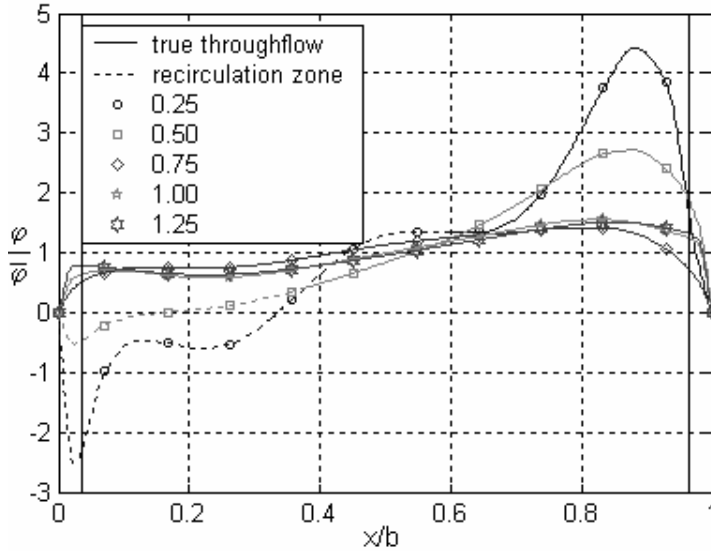


Figure 4. Distribution of the meridional velocity, without casing

At strongly reduced flow rates ($Q/Q_{des} = 0.50$ and 0.25), backflow occurs at the measuring location near the front shroud. Because of the flow recirculation inside and outside the impeller, part of the outflow from the impeller serves to compensate the backflow in the balance of mass flow. Therefore, only the remaining part of the outflow is representative for the mass transport through the pump and is called ‘true throughflow’. In Figure 4, the broken part of the curves indicates the width of the recirculation zone within which the part of the outflow only compensates the backflow. All distributions are rotationally symmetrical.

3.2. Impeller without casing, head. The distribution of the local head is shown in Figure 5. While the head is nearly independent of the axial coordinate at high flow rates, higher heads are measured near the rear shroud at low flow rates. This is somewhat surprising because this is also the area with the higher meridional velocities, i.e. local throughflow (see Figure 4).

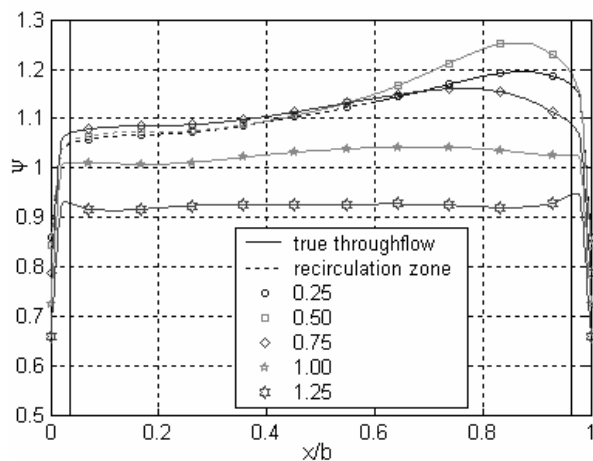


Figure 5. Distribution of local head, without casing

3.3. Throughflow distribution at the volute inlet. The meridional component characterising the local throughflow in the measuring section (that is now the volute inlet) is shown for 5 values of the normalized flow rate in Figure 6.

The broken curves on the diagrams for 75%, 50% and 25% of the design flow rate represent the limit of the true throughflow area. The remaining area characterises the recirculation zone with a negative and the corresponding positive flow rate. Whereas the high meridional velocities are still found near the rear shroud, the circumferential distribution becomes the more irregular the more the flow rate deviates from the design value. It can clearly be observed from the distributions that at part load flow rates, only part of the volute width and circumference contribute to the true throughflow while outside this area backflow and forward flow compensate each other and no net mass flow results. The borderline between the backflow area and the forward flow area can be identified from the isocontour having the value 0 of the dimensionless meridional component.

At 125% of the design flow rate, the highest throughflow component has been measured approximately 30° upstream of the tongue, which means that the local flow rate increases along the circumference as is found also by theoretical considerations.

Contrary to this, the local flow rate decreases along the circumference if the pump is operated at low flow rates which is also in correspondence with the theory.

At 25% of design flow rate, less than half of the volute inlet cross-section contributes to the throughflow. The rest consists of a strong recirculation especially just upstream of the tongue where no true throughflow exists. Referring to the impeller frame of reference, it becomes evident that blade channels passing through this area of the volute do not contribute to the net impeller mass flow and are exposed to strong backflow once per each impeller revolution.

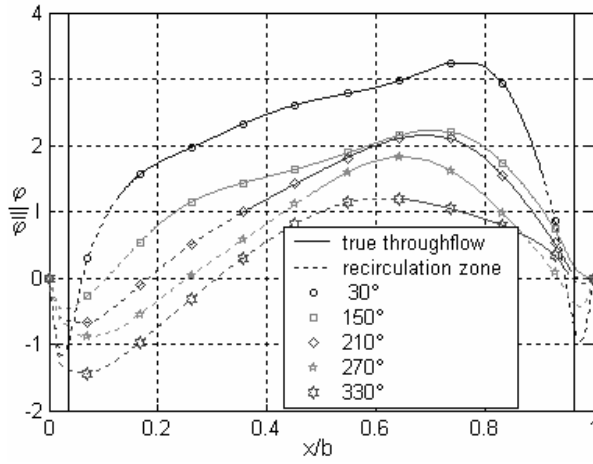


Figure 7. $\varphi/\bar{\varphi}$ for different circumferential positions. $\varphi = 0.5 \cdot \varphi_{des}$

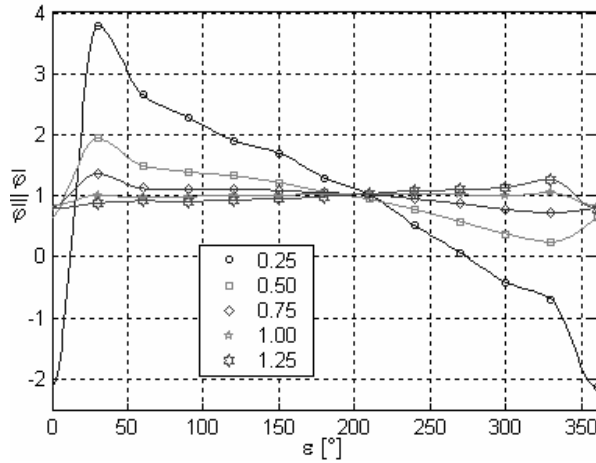


Figure 8. Local $\bar{\varphi}$ -values depending on the angular position

Two facts are striking in the context:

- i) $\bar{\varphi} = \bar{\varphi}$ at approximately 205° for all flowrates.
- ii) $\bar{\varphi}$ is approximately independent of the flow rate at ca. 30° downstream of the tongue ($3.8 \times 0.25 \approx 1.95 \times 0.5 \dots$ etc.)

This seems to be an interesting feature of the impeller-volute interaction but cannot yet be explained at present.

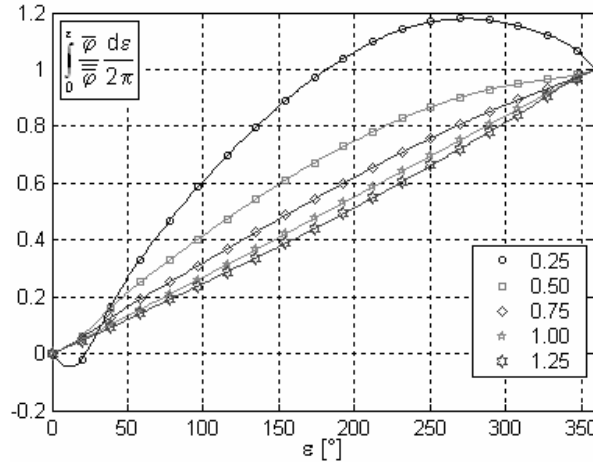


Figure 9. Flow rate integrated along the circumference

Integrating the local flow rates along the circumference leads to Figure 9.

As it could be expected already from Figure 6 there is a linear dependence between the flow rate and the angular position at $\varphi = \varphi_{des}$, while the local flow rate increases up to $1.2 \times \bar{\varphi}$ ($\epsilon \approx 270^\circ$) and falls down to $1.0 \times \bar{\varphi}$ in the following sections due to the strong backflow in this area (see Figure 6).

3.4. Head distribution at the volute inlet. In addition to the throughflow distribution of Figure 6, the distribution of head is shown in Figure 10. Again, the broken lines characterize the true throughflow areas.

In comparison to the distribution of the meridional velocity, the distribution of head is more regular along the width of the measurement section for overload and design point. For part load, the shape along the width deviates from a flat distribution to a distribution with increased head near the rear shroud as this can also be found for the head distribution of the impeller without casing in Figure 5.

As expected, the circumferential distribution becomes more irregular with increasing deviation from the design flow rate. This could at least partially be caused by the variation of the circumferential velocity components. The lowest pressure coefficients have been measured in the backflow zones ($\varphi < 0$) where a part of the energy has been lost through wall friction and mixing losses.

A detailed explanation of the relations between flow and head distribution is rather difficult due to the lack of information about what is caused by separation and recirculation within the impeller on the one side and within the volute only on the other side.

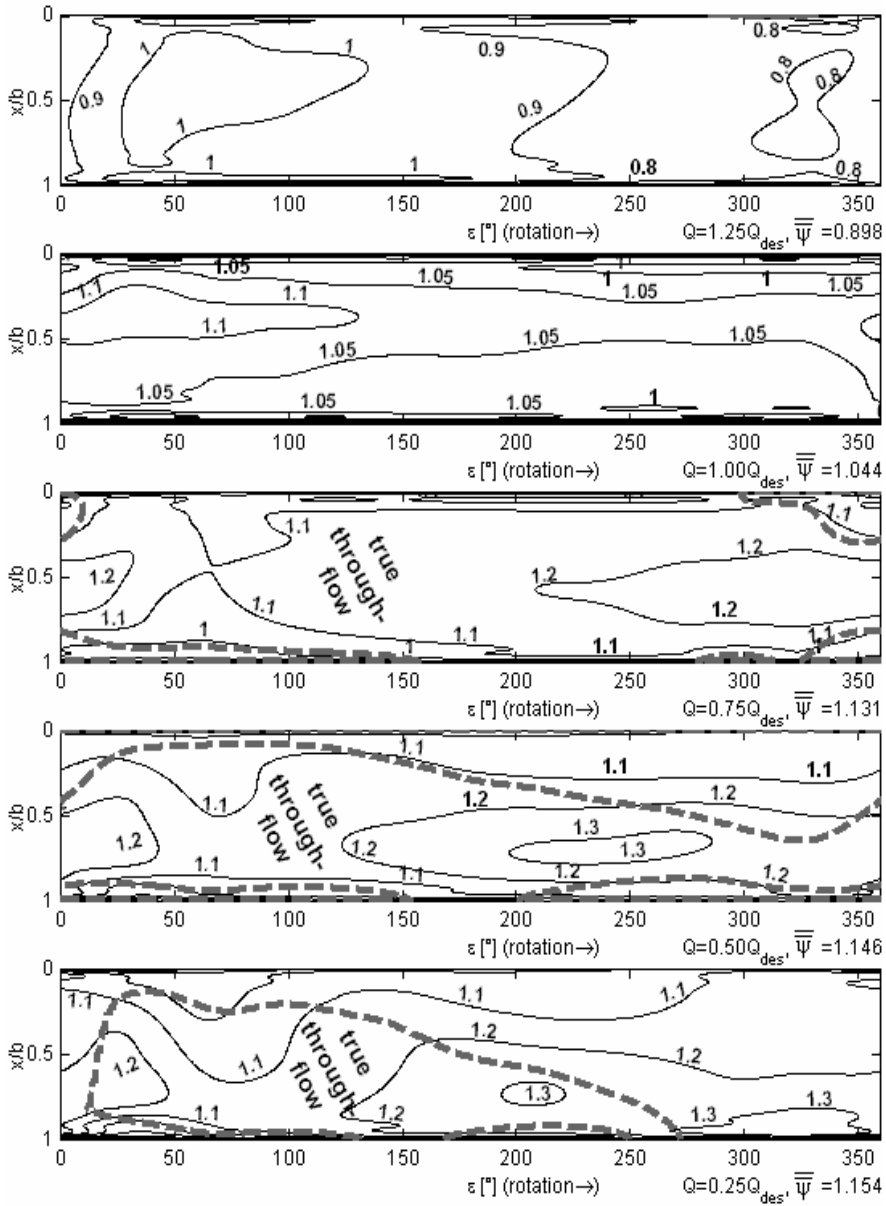


Figure 10. Distribution of local head at the volute inlet

To get this information, measurements within the impeller would be necessary in addition.

4. Summary

Distributions of flow and head at the impeller outlet in a centrifugal pump with volute casing were shown. Some typical distributions for these kinds of pumps were explained and discussed. Most of the results are strictly related to theory. Thus the findings and the qualitative shape of the illustrated graphs and distributions can serve as an orientation for computational fluid dynamics and may encourage researchers to do similar analysis in the frame of postprocessing such calculations.

Acknowledgement. Thanks are due to the KSB-foundation whose financial and technical support made this work possible.

References

1. FLÖRKEMEIER K.H.: *Experimentelle Untersuchungen zur Optimierung von Spiralgehäusepumpen mit tangentialem und radialem Druckstutzen*, PhD-Thesis, TU Braunschweig, 1977.
2. FRITZ, J.: *Strömungswechselwirkungen in hydraulischen Maschinen*, PhD-Thesis, TU München, 1999.
3. SCHLICHTING, H. AND GERSTEN, K.: *Boundary Layer Theory*, Springer-Verlag, Berlin, New York, 1999.
4. STOFFEL, B. AND MESCHKAT, S.: The local specific head at different circumferential positions in a volute casing centrifugal pump in comparison to the characteristic curve of the single rotor, *Proceedings of the Hydraulic Machinery and Systems 21st IAHR Symposium*, Lausanne, 2002.
5. TREUTZ, G.: *Numerische Simulation der instationären Strömung in einer Kreiselpumpe*, PhD-Thesis, TU Darmstadt, 2002.
6. WEISS, K.: *Experimentelle Untersuchungen zur Teillastströmung bei Kreiselpumpen*, PhD-Thesis, U Darmstadt, 1995.
7. UBALDI, M.: An experimental investigation of stator induced unsteadiness on centrifugal impeller outflow. *Journal of Turbomachinery*, **118**, (1996), 41–54.
8. UBALDI, M.: Relative flow and turbulence measurements downstream of a backward centrifugal impeller. *Journal of Turbomachinery*, **113**, (1993), 543–551.

OPTIMUM DESIGN OF A UNIPLANAR CHS TRUSS FOR FATIGUE

KÁROLY JÁRMAI

Department of Materials Handling and Logistics, University of Miskolc
3515 Miskolc-Egyetemváros, Hungary
`altjar@gold.uni-miskolc.hu`

[Received: December 20, 2003]

Dedicated to Professor József FARKAS on the occasion of his seventy-fifth birthday

Abstract. The new IIW (International Institute of Welding) fatigue design recommendations are used for the determination of the optimum strut dimensions and truss height minimizing the structural mass or cost. In an illustrative numerical example a simply supported uniplanar CHS truss with parallel chords is designed, which is loaded by a pulsating force. An advanced cost function is minimized which contains the costs of material, cutting and grinding of strut ends, assembly, welding and painting. Fatigue design constraints are formulated for governing X- and K-gap joints. Six strut dimensions are optimized for a series of discrete truss height ratios and the optimum height ratio is selected considering the minimum cost. A parametric investigation is made to find the relation between the optimum truss height ratios and the span length.

Mathematical Subject Classification: 73A05

Keywords: truss structures, fatigue design, optimization, tubular structures, welded structures, cost function

1. Introduction

Tubular trusses are recently more popular, due to their high strength and low weight. They are in many cases subject to fluctuating loads, e.g. cranes, vehicles, bridges, offshore structures, bodies of agricultural machines, etc. Since high stress concentrations arise in their welded joints, it is important to have a reliable fatigue design method. The IIW Subcommission XV-E for welded tubular joints has made great efforts to give designers such methods.

In 1985 design rules were given for fatigue design [1], which made it possible to work out some optimum design applications in this field [2], [3]. Based on a wide international experimental work, the subcommission has developed a modern version of design rules [4], [5]. Our aim is to show how to apply these rules for the optimum fatigue design of a simply supported uniplanar truss constructed from circular hollow section (CHS) rods subject to a fluctuating force (Figure 1).

For the optimization continuous functions are necessary, therefore we use approximate polynomials for stress concentration factors instead of diagrams given in [1]. For correction factors we use the formulae given by Zhao et al. [4] instead of diagrams.

The optimum height (distance between the parallel chords) is determined, which minimizes the mass or cost of the structure. From the point of view of economy it is important to formulate a realistic cost function. For welded plated structures we have developed and applied a relatively simple cost function containing material and welding costs, based on welding times given by the Netherlands Welding Institute [6], [7], [8], [9]. On the basis of cost data given by Tizani et al. [10], we have developed a modified cost function, which considers the specialties of tubular trusses.

2. Problem formulation

A simply supported uniplanar truss with parallel chords is designed (Figure 1). The truss is welded from CHS rods with K-type gap joints and loaded by a pulsating force at midspan.

Data: $a = 2$ m, $L = 12 \times 2 = 24$ m, the range of the pulsating force is $\Delta F = 160$ kN, the number of cycles is $N_F = 10^5$. Three groups of rods are considered having the same cross-sectional area, one for lower chords (d_0, t_0), one for upper chords (d_2, t_2) and one for braces (d_3, t_3). Thus, the number of unknown strut dimensions is 6. The truss height ratio of $\omega = h/a$ is discretely varied with steps of 0.1.

The truss mass as well as cost is minimized for each h/a ratio to obtain the optimum h/a ratio. Design constraints relate to the fatigue strength of governing joints E, F and A. Ranges of validity defined by [5] are related to zero joint eccentricity and limit the main ratios of strut dimensions.

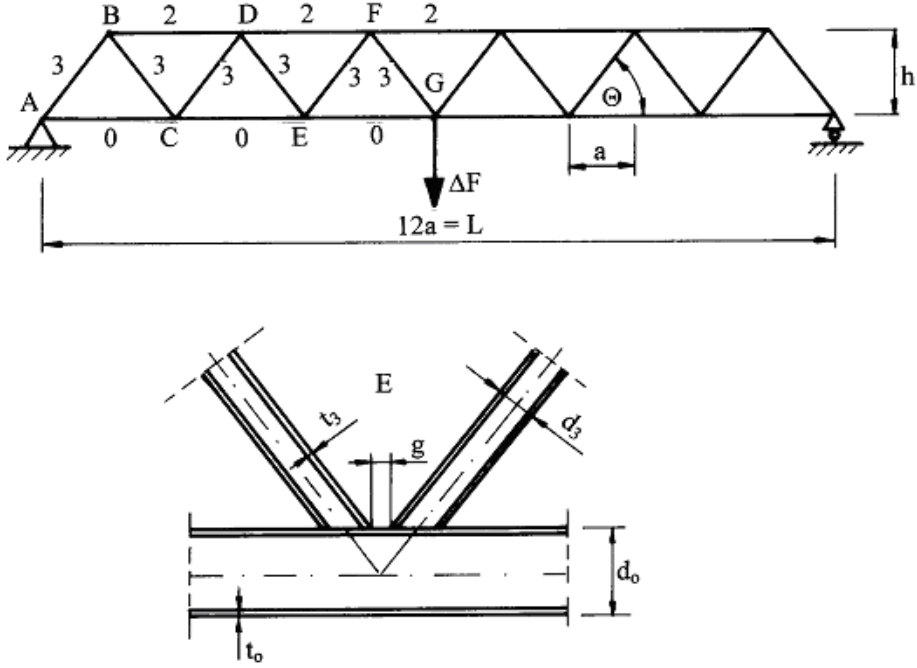
3. Design constraints

3.1. Fatigue strength. The fatigue strength constraints have the following form

$$(MF) \frac{\Delta F_i}{A_i} SCF_0(\beta, \theta) CF(\gamma, \tau) \leq \frac{S_{rhs}}{\gamma_{Mf}}, \quad (3.1)$$

where (MF) is the magnification factor expressing the effect of additional bending moments. Note that other bending effects are not considered, since a geometrical constraint on zero eccentricity is taken into account. SCF_0 is the stress concentration factor depending on $\beta = d_{brace}/d_{chord}$ and on $\theta = \arctan \omega$; CF is the correction factor depending on $\gamma = d_i/2t_i$ and on $\tau = t_{brace}/t_{chord}$, $A_i = \pi(d_i - t_i)t_i$ is the cross-sectional area of rods. Note that, in some cases, instead of $SCF_0 \times CF$ other formulae are used. S_{rhs} is the hot spot stress range depending on the number of cycles and the member thickness. For $N_F = 10^5$ equation (3.2) is used:

$$\log S_{rhs} = \frac{1}{3} (12.476 - \log N_F) + 0.06 \log N_F \log \frac{16}{t_i}, \quad (3.2)$$



Simply supported uniplanar CHS truss with parallel chords subject to a fluctuating force

Figure 1. Simply supported uniplanar CHS truss with parallel chords subject to a fluctuating force

where $\gamma_{Mf} = 1.25$ is the fatigue safety factor. It should be mentioned that, for K-gap joints, in the case of axial balanced brace, the values of SCF_0 are given in diagrams. Since for the optimization continuous functions are needed, we have replaced these diagrams by approximate second order polynomials. For CF we have used the formulae given in Zhao et al. [4] instead of the diagrams in [5].

3.2. Fatigue strength of the chord of joint E. The joint E is selected instead of G, since in the chord wall at joint E stress concentration arises also from the balanced axial loading.

$$1.5 \frac{N_{E0}}{A_0} SCF_{CH,CH} + 1.3 \frac{N_{E3}}{A_3} SCF_{0,CH,AX} CF_{CH,AX} \leq \frac{S_{rhs}}{\gamma_{Mf}}. \quad (3.3)$$

The axial member forces are as follows:

$$N_{E0} = \frac{2\Delta F}{\omega}; N_{E3} = \frac{\Delta F(1 + \omega^2)^{0.5}}{\omega}. \quad (3.4)$$

In the calculation of SCF for chord loading the formula given by Zhao et al. [4] in Table D.3 is used instead of Figure D.8 in [5]:

$$SCF_{CH,CH} = 1.2 \left(\frac{t_3}{t_0} \right)^{0.3} (\sin \theta)^{-0.9}. \quad (3.5)$$

In the calculation of SCF_0 for balanced axial loading in the two braces the following approximate continuous formula is used instead of the diagram of Figure D.6 given by [5]

$$SCF_{0,CH,AX} = 0.217 + 0.1171\theta - 0.0009311\theta^2 + (2.99 - 0.173\theta + 0.0017111\theta^2) \frac{d_3}{d_0}. \quad (3.6)$$

In the calculation of CF for balanced axial loading the formula given by Zhao et al. [4] in Table D.3 is used instead of the diagram in Figure D.6 in [5]

$$CF_{CH,AX} = \left(\frac{d_0}{24t_0} \right)^{0.4} \left(\frac{t_3}{0.5t_0} \right)^{1.1}. \quad (3.7)$$

In S_{rhs} (equation 3.2) $t_i = t_0$.

3.3. Fatigue strength of the brace of joint E.

$$1.3 \frac{N_{E3}}{A_3} SCF_{0,B,AX} CF_{B,AX} \leq \frac{S_{rhs}}{1.25}, \quad (3.8)$$

where

$$SCF_{0,B,AX} = 2.49 - 0.078\theta + 0.001664\theta^2 - (3.6 - 0.186\theta + 0.0029333\theta^2) \frac{d_3}{d_0}, \quad (3.9)$$

$$CF_{B,AX} = \left(\frac{d_0}{24t_0} \right)^{0.5} \left(\frac{t_3}{0.5t_0} \right)^{0.5}. \quad (3.10)$$

In S_{rhs} (equation 3.2) $t_i = t_3$.

3.4. Fatigue strength of the chord of joint F.

$$1.5 \frac{N_{F2}}{A_2} SCF_{CH,CH} + 1.3 \frac{N_{F3}}{A_3} SCF_{0,CH,AX} CF_{CH,AX} \leq \frac{S_{rhs}}{1.25}, \quad (3.11)$$

where

$$N_{F2} = \frac{3\Delta F}{\omega}, N_{F3} = N_{E3}. \quad (3.12)$$

For $SCF_{CH,CH}$ equation (3.4) is used, but with t_2 instead of t_0 .

For $SCF_{0,CH,AX}$ equation (3.5) is used, but with d_2 instead of d_0 .

For $CF_{CH,AX}$ equation (3.6) is used, but with d_2 and t_2 instead of d_0 and t_0 .

In S_{rhs} (equation 3.2) $t_i = t_2$.

3.5. Fatigue strength of the brace of joint F.

$$1.3 \frac{N_{F3}}{A_3} SCF_{0,B,AX} CF_{B,AX} \leq \frac{S_{rhs}}{1.25}. \quad (3.13)$$

For $SCF_{0,B,AX}$ equation (3.8) is used, but with d_2 instead of d_0 .

For $CF_{B,AX}$ equation (3.9) is used, but with d_2 and t_2 instead of d_0 and t_0 .

In S_{rhs} (equation 3.2) $t_i = t_3$.

3.6. Fatigue strength of the chord of joint A. Joint A is calculated as an X-joint.

$$\gamma = \frac{d_0}{2t_0}; \tau = \frac{t_3}{t_0}; \beta = \frac{d_3}{d_0}, \quad (3.14)$$

$$1.5 \frac{N_{A0}}{A_0} X_{1,2\max} \leq \frac{S_{rhs}}{1.25}, \quad (3.15)$$

$$N_{A0} = \frac{\Delta F}{2\omega}, \quad (3.16)$$

$$X_1 = 3.87\gamma\tau\beta (1.1 - \beta^{1.8}) \sin^{1.7} \theta, \quad (3.17)$$

$$X_2 = \gamma^{0.2}\tau \left[2.65 + 5(\beta - 0.65)^2 \right] - 3\tau\beta \sin \theta. \quad (3.18)$$

Note that the approximate value of α is calculated as

$$\alpha = \frac{2a}{d_0} = \frac{2 \times 4000}{400} = 80 > 12, \quad (3.19)$$

thus, $F_2 = 1$. In S_{rhs} (equation 3.2) $t_i = t_0$.

3.7. Fatigue strength of the brace of joint A.

$$1.3 \frac{N_{A3}}{A_3} X_{3,4\max} \leq \frac{S_{rhs}}{1.25}, \quad (3.20)$$

where $N_{A3} = N_{E3}$;

$$X_3 = 1 + 1.9\gamma\tau^{0.5}\beta^{0.9} (1.09 - \beta^{1.7}) \sin^{2.5} \theta, \quad (3.21)$$

$$X_4 = 3 + \gamma^{1.2} 0.12 \exp(-4\beta) + 0.011\beta^2 - 0.045, \quad (3.22)$$

In S_{rhs} (equation 3.2) $t_i = t_3$. γ, τ, β are defined in Section 3.5.

3.8. Size constraints. The ranges of validity are as follows:

$$0.3 \leq \frac{d_3}{d_0}, \frac{d_3}{d_2} \leq 0.6, \quad (3.23)$$

$$24 \leq \frac{d_0}{t_0}, \frac{d_2}{t_2} \leq 60, \quad (3.24)$$

$$0.25 \leq \frac{t_3}{t_0}, \frac{t_3}{t_2} \leq 1.0, \quad (3.25)$$

$$30^\circ \leq \theta \leq 60^\circ, \quad (3.26)$$

$$4 \leq t_{0,2,3} \leq 50 \text{ mm}. \quad (3.27)$$

3.9. Constraint on zero joint eccentricity. From the limitation for the gap g that

$$g = \frac{d_{0,2}}{\tan \theta} - \frac{d_3}{\sin \theta} \geq 2t_3, \quad (3.28)$$

one obtains

$$d_{0,2} \geq 2t_3\omega + d_3 (1 + \omega^2)^{0.5}. \quad (3.29)$$

4. The cost function

4.1. Cost function components. The cost function contains the costs of material, cutting and grinding of strut ends, assembly, welding and painting

$$K = K_M + K_C + K_A + K_W + K_P \quad (4.1)$$

In the material cost

$$K_M = \rho \sum_i k_{Mi} A_i L_i \quad (4.2)$$

the material cost factors of Price List [11] are used as given in Table 1. The material density is $\rho = 7.85 \times 10^{-6} \text{ kg/mm}^3$. The hot formed CHS profiles are selected according to prEN 10210-2 [12]. Some new profiles are given in [13].

The strut lengths are as follows $L_0 = 24000$, $L_2 = 20000$, $L_3 = 24000 (1 + \omega^2)^{0.5}$ mm.

For the calculation of cutting and grinding times of strut ends an empirical formula is developed on the basis of measurements in a Hungarian steel construction factory as follows:

$$T_i = 3.0442x1.007^{di} \text{ (min)}, \quad (4.3)$$

di in mm.

This formula is valid for diagonals. In our example

$$K_C = k_F \Theta_C x 3.0442 (2x1.007^{d_0} + 2x1.007^{d_2} + 24x1.007^{d_3}), \quad (4.4)$$

where the difficulty factor is taken as $\Theta_C = 2$ and the fabrication cost factor is selected using the data of Tizani et al [10] as $k_F = 0.6667$ \$/min. Note that the cutting time data of Tizani et al. [10] cannot be used here, since they are related to too small a diameter of 60 mm [14]. It should be mentioned that in our other paper [15] another formula is used which contains also the effect of strut thickness.

$$K_A = C_A k_F \Theta_A (\kappa \rho V)^{0.5}, \quad (4.5)$$

where $C_A = 1.0 \text{ min/kg}^{0.5}$; $\Theta_A = 3.5$; the number of structural elements to be assembled is $\kappa = 14$.

The cost calculation of welding is based on welding times developed from the COST-COMP [6] software for different welding technologies and weld types.

$$K_W = k_F \Theta_W \sum_i C_{Wi} a_{Wi}^n L_{Wi}, \quad (4.6)$$

where the difficulty factor is taken as $\Theta_W = 2$. The fillet weld size is $a_W = t_3$. For fillet welds performed by SMAW (shielded metal arc welding)

$$C_W a_W^n = 0.7889 \times 10^{-3} a_W^2. \quad (4.7)$$

d (mm)	k_M (\$/kg)
88.9, 101.6, 114.3	1.0553
139.7, 168.3, 177.8, 193.7	1.1294
219.1, 244.5, 273.0, 323.9	1.2922
355.6, 406.4	1.3642
457.0, 508.0	1.4081

Table 1. Material cost factors for available hot formed CHS profiles

The weld length in our example is

$$L_W = \pi d_3 (1 + \omega^2)^{0.5} / \omega. \quad (4.8)$$

The painting cost is calculated as

$$K_P = k_P S_P, \quad (4.9)$$

where, according to Tizani et al. [10] the cost factor is $k_P = 14.4$ \$/m². The painted surface in our example is

$$S_P = 10^{-6} \pi (24.000 d_0 + 20.000 d_2 + 24.000 d_3 (1 + \omega^2)^{0.5}). \quad (4.10)$$

5. Mathematical optimization and results

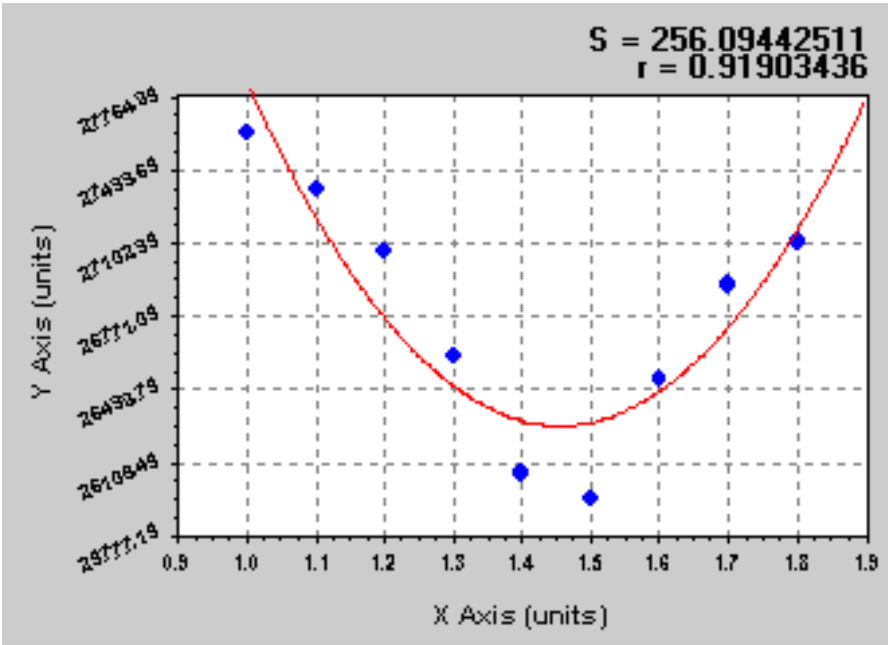
5.1. Constrained function minimization. The constrained function minimization is performed using the Rosenbrock's hillclimb method with additional discretization to find the corresponding available cross-sectional dimensions [8]. The results are summarized in Tables 2, 3 and Figure 5.1.

The optimum solution of $h/a = 1.5$ is marked by bold letters.

The optimum strut dimensions in the case of $h/a = 1.5$ are given in Table 3.

$\omega = h/a$	K (\$)
1.0	27599.3
1.1	27344.5
1.2	27061.8
1.3	26592.2
1.4	26061.3
1.5	25942.8
1.6	26491.1
1.7	26912.8
1.8	27112.5

Table 2. The cost of continuous (nondiscrete) solutions against the truss height ratio h/a



Cost against h/a ratio

d_0, t_0	323.9x12.5
d_2, t_2	323.9x12.5
d_3, t_3	168.3x5

Table 3. Optimum strut dimensions in mm for $h/a = 1.5$

L (m)	optimum value of $\omega = h/a$
15	1.3
20	1.4
24	1.5
30	1.5
35	1.6
40	1.6
45	1.7
50	1.7

Table 4. Optimum value of $\omega = h/a$ for different span lengths

We have made a parametric survey changing the span length keeping all other parameters at the same values and calculating the optimum values of $\omega = h/a$. Due to the limits on θ , i.e. $30^0 \leq \theta \leq 60^0$, ω can be varied between 0.6 and 1.8 .

It is visible from Table 4 that the optimum value of ω is proportional to the span length. All optima in the calculation were nondiscrete, so the discrete solution distances can be different from the nondiscrete ones. The optimum value of ω is changing, depending on the shape of structure, loadings, supports, etc. so it is difficult to arrive at a general conclusion. At least we can say that ω has an optimum value and it is worth finding.

6. Conclusions

In the welded joints of tubular trusses high stress concentrations occur. The new IIW fatigue design rules enable designers to calculate the stress concentration factors more precisely than previously. This calculation method is used for the optimum design of a uniplanar CHS truss subject to a fluctuating force.

In the optimization process the cross-sectional dimensions and the distance between the parallel chords (truss heights) are optimized, which minimizes the structural cost. The height is discretely varied. Three rod groups are defined having the same cross-sectional area, thus six unknown variables are optimized for each truss height ratio.

The existence of an optimum height can be explained by the fact that, increasing the height, the chord forces decrease, but the branch length increases and this tendency turns back when the height decreases.

The difference between the cost corresponding to the best and worst solution, indicated in Table 2, is 6.4%.

After a parametric survey, changing the span length, we have found that ω has an optimum value and it is proportional to the span length.

The advanced cost function, which contains the costs of material, cutting and grinding of strut ends, assembly, welding and painting, enables designers to calculate the costs more realistically than previously.

Acknowledgement. The research work was supported by the Hungarian Scientific Research Foundation grants OTKA T38058, and T37941. The author gratefully acknowledges the help of Prof. József Farkas (University of Miskolc, Hungary) and Prof. Erkki Niemi (Lappeenranta University of Technology, Finland) in formulating the problem.

References

1. Recommended fatigue design procedure for hollow section joints: Part 1. Hot spot stress method for nodal joints, IIW Subcomm. XV-E. IIW-Doc. Strasbourg, 1985, pp. 582–585.
2. FARKAS, J.: Optimum design for fatigue of trusses welded from circular hollow sections. *Acta Technica Acad. Sci. Hung.* **100**(1-2), (1987)
3. FARKAS, J.: Minimum cost design of tubular trusses considering buckling and fatigue constraints. Niemi, E. and Mäkeläinen, (eds.) *Tubular Structures*. P. Elsevier, London-New York, 1990, pp. 451–459.
4. ZHAO, X.L. AND HERION, S. ET AL.: Design guide for circular and rectangular hollow section joints under fatigue loading, IIW-Doc. XV-E, 1998, pp. 98–236.

5. Recommended fatigue design procedure for welded hollow section joints: Part 1-2, IIW-Doc.XIII-1804-99, IIW-Doc.XV, 1999, pp. 1035–1099.
6. COSTCOMP: Programm zur Berechnung der Schweisskosten, Düsseldorf: Deutscher Verlag für Schweissttechnik, 1990.
7. BODT, H.I.M.: *The global approach to welding costs*. The Hague: The Netherlands Institute of Welding, 1990.
8. FARKAS, J. AND JÁRMAI, K.: *Analysis and Optimum Design of Metal Structures*. Rotterdam-Brookfield, Balkema, 1997.
9. JÁRMAI, K. AND FARKAS, J.: Cost calculation and optimisation of welded steel structures. *J. Constructional Steel Research*, **50**, (1999), 115–135.
10. TIZIANI, W.M.K. AND YUSUF, K.O. ET AL.: A knowledge based system to support joint fabrication decision making at the design stage – Case studies for CHS trusses, Farkas, J., and Jármai, K., (eds.) *Tubular Structures VII.*, Balkema, Rotterdam-Brookfield, 1996, 483–489.
11. *PRICE LIST 20*. Steel tubes, pipes and hollow sections. Part 1b. Structural hollow sections, British Steel Tubes and Pipes, 1995.
12. *prEN 10210-2*. Hot finished structural hollow sections, 1996.
13. DUTTA, D.: *Structures with hollow sections*. Ernst & Sohn, Berlin, 2002.
14. FARKAS, J. AND JÁRMAI, K.: *Economic design of metal structures*. Millpress Science Publisher, Rotterdam, 2003.
15. FARKAS, J. AND JÁRMAI, K.: Weight optimization of a triangular CHS truss using an improved cost function, R. Puthli, and H. Herion, (eds) 9th International Symposium on Tubular Structures, April 4-8. 2001. Düsseldorf, Balkema Publishers, Rotterdam, 2001, 429-435.

INFLUENCE OF CROSS-SECTIONAL CONFIGURATION ON KÁRMÁN VORTEX EXCITATION

MIZUYASU KOIDE

Life Engineering Research Center, Niigata Sangyo University
4730 Karuigawa, Kashiwazaki, Niigata, 945-1393, Japan
mkoide@life-eng.nsu.ac.jp

TSUTOMU TAKAHASHI, MASATAKA SHIRAKASHI

Department of Mechanical Engineering, Nagaoka University of Technology
1603-1 Kamitomioka, Nagaoka, Niigata, 940-2188, Japan

[Received: November 12, 2003]

Abstract. Three cylindrical bodies with different cross-sectional configurations, i.e. a circular, semi-circular and triangular cylinder, are used as the test cylinders, in order to investigate the influence of movement of the separation point on the Kármán vortex excitation. The cylinders were supported elastically by plate springs. The synchronization of Kármán vortex shedding occurs on all three cylinders over almost equal ranges of oscillation amplitude and frequency given by the mechanical oscillator. However, the Kármán vortex excitation behavior differs drastically among the three cylinders in spite of the fact that the cylinders are supported elastically with virtually equal structure parameters.

Mathematical Subject Classification: 76B47, 76D25

Keywords: Kármán vortex excitation, cross-sectional configuration, synchronization

1. Introduction

The Kármán vortex excitation is an oscillation caused by the hydrodynamic force which originates from periodic Kármán vortex formation and shedding, and it has basically the nature of resonance of a linear system. That is, the cylinder is oscillated by the alternating force due to Kármán vortex shedding and the amplitude is large when the vortex shedding frequency f_v is equal to the natural frequency of the structure f_n . The cylinder motion affects the flow around it and then the magnitude and frequency of exciting force in turn.

Therefore, the Kármán vortex excitation is regarded as non-linear self-excitation caused by the feedback loop which is constituted by two interactions, i.e. the effect of cylinder motion on the fluid force due to the periodic vortex shedding and the response of the structure to the resulting fluid force. Hence, its mechanism can be discussed by separating the process into the two interactions.

Funakawa [1] showed that the separation point on an oscillating circular cylinder moves forward and backward, synchronized with the cross-flow oscillation. Based

on this observation he suggested a self-excitation mechanism for the Kármán vortex excitation.

In this work, influence of the cross-sectional configuration of a cylindrical body on the Kármán vortex excitation was investigated experimentally by using a circular cylinder, a semi-circular cylinder and a triangular cylinder, in order to investigate the role of separation point movement in the mechanism of the Kármán vortex excitation.

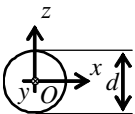
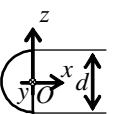
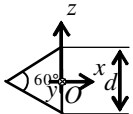
2. Experimental apparatus and measurements

Table 1 shows cross-sectional configurations of the cylinders used in this investigation. They were set in a uniform flow from left to right (in the x -direction) in a wind tunnel. When the cylinders are set in a uniform flow, the separation point movement is free on the circular cylinder surface, restricted to the upstream circular arc of the semi-circular cylinder and fixed at the downstream vertices of the triangular cylinder [2]. Measurements were carried out in a blow-down type wind tunnel with a measuring section of $320 (H) \times 320 (W) \times 1000 (L) \text{ mm}$. The turbulence level at the center of the measuring section is less than 0.6 % at $U = 2.0 \text{ m/s}$. A ring type vortex anemometer [3] was applied to measure U .

Figure 1 shows the experimental apparatus arrangement for the measuring section. The test cylinder was set horizontally and perpendicularly to the free stream. The height d of each cylinder was 26 mm and the blocking ratio was about 8 %. The cylinder was passing through slots on the side walls and supported at both ends outside the measuring section, as shown in Figure 1. End plates were attached to the cylinder to remove influence of flow through the slots [4].

The elastically supported system is composed of two cantilever plate springs. Since the length of the cantilever plate is much longer than the oscillation amplitude A , the cylinder motion is regarded as translational oscillation in the vertical direction (z -direction), i.e. cross-flow oscillation. Two laser displacement meters were used to measure cylinder displacement Z at both ends of the cylinder, as shown in Figure 1. The oscillation amplitude A was calculated from root-mean square (rms) value of Z , i.e. $A = \sqrt{2}Z_{rms}$.

Table 1. Cross-sectional configuration and effective mass m_e of the elastically supported cylinders ($d = 26 \times 10^{-3} \text{ m}$)

	Circular cylinder	Semi-circular cylinder	Triangular cylinder
Effective Mass [kg]	53.7×10^{-3}	50.1×10^{-3}	50.7×10^{-3}
Cross-sectional Configuration			
Flow direction: from left to right			

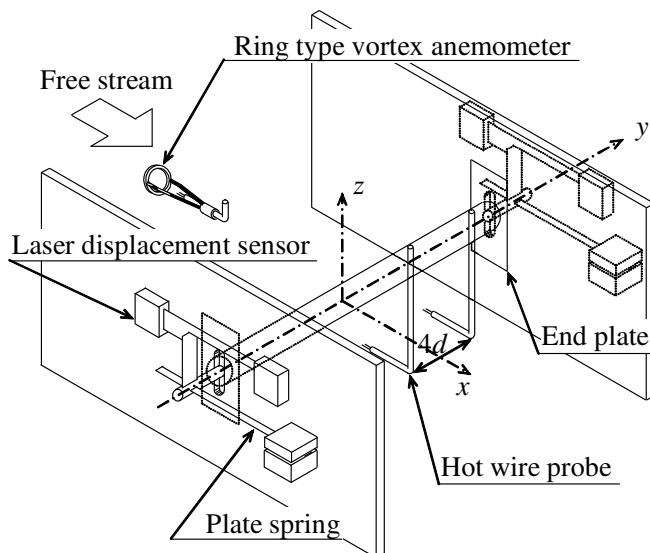


Figure 1. Arrangement of the experimental apparatus (elastically-supported system) and the coordinate system

The natural frequency f_n , effective mass m_e and logarithmic damping factor δ of the system were determined by free damping oscillation in otherwise quiescent air. The values of f_n , m_e and δ were set virtually equal for all the three cylinders.

The vortex shedding frequency f_v was obtained by applying FFT analysis to the streamwise fluctuating velocity u detected by a hot wire probe at a location in the near wake of the cylinder ($x = 2d$, $z = d$). The spectrum of u was averaged over 20 data to reduce the effect of turbulence. The vortex shedding frequency f_v was determined as the frequency at which the spectrum of u had the maximum peak. Furthermore, the phase difference between u and Z was calculated and its average value ϕ_{uZ} was obtained from 20 data. The standard deviation of ϕ_{uZ} , σ_ϕ was also obtained. The cross-correlation coefficient R_{uu} was obtained from two u signals detected by two hot wire probes set with $4d$ spanwise separation. The cross-correlation coefficient R_{uu} increases due to Kármán vortex excitation since it shows an enhancement of spanwise coherency of the Kármán vortex [2]. In this paper, the increase of R_{uu} is adopted as one of criteria to decide whether Kármán vortex excitation occurs or not.

The lift force F_L exerted on the stationary cylinder was measured by load transducers at both ends of the cylinder outside the measuring section.

3. Results and discussion

3.1. Behavior of the cylinder oscillation and vortex shedding in Kármán vortex excitation. Figures 2, 3 and 4 show the behavior of the cylinder oscillation

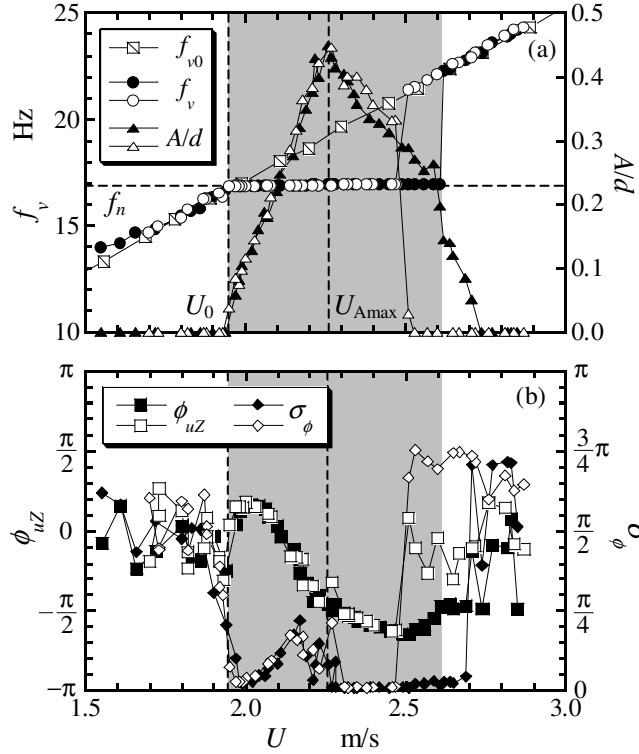


Figure 2. f_v , A/d , ϕ_{uZ} and σ_ϕ versus U for the circular cylinder. $f_n = 16.93$ Hz, $\delta = 0.00958$ (Closed symbols: U increased, open symbols: U decreased)

and vortex shedding against the free stream velocity U for the circular cylinder, the semi-circular cylinder and the triangular cylinder, respectively. In one run of the wind tunnel experiment, U was first increased stepwise from the lowest value of around 1.5 m/s to the velocity beyond the Kármán vortex excitation range, and then decreased again to the lowest velocity. The closed symbols are for increasing U and the open symbols for decreasing U , respectively.

The vortex shedding frequency f_v and the non-dimensional oscillation amplitude A/d are plotted in Figures 2(a), 3(a) and 4(a). The Kármán vortex shedding frequency from the stationary cylinder f_{v0} is also plotted to compare with f_v . In these Figures, U_0 is the velocity at which f_{v0} coincides with the natural frequency of the system f_n , and U_{Amax} indicates the velocity at which A/d is maximum. Figures 2(b), 3(b) and 4(b) show the phase difference ϕ_{uZ} between velocity fluctuation u and the cylinder displacement Z and its standard deviation σ_ϕ . The shaded region is the Kármán vortex excitation region when U is increased.

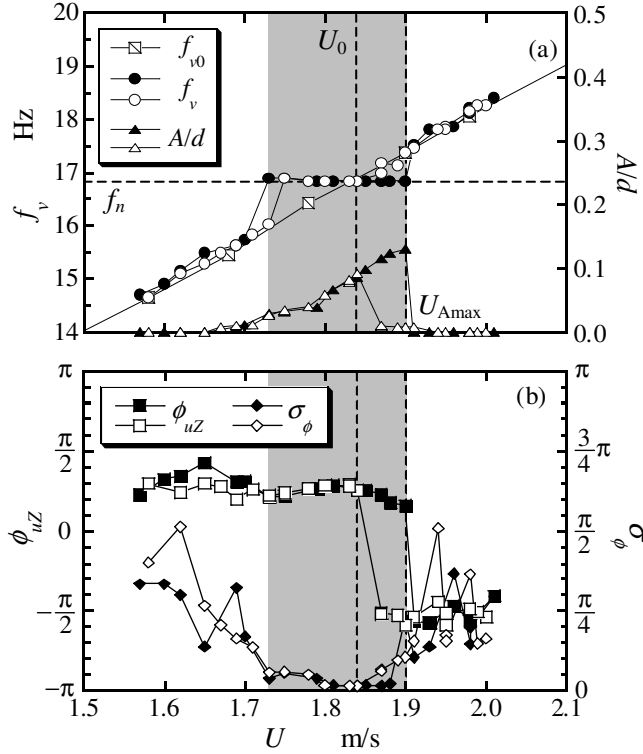


Figure 3. f_v , A/d , ϕ_{uZ} and σ_ϕ versus U for the semi-circular cylinder. $f_n = 16.86$ Hz, $\delta = 0.0116$ (Closed symbols: U increased, open symbols: U decreased)

3.1.1. *Circular cylinder.* Figure 2 shows the results of the circular cylinder. As shown in Figure 2(a), the oscillation amplitude A/d is large and the vortex shedding frequency f_v coincides with f_n over a certain velocity range including U_0 , showing that the Kármán vortex excitation occurs there. In the case of the circular cylinder, the velocity U_0 is very close to the lower velocity edge of the Kármán vortex excitation range. In contrast, the synchronization of Kármán vortex shedding was observed at both sides of U_0 when the circular cylinder was oscillated with a certain amplitude and frequency using a mechanical oscillator [2].

The amplitude of the circular cylinder due to the Kármán vortex excitation has a maximum value of $A/d = 0.4$ at U_{Amax} , which is considerably larger than U_0 . In a linear oscillation model, the oscillation amplitude reaches its maximum when the frequency of the excitation force coincides with the natural frequency, which means that A/d would be maximum at U_0 in the present experiment. From the discrepancy between U_0 and U_{Amax} , it is inferred that the alternating lift force F_L exerted on

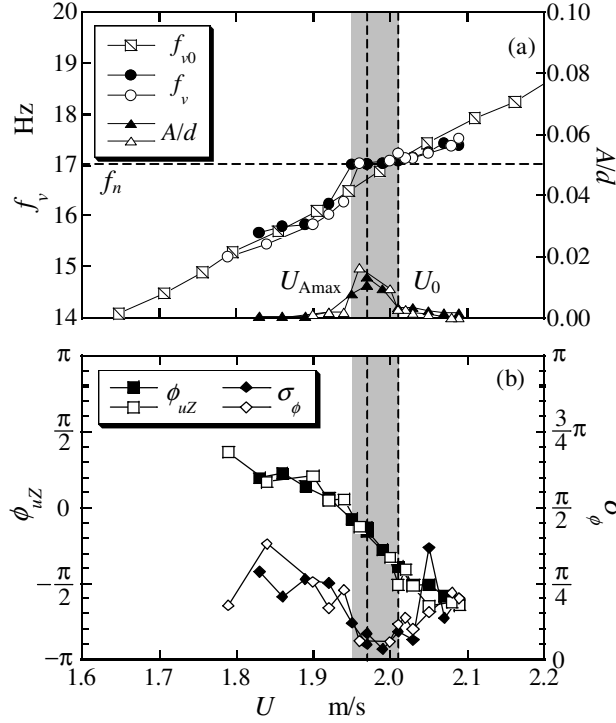


Figure 4. f_v , A/d , ϕ_{uZ} and σ_ϕ versus U for the triangular cylinder. $f_n = 17.03$ Hz, $\delta = 0.0141$ (Closed symbols: U increased, open symbols: U decreased)

the oscillating cylinder is larger than that on the stationary cylinder and enhanced with the oscillation amplitude due to the influence of the cylinder oscillation on the Kármán vortex shedding.

A remarkable hysteresis is observed near the higher velocity edge of the excitation range, where both A/d and f_v at a same value of U differs depending on whether U is increased or decreased. When the circular cylinder was oscillated using a mechanical oscillator, such hysteresis was not observed. The phase difference ϕ_{uZ} changes gradually in the excitation range around U_{Amax} , and the total amount of the change is approximately π , as seen in Figure 2(b). This shows that the timing of the vortex shedding becomes anti-phase against the cylinder oscillation. The standard deviation σ_ϕ represents the extent of disturbance in ϕ_{uZ} , and it is an index of coherency between the cylinder oscillation and the vortex shedding. In Figure 2(b), ϕ_{uZ} varies continuously in the range $U_0 < U < U_{Amax}$, and σ_ϕ considerably increases at the same time. This result shows that the coherency of vortex shedding with the cylinder

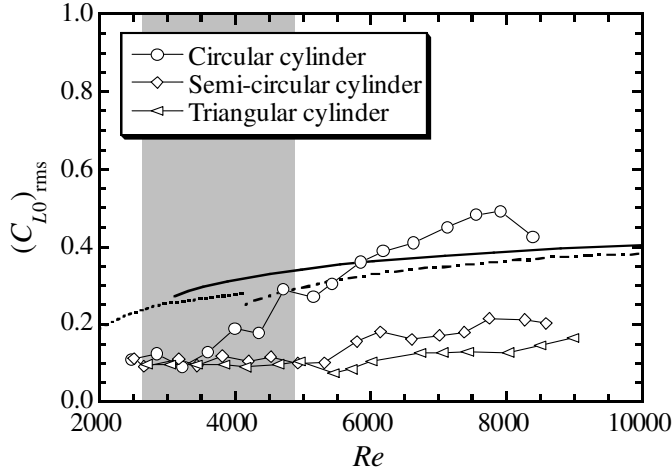


Figure 5. Lift coefficient on stationary cylinder $(C_{L0})_{rms}$ versus Reynolds number Re . — · — · — Vickery; — Bishop and Hassan; — · — Keefe; for circular cylinder [5]. The shaded region shows the range of Kármán vortex excitation experiments for circular cylinder

oscillation becomes lower with U in this range. In contrast, ϕ_{uZ} is nearly constant and σ_ϕ is almost suppressed in the range of $U > U_{Amax}$ in the excitation range, showing that the vortex shedding is completely synchronized with the cylinder oscillation.

3.1.2. Semi-circular cylinder. The Kármán vortex excitation occurs over a considerable velocity range in the case of the semi-circular cylinder as seen in Figure 3. However, the maximum amplitude for the semi-circular cylinder is $1/3$ of that for the circular cylinder, in spite of the fact that the height d , the effective mass m_e , the logarithmic damping factor δ and velocity U are almost the same in the two cases. When U increases, the non-dimensional amplitude A/d continues increasing in the excitation range, and the oscillation suddenly ceases soon after A/d reaches its maximum. The excitation range of the semi-circular cylinder lies on both sides of U_0 , while that of the circular cylinder exists only on $U \geq U_0$.

A definite hysteresis is observed for the semi-circular cylinder in f_v and $A/d \sim U$ curves at higher velocity edge of the excitation range, and the repeatability of the hysteresis behavior is much higher for the semi-circular cylinder than for the circular cylinder.

In the excitation range, ϕ_{uZ} is virtually constant and σ_ϕ is very small, showing that the vortex shedding is well synchronized with the cylinder oscillation. A sudden change of ϕ_{uZ} is observed simultaneously with the cessation of the oscillation at the higher velocity edge. However, it cannot be concluded whether this change of ϕ_{uZ} is caused by the same phenomenon that caused the change of ϕ_{uZ} in the excitation range of the circular cylinder.

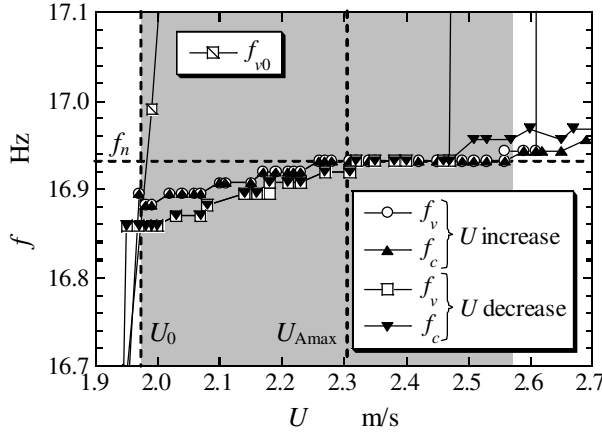


Figure 6. The details of vortex shedding frequency f_v and oscillation frequency f_c of the circular cylinder in Kármán vortex excitation region

3.1.3. Triangular cylinder. Although experimental conditions for the triangular cylinder are the same as those of the circular cylinder and the semi-circular cylinder, the maximum value of A/d is $1/30$ of the circular cylinder as shown in Figure 4(a). The vortex excitation is observed over a narrow velocity range. It seems that the vortex excitation range lies on $U \leq U_0$ in contrast to the cases of the circular and the semi-circular cylinders. The hysteresis is not discerned clearly, maybe because A/d is small and the vortex excitation range is narrow.

Figure 4(b) shows that ϕ_{uZ} steeply decreases with U in the vortex excitation range. However, the standard deviation σ_ϕ in Figure 4(b) is small over the same range, which indicates the occurrence of definite synchronization of Kármán vortex shedding in spite of the large change in ϕ_{uZ} .

3.2. Lift force acting on the cylinder.

3.2.1. Lift force acting on the stationary cylinder. The alternating lift force F_L , which acts on the fixed cylinders, was measured over a free stream velocity U range including the vortex excitation range presented in Section 3.1. Since F_L was composed of the contributions of Kármán vortex shedding and other unsteady turbulence, the root mean square value of F_L , $(F_L)_{rms}$, was used to estimate the magnitude of F_L . Hence, the fluctuating lift coefficient of a stationary cylinder $(C_{L0})_{rms}$ was calculated by the following equation:

$$(C_{L0})_{rms} = \frac{(F_L)_{rms}}{\frac{1}{2}\rho U^2 dl}, \quad (3.1)$$

where ρ is air density, d is the height of the cylinder and l is the effective length of the cylinder defined as the distance between the two end plates (see Figure 1).

The lift coefficients $(C_{L0})_{rms}$ for the three cylinders were plotted against the Reynolds number Re in Figure 5. The shaded region shows the range where the oscillation measurement for the circular cylinder was carried out. $(C_{L0})_{rms}$ for a circular cylinder measured by Vickery, Bishop and Hassan, Keefe [5] was also plotted in Figure 5 for comparison. The lift coefficient $(C_{L0})_{rms}$ of the circular cylinder obtained in this work agrees well with those by others when $Re > 5000$, but is considerably lower when $2500 < Re < 4500$.

The lift coefficient $(C_{L0})_{rms}$ of the circular cylinder increases gradually with Re in the range of the oscillation experiment, say from 0.1 at $Re = 2500$ to 0.3 at $Re = 5000$. While $(C_{L0})_{rms}$ for the semi-circular cylinder and the triangular cylinder are equal to that of the circular cylinder when $Re = 2500$, they remain constant in the same Re range. Hence, $(C_{L0})_{rms}$ of the circular cylinder is larger than those of the other two cylinders by a factor of 3 at $Re = 5000$.

3.2.2. Lift force acting on the oscillating cylinder excited by Kármán vortex excitation. In order to estimate the alternating fluid force exerted on the cylinder under the Kármán vortex excitation, it is assumed that the cylinder supported elastically by two plate springs is a linear system with constant mass, spring and damping. Based on this assumption, the following equation determines the cylinder motion Z

$$m_e \ddot{Z} + c \dot{Z} + kZ = F_L, \quad (3.2)$$

where m_e is the effective mass of the cylinder, c is the damping factor and k is the spring constant. F_L is the lift force caused by the periodic Kármán vortex shedding, and is assumed to be sinusoidal. That is,

$$F_L = F_0 \sin(2\pi f_v t). \quad (3.3)$$

From the solutions of equations (3.2) and (3.3) together with the definition of the lift coefficient $(C_{LR})_{rms}$ as equation (3.1), we obtain

$$(C_{LR})_{rms} = \frac{8\pi^2 m_e f_n^2 A \sqrt{(1 - \eta^2)^2 + (2\zeta\eta)^2}}{\sqrt{2}\rho U^2 dl}, \quad (3.4)$$

where $\eta = f_v/f_n$ and ζ is the damping ratio ($= \delta/(2\pi)$). From equation (3.4) it is seen that a slight difference between f_v and f_n in the vortex excitation range affects $(C_{LR})_{rms}$ drastically when the damping ratio ζ is very small like in the experiments in this work. Therefore, the results for the circular cylinder in Figure 2(a) were examined more precisely. Figure 6 shows the oscillation frequency f_c and the vortex shedding frequency f_v in the vortex excitation range in detail. In this Figure, it is seen that f_c coincides with f_v but they do not coincide with f_n when U is smaller than U_{Amax} . The slight difference between f_v and f_c reflects the large value of σ_ϕ in the range $U_0 < U < U_{Amax}$ shown in Figure 2(b). When $U > U_{Amax}$ in the vortex excitation range, f_c and f_v are strictly equal to f_n .

$(C_{LR})_{rms}$ was calculated using equation (3.4), based on the results that are described in Section 3.1. In Figure 7, $(C_{LR})_{rms}$ of the circular cylinder, the semi-circular cylinder and the triangular cylinder are plotted against A/d for the cases of increasing U . In the Figure, the arrows indicate the order of measurement. The alternating

lift coefficients of the oscillating circular cylinder by Khalak and Williamson [6] and Hayashi et al. [7] are added for comparison. The former was measured directly in water and the latter in air.

The lift coefficient $(C_{LR})_{rms}$ of the circular cylinder and the semi-circular cylinder are equal to each other and increase with A/d when $A/d < 0.13$. However, the maximum value of $(C_{LR})_{rms}$ of the semi-circular cylinder is around 0.4 at $A/d = 0.13$ while $(C_{LR})_{rms}$ of the circular cylinder continues to increase till it attains the maximum value around unity, at $A/d = 0.45$. The lift coefficient $(C_{LR})_{rms}$ of the triangular cylinder at very small amplitude is nearly equal to that of the other two cylinders, and no definite increase is observed since the range of A/d is limited. Although the experimental conditions for the three cylinders are almost the same, the maximum value of $(C_{LR})_{rms}$ is quite different among them, e.g. maximum value of $(C_{LR})_{rms}$ for the circular cylinder is about 10 times that for the triangular cylinder.

The difference between $(C_{LR})_{rms}$ of the three cylinders with different cross-sectional configurations is attributed to the separation point movement of these cylinders [2]. For the circular cylinder, the separation point moves widely on the arc of surface synchronized with the cylinder oscillation. In contrast, the separation point on the triangular cylinder is fixed at the rear vertex irrespective of the cylinder oscillation.

The lift coefficient $(C_{LR})_{rms}$ of the circular cylinder based on the linear analysis in this work coincides with the direct measurements by Khalak et al. [6] and Hayashi et al. [7] in the range of $A/d < 0.13$. When $0.13 < A/d < 0.45$, $(C_{LR})_{rms}$ of the higher stem (i.e. $U < U_{Amax}$) in this work agrees well with that by Khalak et al., while that by Hayashi et al. is considerably higher. When A/d is still higher, or begins to decrease passing its maximum, results of the three works are largely different from each other. This may be because of the fact that the assumption of a linear model does not hold when A/d is large, or because of the difference between experimental conditions and ways of measurements.

3.3. Occurrence region of the Kármán vortex excitation. The synchronization region of the Kármán vortex shedding was investigated for all the three cylinders by giving them a controlled oscillation using a mechanical oscillator by the present authors [2]. Since the behavior of Kármán vortex excitation is disturbed by irregular modulation and its magnitude is drastically different among the three cylinders, the criterion of Kármán vortex excitation should be defined more precisely. According to the earlier study, occurrence of the Kármán vortex excitation is defined by a criterion composed of the following four conditions:

- i) an increase of the oscillation amplitude,
- ii) $f_c = f_v$,
- iii) an increase of the cross-correlation coefficient R_{uZ} between the velocity u and the cylinder displacement Z , and
- iv) an increase of the cross-correlation coefficient R_{uu} .

When all of these four conditions are satisfied, the Kármán vortex excitation, and

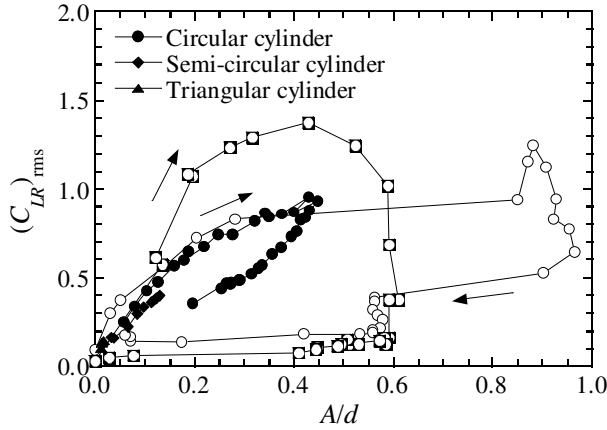


Figure 7. Lift coefficient C_{LR} for oscillating cylinder versus non-dimensional oscillation amplitude A/d under Kármán vortex excitation, when U increases. —○—, Khalak and Williamson [6], —□—, K. Hayashi et al. [7], for circular cylinder

and hence the synchronization of vortex shedding with the cylinder oscillation, i.e. ‘Lock-in’, is decided to occur. When none of the four conditions are satisfied, it is taken to be no vortex excitation and ‘No Lock-in’. The remaining cases are defined as ‘Transition’.

The occurrence regions of the Kármán vortex excitation on the plane of frequency ratio f_{v0}/f_n and the non-dimensional amplitude A/d are plotted in Figures 8(a), 8(b) and 8(c) for each of the cylinders, where the synchronization data obtained by the controlled oscillation experiment are also added [2]. In these controlled oscillation experiments, Re was fixed at about 3500, i.e. U was constant at 2 m/s, to exclude the influence of Re . Since the measurement of Kármán vortex excitation was carried out for increasing or decreasing U , Re is not constant in these Figures. Some of the data were obtained by using systems with different damping factors.

As seen by comparing Figures 8(a), (b) and (c), the Kármán vortex excitation regions for the elastically supported cylinder are drastically different among them, although the synchronization regions for a controlled oscillation experiment are almost the same for all of the cylinders. The Kármán vortex excitation region for the semi-circular cylinder and the triangular cylinder lies within the synchronization region of controlled oscillation experiment. The Kármán vortex excitation region for the circular cylinder is the broadest among the three cylinders and exceeds beyond the lock-in region of controlled oscillation experiment when $f_{v0}/f_n > 1$. The following can be considered the causes for the discrepancy:

- i) Re was not kept constant for the vortex excitation experiment different from the controlled oscillation experiments,

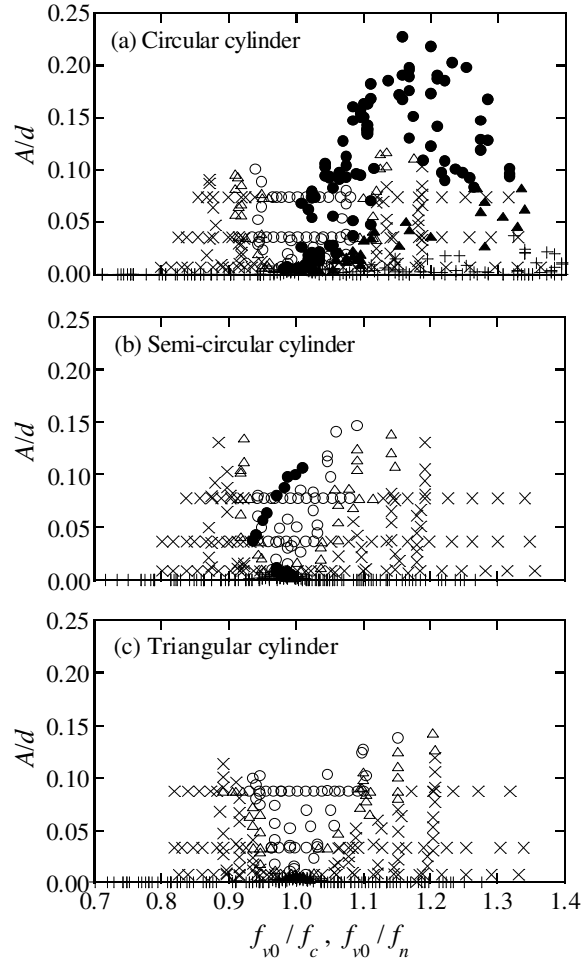


Figure 8. Kármán vortex excitation region on a plane of frequency ratio and non-dimensional amplitude. ● : Kármán vortex excitation, +: No excitation, ▲: Transition; Controlled oscillation, ○: Lock-in, ×: No Lock-in, △: Transition. [2]

- ii) the mechanical oscillator gives the cylinder a precise sinusoidal oscillation, while the Kármán vortex excitation includes considerable modulation of amplitude,
- iii) the cantilever support system induces an attack angle fluctuation synchronized with the cylinder oscillation superimposed on the z -displacement oscillation.

4. Concluding remarks

In the previous work by the present authors the synchronization of Kármán vortex shedding was investigated by giving a controlled cross-flow oscillation to a circular, a semi-circular and a triangular cylinder, and it is shown that the synchronization region is almost the same for the three cylinders in spite of the different behaviors of separation point movement [2].

In this work, influence of the cross-sectional configuration of a cylindrical body on the Kármán vortex excitation was investigated experimentally by using the same cylinders to investigate the role of separation point movement in the Kármán vortex excitation. The three cylinders were supported elastically by cantilever plate springs so that the experimental conditions, such as the mass, natural frequency and damping factor, were almost equal.

Kármán vortex excitation appears on all the three cylinders. However, the oscillation behavior was drastically different among them.

The alternating lift coefficient is equal for the three cylinders when they are at rest. However, the lift coefficient $(C_{LR})_{rms}$ obtained from measured oscillation amplitude A/d are largely different from each other. Although $(C_{LR})_{rms}$ increases with A/d for all the three cylinders, the maximum value is largely different in each case, that is, $(C_{LR})_{rms}$ is around 1.0 at $A/d = 0.45$ for the circular cylinder, 0.4 at $A/d = 0.15$ for the semi-circular cylinder and 0.1 at $A/d = 0.05$, for the triangular cylinder. This tendency of enhancement of lift coefficient by the oscillation corresponds with the separation point movement on these cylinders shown by the controlled oscillation experiment in the previous work.

In conclusion, the mechanism of the Kármán vortex excitation can be explained as follows. A cylinder is oscillated by the alternating lift force due to the periodic Kármán vortex shedding, and the amplitude reaches its maximum when the flow velocity is around U_0 . The resulting cylinder oscillation causes the synchronization of the vortex shedding, which makes the resonance range of flow velocity broader than otherwise. At the same time, the cylinder oscillation influences the movement of the separation point and enhances the lift, depending on the cross-sectional configuration. This enhancement effect is largest for the circular cylinder and negligibly small for the triangular cylinder.

References

1. FUNAKAWA, M.: Excitation mechanism of elastically supported circular cylinder in the flow. *Bulletin of the Japan Society of Mechanical Engineers*, **36**(285), (1970), 337-356. (in Japanese)
2. KOIDE, M., TOMIDA, S., TAKAHASHI, T., BARANYI, L. AND SHIRAKASHI, M.: Influence of cross-sectional configuration on the synchronization of Kármán vortex shedding with the cylinder oscillation. *Japan Society of Mechanical Engineers, International Journal*, **45**(2), (2002), 249-258.

3. KOIDE, M., TAKAHASHI, T. AND SHIRAKASHI, M.: Development of a ring-type vortex anemometer for low-velocity wind tunnel experiments. *Bulletin of Japan Society of Mechanical Engineers*, **7**(657), (2001), 1105-1111. (in Japanese)
4. SHIRAKASHI, M., ISHIDA, Y. AND WAKIYA, S.: Higher velocity resonance of circular cylinder in cross flow. *Transaction of the ASME Journal of Fluids Engineering*, **107**, (1985), 392-396.
5. GARTSHORE, I. S.: Some effects of upstream turbulence on the unsteady lift forces imposed on prismatic two dimensional bodies. *Journal of Fluids Engineering*, **106**, (1984), 418-424.
6. KHALAK, A. AND WILLIAMSON, C. H. K.: Motions, forces and mode transitions in vortex-induced vibrations at low mass-damping. *Journal of Fluids and Structures*, **13**, (1999), 813-853.
7. HAYASHI, K., TANAKA, K., FUJIMA, K. AND SHIGEMURA, T.: Fluid Force Acting on a Vortex Excited Circular Cylinder Vibrating in Steady Flow, National Defense Academy Science and Engineering Research Report, 34(2), (1997), 11-23. (in Japanese)

NUMERICAL OPTIMIZATION OF A HIGH PRESSURE STEAM TURBINE STAGE

PIOTR LAMPART

Institute of Fluid Flow Machinery, Polish Academy of Sciences
Gdańsk, Poland

`lampart@imp.gda.pl`

[Received: November 15, 2003]

Abstract. Blading of a high-pressure (HP) steam turbine stage is optimized using an idea of direct constraint optimization. The objective function to be minimized is the enthalpy loss of the stage. A simplex method of deformed polyhedron proposed by Nelder-Mead is used for optimization. Current values of the objective function are found from 3D Reynolds-averaged Navier Stokes (RANS) computations. To secure global flow conditions, there are constraints imposed on the mass flow rate, exit swirl angle, and reaction. The optimized parameters here are the stator and rotor blade numbers and stagger angles, rotor blade twist angle and parameters of stator blade compound lean at root and tip. Blade profiles are not changed. Optimization gives a design with new 3D stacking lines of the blades and increased flow efficiency, compared to the original design.

Mathematical Subject Classification: 76F99

Keywords: HP axial-flow turbine stage, blade shape optimization, simplex method, blade lean and twist, 3D RANS solver

1. Introduction

Optimization of 3D blading in turbomachinery is a relatively new field of research. It has become possible only with the development of 3D Navier-Stokes codes for turbomachinery applications capable of locating and quantifying loss generation processes in complex turbomachinery geometries, and also thanks to increasing capabilities of computing machines. A robust 3D solver in collaboration with a reliable optimization technique can be a powerful design tool, also in the turbomachinery environment. At present two optimization/design approaches become conspicuous with respect to turbine blading systems. One approach concentrates on development of 3D inverse design using Euler or Navier-Stokes codes where the shape of the blading changes during an iterative procedure until the target distribution of, for example, blade surface static pressure, or downstream velocity is reached, guaranteeing the required performance, e.g. [1,2]. Another approach focuses on optimization of global characteristics of the stage, and the final shape is obtained from minimising/maximising an objective function, for example the total energy loss or efficiency, total pressure loss of the

stage, etc. Values of the objective function for new geometries can be found directly from 3D viscous flow computations, e.g. [3,4]. However, as the direct optimization is time consuming and the main cost is time required for the Navier-Stokes solver, an interesting idea of approximate representation of the objective function using an artificial neural network trained over a data base of RANS solutions was put forward in [5]. In the process of optimization new geometries can be selected using a number of optimization methods, the most popular of which are the steepest gradient method, simplex methods and genetic algorithms.

Optimization of 3D blading in low-pressure (LP) steam turbine stages, especially for exit stages, is shown in [4,6] to bring considerable efficiency gains. There seems to be less room for efficiency improvements in low-load high-pressure (HP) steam turbine stages, [3,7]. Efficiency of cylindrical (radially stacked and straight) blades is relatively high here unless a mistake was made while selecting basic parameters of the blading, like stator and rotor blade numbers and stagger angles. This, however, makes the optimization task even more challenging.

A typical 3D design to raise the efficiency of HP stages is compound lean where some blade sections, usually at the root and tip, are linearly or non-linearly displaced in circumferential direction with respect to other sections. The effects of this design were investigated e.g. in [7-9]. It was found there that lean redistributes blade load, mass flow rate and loss span-wise, compared to the cylindrical blading, and can serve as a means of controlling secondary flow and tip leakage losses in HP turbines. Lean can change the state of boundary layers at the blade suction surface and at the end-walls, as well as can reduce span-wise variations of the exit swirl angle, which is likely to reduce downstream mixing losses and make stator/rotor matching easier. The quantitative effect of lean on the stage loss varies with turbine stage geometry and operation conditions. Due to a number of shape parameters involved in this design it is required that automatic optimization techniques are used to find the optimum design.

The procedure for optimization of an HP steam turbine stage is based on the concept of direct constrained optimization, using the Nelder-Mead method of deformed polyhedron and a 3D RANS solver for turbomachinery applications. Direct optimization is considered highly time consuming. The main cost is CPU time required for the Navier-Stokes solver that computes changing flow geometries. Therefore, 3D computational grids used during optimization will be relatively coarse. However, some experience of the author shows that major tendencies in changing flow patterns with changing geometry of the turbine stage can already be discovered on coarse grids. Anyway, at least the original and final geometries will be checked on refined grids, and possible changes in flow patterns and efficiency gains will be implied based on the comparison of post-optimization computations of the original and final geometries on refined grids.

2. Method of optimization

2.1. Optimised functions and parameters. Shape optimization of turbine blading is carried out with the help of a code Optimus, [10]. Optimization is understood here as an iterative procedure that seeks for an extremum of an objective function – a function of some shape parameters.

In this investigation, the optimized (minimized) objective function is the enthalpy loss of the stator/rotor stage (the leaving energy not considered a loss and assumed to be used in the subsequent stage), defined as $\xi = (h_2 - h_{2s})/(h_{0T} - h_{2s})$ where h_{0T} , h_2 , h_{2s} are the inlet total enthalpy, exit static enthalpy and isentropic enthalpy referred to the exit static pressure, respectively. Alternatively, one can also choose the total enthalpy loss of the stage including the leaving energy (as for the exit turbine stages), or stage power as an objective function. The following parameters of blade shape can be considered during the optimization for each blade row: blade number, stagger angle, blade height, linear twist angle, linear lean angle, and linear sweep angle, 4 parameters of compound twist (2 at hub, 2 at tip), 4 parameters of compound lean (2 at hub, 2 at tip), and 4 parameters of compound sweep (2 at hub, 2 at tip). Each parameter is allowed to vary in a prescribed range of variation.

2.2. Flow constraints. To secure global flow conditions, there are also constraints imposed on the mass flow rate, exit angle, average reaction, reaction at tip and root. The exit angle and reactions are not allowed to assume values beyond the prescribed ranges, which is pronounced in the shape of the objective function f , that is $f = \zeta$, if the exit angle and reactions fall within the prescribed range, or $f = \infty$ (a very large number) otherwise, where ζ is a value of an optimized characteristic (enthalpy loss of the stage) obtained from the RANS solver. The penalty function is imposed on the mass flow rate if it falls beyond a required very narrow interval $[G_-, G_+]$: $f = \zeta$, if $G_- \leq G \leq G_+$, or $f = \zeta + \min[(G - G_{\pm})^2]/\varepsilon$ otherwise, where G - current mass flow rate, ε - penalty coefficient prescribed in a way that the objective function sharply rises to infinity with increasing distance from the limits of the assumed range of variation. As the pressure drop during the optimization is kept constant and the mass flow rate is constrained in a very narrow range of variation, any change of power of the optimized stage can be attributed to the reduced flow losses only.

2.3. Method of deformed polyhedron. It is generally accepted that none of the available optimization methods can be considered superior for all types of turbomachinery applications. The most popular seem to be the steepest gradient method, simplex-based methods and genetic algorithms. In this investigation, subsequent geometries in the course of optimization are selected using a simplex method of deformed polyhedron proposed by Nelder & Mead [11]. In this method, optimization of the objective function of n independent variables is performed using $n + 1$ points being vertices of a polyhedron in the space of optimized parameters R^n . The initial polyhedron is usually generated in a random way from the prescribed range of variation of the optimized parameters, or the choice of initial vertices can also be supported by an educated guess, which is drawing on some engineering knowledge. The first aim

of each iteration during the optimization procedure is to replace the least favorable vertex for which the objective function reaches the ‘worst’ value with a new vertex, and to form a new polyhedron. This is done with the help of the following operations: symmetrical reflection with respect to a gravity center, stretching, compression or reduction. These operations enable deformation of the polyhedron and its adapting to the topography of the objective function. An extremum of the objective function can be found even far away from the initial polyhedron. Of great importance for the effective operation of the algorithm is proper selection of the reflection ratio α , compression ratio β , stretching ratio γ and reduction ratio δ . An adequately chosen reflection ratio is decisive for the rate of convergence of the algorithm and its ability to go beyond the vicinity of local extrema and to find a path towards a global extremum. Certainly there is no guarantee that an extremum to which the algorithm would converge is a global extremum. Anyway, there are at least three ways of further treatment if the designer feels that the algorithm holds on to a local extremum. First, to recognise the fact that a local minimum is a solution whose objective function is ‘better’ than that of the original design. Second, to increase the reflection ratio, and third, to begin the optimization process from another initial polyhedron.

Usually, Nelder-Mead’s method of deformed polyhedron enables efficient optimization of 5-10 geometrical parameters of 3D blading. Unlike for gradient-based methods, the efficiency of the deformed polyhedron method measured by the number of calculations of the objective function within one iteration, does not depend on the number of optimized parameters, and on average is limited to 2-3 RANS calculations per iteration. Yet it usually requires more iterations to converge, as compared to the steepest gradient method, however, fewer than in the case of genetic algorithms. Details of the algorithm used can be found in [3,6].

2.4. 3D RANS solver. Values of the objective function are found from postprocessing CFD computations performed with the help of a code FlowER - solver of viscous compressible flows through multi-stage turbomachinery [12]. The solver draws on the set of Reynolds-averaged Navier-Stokes equations for perfect gas. During the optimization on coarse grids the effects of turbulence are taken into account with the help of a modified algebraic model of Baldwin-Lomax [13], whereas verifying computations of original and final geometries on refined grids are made using the Menter SST turbulence model [14]. This is a two-equation eddy-viscosity model where the standard $k - \omega$ model is activated in the sublayer and logarithmic region, and then switched to the $k - \varepsilon$ model in the wake region of the boundary layer, and where the eddy viscosity is redefined so as to guarantee the proportional relationship between the principal turbulent shear stress and the turbulent kinetic energy in the boundary layer. The governing equations are solved numerically based on the Godunov-type upwind differencing, high resolution ENO scheme and implicit operator δ of Beam & Warming, assuring second-order accuracy everywhere in space and time. An H-type multi-grid refined at the endwalls, blade walls and trailing and leading edges is used. The computations are carried out in one blade-to-blade passage of the stator and rotor, and converge to a steady state, with the condition of spatial periodicity, and

mixing plane approach assumed. The assumed inlet/exit boundary conditions impose the pressure drop and let the mass flow rate be resultant.

The code has recently been validated on a number of turbomachinery test cases, including Durham Low Speed Turbine Cascade, NASA Rotor37, NASA Low Speed Centrifugal Compressor and a model air turbine of ITC Łódź. For details of the flow solver and its validation the reader is referred to [15-18].

3. Optimization of a high-pressure steam turbine stage

The optimized stage is an HP impulse stage of a 200 MW steam turbine with originally cylindrical blades and shrouded rotor blades. The stage power is about 5 MW, its average reaction 17%. The stage operates at a pressure drop $p_2/p_0 = 0.9$. Initial geometrical parameters of the stator and rotor are as follows: span/chord - 0.8 (stator) and 2 (rotor); stagger angles as defined between the profile chord and the normal to the cascade front - 46° (stator) and 72° (rotor), blade numbers - 50 (stator), 120 (rotor).

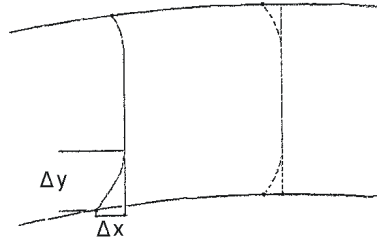


Figure 1. Compound lean geometry of stator blade – leading and trailing edge in circumferential view

In this investigation, the 3D-shaped compound leaned stator blade is optimized together with stator and rotor blade numbers and stagger angles as well as rotor blade twist. There are nine geometrical parameters for the Nelder-Mead method - stator blade number and stagger angle, rotor blade number and stagger angle, rotor blade linear twist angle, and four parameters of stator blade compound lean – two compound lean displacements at each endwall as defined in Figure 1. The blade sections (profiles) are assumed not to change during the optimization. The objective function is the enthalpy loss of the stage not including the leaving energy. A penalty is imposed on the mass flow rate if it changes by more than $\pm 0.5\%$, compared to the original geometry. The average reaction is assumed not to exceed the original value. To control changes of the exit energy, the absolute exit swirl angle is not allowed to vary beyond the interval $(-10^\circ, 10^\circ)$. Flow computations (3D RANS) are carried out for perfect gas assuming the specific heat ratio $\gamma = 1.3$ and individual gas constant $R = 430 \text{ J/kgK}$. Tip leakage flow over shrouded rotor blades is not evaluated here. Due to time restrictions, RANS computations in the course of optimization are carried out on coarse grids of 100 000 cells (stator + rotor), also using the faster and less

expensive turbulence model of Baldwin-Lomax. After optimization, the original and optimized geometries were recalculated on refined grids – 800 000 cells (stator + rotor), using the Menter SST turbulence model.

The optimization process was completed after 65 iterations (with 120 geometries calculated). The objective function was decreased by 0.4% on a coarse grid. The previously cylindrical stator blades acquired compound lean shapes with the lean direction opposite to that of rotation of the rotor blades at both endwalls. At the trailing edge of the new stator blade the compound lean displacements at the tip are larger, compared to those at the root. Some rotor blade twist was introduced, closing throats towards the tip. Stator and rotor blade numbers and stagger angles were also modified. Changes of the optimized parameters are given in Table 1.

Table 1. Change of the optimized parameters of the HP turbine stage
(1 - blade height)

Optimised parameter	Its change
Stator blade number	3
Rotor blade number	−3
Stator stagger angle at hub ¹ [°]	0.7
Rotor stagger angle at hub ¹ [°]	−0.5
Rotor twist angle ² [°]	−1.3
Stator compound lean displacement at tip ³ $\Delta x/l$	−0.08
Stator compound lean displacement at tip ¹ $\Delta y/l$	0.28
Stator compound lean displacement at hub ³ $\Delta x/l$	−0.05
Stator compound lean displacement at hub ¹ $\Delta y/l$	0.20

¹ positive value of stagger angle increment opens throats, negative value closes throats

² positive value of twist angle opens throats towards tip, negative value closes throats towards tip,

³ positive value of stator blade at the hub/tip is protruded with rotation of the moving blades

A comparison of the flowfield results for the original and optimized stage (obtained on refined grids using the Menter SST turbulence model) is presented in Figures 2 to 6. The comparison exhibits significant differences in total pressure and entropy patterns in characteristic sections of the stator and rotor, as well as in span-wise distribution of pressures, velocities and losses. Changes of each optimized parameter have an effect on the stage performance. Two groups of parameters can be distinguished whose effects can clearly be separated – the first group consisting of stator and rotor blade numbers and stagger angles plus rotor blade twist (5 parameters), the other group consisting of four parameters of stator blade compound lean at the hub and tip.

The effect of the first group is best observed in Figure 2 showing the entropy function contours in the rotor 10% of the blade span from the root. The contours exhibit the presence of a separation zone at the front part of the rotor blade suction surface at the root in the original design. The size of the separation zone at the root in the optimized design is considerably reduced. This is owing to changes of stator blade number and stagger angle which decrease the incidence on the rotor blade by about 2 degrees (in the rotating frame of reference). At the same time changes in the rotor

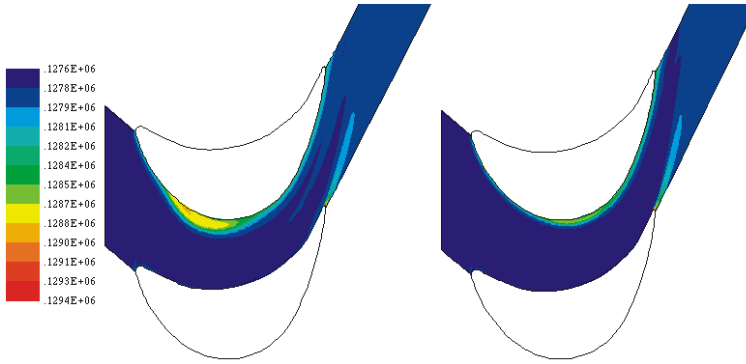


Figure 2. Entropy function contours in rotor 10% blade span from root; original (left), optimized (right)

blade number and stagger angle together with introduced rotor blade twist keep the well-streamlined flow patterns at the mid-span and tip, as well as the average reaction unchanged.

The effect of the second group of parameters is best observed in Figures 3 to 5. The chosen direction of compound lean (opposite to that of rotation of the moving blades) increases pressure at the endwalls in the stator, unloads stator blades and

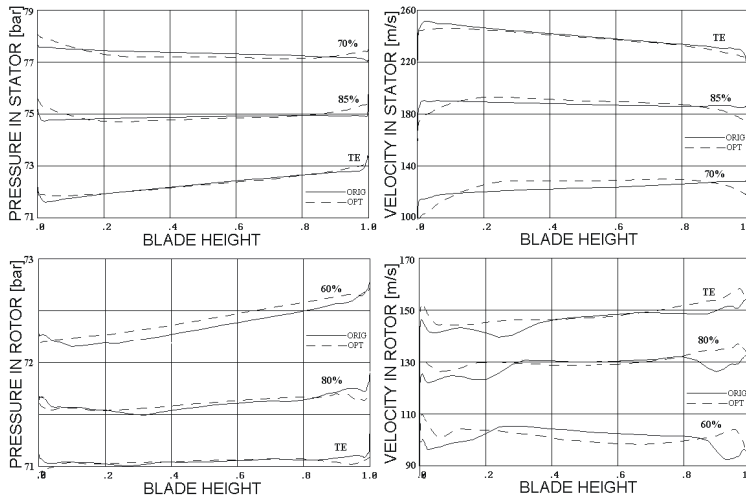


Figure 3. Span-wise distribution of pressure (right) and velocity (left) in the stator (top) and rotor (bottom)

reduces velocities there – Figure 3. This should reduce boundary layer losses near the endwalls. Let us note here that the boundary layer losses can be assumed proportional to the integral from the boundary layer edge velocity (relative to the exit isentropic velocity) in third power over the wall area, Denton [19]. However, as a result of additional span-wise pressure gradient there is increased convection of boundary layer fluid toward mid-span sections in the optimized design, which can be observed from total pressure contours downstream of the stator presented in Figure 4. The secondary flow maxima downstream of the stator at the mixing plane are less intensive in the optimized design, however, the wake seems to be slightly thicker at the mid-span.

The streamline curvature changes in the axial gap between the stator and rotor. In the optimized design, the pressure and velocity near the endwalls in the rotor exhibit opposite tendencies to those in the stator. The pressure decreases and velocity increases at the endwalls in the rotor, as compared to the original design. More mass is passed through the endwall regions, which is likely to increase endwall losses. However, the centres of loss due to secondary flows stay nearer the endwalls, see total pressure contours at the rotor trailing edge presented in Figure 4.

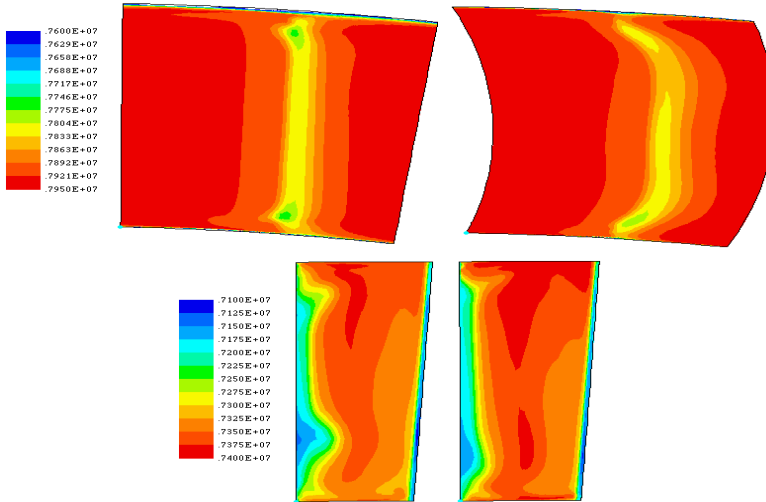


Figure 4. Total pressure contours downstream of the stator (top) and at the rotor trailing edge; original (left), optimized (right)

Figure 5 shows the comparison of span-wise distribution of enthalpy losses in the stator, rotor and stage for the original and optimized design. In the optimized design, stator losses are considerably decreased near the endwall sections, and negligibly increased at the mid-span. Quantitatively, the stator losses (mass-averaged) are decreased by 0.3%. Rotor losses are increased at the endwalls. However, peaks due to secondary flows and separation at the root are considerably lower. Quantitatively, the rotor losses are decreased by 0.8% here. The combination of stator and rotor losses shows that stage losses without the exit energy are decreased near the endwalls, and

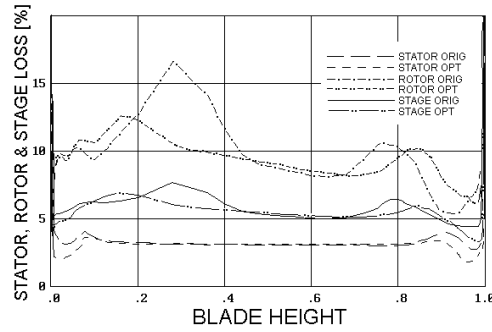


Figure 5. Span-wise distribution of enthalpy losses in stator, rotor and stage (without leaving energy)

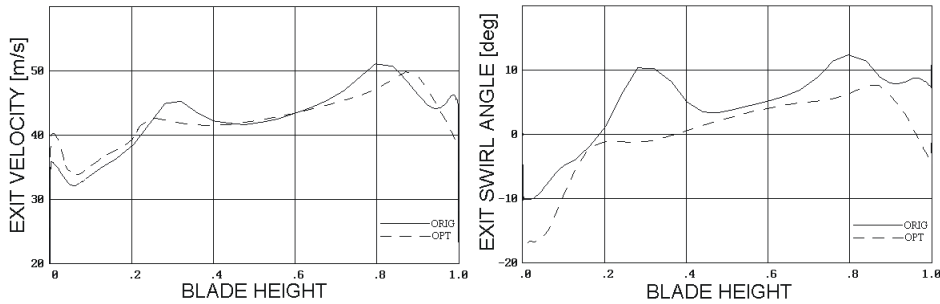


Figure 6. Span-wise distribution of exit velocity (left) and exit swirl angle (right)

3D peaks are lower than in the original design. Quantitatively, the stage losses are decreased from the calculated value of 5.9% down to 5.5%, that is by 0.4%. The level of loss decrease on a refined grid is here the same as on a coarse grid. Note that the stator losses are determined at the mixing plane, whereas the rotor and stage losses at a section located 40% of the rotor axial chord downstream of the rotor trailing edge.

The exit energy was not optimized in the process of optimization, but its value was controlled due to constraints imposed on the mass flow rate and mean exit swirl angle. Figure 6 shows the comparison of exit velocity and exit swirl angle in the non-rotating reference frame for the original and the optimized stage. For approximately the same mass flow rate (it turned out to be decreased by 0.1% compared to the original design), the mean exit velocity is slightly decreased in the optimized design. This is largely due to reduction of 3D peaks in exit swirl angle. Apart from the root section, the redistribution of the exit swirl angle should reduce downstream mixing loss and provide more favorable inlet conditions to the subsequent stage.

4. Summary

Stator blade compound lean was optimized together with stator and rotor blade numbers and stagger angles, as well as rotor blade twist in a low-load HP steam turbine stage. Nine geometrical parameters were optimized to reduce the stage loss (without the leaving energy). The idea of direct constrained optimization was presented. Geometries changing in the course of optimization were found using Nelder-Mead's method of deformed polyhedron, whereas the corresponding values of the objective function were found using a 3D RANS solver. There were also constraints imposed on the mass flow rate, exit swirl angle, and reaction. As a result of optimization, the stator of the tested stage acquired a new 3D stacking line, and the calculated stage loss without the leaving energy was decreased by 0.4%. The loss decrease can be attributed here to a reduced size of the separation zone at the rotor root, and decreased endwall and secondary flow losses. The obtained efficiency gains are not impressive here. However, further efficiency gains can still be expected due to a more favourable distribution of exit velocity and swirl angle, which is likely to reduce the downstream mixing loss and provide more favourable inlet conditions for the subsequent stage.

References

1. DEMEULENAERE, A. AND VAN DEN BRAEMBUSSCHE, R.: Three-dimensional inverse method for turbomachinery blading design. *Trans. ASME, J. Turbomachinery*, **120**, (1998), 247-254.
2. TIOW, W.T. AND ZANGENEH, M.: A three-dimensional viscous transonic inverse design method. *ASME Paper* 2000-GT-0525.
3. YERSHOV, S., RUSANOV, A., SHAPOCHKA, A., LAMPART, P., ŚWIRYDCZUK, J. AND GARDZILEWICZ, A.: Shape optimization of two turbine stages using the deformed polyhedron method and a 3D RANS solver. *Proc. Inst. Mech. Engrs, Part A, J. Power Energy*, 216(2), (2002), 203-213.
4. LAMPART, P. AND YERSHOV, S.: Direct constrained CFD-based optimization of 3D blading for the exit stage of a large power steam turbine. *Trans. ASME, J. Engng. Gas Turbines & Power*, **125**, (2001), 385-390.
5. PIERRET, S. AND VAN DEN BRAEMBUSSCHE, R.: Turbomachinery blade design using a Navier-Stokes solver and artificial neural network. *ASME Paper* 1998-GT-4.
6. LAMPART, P.: Numerical optimization of stator blade sweep and lean in an LP turbine stage. *ASME Paper* IJPGC2002-26161.
7. LAMPART, P. AND GARDZILEWICZ, A.: Numerical study of 3D blading in HP impulse turbines. *Ciepłne Maszyny Przepływowe (Turbomachinery)*, **115**, (1999), 297-310.
8. HARRISON, S.: The influence of blade lean on turbine losses. *Trans. ASME J. Turbomachinery*, **114**, (1992), 184-190.
9. SINGH, G., WALKER, P.J. AND HALLER, B.R.: Development of three-dimensional stage viscous time marching method for optimization of short height stages, *Proc. European Conference on Turbomachinery, Fluid Dynamics and Thermodynamic Aspects*, Erlangen, Germany, 1995, March 1-3.

10. YERSHOV, S., SHAPOCHKA, A. AND RUSANOV A.: 3D shaping of turbine blading based on 3D solutions of viscous compressible flow and optimization, *Proc. Conference on Improvements in Turbomachinery Using Methods of Mathematical and Physical Modelling*, Kharkov-Zmiev, Ukraine, September 18-22, 2000, 171-178, (in Russian).
11. NELDER J.A. AND MEAD R.: A simplex method for function minimisation. *Computer Journal*, **7**(1), (1965), 308-313.
12. YERSHOV S. AND RUSANOV A.: The application package FLOWER for the calculation of 3D viscous flows through multi-stage turbomachinery, Certificate of State Registration of Copyright, Ukrainian State Agency of Copyright and Related Rights, 1997, February 19, (in Russian).
13. BALDWIN B.S. AND LOMAX H.: Thin layer approximation and algebraic model for separated turbulent flows, *AIAA Paper*, 78-257.
14. MENTER, F.R.: Two-equation eddy-viscosity turbulence models for engineering applications, *AIAA J.*, **32**(8), (1994), 1598-1605.
15. YERSHOV, S. AND RUSANOV, A.: The high resolution method of Godunov's type for 3D viscous flow calculations, *Proc. 3 Colloquium on Process Simulation*, Espoo, Finland, June 13-16, 1996, 69-85.
16. YERSHOV, S., RUSANOV, A., GARDZILEWICZ, A., LAMPART, P. AND ŚWIRYDCZUK J.: Numerical simulation of 3D flow in axial turbomachines. *TASK Quarterly*, **2**(2), (1998), 319-347.
17. LAMPART, P., ŚWIRYDCZUK J. AND GARDZILEWICZ A.: On the prediction of flow patterns and losses in HP axial turbine stages using 3D RANS solver and two turbulence models. *TASK Quarterly*, **5**(2), (2001), 191-206.
18. LAMPART, P., YERSHOV, S. AND RUSANOV A.: Validation of turbomachinery flow solver on turbomachinery test cases. *Ciepłne Maszyny Przepływowe (Turbomachinery)*, **122**, (2002), 63-70.
19. DENTON, J.D.: Loss mechanisms in turbomachines. *Trans. ASME J., Turbomachinery*, **115**, (1993), 621-656.

STUDY OF BLADE TO BLADE FLOWS AND CIRCUMFERENTIAL STALL PROPAGATION IN RADIAL DIFFUSERS AND RADIAL FANS BY VORTEX CLOUD ANALYSIS

R. IVAN LEWIS

University of Newcastle
Newcastle upon Tyne, NE1 7RU
`r.i.lewis@ncl.ac.uk`

[Received: October 14, 2004]

Abstract. The objective of this paper is extension of vortex cloud simulation to the study of deep rotating stall cell propagation in radial turbomachines. Previous studies [1][2] provided the basic analysis, summarized in part here, for radial and mixed-flow blade rows but with identical blade-to-blade flow. Lifting of this restriction here permits the natural development of circumferential flow variations, revealing the growth of major upstream rotating stall cells for a radial diffuser with ten log-spiral blades but with high angle of attack (deep stall). For the same blade row run as a radial fan, however, stall cell formation and propagation is found to be inhibited. Additional studies are included for a cambered blade geometry typical of axial compressors. Used as an eight bladed radial diffuser, classical rotating stall is predicted. When operated as a rotor, rotating is again inhibited and modified.

Mathematical Subject Classification: 76B47, 76M23

Keywords: radial turbomachines, rotating stall, vortex dynamics

1. Introduction

A full statement and development of the underlying equations for vortex cloud simulation of mixed-flow and radial turbomachines have been given in previous presentations [1][2] and a brief summary only of these techniques will be given here. A detailed exposition of the underlying methodology of vortex cloud analysis has been given in ref. [3] and a more recent review of numerical developments and applications in ref. [4]. First, the basic equations for surface vorticity flow modelling will be given in Sections 2 & 3 including extension to vortex cloud modelling of turbomachine linear cascades. Second, the transformation techniques for applying these equations to radial cascades will be summarized in Section 4. Investigations of the stalling flow of a ten bladed radial diffuser will also be studied in Section 4, followed by studies of an identical blade row run as a fan rotor, Section 5. A second radial blade row will be considered in Section 6 based on typical axial compressor geometry with a cambered blade profile. A summary of conclusions will follow in Section 7.

2. Vorticity modelling of cascades

The fundamental basis of vortex element representation of the Navier-Stokes equations has been given by the author [3], beginning with the boundary integral equation for potential flow past an arbitrary body, equation (1), with reference

$$\frac{1}{2}\gamma(s_m) + \oint k(s_m, s_n)\gamma(s_n)ds_n + W_\infty(\cos \alpha_\infty \cos \beta_m + \sin \alpha_\infty \sin \beta_m) = 0 \quad (1)$$

where, for the boundary condition of zero internal velocity inside the body, the surface velocity v_{sn} is equal to the surface vorticity $\gamma(s_n)$.

$$v_{sn} = \gamma(s_n) \quad (2)$$

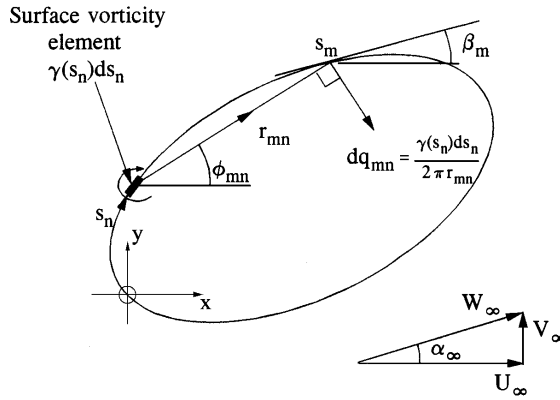


Figure 1. Surface vorticity model for flow past a body in a uniform stream W_∞

The coupling coefficient $k(s_m, s_n)$ linking points m & n on the body surface is given by

$$k(s_m, s_n) = \frac{1}{2\pi} \left\{ \frac{(y_m - y_n) \cos \beta_m - (x_m - x_n) \sin \beta_m}{(x_m - x_n)^2 + (y_m - y_n)^2} \right\}. \quad (3)$$

For a turbomachine cascade blade periodic in the y direction with pitch t , this becomes

$$k(s_m, s_n) = \frac{1}{2t} \left\{ \frac{\sin \frac{2\pi}{t}(y_m - y_n) \cos \beta_m - \sinh \frac{2\pi}{t}(x_m - x_n) \sin \beta_m}{\cosh \frac{2\pi}{t}(x_m - x_n) - \cos \frac{2\pi}{t}(y_m - y_n)} \right\}. \quad (4)$$

The standard numerical strategy is to represent the body surface by M discrete elements as shown in Figure 2, whereupon equation (1) transforms to the set of M linear equations

$$\sum_{n=1}^M K(s_m, s_n)\gamma(s_n) = -U_\infty \cos \beta_m - V_\infty \sin \beta_m. \quad (5)$$

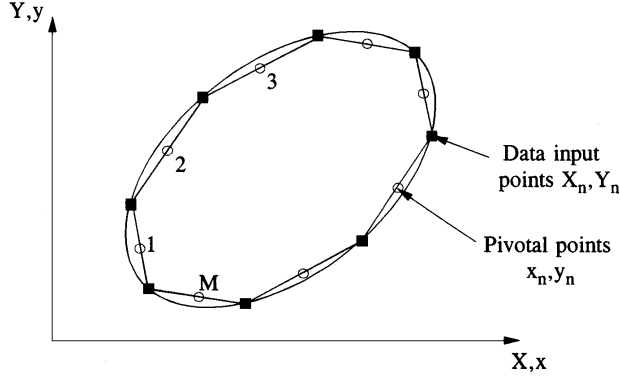


Figure 2. Numerical discretisation of the body surface

The revised coupling coefficients are then given by

$$K(s_m, s_n) = k(s_m, s_n) \Delta s_n. \quad (6)$$

These equations are of course only applicable to inviscid/potential flows, but may be extended to handle viscous fluids by vortex dynamics modelling, for which additional terms appear on the right hand side to account for the influence of the distributed vorticity of the external flow field. Thus we have

$$\sum_1^M K(s_m, s_n) \gamma(s_n) = -U_\infty \cos \beta_m - V_\infty \sin \beta_m - \sum_{j=1}^Z \Delta \Gamma_j (U_{mj} \cos \beta_m + V_{mj} \sin \beta_m), \quad (7)$$

where the spatially distributed vorticity has been discretised into a large number Z of small discrete vortices $\Delta \Gamma_j$. The unit velocities induced by $\Delta \Gamma_j$ are given by

$$\left. \begin{aligned} U_{mn} &= \frac{1}{2t} \frac{\sin \frac{2\pi}{t}(y_m - y_n)}{\cosh \frac{2\pi}{t}(x_m - x_n) - \cos \frac{2\pi}{t}(y_m - y_n)} \\ V_{mn} &= -\frac{1}{2t} \frac{\sinh \frac{2\pi}{t}(x_m - x_n)}{\cosh \frac{2\pi}{t}(x_m - x_n) - \cos \frac{2\pi}{t}(y_m - y_n)} \end{aligned} \right\}. \quad (8)$$

The numerical analysis is conducted over a series of small discrete time steps Δt for each of which a discrete vortex element $\Delta \Gamma_j$ is shed from each body surface element which, for a typical element j , will be of strength

$$\Delta \Gamma_j = \gamma(s_j) ds_j. \quad (9)$$

The right-hand side of the basic governing equation, i.e., equation (7) thus includes the influence of the superimposed uniform stream W_∞ plus the vorticity already shed into the mainstream flow. In the author's previous publications [1] to [3], for cascades the assumption was made that each blade flow was identical, a not unreasonable assumption for unstalled turbine or fan blade rows. However, for off-design angles of attack leading to stall it is well known that there can be significant blade-to-blade

variations particularly in fan and compressor cascades and the aim here is to extend the analysis to deal with such situations. We will deal with this in the next section.

3. Revised cascade modelling

Adaption of the previous vortex cloud model to allow simulation of at least some blade-to-blade variations is in fact relatively simple and is as illustrated in Figure 3.

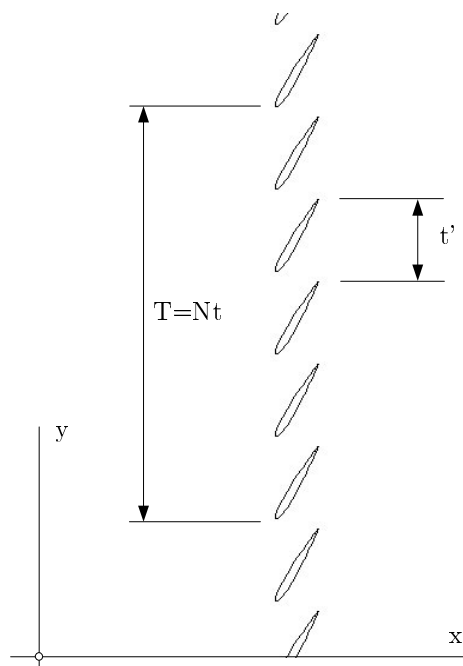


Figure 3. Revised model for the cascade with N independent blade profiles and group pitch T .

The approximation here is that there are N independent blades, (in this example 5) and that the flow pattern will thus repeat at the revised cascade pitch $T = Nt$. The group of $N = 5$ blades selected here may then be regarded as a single body shape when making up the $K(s_m, s_n)$ matrix of equations (7). The blade pitch t in equations (4) and (8) is then replaced by the group pitch T . In effect we are now analysing the flow through a group of N separate bodies, but cascaded as a group at pitch T in the y direction. Choice of the group size N is then a matter of computational limitations including available memory, time of execution and numerical accuracy available for inversion of the large $K(s_m, s_n)$ matrix. The outcome is best illustrated at this point by a typical solution as shown below in Figure 4.

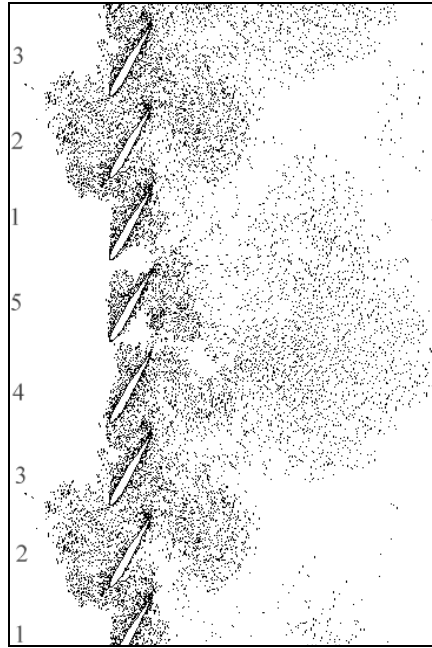


Figure 4. Simulation of deep propagating stall through a fan cascade at high angle of attack.

The fan cascade shown here consists of five C4 profiled blades with zero camber θ , a stagger angle of $\lambda = 60^\circ$ and a pitch/chord ratio $t/l = 1.0$. We note that the predicted pattern is repeated after every five normal blade pitches t as indicated by the repeated blade numbering from 1 to 5.

The inflow angle β_1 of 85° for this example corresponds to 25° angle of attack and is naturally excessive, ensuring a state of deep stall. The outcome of this is well known but none the less remarkable. After a period of time as the motion proceeds, we observe the development of a large stall cell actually upstream of the blade row which propagates in the vertical direction. The reason for this behaviour can be deduced from the vortex dynamics simulation demonstrating the power of this CFD technique for prediction and diagnosis. Thus we may observe that the major blockage of the blade passage at position 2 due to the stall cell is causing increased flow through the passages adjacent to blade 5 due to the consequent decrease in angle of attack of the blades behind the moving stall cell. Shortly blade No.1 will also begin to unstall as the cell proceeds upward. Thus blades 4,5 and 1 are delivering a pressure rise locally across the blade row whereas the adjacent blades 2 and 3 are totally stalled. The outcome of this is that the stagnant fluid in the blade passages adjacent to blade 2 is blown upstream to augment the developing upstream stall cell causing a periodic fluctuation and thus likely strong aerodynamic excitation of the blades.

In this example there were only five independent blade profiles resulting in one large stall cell. In practice there could be several cells developing and propagating and one simulation with ten independent blades of a compressor cascade undertaken by the author revealed two cell regimes, i.e. one every 5 blade pitches. This situation is illustrated in the next example to be investigated in Section 4, namely the case of a radial diffuser.

4. Extension to radial diffusers

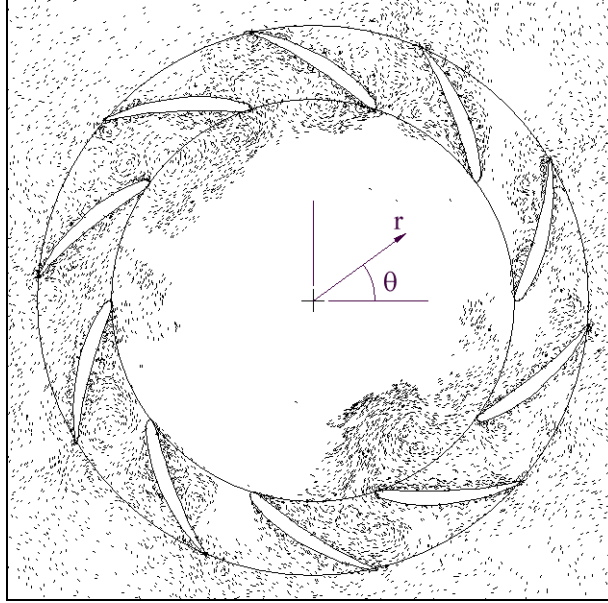


Figure 5. Simulation of deep stall in a radial outflow diffuser with ten blades.

Because the distributed vorticity of the mainstream flow has been replaced in the numerical model by a cloud of discrete vortices, it is valid to apply conformal transformations to the linear cascade and its flowfield provided the vortex element strengths $\Delta\Gamma$ remain unchanged. Thus the previous analysis may be applied directly to radial stators by means of the following transformation [3][4] between a radial diffuser in the Z plane and a rectilinear cascade parallel to the η axis in the ζ plane,

$$\zeta = \ln Z, \quad (10)$$

where $Z = re^{i\theta}$ and $\zeta = \xi + i\eta$. The coordinate and velocity transformations are then given by

$$\xi = \ln r, \quad \eta = \theta, \quad (11a)$$

$$q_\zeta = q_z r, \quad (11b)$$

where r, θ are polar coordinates of the actual radial blade row.

Figure 5 shows the outcome of applying this transformation to analysis of a ten bladed radial outflow diffuser. The blade geometry in the cascade ζ plane is identical to that used in Section 3, namely a C4 base profile with $\theta = 0^\circ$, $\lambda = 60^\circ$, $t/l = 1.0$ and with a pre-whirl inlet angle $\beta_1 = 85^\circ$ (anti-clockwise outflowing swirl). For this computation the number of blades was set at $N = 10$ to achieve full simulation of flow through the radial diffuser.

The main observation to note here is the development of two major rotating stall cells on the upstream (inner) side of the diffuser. These are not identical but very similar in size and extent and are found to precess around the inner region in the well known manner of rotating stall in axial compressors and fans. At circumferential locations between the two stall cells the blades are less stalled (and sometimes temporarily unstalled) due to their increased local distribution of the mass flow and hence reduced local angles of attack. In these regions pressure recovery through the diffuser is achieved resulting in higher pressure surrounding the exit regions. This higher pressure forces the stagnant fluid in the stall cell regions to be pushed back inwards with a consequent build up of the stall cells and a perpetuation of the large scale disturbances. In the case of a centrifugal fan it can be expected that these stall cells would cause serious fluctuating interference with the rotor and be a serious source of unwanted vibrations.

It is of considerable interest to extend these studies from radial stators to radial rotors since in the latter we would expect the additional influence of work input including those due to relative eddy and Coriolis forces. The question raised then is whether these additional effects would enhance stall cell development or inhibit it. Fortunately all the relevant equations to handle this have already been derived [3] and applied to potential flow through radial and mixed-flow turbomachines. To summarise, the governing equation (7) develops into the extended form

$$\left. \begin{aligned} \sum_{n=1}^M K(s_m, s_n) \gamma(s_n) &= -U_\infty \cos \beta_m \\ &- [V_\infty + \Omega \{r^2 - \frac{1}{2} (r_1^2 + r_2^2)\}] \sin \beta_m \\ &- \sum_{j=1}^Z \Delta \Gamma_j (U_{mj} \cos \beta_m + V_{mj} \sin \beta_m) \end{aligned} \right\}, \quad (12)$$

where the new middle line includes the influence of blade row rotation with angular speed Ω . From the appearance of this term $\Omega \{r^2 - \frac{1}{2} (r_1^2 + r_2^2)\}$ one can immediately detect that it represents the additional influence upon the flow due to Coriolis accelerations of fluid particles as they pass through the rotor and one might anticipate some considerable influence upon the consequent flow. This is indeed the case as we shall see from the following example.

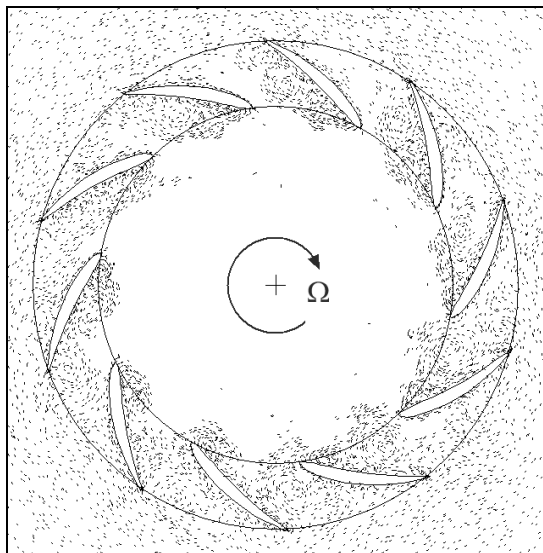


Figure 6. Flow through a backward sloping radial fan with relative inlet angle $\beta_1 = 85^\circ$.

In this example the previous blade row as shown in Figure 5 was rotated clockwise as a radial fan rotor with zero prewhirl but with sufficient angular velocity Ω to deliver the same relative inflow angle of $\beta_1 = 85^\circ$ and thus 25° angle of attack. A summary of the data is as follows:

Table 1. Design data for radial fan

Inlet radius r_1	1.0 m
Outlet radius r_2	1.3691 m
Meridional velocity at r_1	1.0 m/s
Angular velocity	109.15 revs/min
Prewhirl angle α_1	0°
Relative inlet angle β_1 at r_1	85°
Camber θ	0°
Stagger λ	60°
Pitch/chord ratio t/l	1.0
Time step Δt	0.005 sec

As can be seen from the predicted flow pattern after 300 time steps, Figure 6, although there is clear evidence of stall with some circumferential variation from blade to blade, there has been no establishment of the upstream eddy regimes characteristic of the stationary blade row, Figure 5. It is quite clear that the presence of Coriolis accelerations and relative eddy effects have had a major stabilising effect in the case of this radial fan rotor as compared with its stator equivalent Figure 5.

5. Axial compressor type blade rows

In the foregoing fan *uncambered* blade row studies it was difficult to detect classical cascade stall propagation or regular rotating stall in the radial diffuser at smaller angles of attack. Although some stall propagation was present below 15° angle of attack it was largely intermittent. It was decided therefore to consider also a typical axial compressor blade row with the following specification.

Table 2. Axial compressor cascade design data

Chord length	1.0 m
Velocity normal to cascade	1.0 m/s
Camber θ	44.49 °
Stagger λ	41.11 °
Pitch/chord ratio t/l	1.162
Design inlet angle β_1	54.59 °
Predicted design outlet angle β_2	30.69 °

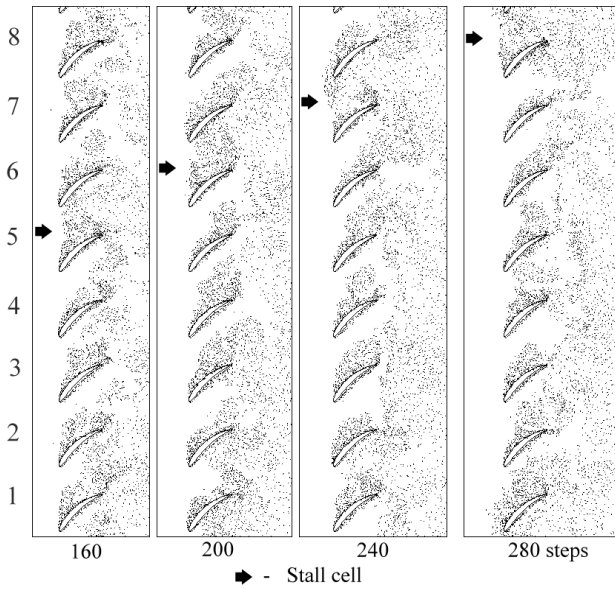


Figure 7. Stall propagation in a compressor cascade (Table 2 data with $\beta_1=74.59^\circ$ & $\delta t=0.015$)

Adopting here the cascade geometry studied in refs. [5]&[6], we note the introduction of typical camber $\theta=44.49^\circ$ and stagger $\lambda=41.11^\circ$. The design inlet angle given above is that for shock-free inflow for which the inlet stagnation point is precisely on the leading edge. Vortex cloud analysis was undertaken with a time step $\delta t=0.015s$ for angles of attack of 0, 5, 10, 15 and 20° angle of attack above this for a cascade with eight independent blades. Only for the last of these studies, with an inlet angle

$\beta_1=74.59^\circ$, was regular stall propagation actually found to develop in this cascade and a sample of the results is shown in Figure 7.

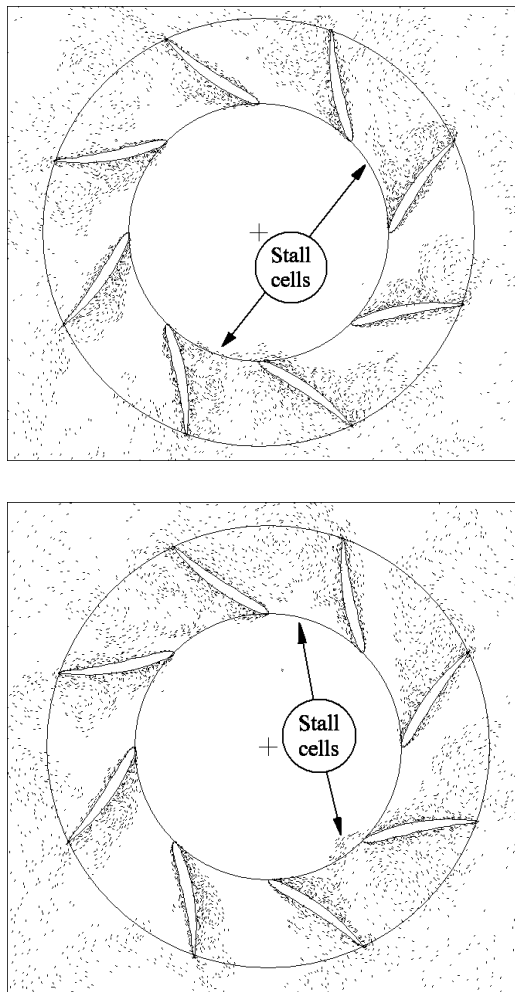


Figure 8. Development of rotating stall cells in an eight bladed 'axial compressor type' radial diffuser

As may be observed, after 160 time steps a stall cell has built up in blade passage No. 5. After successive intervals of 40 time steps this stall cell has propagated upwards to blade passages 6, 7 and 8. It should be noted that this pattern behaviour was found to occur only with 20° angle of attack. At lower inlet angles there was evidence of developing stall propagation but with less firm regularity.

To conclude, let us consider adaption of the above cascade geometry for design of an equivalent radial diffuser. Application of the conformal transformation equations (10)

and (11) results in the circular radial outflow cascade shown in Figure 8. Adopting an inlet prewhirl angle of $\beta_1=74.59^\circ$, with time steps of magnitude $\delta t = 0.015$ and a meridional velocity at the inlet radius r_1 of value 1.0, the predicted flow pattern after 300 and 335 time steps is shown in Figures 8(a) and 8(b), respectively.

We observe from Figure 8 the presence of a single passage stall cell at the bottom region which has moved anticlockwise into the next blade passage after 35 time steps. We also note, however, the presence of a second but less concentrated cell located at the top of the diffuser also rotating anticlockwise at the same speed. Reference back to Figure 7 in fact reveals the presence of a similar second stall cell region around passage 1 to begin with, moving upwards to passage 4 finally. The main difference fluid dynamically between the two axial and radial cascades lies in the influence of viscous diffusion. For infinite Reynold's number viscous effects would have little influence. For the cascade Reynold's number of 1×10^5 selected here on the other hand, viscous diffusion will differ considerably due to the additional mainstream radial diffusion in the case of the radial diffuser. Despite this, stall cell propagation is remarkably similar for both cases considered comparing Figures 7 and 8.

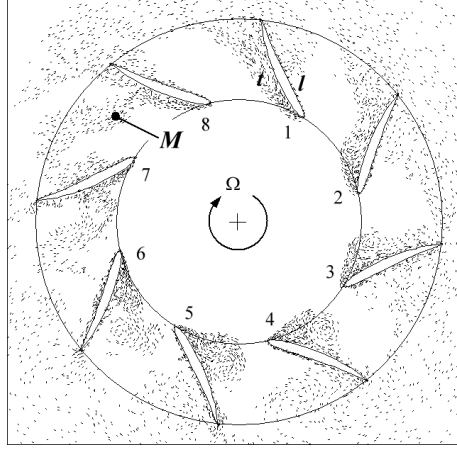
To conclude finally, the flow through the previous cambered radial blade row was investigated when used as a radial fan rotor with two speeds of rotation, Figure 9.

Figure 9(b) shows the typical long term flow pattern for $\Omega=34.644$ revs/s, at which angular velocity zero prewhirl α_1 provides the same relative inlet angle as the stator just considered in Figure 8, $\beta_1=74.59^\circ$. Figure 9(a), on the other hand, shows the predicted flow pattern for half this speed of rotation, $\Omega=17.322$ revs/s, but with sufficient prewhirl $\alpha_1=61.15^\circ$ to give the same relative inlet angle $\beta_1=74.59^\circ$. Three important observations may be made:

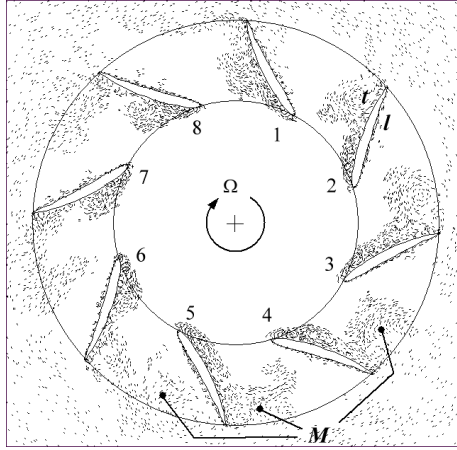
- (a) Although some rotating stall still occurs, there is decreasing evidence of major stall cells as the rotor angular velocity increases.
- (b) Major separation seems to be limited largely to the leading edge region with evidence of what seems to be an approach towards reattachment at mid-chord on the trailing surface t .
- (c) From mid-chord towards the trailing edge region there is evidence of migration of diffused vorticity from the trailing surface t to the leading surface l , indicated by M in Figure 9(b).

Undoubtedly the explanation for the above is the influence of Coriolis accelerations upon the relative flow through these radial rotors. Specific work input due to associated Coriolis forces is dependent only upon the radial shift of the fluid from inlet r_1 to outlet r_2 and the rotor angular velocity Ω as shown by the Euler Pump Equation, namely

$$\left. \begin{aligned} \frac{1}{\rho} (p_{02} - p_{01}) &= U_2 c_{\theta 2} - U_1 c_{\theta 1} = \Omega(r_2 c_{\theta 2} - r_1 c_{\theta 1}) \\ &= \underbrace{\Omega(r_2 w_{\theta 2} - r_1 w_{\theta 1})}_{\text{Aerodynamic specific work input}} + \underbrace{\Omega^2(r_2^2 - r_1^2)}_{\text{Coriolis specific work input}} \end{aligned} \right\}, \quad (13)$$



$\Omega = 17.322\text{revs/s}$, Prewhirl angle $\alpha_1=61.15^\circ$ 280 iterations with $\delta t=0.015$.



$\Omega = 34.644\text{revs/s}$, Prewhirl angle $\alpha_1=0.0^\circ$, 360 iterations with $\delta t=0.01$.

l - leading surface. t - trailing surface.

M - Circumferential vorticity migration.

Figure 9. Flow through the radial diffusing blade row operating as a radial fan rotor

where w_θ is the swirl velocity measured relative to the rotor, and is related to the absolute swirl velocity c_θ through

$$c_\theta = w_\theta + r\Omega . \quad (14)$$

It is clear that although there is leading edge flow separation due to the sharp angle of attack, the specific work input imposed by Coriolis effects has a stabilising effect as the fluid proceeds further through the blade passages. However, partly due to

the anticlockwise ‘relative eddy rotation’ or ‘slip flow’ in the passage exit region, free vorticity tends to migrate from where it has been created on the unstable trailing surface t towards the leading surface l .

6. Conclusions

The following summary of conclusions may be drawn from these fluid dynamic developments and studies:

1. The basic linear cascade vortex dynamics code developed here has successfully predicted the presence of rotating stall in fan and compressor cascades in agreement with earlier work.
2. At high incidence angles in deep stall, substantial stall cells intrude back upstream of the blade row.
3. A conformal transformation technique has succeeded in extending these flow simulations to deal with radial blade rows used as either stators or rotors.
4. At large relative inlet angles a couple of large rotating deep-stall cells were found to develop on the inlet side of a radial outflow diffuser stator comprising a backward swept zero camber fan cascade at high stagger.
5. For the cambered compressor type radial diffuser stator no deep-stall cells of this kind developed for the same leading edge angle of attack of 20° , although rotating stall was present.
6. For the same blade row employed as a radial fan rotor, work input due to Coriolis forces leads to general stabilization of the initial leading edge stall regime. The same ‘relative eddy’ effects result in vorticity migration at the outlet radii from the trailing (highly loaded) blade surface towards the (generally low velocity) leading edge surface.

References

1. LEWIS, R.I.: Development of vortex dynamics for simulation of turbomachine cascades and blade rows. *Journal of Computational and Applied Mechanics*, **2**(1), (2001), 73-85.
2. LEWIS, R.I.: Extension of vortex methods to the flow simulation of mixed-flow turbomachines. *Proc. of the Second International Conference on Vortex Methods*, Istanbul, Turkey, Sept 2001.
3. LEWIS, R.I.: *Vortex Element Methods for Fluid Dynamic Analysis of Engineering Systems*. Cambridge University Press, 1991.
4. LEWIS, R.I.: Vortex element methods, the most natural approach to flow simulation - a review of methodology with applications. *Proceedings of the First International Conference on Vortex Methods*, Kobe, Japan, (1999), 1-15.
5. CHUNJUN JI: *Vortex Cloud Method and its Applications to Turbomachine Cascades*. Ph.D. Thesis, Newcastle University, 1997.
6. LEWIS, R.I. AND CHUNJUN JI: Extension of vortex cloud modelling to cylinder arrays and cascades in relative motion. *Proceedings of the Fourth European Computational Fluid Dynamics Conference*, Athens, pp. 642-647, J. Wiley & Sons, 1998.

ELECTROMAGNETICALLY FORCED SWIRLING FLOW DURING SOLIDIFICATION OF A BINARY METAL ALLOY

PETR A. NIKRITYUK, KERSTIN ECKERT AND ROGER GRUNDMANN
Institute for Aerospace Engineering, Dresden University of Technology
01062 Dresden, Germany
`nikrityu@tfd.mw.tu-dresden.de`

[Received: November 12, 2003]

Abstract. The main aim of this work is to study numerically the influence of an external rotating magnetic field with magnetic Taylor number between $10^4 \dots 10^5$ on the convection process within liquid binary metal alloy undergoing solidification. Based on the continuum model of two-phase flow the transient transport of momentum, energy and species in presence of a Lorentz force during solidification of Pb85wt%Sn alloy is modeled. The geometry under study is a cylindrical mold with adiabatic walls and cooled bottom. The calculations showed that when meridional flow velocity exceeded solidification front velocity a mushy zone front with convex shape developed with the maximum located on the axis of rotation.

Mathematical Subject Classification: 80A20

Keywords: solidification, mushy zone, stirring, magnetic field

1. Introduction

Rotating magnetic fields (RMF) are widely used in metallurgical applications for stirring and mixing liquid metals and electrically conducting liquids in general [1]. Particularly, the stirring, i.e. the generation of swirling flow by a rotating magnetic field, is used during solidification processes to homogenize the liquid phase by modifying the internal convection, namely thermosolutal and shrinkage-driven flow. The homogenization of the liquid zone promotes the isotropy of the solid phase, which leads in turn to isotropic mechanical properties of the solidified material. Certainly the existence of favorable combinations of magnetic induction and cooling rate values for optimal properties of a given alloy can be assumed. To study this question it is necessary to model not only the interaction of the liquid alloy phase with the magnetic field but also to simulate the solid and the mushy-zone domains.

Mathematical models and numerical procedures to study solidification processes have been improved over the past ten years [2]–[8]. Basically there are two concepts of mathematical models for transport phenomena during solidification. The first concept has been introduced by Beckermann [3],[4] and is called Representative Volume Element (REV). This model uses volume-averaged conservation equations for each phase. The second concept is based on the mixture theory [5]–[8] which describes a

two-phase flow as a mixture of solid and liquid phases. In this model microstructure evolution as well as the macroscale transport in solidification of alloys is governed by the progress of the two-phase ‘mushy-zone’. This model is able to predict both the macrosegregation [9] and the channel formations in the mushy zone [10] in a unidirectional solidification. In this work the second concept is used.

Experimental and theoretical works analyzing the influence of external magnetic fields on the convection of liquid metal without [11]–[15] and with solidification [16]–[20] of binary metal alloy have demonstrated that the motion of the melt depends on the particular type of the magnetic field applied to the molten metal alloy. The influence of a time-harmonic (a.c.) magnetic field on the Pb19%wtSn alloy solidification was studied numerically in a 2D geometry in [19, 20]. Particularly in [19] it was shown that turbulence, induced by the electromagnetic stirring, has a significant effect on the solidification.

In this work the influence of a rotating magnetic field on the liquid phase flow during the solidification of the Pb85%wtSn alloy is studied.

2. Numerical formulation

2.1. Assumptions. The continuum model [5] has been adopted for the binary alloy solidification under the following assumptions:

1. All of the properties of the mixture can be obtained from the properties of its components in each phase.
2. All transport properties of each phase, such as thermal and electrical conductivity or viscosity, are constants.
3. The density is constant in each phase and the densities of the two phases are similar.
4. The mushy region is modeled by means of using the mixture viscosity (mushy fluid model [2]).
5. The phases are in local thermodynamic equilibrium. The phase diagram is applied.
6. The flow of the liquid phase is assumed to be laminar and axisymmetric.
7. The liquid and solid phases move at the same mass average velocity.
8. The gravity is zero.

2.2. Governing Equations. Based on the assumptions made above, the set of equations has the following form:

Mass Conservation Equation:

$$\frac{\partial \rho_m}{\partial t} + \nabla \cdot (\rho_m \vec{u}) = 0, \quad (2.1)$$

where ρ_m is the density of the mixture, \vec{u} is the velocity vector, which has three velocity components u_r , u_θ , u_z .

Momentum Conservation Equation:

$$\frac{\partial(\rho_m \vec{u})}{\partial t} + \nabla \cdot (\rho_m \vec{u} \cdot \vec{u}) = -\nabla p + \nabla \cdot (\mu_m \nabla \vec{u}) + \vec{F}_L, \quad (2.2)$$

where p is the pressure, μ_m is the dynamic viscosity of the mixture, \vec{F}_L is the Lorentz force vector. The projection of the momentum conservation equation in azimuthal direction has the form:

$$\frac{\partial(\rho_m u_\theta)}{\partial t} + \nabla \cdot (\rho_m \vec{u} \cdot u_\theta) = \nabla \cdot (\mu_m \nabla u_\theta) - \frac{\mu_m u_\theta}{r^2} - \frac{\rho u_r u_\theta}{r} + F_{L\theta}, \quad (2.3)$$

where the last term in equations (2.2) and (2.3) involves the Lorentz force, which has only the azimuthal component $F_{L\theta}$. The mixture viscosity is calculated using the approximation formula taken from [20]:

$$\mu_m = \begin{cases} \varepsilon \mu_l + (1 - \varepsilon) \mu_s, & \varepsilon \leq 0.5 \\ k \cdot (1 - \varepsilon) + b, & 0.5 < \varepsilon < 0.6 \\ \mu_l \exp(4.5 \cdot (1 - \varepsilon)), & \varepsilon \geq 0.6 \end{cases}, \quad (2.4)$$

where ε is the volume fraction of liquid. The constants k and b in equation (2.4) were obtained from a linear interpolation between the points $\varepsilon = 0.5$ and $\varepsilon = 0.6$. Dynamic viscosity of the solid phase μ_s was set to $100 \frac{Ns}{m^2}$.

Energy Conservation Equation:

$$\frac{\partial(\rho_m h_m)}{\partial t} + \nabla \cdot (\rho_m h_m \cdot \vec{u}) = \nabla \cdot \left(\frac{\lambda_m}{c_{ps}} \nabla h_m \right) + \nabla \cdot \left(\frac{\lambda_m}{c_{ps}} \nabla (h_s - h_m) \right) \quad (2.5)$$

Here h_s and h_l refer to the enthalpy of the solid and liquid phase, respectively, λ_m is the thermal conductivity of the mixture, c_{ps} is the specific heat of the solid phase. The liquid and solid enthalpies are related to the equilibrium temperature through the following thermodynamic relations:

$$h_l = c_{pl}T + (c_{ps} - c_{pl})T_e + L \text{ and } h_s = c_{ps}T, \quad (2.6)$$

where c_{pl} is the specific heat of the liquid phase, T_e is the eutectic temperature, L is the latent heat. The first two terms on the right-hand side of equation (2.5) represent the net Fourier diffusion flux $\nabla \lambda_m \nabla T$. It can be seen by substituting $\nabla h_s = c_{ps} \nabla T$ into the second term on the right-hand side of equation (2.5). Note that expressing the net Fourier diffusion flux in the manner of equation (2.5) makes this equation suitable for solving it using an implicit scheme.

Species Mass Conservation Equation:

$$\frac{\partial(\rho_m f^\alpha)}{\partial t} + \nabla \cdot (\rho_m f^\alpha \cdot \vec{u}) = \nabla \cdot (\rho_m D_m \nabla f^\alpha) + \nabla \cdot \rho_m D_m \nabla (f_l^\alpha - f^\alpha), \quad (2.7)$$

where f^α is the mass concentration of Sn, D_m is the mass diffusion coefficient of the mixture. The first two terms on the right-hand side of equation (2.7) represent the net diffusive (Fickian) species flux. Note that for a two-phase, solid-liquid system,

the diffusion in the solid phase can be neglected relative to that in the liquid phase [5], so that $D_m \approx f_l D_l^\alpha$. Mixture quantities are defined in the following manner:

$$\begin{aligned}\rho_m &= (1 - \varepsilon) \rho_s + \varepsilon \rho_l, \\ f_s &= (1 - \varepsilon) \frac{\rho_s}{\rho_m}, \quad f_l = \varepsilon \frac{\rho_l}{\rho_m}\end{aligned}\tag{2.8}$$

$$h_m = f_s h_s + f_l h_l, \quad f^\alpha = f_s f_s^\alpha + f_l f_l^\alpha,\tag{2.9}$$

where f_l , f_s are mass fraction of the liquid and the solid phases, respectively.

2.3. Lorentz Force. The interaction of a RMF with a conducting liquid depends on several parameters including the material properties of the liquid, the characteristics of the RMF (magnetic induction B , angular frequency of the magnetic field $\omega = 2\pi\nu$, where ν is the frequency of the alternating current, and the ratio of the number of poles to the number of phases in the current source p_B) and the geometry of the system (height, H , and radius, R , of cylinder). These parameters can be grouped into the following dimensionless quantities: the Hartmann number $Ha = B \cdot R \sqrt{\frac{\sigma}{2\mu}}$, the Reynolds number $Re_\omega = \frac{\rho \omega R^2}{\rho_B \mu}$ corresponding to the magnetic field rotation, the relative frequency of the magnetic field $\bar{\omega} = \mu_0 \sigma \omega R^2$ (μ_0 is the magnetic permeability of free space) and the aspect ratio $A = \frac{H}{2R}$. Ha and Re_ω can be unified in the magnetic Taylor number $Ta = Ha^2 Re_\omega$.

To calculate these dimensionless parameters we use material properties of liquid Pb85wt%Sn: $\rho_m = 7889 \frac{kg}{m^3}$, $\mu_l = 1.873 \cdot 10^{-3} \frac{N \cdot s}{m^2}$, $\sigma = 1.5 \cdot 10^6 \frac{A}{V \cdot m}$. Together with $\nu = 50 Hz$ and $p_B = 1$ we arrive at $A = 1.26$, $\bar{\omega} = 0.471$, $Re_\omega = 8.15 \cdot 10^5$. The corresponding values of Taylor and Hartmann numbers are given in Table 1.

Table 1. The correspondence of magnetic induction to the Taylor and Hartmann numbers

B, mT	Ta	Ha
0.2	$8.15 \cdot 10^3$	0.1
0.5	$5.1 \cdot 10^4$	0.25
1	$2.04 \cdot 10^5$	0.5

It can be seen that $\bar{\omega} < 1$, i.e., the skin depth of the RMF is larger than the radius of the cylinder. In this case the low-frequency approximation can be used [13]. The low-induction condition implies that the angular velocity induced by the RMF does not change the magnetic field applied. This condition is satisfied by $\frac{Ha^4}{Re_\omega} \ll 1$ [13]. The substitution of the Hartmann number, given in Table 1, into the expression written above shows that the low-induction condition is satisfied for all three B . Once the low-frequency and low-conduction conditions are fulfilled for $p_B = 1$ (if the ratio is

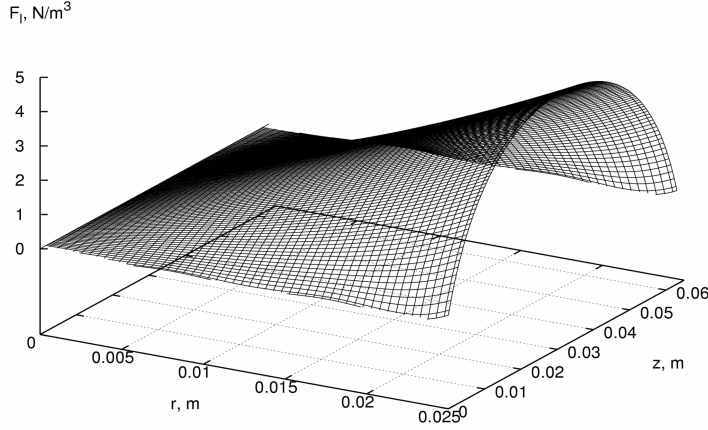


Figure 1. The time averaged azimuthal Lorentz force induced by rotating magnetic field with $B = 1\text{ mT}$, $\nu = 50\text{ Hz}$ for a finite cylinder with a radius of 25 mm and a height of 63 mm .

unity, the applied rotating magnetic field can be treated as a spatially uniform field), an analytical solution can be written for the time-averaged Lorentz force, which solely has an azimuthal component. Under the condition of the infinite cylinder an analytical solution in cylindrical coordinates can be written for the time-averaged Lorentz force [1]:

$$F_{\theta\infty} = \frac{1}{2} \sigma \cdot \omega \cdot B^2 \cdot r. \quad (2.10)$$

For a finite cylinder there is an analytical solution for the time-averaged azimuthal Lorentz force [14], which has the form:

$$f_{\theta} = F_{\theta\infty} \cdot f(r, z),$$

$$f(r, z) = 1 - \frac{2R}{r} \sum_{k=1}^{\infty} \frac{J_2(\lambda_k) \cdot \lambda_k \cdot J_1\left(\lambda_k \frac{r}{R}\right) \cdot \text{ch}\left(\lambda_k \frac{z}{R}\right)}{(\lambda_k^2 - 1) \cdot J_1^2(\lambda_k) \cdot \text{ch}\left(\lambda_k \frac{H}{2R}\right)}, \quad (2.11)$$

where J_1 , J_2 are Bessel functions, λ_k are the roots of $J'(x) = 0$. The time-averaged azimuthal Lorentz force calculated by (11) for a cylinder with a height of 63 mm and a radius of 25 mm is shown in Figure 1.

2.4. Closure of Energy and Species Conservation Equations. The closure of the system of conservation equations requires supplementary relationships between f_s , T and f^{α} . With the assumption of local equilibrium, the expressions required may be obtained from the equilibrium phase diagram [21]. The volume fraction of liquid ε in the mushy zone is approximated by means of a conduction-dominated solidification rule [22]:

$$\varepsilon = \frac{T - T_s}{T_l - T_s}, \quad (2.12)$$

where T_s and T_l are the temperatures on the solidus and liquidus line in the phase diagram, respectively. The functional dependencies of T_s and T_l from the mixture concentration have been calculated by means of the least square method:

$$T_l = \begin{cases} 600.5 - 3.38386 \cdot C + 0.0479617 \cdot C^2 - 0.000500933 \cdot C^3, & \text{if } C \leq 61.9 \text{ wt\%} \\ 374.001 + 1.34899 \cdot C - 0.000390725 \cdot C^2, & \text{if } 61.9 \text{ wt\%} < C \leq 100 \text{ wt\%} \end{cases}, \quad (2.13)$$

$$T_s = \begin{cases} 600.52 - 8.84703 \cdot C + 0.718111 \cdot C^2 - 0.0363395 \cdot C^3, & \text{if } C \leq 18.3 \text{ wt\%} \\ 456K, & \text{if } 18.3 \text{ wt\%} < C \leq 100 \text{ wt\%} \end{cases}. \quad (2.14)$$

Here $C = f^\alpha \cdot 100$ must be inserted.

In order to define the volume fraction of the liquid, the set of equations (2.6), (2.8), (2.9), (2.12)-(2.14) is solved iteratively. To avoid oscillations, arising from the volume fraction calculation on the liquid/mush- and solid/mush-boundaries, the following relaxation is used:

$$\varepsilon = (1 - \alpha_\varepsilon) \cdot \varepsilon^* + \alpha_\varepsilon \cdot \varepsilon, \quad (2.15)$$

where α_ε is the relaxation factor which was set equal to 0.5. ε^* is the liquid volume fraction of the previous iteration.

2.5. Calculated Domain and Boundary Conditions. The equations of conservation of mass, momentum, energy and solute are solved in a two-dimensional domain, see Figure 2, with boundary conditions cited in Table 2. Following Figure 2, AB is

Table 2. Boundary conditions

	AB	BC	CD	AD
u_r	$\frac{\partial u_r}{\partial z} = 0$	0	0	0
u_θ	$\frac{\partial u_\theta}{\partial z} = 0$	0	0	0
u_z	0	0	0	$\frac{\partial u_z}{\partial r} = 0$
p'	$\frac{\partial p'}{\partial z} = 0$	$\frac{\partial p'}{\partial r} = 0$	$\frac{\partial p'}{\partial z} = 0$	$\frac{\partial p'}{\partial r} = 0$
h_m	$\frac{\partial T}{\partial z} = 0$	$\frac{\partial T}{\partial r} = 0$	$f(time)$	$\frac{\partial T}{\partial r} = 0$
f^α	$\frac{\partial f^\alpha}{\partial z} = 0$	$\frac{\partial f^\alpha}{\partial r} = 0$	$\frac{\partial f^\alpha}{\partial z} = 0$	$\frac{\partial f^\alpha}{\partial r} = 0$

the top of the cylinder with a height of 63 mm and a radius of 25 mm, BC is the cylindrical wall, CD represents the cooled bottom and AD is the symmetry axis of the cylinder. The time dependent temperature at the bottom is prescribed in the cooling curve, which has been taken from the experiment [23].

3. Code validation

The solidification model described above has been implemented into the open source code of a 2D Navier-Stokes solver [24], where the SIMPLE algorithm with collocated-variables arrangement is used to calculate the pressure and the velocities. For the stabilization of pressure-velocity coupling the interpolated cell face velocities are modified by the difference between the interpolated pressure gradient and the gradient calculated at the cell face. More details describing the whole coupling algorithm can be found in [24]. The set of equations has been discretized by a finite-volume-finite-difference based method. The system of linear equations is solved by using Stone's strongly-implicit procedure (SIP). The time derivatives are discretized by a three-time-level scheme. The convection terms are discretized by a central difference second order scheme (CDS).

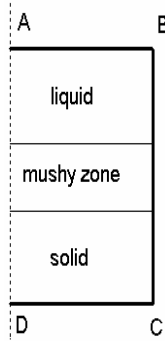


Figure 2. Scheme of calculated domain

To validate the code, a verification test case was performed. The test case corresponds to the laminar steady flow in an infinite cylinder induced by the time-averaged Lorentz force (2.10). Also an analytical solution exists for this test case [1]:

$$u_{\theta} = \frac{U^2 \cdot r \cdot \rho}{16 \cdot \mu_l \cdot R^2} \cdot (R^2 - r^2) . \quad (3.1)$$

The comparison of the calculated azimuthal velocity with the analytically predicted one is shown in Figure 3. It can be seen that the velocities are identical.

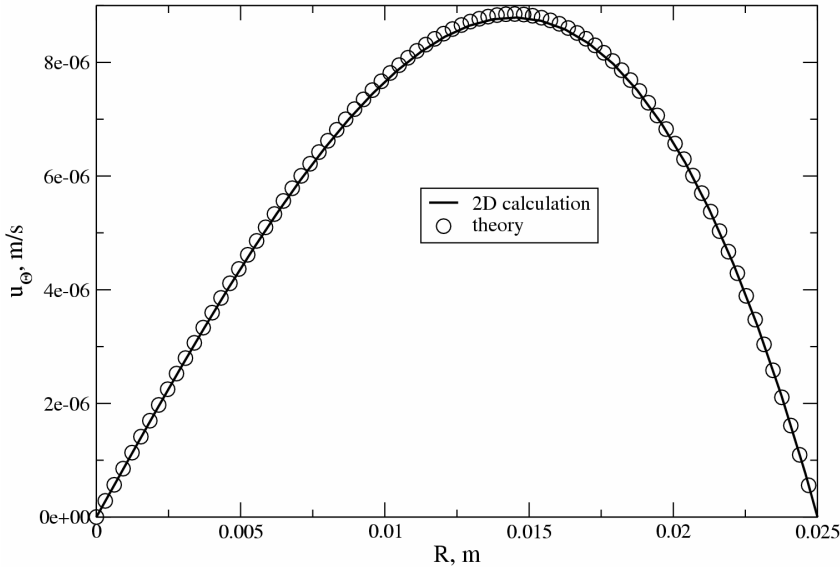


Figure 3. The radial distribution of azimuthal velocity of a liquid metal induced by RMF with $B = 0.01 \text{ mT}$, $\nu = 50 \text{ Hz}$. The properties of the metal are: $\sigma = 1.5 \cdot 10^6$, $\rho = 10^4 \frac{\text{kg}}{\text{m}^3}$, $\mu = 2 \cdot 10^{-3} \frac{\text{Ns}}{\text{m}^2}$. The theoretical curve corresponds to equation (3.1)

4. Computational results

In this section we present the results of numerical simulations of transient flows driven by low-frequency, low-induction RMF ($0.2 \text{ mT} \leq B \leq 1 \text{ mT}$) during Pb85wt%Sn alloy solidification. Beside exploring the flow structure, a main goal of the simulations is to define the influence of magnetic field strength on the shape of the mushy zone. The time step was fixed at maximum 0.1 sec. The maximal number of outer iterations per each time step was equal to 500 allowing to reach residual of less than 10^{-4} . The material properties used in simulations were calculated from the mixture rule according to the 85 wt% of Sn composition. The transport properties of pure Sn and Pb were taken from [17].

The initialization temperature was set to 570 K. The stirring and cooling begin simultaneously. The calculated domain was discretized with a uniform mesh of 130 control volumes (CV) in the vertical z -direction and 45 CV in the radial r -direction.

For the analysis of convection within the liquid phase we use the volume averaged azimuthal U_θ and meridional U_{rz} velocities, which showed a good capability of prediction of flow transition from laminar to turbulent regime [25]. The volume-averaged velocities U_θ and U_{rz} , characterizing during the time the strength of the primary and

secondary flow, respectively, are calculated from the following equations:

$$U_{\theta} = \frac{2 \cdot \pi \cdot \int_0^H \int_0^R r \sqrt{u_{\theta}^2} dr dz}{\pi R^2 H}, \quad (4.1)$$

$$U_{rz} = \frac{2 \cdot \pi \cdot \int_0^H \int_0^R r \sqrt{u_r^2 + u_z^2} dr dz}{\pi R^2 H}. \quad (4.2)$$

Figures 4 and 5 show the time histories of U_{θ} and U_{rz} calculated for different magnetic field inductions B . It can be seen that during the first period of time the liquid is accelerated due to the beginning of the stirring, e.g. the spin-up period for $B = 1 \text{ mT}$ corresponds to about 50 sec, but the time needed to establish the meridional flow is about 20 sec. Interestingly, the duration of U_{rz} increases till the first maximum corresponds to the Stokes flow regime shown in Figure 6. The following after spin-up slow decrease of the volume-averaged azimuthal velocity (Figure 4) corresponds to the cutting down of the aspect ratio of the volume with the liquid due to solidification. An analysis of Figure 5 shows that by $B = 1 \text{ mT}$ between spin-up and spin-down regimes a turbulent regime exists. In addition, the time histories of volume-averaged velocities show that the whole time of solidification is about 200 sec, which corresponds to the averaged solidification front velocity of $0.2 \div 0.3 \text{ mm/s}$.

The spatial distribution of azimuthal and meridional velocities predicted at 60 and 100 sec for different magnetic field strengths are shown in Figures 7, 8 and 9. The velocity vectors show that due to rotation of the liquid so-called Ekman layers begin to form on the bottom of the cylinder. This phenomenon is very well described in the literature [1] and [26]. Inspecting Figures 7, 8 and 9 in more detail, three regimes depending on the magnetic field strength can be identified.

The first regime is characterized by the presence of laminar meridional flow or so called Stokes flow. Its flow structure for $B = 0.2 \text{ mT}$ at different times of solidification is plotted in Figure 7. The analysis of Figure 7 shows that the mushy zone front evolution is not affected by the meridional flow. Note that the mushy zone front can be considered to be the boundary between zero and non-zero velocities.

The increase of magnetic field strength leads ($B = 0.5 \text{ mT}$) to the second regime. We call it nonlinear flow. The swirling flow induces a secondary meridional flow in the shape of two toroidal vortices with different sizes. The big one is the result of Ekman pumping and located near the mushy zone front. The small one is placed in the corner zone near the top free surface, see Figure 8. It can be seen that already in 60 sec the secondary flow affects the mushy zone formation, which is explained by fact that the meridional flow velocity near the mushy front exceeds the solidification front velocity, which is about 0.3 mm/s .

The third regime following after spin-up is a turbulent one. It is characterized by the occurrence of Taylor vortices along the cylindrical wall, see Figure 9a. By decreasing the aspect ratio of the liquid part of the alloy due to its solidification, the turbulence is suppressed and the meridional flow becomes nonlinear, see Figure

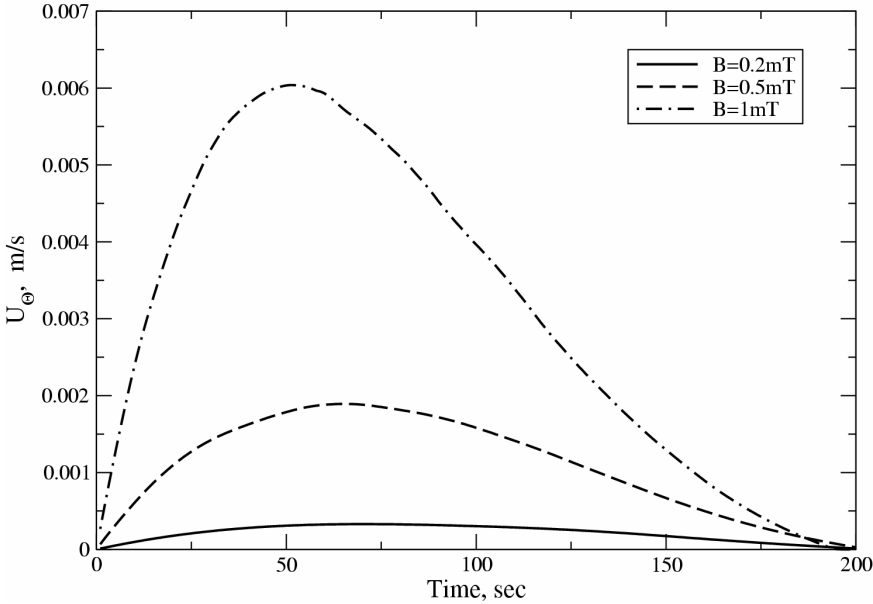


Figure 4. Predicted time histories of volume-averaged azimuthal velocity

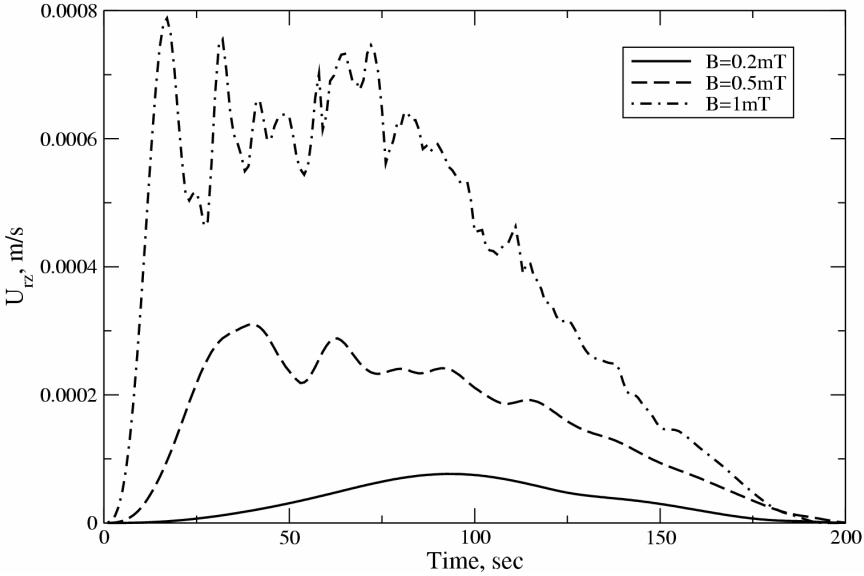
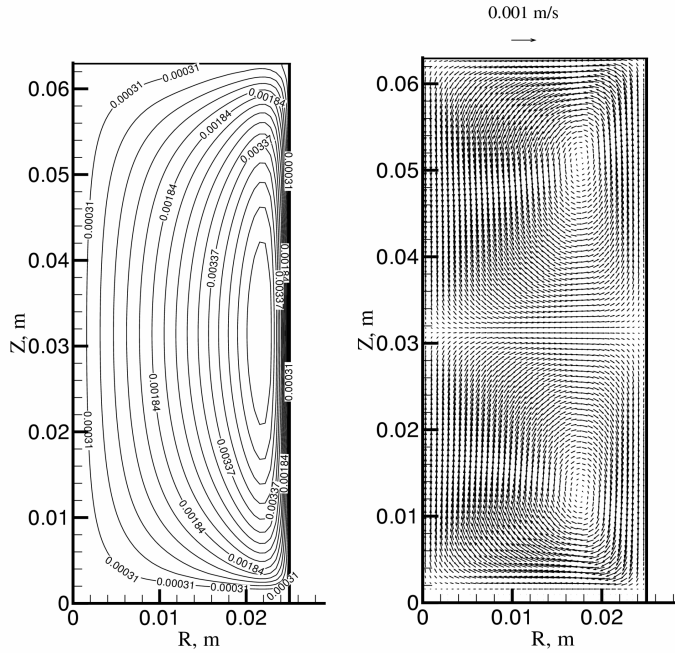


Figure 5. Predicted time histories of volume-averaged meridional velocity

9b. The mushy zone has a convex shape due to the high meridional velocity near the mushy zone which exceeds the velocity of the solidification front. The results presented in Figures 8 and 9 are in qualitative agreement with [20], [27].

The analysis of Figures 5, 8 and 9 shows that the change of the mushy zone shape happens when the volume-averaged meridional velocity exceeds the local velocity of the solidification front.

It should be noted that after the whole material solidification no macrosegregations were predicted for all three inductions. Probably it is explained by the high cooling rate.



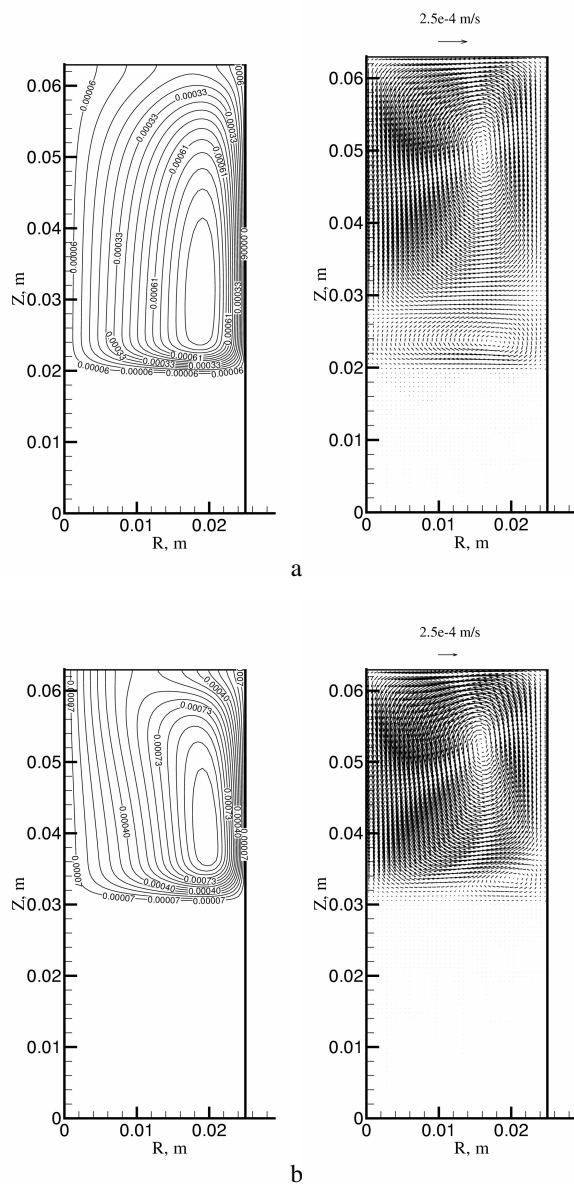


Figure 7. Predicted flow pattern at different times of simultaneous stirring and cooling. $B = 0.2 \text{ mT}$: *a* – time = 60 sec, isowirls (left) and meridional velocity vectors (right); *b* – time = 100 sec, isowirls (left) and meridional velocity vectors (right)

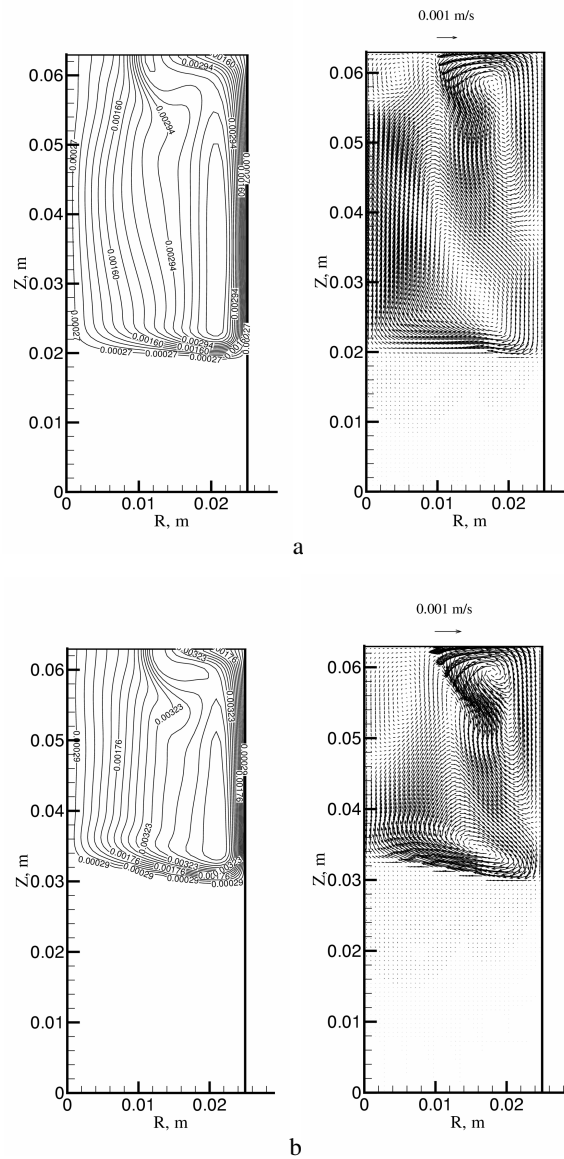


Figure 8. Predicted flow pattern at different times of simultaneous stirring and cooling. $B = 0.5 \text{ mT}$: *a* – $time = 60 \text{ sec}$, isoswirls (left) and meridional velocity vectors (right); *b* – $time = 100 \text{ sec}$, isoswirls (left) and meridional velocity vectors (right)

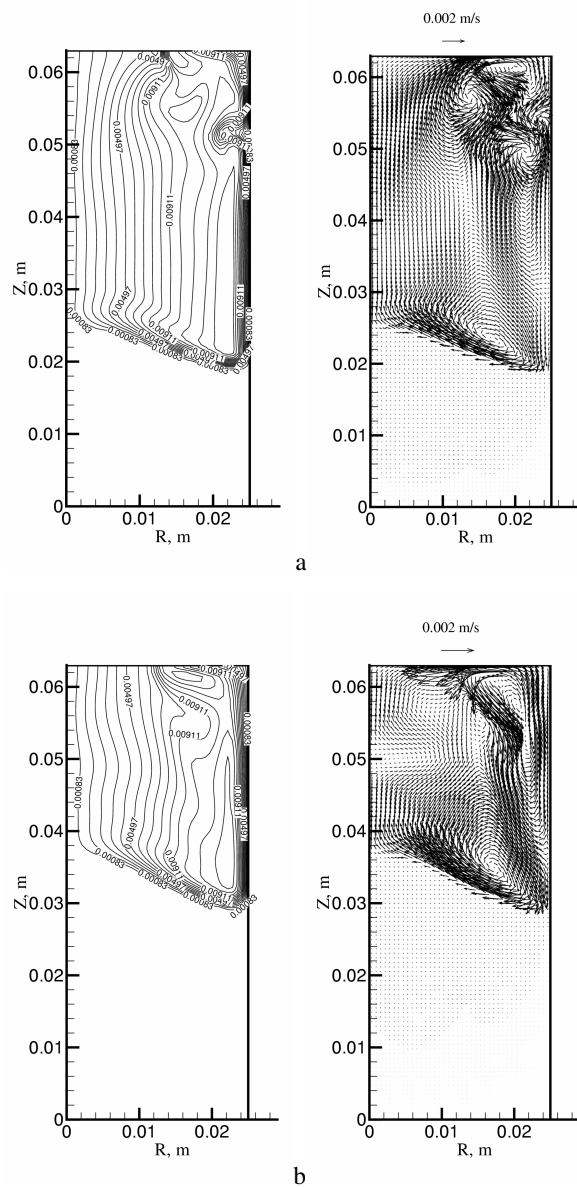


Figure 9. Predicted flow pattern at different times of simultaneous stirring and cooling. $B = 1 \text{ mT}$: *a* – $t = 60 \text{ sec}$, isoswirls (left) and meridional velocity vectors (right); *b* – $t = 100 \text{ sec}$, isoswirls (left) and meridional velocity vectors (right)

respectively. A rotating magnetic field with $B = 1 \text{ mT}$ produces a turbulent flow in the liquid phase. Furthermore, the calculations showed that when the volume averaged meridional velocity exceeds the solidification front velocity, the liquid-mushy zone and solid-mushy zone interfaces are of convex shape, which is attributed to the Ekman pumping effect.

Acknowledgement. The authors are grateful to Dr. M. Peric for the source code of the 2D Navier-Stokes solver. Financial support by the Deutsche Forschungsgemeinschaft (SFB-609, B2) is gratefully acknowledged.

References

1. DAVIDSON, P.A.: *An Introduction to Magnetohydrodynamics*, Cambridge University Press, 2001, 431.
2. VOLLER, V.R., BRENT, A.D. AND PRAKASH, C.: The modeling of heat, mass and solute transport in solidification systems. *Int. J. Heat Mass Transfer*, **32**(9), (1989), 1719-1731.
3. BECKERMANN, C. AND WANG, C.Y.: Multiphase-scale modeling of alloy solidification. *Annual Review of Heat Transfer*, **6**, (1995), 115-198.
4. SCHNEIDER, M.C. AND BECKERMANN, C.: A numerical study of the combined effects of microsegregation, mushy zone permeability and flow, caused by volume contraction and thermosolutal convection, on macrosegregation and eutectic formation in binary alloy solidification. *Int. J. Heat Mass Transfer*, **38**(18), (1995), 3455-3473.
5. BENNON, W.D. AND INCROPERA, F.P.: A continuum model for momentum, heat and species transport in binary solid-liquid phase change systems - I. Model formulation. *Int. J. Heat Mass Transfer*, **30**(10), (1987), 2161-2170.
6. SWAMINATHAN, C.R. AND VOLLER, V.R.: Towards a general numerical scheme for solidification systems. *Int. J. Heat Mass Transfer*, **40**(12), (1997), 2859-2868.
7. SWAMINATHAN, C.R. AND VOLLER, V.R.: A general enthalpy method for modeling solidification processes. *Metallurgical Transactions B*, **23B**, (1992), 651-664.
8. NI, J. AND INCROPERA, F.P.: Extension of the continuum model for transport phenomena occurring during metal alloy solidification - I. The conservation equations. *Int. J. Heat Mass Transfer*, **38**(7), (1995), 1271-1284.
9. YOO HOSEON AND VISKANTA, R.: Effect of anisotropic permeability on the transport process during solidification of a binary mixture, *Int. J. Heat Mass Transfer*, **35**(10), (1992), 2335-2346.
10. NEILSON, D.G. AND INCROPERA, F.P.: Three-dimensional considerations of unidirectional solidification in a binary liquid. *Numerical Heat Transfer, Part A*, **23**, (1993), 1-20.
11. MOFFATT, H.K.: On fluid flow induced by a rotating magnetic field. *J. Fluid Mech.*, **22**, (1965), 521-528.
12. DAVIDSON, P.A. AND HUNT, J.C.R.: Swirling recirculating flow in a liquid-metal column generated by a rotating magnetic field. *J. Fluid Mech.*, **185**, (1986), 67-106.
13. PRIEDE, J. AND GELFGAT, YU.M.: Mathematical model of the mean electromagnetic force induced by a rotating magnetic field a liquid column of a finite length. *Magneto-hydrodynamics*, **32**, (1996), 249-256.

14. KAISER, TH. AND BENZ, K.W.: Taylor vortex instabilities induced by a rotating magnetic field: A numerical approach. *Physics of Fluids.*, **10**(5), (1998), 1104-1110.
15. MOESSNER, R. AND GERBETH, G.: Buoyant melt flows under the influence of steady and rotation magnetic fields. *Journal of Crystal Growth*, **197**, (1999), 341-354.
16. PRESSCOTT, P.J.: *Convection transport phenomena during solidification of binary metal alloys and the effects of magnetic fields*, Ph.D. Thesis, Purdue University, West Lafayette, IN, USA, 1992.
17. PRESSCOTT, P.J. AND INCROPERA, F.P.: Magnetically damped convection during solidification of a binary metal alloy. *Journal of Heat Transfer*, **115**, (1993), 302-310.
18. PRESSCOTT, P.J., INCROPERA, F.P. AND GASKELL, D.R.: Influence of electromagnetic stirring on the solidification of a binary metal alloy. *Exp. Heat Transfer*, **9**, (1996), 105-131.
19. PRESSCOTT, P.J. AND INCROPERA, F.P.: The effect of turbulence on solidification of a binary metal alloy with electromagnetic stirring. *Journal of Heat Transfer*, **117**, (1995), 716-724.
20. ROPLEKAR, J.K., AND DANTZIG, J.A.: A study of solidification with a rotating magnetic field. *Int. J. Cast. Metals Research*, **14**(2), (2001), 79-98.
21. MASSALSKI, TH. B., EDITOR-IN-CHIEF.: *Binary Alloy Phase Diagrams*, Vol.3, ASM International, Materials Park, Ohio 44073, USA, 1990, 2nd edition.
22. SINGH, A.K. AND BASU, B.: On convection in mushy phase and its effect on macrosegregation. *Metallurgical and Material Transactions A*, **31A**, (2000), 1687-1692.
23. WILLERS, B., ECKERT, S., MICHEL, U. AND ZOUHAR G.: Effect of the fluid convection driven by a rotating magnetic field on the solidification of a PbSn alloy, Conference Proceedings of the EUROMAT2003 Conference, Wiley-VCH GmbH, to be published, 2004.
24. FERZIGER, J.H. AND PERIC, M.: *Computational methods for fluid dynamics*, Springer-Verlag. 3rd Edition, 2002, 423.
25. NIKRITYUK, P.A., ECKERT, K. AND GRUNDMANN, R.: *Numerical study of spin-up dynamics of a liquid metal stirred by rotating magnetic fields in a cylinder with upper free surface*. Accepted for publication, Magnetohydrodynamics Journal, (2004).
26. GREENSPAN, H.P.: *The theory of rotating fluids*, Cambridge University Press, Cambridge, 1968.
27. NEILSON, D.G., AND INCROPERA, F.P.: Effect of rotation on fluid motion and channel formation during unidirectional solidification of a binary alloy. *Int. J. Heat Mass Transfer*, **36**(2), (1993), 489-505.

DETERMINISTIC UNSTEADY VORTICITY FIELD IN A DRIVEN AXISYMMETRIC CAVITY FLOW

DANIEL RUSCH, AXEL PFAU, JOËL SCHLIENGER, ANESTIS I. KALFAS, AND
REZA S. ABHARI

Turbomachinery Laboratory, Swiss Federal Institute of Technology
ETH Zentrum, ML J33, Sonneggstrasse 3, CH-8092 Zurich
`daniel.rusch@ethz.ch`

[Received: November 21, 2003]

Abstract. This paper introduces a new data visualization technique for the evaluation of 3D unsteady data using the various terms of the deterministic unsteady vorticity transport equation. The toroidal vortex residing in the inlet cavity of an axial turbine rotor labyrinth is discussed using the proposed technique. Especially, secondary flow effects and the effect of unsteadiness with respect to its contribution to loss generation were investigated. The analysis allowed further insight in flow physics. It was found that the rotational acceleration of the vortex shows a phase shift of one quarter of blade passing period relative to the vortex strength.

Mathematical Subject Classification: 76B47

Keywords: toroidal vortex, visualization technique, vorticity transport equation

Nomenclature

C	$[-]$	circumferential position, θ/p_{blade}
f_{bp}	$[Hz]$	blade passing frequency
h	$[J/kg]$	specific enthalpy
\vec{b}	$[-]$	unit vector
p	$[Pa]$	static pressure
p_{blade}	$[deg]$	blade pitch, $360^\circ/42$
r	$[m]$	radial position
R	$[-]$	radial height, $(r - r_{Hub})/(r_{Tip} - r_{Hub})$
s	$[J/(kgK)]$	specific entropy
t	$[s]$	time
t_{bp}	$[s]$	blade passing period, $1/f_{bp}$
T	$[K]$	temperature
\vec{v}	$[m/s]$	velocity vector
v_∞	$[m/s]$	undisturbed velocity
v_\perp	$[m/s]$	velocity component perpendicular to $\vec{\omega}$
v_\uparrow	$[m/s]$	velocity component parallel to $\vec{\omega}$
v_z	$[m/s]$	axial velocity component

z	$[mm]$	axial direction parallel to machine axis
$\hat{\alpha}$	$[1/s^2]$	rotational acceleration
$\vec{\beta}$	$[-]$	unit vector
ρ	$[kg/m^3]$	density
σ	$[m]$	coordinate along a vortex line
$\Delta\sigma$	$[m]$	coordinate increment along a vortex line
τ	$[N/m^2]$	stress tensor
$\vec{\omega}$	$[1/s]$	vorticity vector
ω_θ	$[1/s]$	circumferential component of $\vec{\omega}$
$\hat{\omega}$	$[1/s]$	rotational speed
Y	$[-]$	non dimensional time, t/t_{bp}

1. Introduction

One of the key issues in modern turbomachinery design is the improvement of component efficiency. The aerodynamic efficiency of a turbine stage is drastically reduced by secondary flows. Langston [1] estimates the contribution of the secondary loss to be up to 50% of the total aerodynamic loss. Hence, secondary flow control plays a key role in the strive for more efficient and environmentally friendly turbomachines. This goal can only be reached through improved understanding of the secondary flow development and interactions. There have been a number of investigations focusing on the total pressure loss coefficients, secondary velocity [2] and - in more recent papers - the vorticity distribution [3].

Pullan and Denton [4] presented a visualization method using a passive scalar technique which was found to greatly enhance the analysis of their numerical simulations of vortex-blade interaction. The kinematic behavior of a stator passage vortex within the downstream rotor has been studied both with and without the influence of rotor endwall flows.

A large body of research work has been devoted to secondary flows within turbomachines. Sieverding [5] summarized recent progress in the understanding of basic aspects of secondary flows in turbine blade passages and Langston [1] recently presented a comprehensive review of secondary flows in axial turbines.

Gregory-Smith et al. [6] showed a method of evaluating streamwise vorticity from traverse data and obtaining a streamwise direction from a least-squares linear fit of pitchwise averaged yaw and pitch angles. This method produces a reduced streamwise vorticity that indicates the number of rotations that a lump of fluid with such a vorticity would make as it travelled the distance between the blade rows.

Roth [7] examined existing extraction algorithms and analyzed their underlying definitions of a vortex. He proposed an elementary operation on a pair of vector fields to be used as a building block for defining and computing global line-type features of vector or scalar fields.

The present work proposes a novel technique to analyze complex flow fields involving vortical structures. Considering the terms of the vorticity equation, such as the

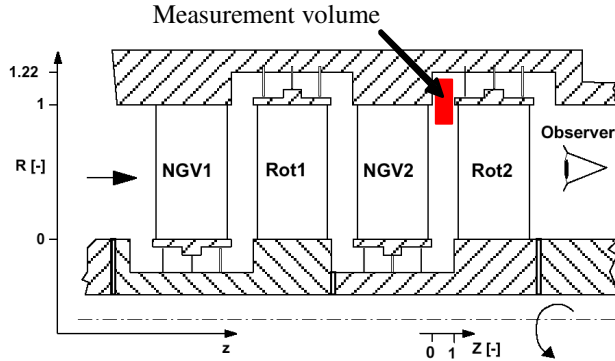


Figure 1. Geometry overview. The box indicates the location of the measurement volume

vortex stretching and the time derivative term, a deeper insight in flow physics is gained.

2. Experimental setup

The data presented in this paper were taken from a two-stage axial research turbine, which is described in detail in Sell et al. [8]. All measurements were taken at the same operating point using a single sensor fast response aerodynamic pressure probe (FRAP) [9,10]. The raw data is phase-lock averaged using an accurate rotor trigger and finally reduced to the requested time-resolved flow parameters such as the 3D, unsteady velocity vector, as well as the total and static pressure.

The location of the measurement volume is indicated in Figure 1. The resolved volume covers both the cavity and a part of the main flow region. The coordinate system is defined as follows: C denotes the non-dimensional circumferential and R the non-dimensional radial position. According to the definition, $R = 1$ represents the tip radius. The z axis denotes the axial direction as indicated in Figure 1. A local axial coordinate axis is introduced denoting the first measurement plane with $z = 0$. The last of the 5 measurement planes is found at $z = 7.5 \text{ mm}$.

As an example for the way how secondary flow effects the cavity flow situation, the time-averaged total pressure distribution downstream the second nozzle guide vane (NGV2) is depicted in Figure 2. The data range covers both, main and cavity flow in radial direction and 1.1 pitches in circumferential direction. The hub is located at $R = 0$ and the tip at $R = 1$, respectively. In order to visualize the periodicity of the flow, the results are copied three times in circumferential direction. The view is from a downstream position into the upstream direction. The flow region of low total pressure behind the blade shows the typical wake-loss core structure in the main flow. Both the passage vortices at the hub as well as at the tip can be clearly identified. These loss cores are created by the passage vortices, which entrain all incoming boundary

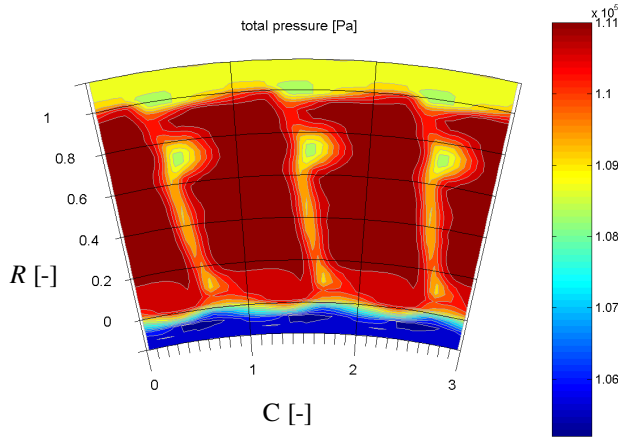


Figure 2. Total pressure distribution downstream of the second stator (NGV2)

layer fluid and move it to the suction side of the wake. The cavity flow regions at hub and tip are characterized with significantly lower total pressure. The interface between main and cavity flow both at hub and tip shows a wavy structure.

3. Data Postprocessing

The new flow visualization technique is based on the vorticity transport equation (3.2). The resolution of the volume data set in both space and time is high enough to evaluate derivatives using finite differences. For each time step, the unsteady vorticity field is evaluated directly using the definition

$$\omega = \nabla \times \vec{v}. \quad (3.1)$$

Having both the full three dimensional time resolved vorticity and velocity field, the evaluation of the substantial derivative within the compressible unsteady vorticity transport equation (3.2) [11] is straightforward using its definition (3.3).

$$\frac{D}{Dt} \left(\frac{\vec{\omega}}{\rho} \right) = \frac{1}{\rho} \vec{\omega} \cdot \nabla \vec{v} + \frac{1}{\rho^3} \nabla \rho \times \nabla p + \frac{1}{\rho} \nabla \times \left(\frac{1}{\rho} \nabla \cdot \tau \right), \quad (3.2)$$

$$\frac{D}{Dt} \left(\frac{\vec{\omega}}{\rho} \right) = \frac{\partial}{\partial t} \left(\frac{\vec{\omega}}{\rho} \right) + (\vec{v} \cdot \nabla) \left(\frac{\vec{\omega}}{\rho} \right). \quad (3.3)$$

For visualization reasons, both terms on the right-hand side of equation (3.3) were evaluated and discussed in [12] as they allow flipping between the Lagrangian and the Eulerian frame of reference and describe the acceleration of the vortices. Besides the acceleration term, the new flow visualization technique focuses especially on the

vortex stretching term

$$\frac{1}{\rho} \vec{\omega} \cdot \nabla \vec{v}, \quad (3.4)$$

which describes the vortex tilting and stretching. A discussion of this term and its application to flow field visualization will be done in the next section.

From the application point of view, the baroclinic generation term

$$\frac{1}{\rho^3} \nabla \rho \times \nabla p \quad (3.5)$$

cannot be derived from measurements. The missing information is the unsteady temperature distribution. Together with the static pressure distribution, the time resolved density field could be evaluated. For the evaluation of the other terms in equation (3.2), the lack of accurate density information has only a minor influence, since the values of the temperature distribution are within a relatively narrow band.

Nevertheless, it is worthwhile to theoretically discuss the baroclinic vorticity generation term as it can be related to the entropy distribution. Taking the curl of

$$T ds = dh - \frac{1}{\rho} dp \quad \text{or} \quad T \nabla s = \nabla h - \frac{1}{\rho} \nabla p \quad (3.6)$$

and using the identity $\nabla \times \nabla h \equiv 0$, equation (3.6) can be written as

$$\nabla \times (T \nabla s) = \nabla \times \nabla h - \nabla \times \left(\frac{1}{\rho} \nabla p \right) = -\nabla \times \left(\frac{1}{\rho} \nabla p \right). \quad (3.7)$$

Utilizing equation (3.7) and the vector identity (Wilcox [13])

$$\nabla \times \left(\frac{1}{\rho} \nabla p \right) = \frac{1}{\rho} \nabla \times \nabla p + \nabla \frac{1}{\rho} \times \nabla p = \nabla \frac{1}{\rho} \times \nabla p \quad (3.8)$$

the following relation can be derived:

$$\frac{1}{\rho^3} \nabla \rho \times \nabla p = \frac{1}{\rho} \nabla T \times \nabla s. \quad (3.9)$$

In addition to the ideal gas law, equation (3.9) represents three coupled differential equations for the time-resolved entropy. However, the time-resolved temperature measurement is missing for the presented data set.

4. Results

4.1. Toroidal vortex. In this section, the toroidal vortex located at the inlet cavity of a turbine rotor labyrinth seal - as discussed by Pfau et al. [14] - is under investigation applying both standard as well as the newly proposed visualization technique using the vortex stretching term (3.4). The cavity vortex is driven by the main flow due to viscous interaction. The behavior of this vortex is of interest, as it affects the leakage mass flow over the shroud and redirects cooling air in cooled turbines.

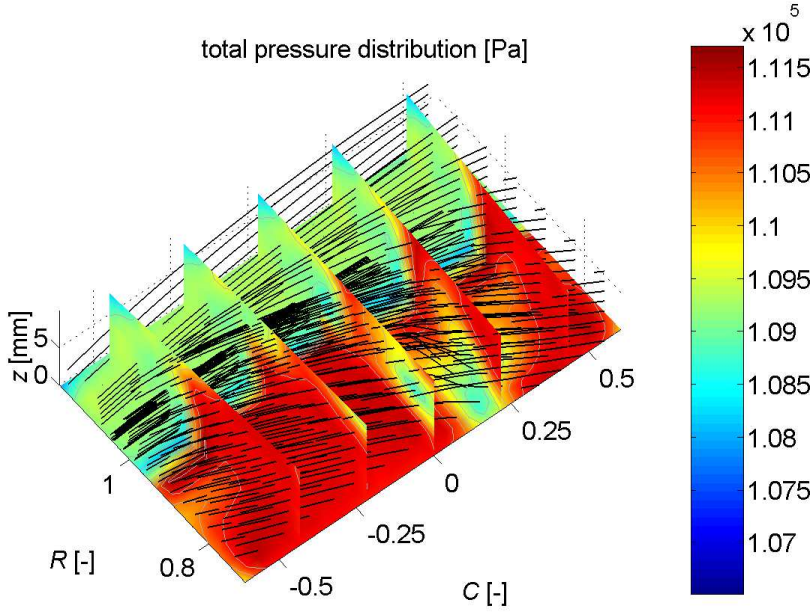


Figure 3. Total pressure distribution behind a stator visualized using radial slices. The black lines represent streamlines

4.2. Steady 3D flow visualization using total pressure. A useful property to study loss generation is the steady total pressure. The corresponding distribution downstream of the second stator is given in Figure 3. Five radial cuts and one axial cut, which is located at $z = 0$, were used to intersect the measurement volume. In addition, streamlines were added in order to visualize the flow.

From the total pressure distribution, the volume under investigation can be split into two regions, one being the main flow region ($R < 1$), which is represented by high total pressure and the other being the cavity flow region ($R > 1$), which is characterized by low total pressure. The motion of the main flow shows a large circumferential component as expected downstream of swirl generating stator. The location of low total pressure within the main flow represents the loss core as found in Figure 2.

Within the cavity, the presence of the toroidal vortex aligned in circumferential direction can be verified by observing the streamlines which show very small axial motion and even back flow at the outer part. A qualitative description of the flow situation within the cavity is depicted in Figure 4. The axial component of the velocity $v_z(r)$ is constant in the main flow region and then decays while moving into the cavity. At the centre of the ring vortex, the sign changes and finally the fluid comes to rest due to the non-slip condition at the cavity wall.

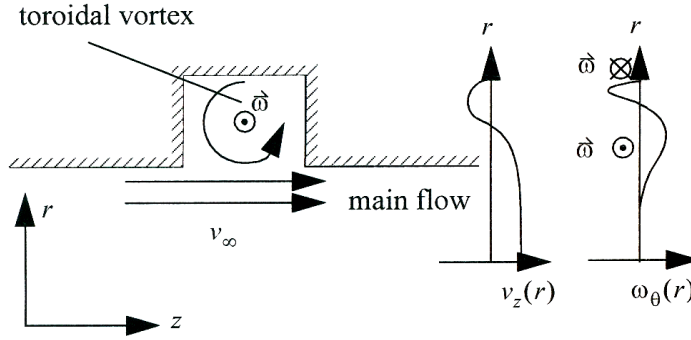


Figure 4. Generic cavity flow structure in an (r, z) cut: expected axial velocity and circumferential vorticity distribution

4.3. Unsteady 3D flow visualization using static pressure and the circumferential vorticity component. In this Section, the unsteady flow structure in the measurement volume is investigated. At first, the time-resolved static pressure distribution is given in Figure 5. The different plots are equidistant in time and represent the flow during one blade passing period.

Vortices create a local minimum of static pressure in their center of rotation. The vortex gets stronger if the static pressure in the center is decreased. The toroidal vortex located in the cavity ($R > 1$) can be identified with this reflection in the plot as a region of low static pressure. This zone of the flow is pointed out in the middle radial cut of Figure 5 using a black circle. Looking at this region for a blade passing period, it can be seen that the level of the static pressure does not remain constant. It shows a cyclic change where the pressure level within this middle radial cut reaches its minimum between $Y = 1/6$ and $Y = 2/6$. The cyclic change is correlated to the blade passing period.

Figure 6 shows the circumferential component of the vorticity vector ω_θ . Considering the cavity flow model depicted in Figure 4, it can be stated that ω_θ changes while going radially outward through the cavity: As ω_θ is proportional to the slope of the axial velocity v_z , it vanishes in the main flow region, where v_z is about constant. In the tip zone, v_z decays and therefore ω_θ gets positive and stays positive as long as the slope of the axial velocity profile shows the same sign. At maximum negative axial velocity, ω_θ is zero. At this radial position, ω_θ changes its sign and remains negative until the cavity wall is reached. The presented idealized radial distribution of the circumferential component of the vorticity vector can also be found in the unsteady measurements presented in Figure 6, considering one of the radial cuts. ω_θ vanishes in the undisturbed main flow. Going radially outward, ω_θ shows at first positive and then negative values as discussed. Moreover, the transient behavior is as expected from the previous reflections on the static pressure distribution. Looking again at the middle radial cut, a maximum value is reached between $Y = 1/6$ and $Y = 2/6$.

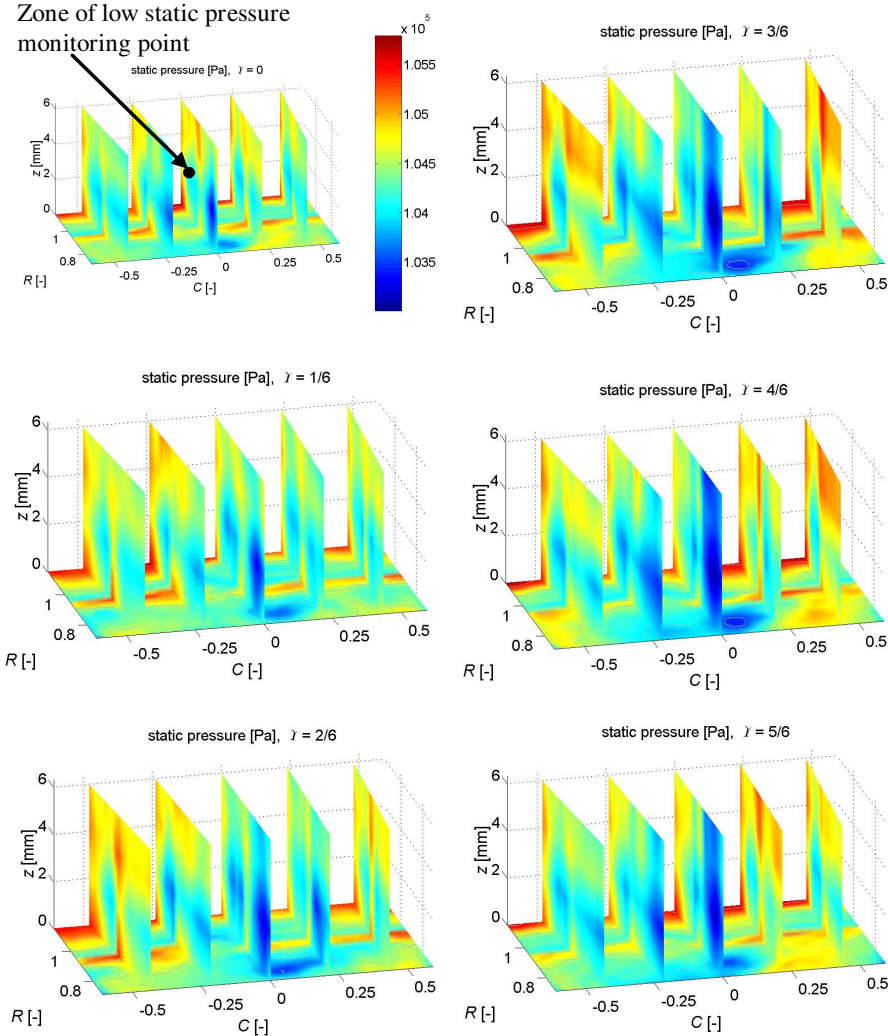


Figure 5. Unsteady static pressure distribution downstream of the second stator: one blade passing period

A monitor point was selected at the middle radial slice within the core of the cavity vortex as indicated in Figure 5 with the black dot. The behavior of p and ω_θ at this point during 3 blade passing periods is given in Figure 8 and allows a direct transient comparison between p and ω_θ . It is evident that ω_θ increases by as much as 100% in a negative pressure gradient zone and decreases gradually by as much in a positive pressure gradient area. Clearly and as expected, the circumferential vorticity and the gradient of the static pressure in the cavity are inversely related.

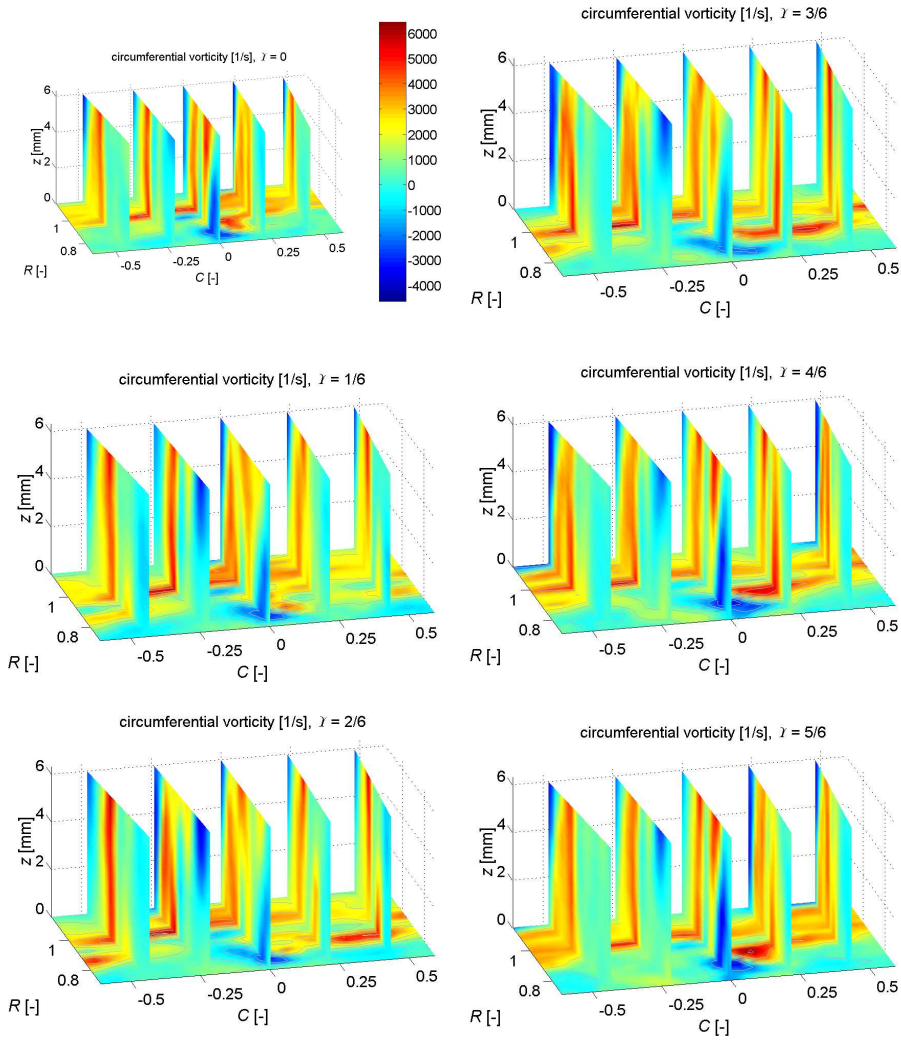


Figure 6. Unsteady circumferential vorticity component downstream of the second stator: one blade passing period

4.4. Unsteady 3D flow visualization using the circumferential component of the vortex stretching term. In Figure 7 the circumferential component of the vortex stretching term is depicted. Consider a vortex line in a velocity field as indicated in Figure 9. According to the definition, vortex lines are tangential to the local vorticity vector $\vec{\omega}$. The local velocity vector \vec{v} can be split into a component tangential v_{\uparrow} and a component normal v_{\perp} to the vortex line as it is described in [15].

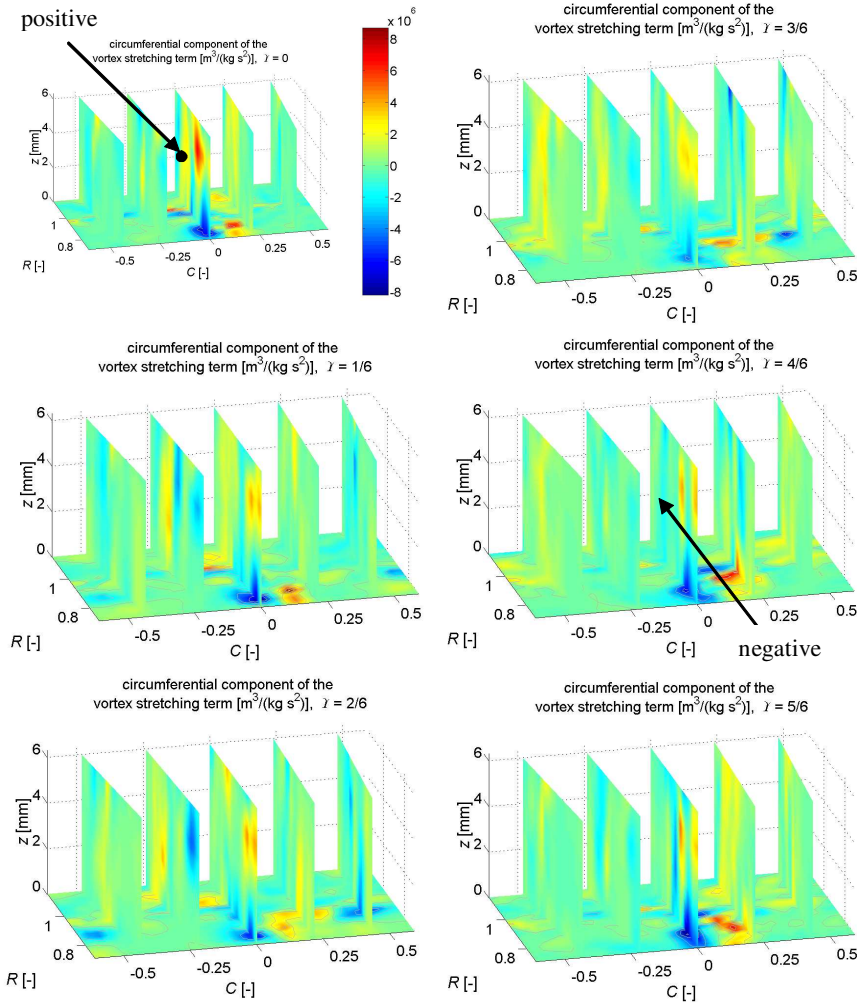


Figure 7. Unsteady component of the circumferential vortex stretching term downstream of the second stator: one blade passing period

Neglecting the density, term (3.4) can be written as

$$\vec{\omega} \cdot \nabla \vec{v} = \left[\vec{\omega} \cdot \left(\vec{b}_\sigma \frac{\partial}{\partial \sigma} + \vec{b}_n \frac{\partial}{\partial n} + \vec{b}_m \frac{\partial}{\partial m} \right) \right] \vec{v} = |\vec{\omega}| \frac{\partial}{\partial \sigma} \vec{v} = |\vec{\omega}| \frac{\partial}{\partial \sigma} \vec{v}_\uparrow + |\vec{\omega}| \frac{\partial}{\partial \sigma} \vec{v}_\perp, \quad (4.1)$$

where σ denotes the coordinate along the vortex line, n away from the center of curvature and m along the third normal. Equation (4.1) makes use of $\vec{\omega} \cdot \vec{b}_n = \vec{\omega} \cdot \vec{b}_m = 0$ and $\vec{\omega} \cdot \vec{b}_\sigma = |\omega|$. Considering the derivative of the first term in equation (4.1) to be

positive, which corresponds to the case that $\vec{v}_{\uparrow}(\sigma + \Delta\sigma) > \vec{v}_{\uparrow}(\sigma)$, the section of the vortex tube under observation will be stretched and the rotational speed will increase as the tube diameter decreases (see Figure 9). The opposite behavior is true for $\vec{v}_{\uparrow}(\sigma + \Delta\sigma) < \vec{v}_{\uparrow}(\sigma)$. The second term on the right-hand side of equation (4.1) is responsible for the vortex tilting as can be seen by considering $\vec{v}_{\perp}(\sigma + \Delta\sigma) \neq \vec{v}_{\perp}(\sigma)$. Going back to Figure 7, one can see that the circumferential component of the vortex stretching term undergoes a cyclic change as well. At $Y = 0$ the stretching term is positive, whereas it is negative at $Y = 3/6$, looking again at the middle radial cut. As mentioned before, a positive component in the direction of the vortex line represents a stretching of the vortex and a negative one squeezes the vortex, if the vortex is aligned with the stretching term vector. In case of the toroidal vortex, the vortex is aligned in circumferential direction and the vortex stretching term will therefore primarily stretch (rather than tilt) the vortex and thus increase the strength of the circumferential vorticity component and decrease the static pressure in its core. The opposite is true for the negative vortex stretching term, which is consistent with the findings up to now. It has to be stated, that the vortex stretching term is ahead of the vortex strength term. That means that the vortex stretching term reaches its maximum before the vortex strength term does. Therefore, the spin-up process of the vortex needs some time, which is discussed in the following paragraph.

At $Y = 3/6$, the vortex stretching term in circumferential direction is negative and thus squeezes the vortex. As it can be seen in Figure 5, the strength of the vortex will decrease. The behavior found in the experiment can be explained by considering a solid body rotation. Let $\hat{\omega}$ denote the rotational speed of the vortex expressed as a harmonic function according to $\hat{\omega} = \bar{\omega} + \omega' \sin(\omega_{bp}t)$ with $\omega_{bp} = 2\pi f_{bp}$. The rotational acceleration is then the time derivative of the rotational speed $\hat{\alpha} = \frac{\partial}{\partial t} \hat{\omega} = \omega_{bp} \omega' \cos(\omega_{bp}t)$ and is thus a quarter of a period ahead of the rotational speed. This is exactly the behaviour found in the measurements: The acceleration term represented by the circumferential component of the vortex stretching is a quarter of a period ahead of the terms which represent the speed or the strength of the vortex (such as the static pressure distribution and the circumferential component of the vorticity).

5. Conclusions

Nowadays, sophisticated probe technology and high computational power make it possible to analyze complex flow in four dimensions, i.e. space and time. Considering the huge amount of data, intuitive visualization is the key for further processing and analyzing data as well as for locating interesting features. It allows us to gain insight in physical mechanisms and promotes flow understanding.

The visualization of the vortex stretching term of the deterministic unsteady vorticity transport equation has proved to be a powerful tool. It makes it possible to locate complex features in the flow, such as the toroidal vortex and to associate different properties with each other. In the example under investigation, the stretching and squeezing of the vortex line around the annulus could be connected with the

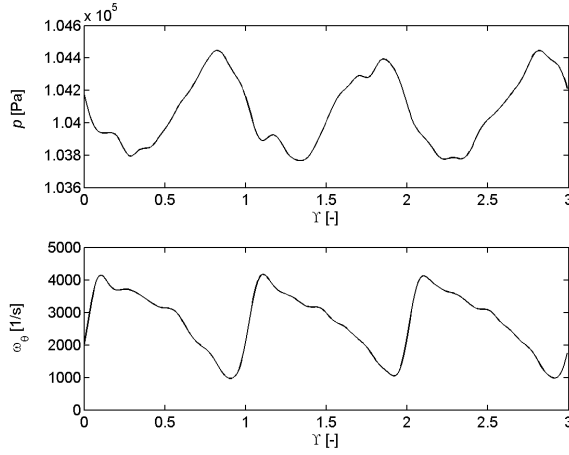


Figure 8. Time series of static pressure and circumferential vorticity component

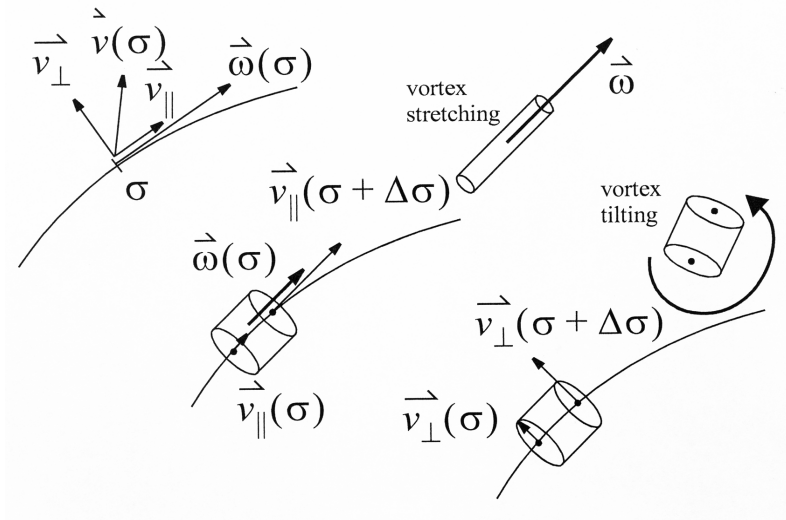


Figure 9. Influence of the velocity field on the vorticity

transient behavior of the static pressure and the circumferential component of the vorticity vector distribution.

The baroclinic vorticity generation term was related to the gradient of the entropy. For the evaluation of the entropy differences, the temperature distribution has to be

time-resolved. Hence, the time-resolved temperature measurement is a very important research area for the future as it would allow us to calculate entropy differences.

Acknowledgement. The flow measurements in the turbine were supported by the German Federal Ministry of Economy (BMWi) under file numbers 0327060D and 0327060F. The authors gratefully acknowledge the support and permission to publish this paper by AG Turbo, Alstom Power and Rolls-Royce Germany.

References

1. LANGSTON, L.S.: Secondary flows in axial turbines – a review. *Annals of the New York Academy of Sciences*, **934**, (2001), 11-26.
2. CHALUVADI, V.S.P., KALFAS, A., HODSON, H.P., OHYAMA, H. AND WATANABE, E.: Blade row interaction in a high pressure steam turbine. *Journal of Turbomachinery*, **125**, (2003), 14-25.
3. TREIBER, M., ABHARI, R.S. AND SELL, M.: *Flow physics and vortex evolution in annular turbine cascades*, ASME Turbo Expo 2002, GT-2002-30540.
4. PULLAN, G. AND DENTON, J. D.: Numerical simulation of vortex turbine blade interaction, paper NO TA-106, *Proceedings of the 5th European Turbomachinery Conference*, Prague, Czech Republic, March 17-22, 2003, 1049-1059.
5. SIEVERDING, C.H.: Recent progress in the understanding of basic aspects of secondary flows in turbine blade passages. *ASME J. Eng. for Power*, **107**(2), (1985), 248-257.
6. GREGORY-SMITH, D.G., GRAVES, C.P. AND WALSH, J.A.: Growth of secondary losses and vorticity in an axial turbine cascade. *ASME J. Turb.*, **110**, (1988), 1-8.
7. ROTH, M.: *Automatic Extraction of Vortex Core Lines and Other Line-Type Features for Scientific Visualization, Selected Readings in Vision and Graphics*, Volume 9, Hartung-Gorre Verlag, Konstanz, ISSN 1439 - 5053, ISBN 3-89649-582-8, 2000.
8. SELL, M., SCHLIENGER, J., PFAU, A., TREIBER, M., AND ABHARI, R.S.: The 2-stage axial turbine test facility LISA, *Proceedings of the ASME Turbo Expo, 2001-GT-492*, June 4-7, New Orleans, Louisiana.
9. PFAU, A., SCHLIENGER, J., KALFAS, A.I. AND ABHARI, R.S.: Unsteady, 3-dimensional flow measurement using a miniature virtual 4 sensor Fast Response Aerodynamic Probe (FRAP), GT2003-38128, *ASME Turbo Expo*, 16-19 June 2003, Atlanta.
10. SCHLIENGER, J., PFAU, A., KALFAS, A.I. AND ABHARI, R.S.: Effects of labyrinth seal variation on multistage axial turbine flow, *Proceedings of ASME Turbo Expo*, GT-2003-38270, 16-19 June 2003, WCC, Atlanta, Georgia, USA.
11. THOMPSON, P.A.: *Compressible Fluid Dynamics*, McGraw-Hill, New York, 1972.
12. RUSCH, D.: *Evaluation of the Steady and Unsteady Vorticity Field from Experimental Data*, Semester Thesis, Turbomachinery Laboratory, ETH Zurich, 2002.
13. WILCOX, D.C.: *Basic Fluid Mechanics*, DCW Industries, Inc., California, 1997.
14. PFAU, A., SCHLIENGER, J., RUSCH, D., KALFAS, A.I. AND ABHARI, R.S.: Unsteady Flow Interactions within the Inlet Cavity of a Turbine Rotor Tip Labyrinth Seal, GT2003-38271, *ASME Turbo Expo*, 16-19 June 2003, Atlanta.
15. KUNDU, P.K. AND COHEN, I.M.: *Fluid Mechanics*, Second Edition, Academic Press, New York, 2002, 139-140.

FLAME STABILIZATION OF HIGHLY DIFFUSIVE GAS MIXTURES IN POROUS INERT MEDIA

DIMOSTHENIS TRIMIS AND KLEMENS WAWRZINEK

Institute of Fluid Mechanics, Friedrich-Alexander-University of Erlangen-Nuremberg
D-91058 Erlangen, Germany
`dimos@lstm.uni-erlangen.de`

[Received: December 18, 2003]

Abstract. Flame propagation experiments in porous media were carried out for mixtures with different Lewis-numbers in order to determine the critical Péclet-number, above which flame propagation is possible. The critical Péclet-number of 65, known from previous studies, was confirmed for mixtures with Lewis-numbers above and equal to unity but for mixtures with a high diffusive mass transport to heat transport ratio, i.e. with Lewis-numbers below unity, the critical Péclet-number was found to lie far below this limit. The experimental results allow for a better design of flame traps for highly diffusive mixtures.

Mathematical Subject Classification: 80A25

Keywords: combustion in porous media, flame quenching, diffusion effects

Nomenclature

a	$[m^2/s]$	thermal diffusivity
l	$[m]$	length
t	$[s]$	time
D	$[m]$	diameter
D	$[m^2/s]$	diffusion coefficient
S_L	$[m/s]$	laminar flame speed
λ_f	$[W/mK]$	thermal conductivity of the fluid
ρ_f	$[kg/m^3]$	density of the fluid
τ	$[s]$	characteristic reaction time
Φ	$[-]$	equivalence ratio

Subscripts

c	component
$crit$	critical
eff	effective
f	fluid, fluidic
p	pore
L	laminar

Abbreviations

<i>HVR</i>	high velocity regime
<i>LVD</i>	low velocity detonation
<i>LVR</i>	low velocity regime
<i>MFC</i>	mass flow controller
<i>ND</i>	normal detonation
<i>RCR</i>	rapid combustion regime
<i>SVR</i>	sound velocity regime
$Le_c \equiv \frac{a_f}{\bar{D}_s}$	Lewis-number
$P_e \equiv \frac{S_L \bar{d}_{p,eff}}{a_f}$	modified Péclet-number

1. Introduction

Flame propagation in porous inert media depends on the structure and physical properties of the solid matrix and on the properties of the combustible gas. The resulting flame propagation modes can be classified into different regimes, of which some important parameters are given in Table 1.

Table 1. Flame propagation regimes in porous media [1], [2], [6], [7]

Regime	Speed of combustion wave m/s	Mechanism of flame propagation
Low velocity (<i>LVR</i>)	$0 - 10^{-4}$	Heat conduction and inter-phase heat exchange
High velocity (<i>HVR</i>)	$0.1 - 10$	High convection
Rapid combustion (<i>RCR</i>)	$10 - 100$	Convection, low pressure gradient
Sound velocity (<i>SVR</i>)	$100 - 300$	Convection with significant pressure gradient
Low velocity detonation (<i>LVD</i>)	$500 - 1000$	Self ignition with shock wave
Normal detonation (<i>ND</i>)	$1500 - 2000$	Detonation with momentum and heat loss

In this paper only such regimes are discussed in which no pressure gradient occurs in the reaction zone, i.e. the low velocity regime (*LVR*) and the high velocity regime (*HVR*). The solid matrix strongly influences the reaction conditions of the combustion, mainly because the heat transport in the burner is dominated by the properties of the solid material. Ceramic spheres and other packing material can be used in this application. In [3] and [4] an overview about applicable porous media for porous burners is given.

Since the major influence of the solid matrix derives from the enhanced heat transport, the effects of the matrix properties on flame stabilization in porous media are

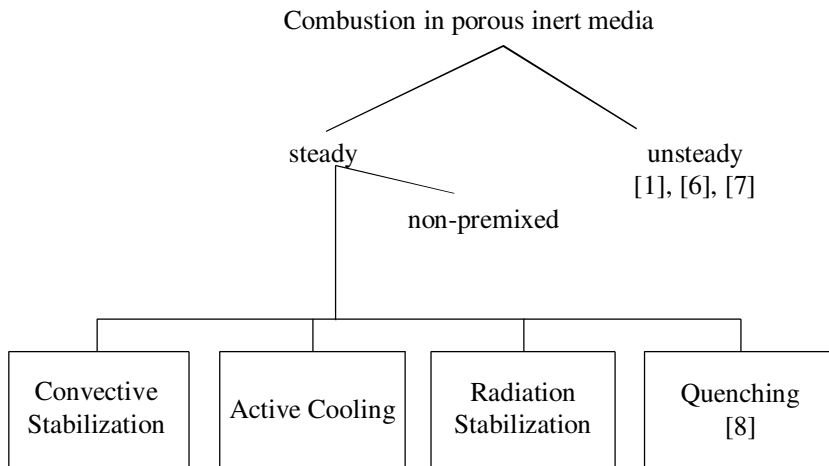


Figure 1. Overview of flame stabilization methods in porous media

described. Furthermore, the diffusive mass transfer and its effects on flame stabilization are discussed and experimentally investigated.

2. Influence of heat transport

2.1. Heat transport in porous medium. Concerning the flame stabilization in porous inert media significant differences occur in comparison with free flames. The stabilization depends mainly on the heat transport properties of the solid matrix. The heat transport inside of a porous medium is often described by an effective heat conductivity which comprises radiation and heat conduction of both solid and gas phase and additionally gas convection and dispersive mechanisms [5]. The effective heat transport inside of a porous medium is 2–3 orders of magnitude higher than in free flames and can be considered the dominant parameter for flame propagation for most cases. Compared with free flames the higher heat transfer leads to a faster flame propagation, which hampers flame stabilization in porous media. For solving the task of flame stabilization in porous media different approaches have been developed, which are summarized in Figure 1.

In the most relevant for burner applications *LVR* and *HVR* regimes flame propagation or extinction can be described by a modified Péclet-number P_e , which is defined by

$$P_e = \frac{S_L d_{p,eff} \rho_f c_{p,f}}{\lambda_f} = \frac{S_L d_{p,eff}}{a_f}. \quad (2.1)$$

P_e is formed with the laminar flame speed S_L instead of a flow velocity and describes the ratio between the heat release due to combustion in a pore and the heat removal on the walls of a pore. This ratio must exceed a critical value for flame propagation in a cold porous medium, which is given by [1] as 65 ± 45 . Flame propagation in this regime

is dominated by convection but also the high conductivity and radiative properties of the solid matrix influence the flame speed. Further parameters of P_e are the effective pore diameter $d_{p,eff}$ and the thermal diffusivity a_f . $d_{p,eff}$ represents an equivalent length scale for heat transport. The decision, whether or not flame propagation in a porous inert medium will occur, can be made by the choice of the pore size of the solid matrix. Thus, a critical pore size exists above which flame propagation and below which flame quenching occurs. Nevertheless, flame propagation may also occur in subcritical cavities if the temperature of the matrix is high enough, so that reactions are not quenched by the low wall temperature. This kind of operation is often called filtration combustion.

2.2. Stabilization by unsteady operation. Combustion in subcritical porous media will only take place if the temperature of the matrix is high enough to ignite the mixture. Flame propagation is driven mainly by the heat conductivity of the solid material and the interphase heat exchange where the heat transport in the gas phase is negligible. The so-called combustion wave travels very slowly through the porous matrix at a speed of $10^{-5} - 10^{-4} \text{ m/s}$ [9], [10], [11]. This wave travels either in or against the flow direction. In the former case superadiabatic and in the latter subadiabatic combustion temperatures occur. The direction of the wave is mainly dependent on the heat capacities of the solid and the gas phase and on the interphase heat exchange. For a standing wave only one single operational point is possible for a certain gas mixture. However, the very low speed of the combustion wave allows operation with varying gas velocities by changing the flow direction when the combustion reaches the end of the reactor. In Figure 2 the temperature profiles inside of a reactor with a subcritical porous matrix are shown. In this case the combustion wave travels in flow direction. The heat of the combustion heats up the porous matrix downstream of the combustion wave.

When the flow direction is reversed, the hot porous matrix preheats the fresh gas mixture and superadiabatic combustion occurs [10], [11]. With this principle gas mixtures with very low heat content can be burned. The flame speeds in such reactors are about 2 – 4 times higher than the laminar flame speed [12], [13].

2.3. Stabilization in steady operation. In supercritical porous media in principle the same mechanisms of flame propagation act as in free flames, but the higher effective heat conductivity must be taken into consideration. The effective heat conductivity as well as the thermal diffusivity are 2-3 orders of magnitude higher than in a gas. Following the simplified theory of flame propagation [14], the flame speed S is proportional to the square root of the temperature diffusivity:

$$S = \sqrt{\frac{a_f}{\tau}} \quad (2.2)$$

with the thermal diffusivity a_f and a characteristic time scale of the reaction τ . From this results that the flame speed in supercritical porous media is 10 – 30 times higher than the laminar flame speed. One possibility to stabilize the combustion in supercritical porous media is to induce a change of the flow speed by a stepwise or

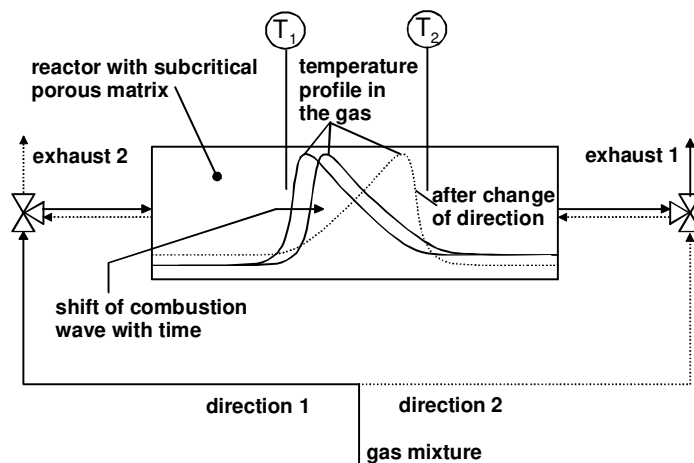


Figure 2. Scheme of a subcritical porous reactor in alternating operation

continuous change of the cross-sectional area. For methane/air mixtures in porous media the required flow speed to avoid flashback lies in the range of $2 - 5 \text{ m/s}$, which is about ten times higher than in free flames.

Another possibility for flame stabilization is to apply cooling of the reaction zone, e.g. by embedded water-cooled tubes in the main reaction zone. The cooling can also be realized by intense radiation from the reaction zone. In Figure 3 these two principles are schematically shown.

In the case on the left-hand side the combustion takes place inside of the pores, and the heat of reaction is conducted to the embedded water tubes. In the other case the combustion region must be located close to the surface of the porous matrix.

The porous surface extracts heat from the flame and radiates to the environment. Effective heat transport by radiation only occurs at high temperatures above the ignition limits. This means that for radiation-cooled burners the porous matrix must be subcritical, because otherwise the flame could slowly move into the porous matrix, which finally would lead to flashback.

In [8] another principle for flame stabilization was introduced, which made use of thermal flame quenching. The combination of two regions with different pore sizes was carried out, which results in supercritical and subcritical Péclet-numbers, respectively. This principle is shown in Figure 4.

In region A, through which the unreacted cold gas mixture flows, combustion is not possible due to the subcritical Péclet-number, so combustion only occurs in the supercritical region C with larger pores. Thus the flame stabilizes at the interface between the two regions. This arrangement allows flame stabilization at the same position over a wide range of flow velocities. In order to prevent flashback the amount

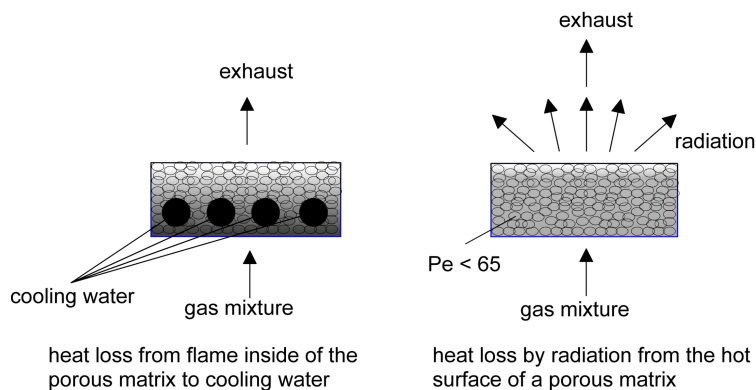


Figure 3. Flame stabilization in porous media by cooling

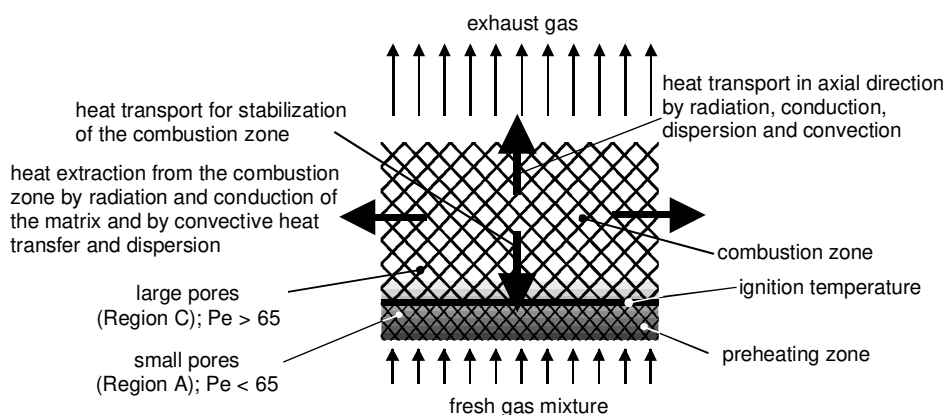


Figure 4. Heat transport and flame stabilization in a two-layer porous burner [8]

of heat which is transported against the flow direction must not be higher than the amount which is carried convectively by the fresh gas mixture into the combustion region, because otherwise a combustion wave can develop starting from the hot interface between region A and C, which possibly travels against the flow direction. This can be satisfied by means of a low conductive region A, which allows only a small amount of heat transport against the flow direction. In contrast, region C should feature a high effective heat conductivity, because this allows operation at high flow rates without the danger of blow-off. Typically, thermal heat loads of 3000 kW/m^2 in steady operation and up to 4500 kW/m^2 for peak loads are feasible. In [15] a power modulation ratio of 20:1 was realized with very low emissions over the whole modulation range and high flame stability in a wide equivalence ratio range. In [16] a flat

porous burner was designed, which is applied in industrial applications and makes use of the high emissivity of a SiC foam. The heat is radiated out of the volume of the SiC foam and enables high radiation efficiency to be achieved compared with standard surface radiating burners.

The principle of flame stabilization by changing the Péclet-number may be used with advantage in many application fields. However, in the Péclet-number criterion mainly heat transport processes are considered, and if diffusive mass transport becomes dominant, inaccurate critical pore diameters are predicted.

3. Influence of diffusive mass transport

3.1. Preliminaries. Up to now the influence of the diffusive mass transport on the stabilization of a flame in a porous medium was not investigated intensively. In [1] and [17] flame instabilities were observed for certain gas mixtures. These instabilities were linked to the increased influence of the diffusive mass transport, which decreased the dominance of the heat transport on the flame stabilization. The ratio between diffusive mass transport and heat transport can be described by the Lewis-number Le_c of a component c of the gas mixture.

$$Le_c = \frac{\lambda_f}{D_c \rho_f c_{P,f}} = \frac{a_f}{D_c}, \quad (3.1)$$

which is the ratio between the temperature diffusivity a_f and the diffusion coefficient of the component D_c . According to [1] and [18] the flame structure changes for Lewis-numbers smaller than unity. For many widely used gases, e.g. methane/air mixtures, Le is close to unity and therefore its influence is often neglected. However, mixtures with Lewis-numbers far below one require the consideration of mass diffusion. For example hydrogen/air and hydrogen/chlorine mixtures feature Lewis-numbers of about 0.4. For such low values one can expect a strong influence of the diffusion on the flame stabilization in porous media. This influence is neglected in the Péclet-number criterion, because only the laminar flame speed is considered, which does not account for deformations of the flame front. Such deformations can be driven by diffusion. This means that the constant value of the critical Péclet-number is not sufficient for the design of a porous burner flame trap.

In this study experiments concerning flame propagation in porous media were performed with gas mixtures of different Lewis-numbers. The aim of these experiments was to gain a better knowledge for the design of the porous burner flame trap.

3.2. Experimental determination of critical Péclet-number at various Lewis-numbers. In the following, experiments concerning the flame propagation of gases at different Lewis-numbers are described, with the aim of finding the critical Péclet-number for each mixture. Packings from steel spheres were used as the porous medium. In Table 2 the gases and the sphere packings which were investigated are summarized.

Table 2. Gas mixtures with different Lewis-number

Composition	Sphere sizes d_{sphere} in mm	Lewis-number
CH_4/air	10.0, 11.9, 14.3	≈ 0.96 in fuel rich flames
C_2H_6/air	10.0, 11.9, 14.3	≈ 1.42 in fuel lean flames
C_3H_8/air	10.0, 11.9, 14.3	≈ 1.8 in fuel lean flames ≈ 0.8 in fuel rich flames
H_2/air	2.5, 3.5, 4.0	≈ 0.4 in fuel lean flames ≈ 2.0 in fuel rich flames
$H_2/Cl_2/HCl$	3	≈ 0.33

It is important to note that the limiting Lewis-number is defined by the lacking component, i.e. oxygen in fuel rich mixtures and the fuel component in fuel lean mixtures. The equivalent pore diameter d_{peff} of the sphere packing can be estimated according to [2] with $d_{sphere} = 2.77 d_{peff}$. The gases in Table 1 cover a wide range of Lewis-numbers and by the investigation of the flame propagation limits in sphere packings a relation between critical Péclet-number and Lewis-number can be given.

3.2.1. Experimental set-up for detection of flame propagation. In order to investigate the critical Péclet-number, the critical pore diameter for the flame propagation of a certain mixture must be determined. The experiments were carried out in cold sphere packings. The gas mixture was ignited at the reactor exit. The detection whether or not the flame propagated through the matrix was carried out by two photo diodes, which gave an opportunity also to measure the propagation velocity of the flame inside of the porous medium. In Figure 5 the experimental set-up is shown schematically. The flow rates of the gas components were adjusted with mass flow controllers (*MFC*) in order to reach the required composition. In order to bring the gas to rest, the valves were closed when the correct composition was reached inside the packing. Just before ignition the upper valve was opened. The flame was detected by the two photo diodes. Figure 6 presents a typical signal sequence.

For each gas and sphere size the flame velocity in the packing and both the rich and the lean limit of flame propagation was determined. From the laminar flame speed at the limits and the corresponding physical properties of the mixture, the actual critical Péclet-number was determined.

For the last gas mixture of Table 1, the $H_2/Cl_2/HCl$ mixture, a different experimental procedure was applied. A closed system was used, because of the toxic gas mixture, with a two layer porous burner in which the flame trap consisted of 3 mm Al_2O_3 spheres. The temperature inside of this region was measured as an indication whether or not the flame was quenched. In these experiments the H_2/Cl_2 ratio was kept constant close to stoichiometry and the HCl fraction was varied until the limit point of flashback was found. This gas mixture was of interest because of its low Lewis-number of around 0.33.

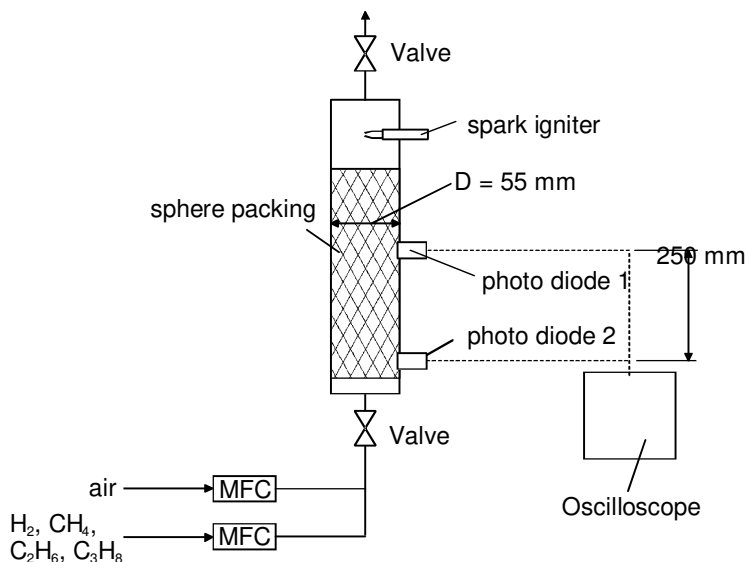


Figure 5. Experimental set-up for the investigation of the critical Péclet-number

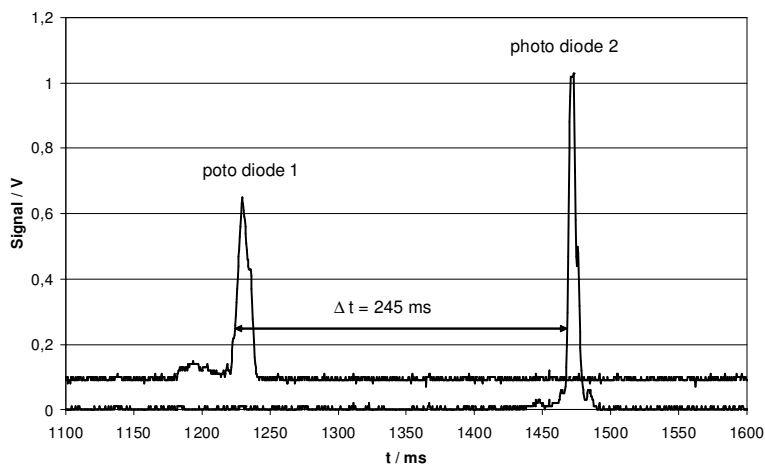


Figure 6. Signal sequence with flame propagation

3.2.2. Results and discussion. In order to investigate the flame propagation behavior, the equivalence ratio was varied in the different sphere packings, until no flame propagation was registered. In the following Figures 7 to 10 the measured flame speeds

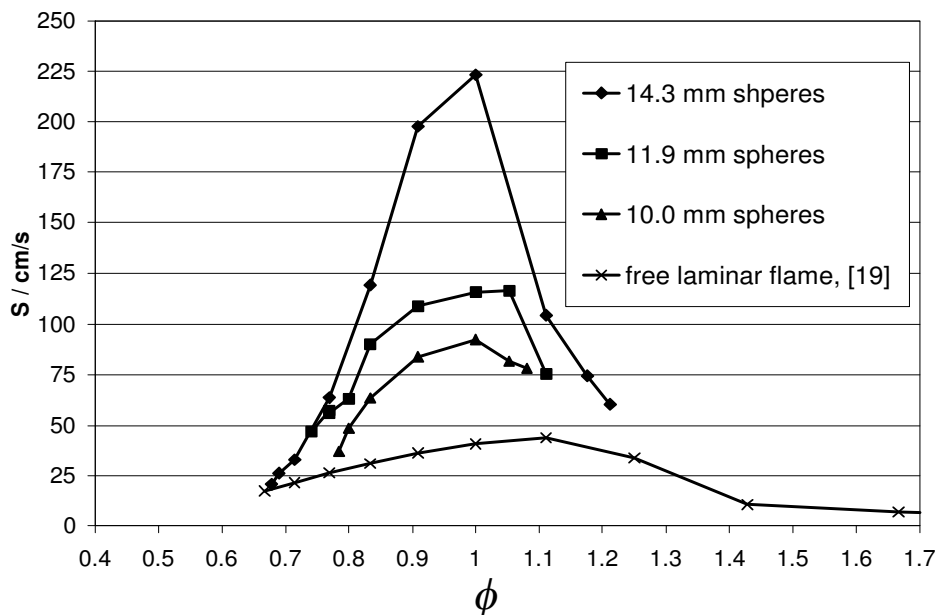


Figure 7. Flame speeds of methane/air mixtures in sphere packings

and the laminar flame speed of the same mixture are plotted against the equivalence ratio. The critical Péclet-number can be calculated for the minimal and the maximal equivalence ratio, the corresponding laminar flame speed, the gas mixture properties and the diameter of the spheres.

In Figure 7 the flame speed of methane/air mixtures in different sphere packings is shown. The flame propagation is 2 to 6 times higher than in a free laminar flame. Similar behavior is observed for ethane/air and propane/air mixtures, for which the measured flame speeds are presented in Figures 8 and 9. In both cases flame propagation in the packings was up to 10 times higher than in the laminar free flame. The maximum value of the flame speed occurred at the same equivalence ratio as for the laminar flame. This does not apply for the hydrogen/air mixtures (Figure 10), for which the maximum flame propagation speed in the packings were measured at equivalence ratios just lower than one, whereas the maximum flame speeds in a laminar hydrogen/air flame occurs at fuel rich conditions. This effect can be explained by the physical properties of the gas mixture. In hydrogen/air flames the heat conductivity of the mixture increases significantly with increasing equivalence ratio and the high heat conductivity of hydrogen becomes dominant in the mixture. This leads to an acceleration of the flame propagation due to the high heat conductivity of hydrogen. In porous media the effective heat conductivity is dominated by the transport properties of the solid phase almost regardless of the equivalence ratio

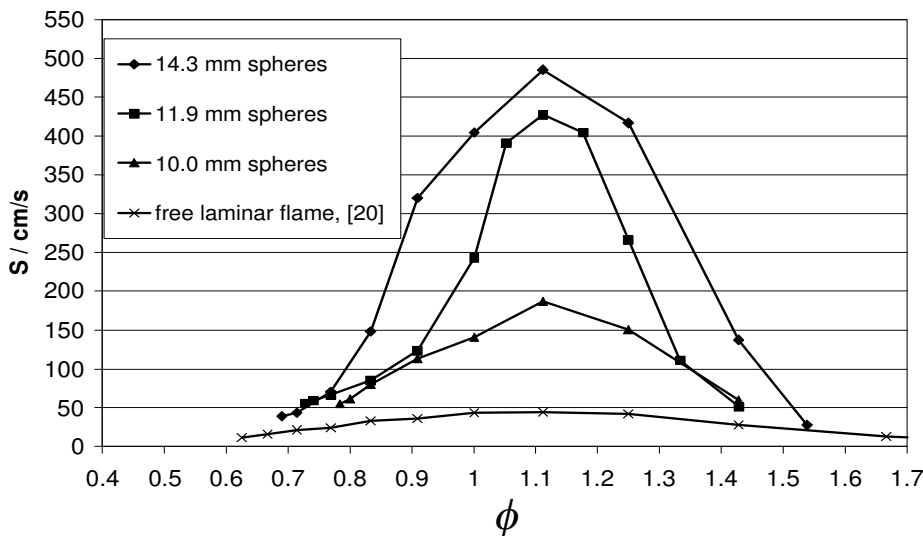


Figure 8. Flame speeds of ethane/air mixtures in sphere packings

of the gas mixture. Therefore, the influence of the increase of the gas conductivity at high equivalence ratios is negligible regarding the flame propagation. With increasing equivalence ratio the influence of the thermal flame propagation gains influence against the diffusive mechanism especially at high reaction temperatures, which occur close to stoichiometry.

A major result of the experiments described was the determination of the flame propagation limits in the applied packings, which is finally expressed by the critical Péclet-number. For each packing the critical Péclet-number was calculated for the lean and the rich flame propagation limit with the laminar flame speed at the corresponding equivalence ratio. The procedure was repeated for different diameters of the spheres. The average of the critical Péclet-numbers is plotted against the Lewis-number in Figure 11. For Lewis-numbers close to and larger than one the criterion of [1] of $P_{e_{crit}} \approx 65$ could be confirmed.

However, for mixtures of Lewis-numbers below one the critical Péclet-number was much lower than this value. For rich C_3H_8/air mixtures with a Lewis-number of 0.8 the critical Péclet-number reached 27. With 17 the critical Péclet-number was even lower for lean hydrogen/air-mixtures with a Lewis-number of about 0.4.

The experiment with the $H_2/Cl_2/HCl$ -mixture also led to an interesting result. For mixtures with a molar HCl/Cl_2 -ratio less than 3, the temperature in the flame trap region was rising significantly fast. Thus, at these conditions the critical Péclet number was reached. The laminar flame speed for the $H_2/Cl_2/HCl$ -mixture upon which the critical Péclet-number was determined was calculated with the CHEMKIN

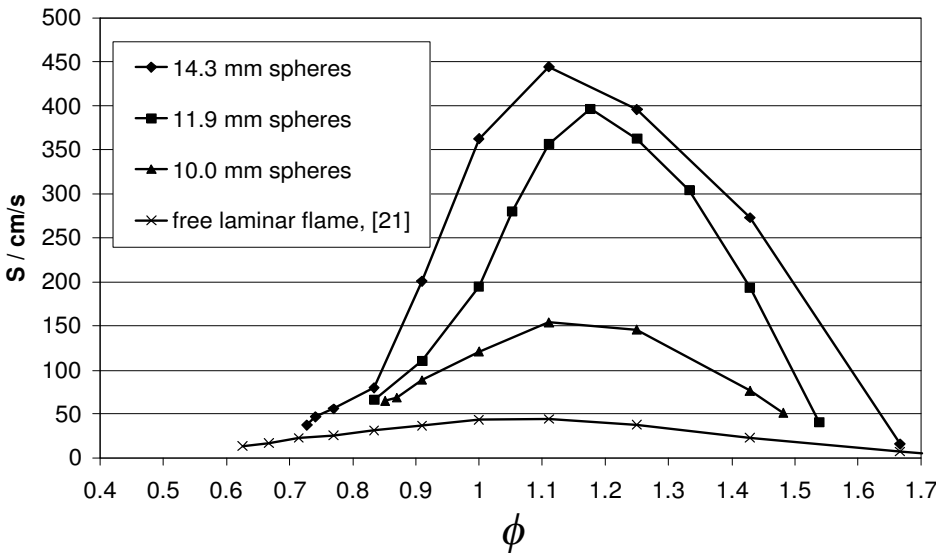


Figure 9. Flame speeds of propane/air mixtures in sphere packings

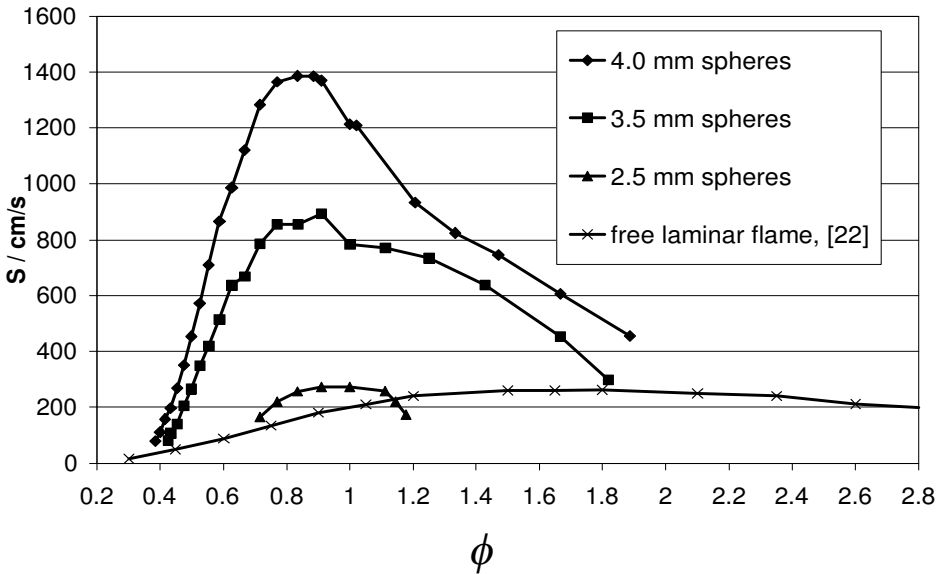


Figure 10. Flame speeds of hydrogen/air mixtures in sphere packings

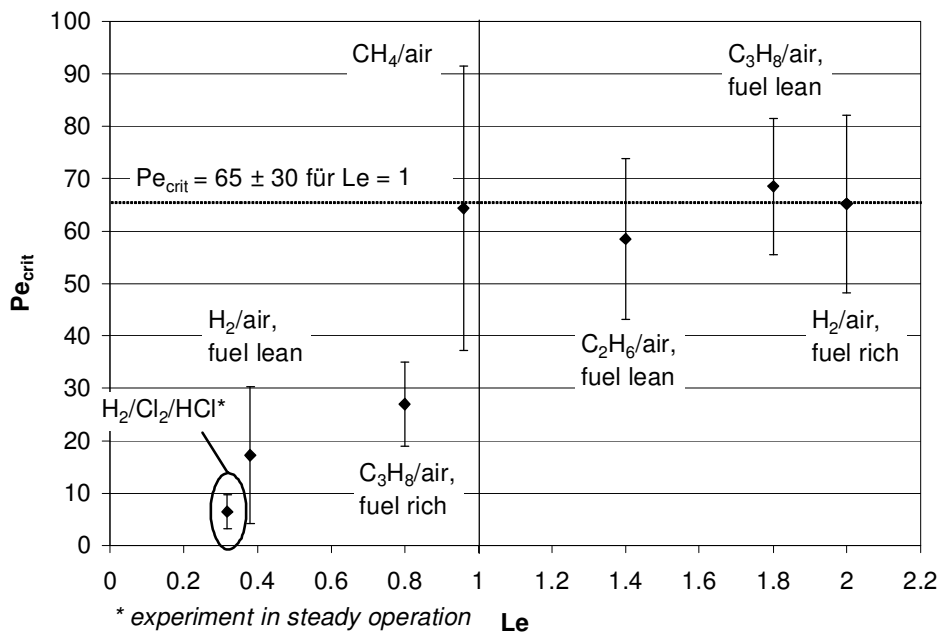


Figure 11. Critical Péclet-number over Lewis-number

3.6 software applying kinetic data of [23]. The resulting critical Péclet-number was with 6.5 the lowest reached in this study.

The uncertainties in Figure 11 derive mainly from the uncertainty about the determination of the laminar flame speed, with which the critical Péclet-number was calculated. The laminar flame speed was determined at the corresponding equivalence ratio, which could be adjusted by means of the mass flow controllers with an accuracy of ± 0.05 . The relative uncertainty of the calculation of the effective pore diameter applying the formula of [2] was estimated with 10 %. The same uncertainty was also estimated for the value of the thermal diffusivity. The spreading of the critical Péclet-numbers for the different sphere sizes fit all well within these calculated limits except for methane/air mixtures. The spreading of the values of the critical Péclet-number for methane/air-mixtures for the different sphere sizes was almost double what would be expected from the above described calculation. A possible explanation for this is the fact that the Lewis-number of these mixtures is almost unity, which means that both heat transport and mass diffusivity play an important role in flame propagation. Therefore, both effects are superposed, which would lead to an increased sensitivity to small variations. However, this effect cannot be calculated exactly. The uncertainty bar of the methane/air-mixture corresponds to the spreading of the critical Péclet-numbers for the different sphere sizes.

4. Conclusion

The results of this experimental study show that gas mixtures with a high diffusivity compared with the thermal diffusivity of the mixture, i.e. Lewis-numbers less than unity, show lower critical pore diameters or critical Péclet-numbers than mixtures with Lewis-numbers equal or larger than unity, concerning flame propagation. The Lewis number is calculated for the reaction component present at a mixture fraction lower than the stoichiometric mixture fraction.

With the presented results quantitative estimation of the influence of the diffusivity on flame stabilization in porous media becomes possible. The results can be used for a more accurate design of flame traps applied in porous media burners.

Acknowledgement. The authors thank the Institute of Environmental Process Technology at the University of Freiberg for the opportunity to carry out experiments with H_2/Cl_2 -flames in their facilities and the SGL-Acotec GmbH for the good partnership and the fruitful discussions.

References

1. BABKIN, V.S., KORZHAVIN, A.A., AND BUNEV, V.A.: Propagation of premixed gaseous explosion flames in porous media. *Combustion and Flame*, **87**, (1991), 182-190.
2. PINAEV, A.V. AND LYAMIN, G.A.: Fundamental Laws Governing Subsonic and Detonating Gas Combustion in Inert Porous Media. *Combustion, Explosion and Shock Waves USSR*, **25**(4), (1989), S.448-458. [Translated from *Fizika Goreniya i Vrzyva*, **25**(4), (1989), 75-85.]
3. PICKENÄCKER, O., PICKENÄCKER, K., WAWRZINEK, K., TRIMIS, D., PRITZKOW, W.E.C., MÜLLER, C., GOEDTKE, P., PAPENBURG, U., ADLER, J., STANDKE, G., HEYMER, H., TAUSCHER, W. AND JANSEN, F.: Innovative ceramic materials for porous-medium burners. *Interceram*, **5** & **6**, (1999), 326-330 & 424-434.
4. PICKENÄCKER, O. AND PICKENÄCKER, K.: Eigenschaften von keramischen porösen Strukturen für die Porenbrennertechnik. *Keramische Zeitschrift*, **53**(9), (2001), 780-787.
5. SCHLÜNDER, E.-U. AND TSOTSAS, E.: Wärmeübertragung in Festbetten, durchmischten Schüttgütern und Wirbelschichten, Georg Thieme Verlag, Stuttgart, 1988.
6. LYAMIN, G.A. AND PINAEV, A.V.: Combustion regimes in an inert porous material. *Combustion, Explosion and Shockwaves, USSR*, **22**(5), (1986), S.553-558. [Translated from *Fizika Goreniya I Vrzyva*, **22**(5), (1986), 64-70.]
7. LYAMIN, G.A. AND PINAEV, A.V.: Fast subsonic combustion of gases in an inert porous medium with a smooth rise in the pressure in the wave. *Combustion, Explosion and Shockwaves, USSR*, **23**(4), (1987), 399-402. [Translated from *Fizika Goreniya I Vrzyva*, **23**(4), (1987), 27-30.]
8. TRIMIS, D. AND DURST, F.: Combustion in a porous medium - advances and applications. *Combustion Science and Technology*, **121**, (1996), 153-168.
9. BINGUE J.P., SAVELIEV, V.A., FRIDMAN, A. A. AND KENNEDY, L.A.: Hydrogen production in ultra-rich filtration combustion of methane and hydrogen sulfide. *International Journal of Hydrogen Energy*, **27**, (2002), 643-649.

10. BANAMURA, K., ECHIGO, R. AND ZHDANOK, S.A.: Superadiabatic Combustion in a Porous Medium. *Int. J. Heat Mass Transfer*, **36**(13), (1993), 3201-3209.
11. GAVRILYUK, V.V., DMITRIENKO, Y.M., ZHDANOK, S.A., MINKINA, V.G., SHABUNYA, S.I., YADREVSKEYA, N.L. AND YAKIMOVICH, A.D.: Conversion of methane to hydrogen under superadiabatic filtration combustion. *Theoretical Foundations of Chemical Engineering*, **35**(6), (2001), 589-596.
12. TSENG, C.: Effects of hydrogen addition on methane combustion in a porous medium burner. *International Journal of Hydrogen Energy*, **27**, (2002), 699-707.
13. DIAMANTIS, D.J., MASTORAKOS, E. AND GOUSSIS, D.A.: Simulations of premixed combustion in porous media. *Combustion Theory and Modeling*, **6**, (2002), 383-411.
14. ZELDOVICH, Y.B., FRANK-KAMENETSKII AND D.A.: The theory of thermal propagation of flames, *Zhurnal of Fizichal Khimii*, **12**, (1938), 100-105. (in Russian)
15. MÖSSBAUER, S.: Entwicklung kompakter emissionsarmer Porenbrennersysteme mit hoher Leistungsmodulation zum Antrieb neuartiger Dampfmotoren, Fortschritt-Berichte VDI, Reihe **6**, Nr. **485**, VDI-Verlag Düsseldorf, 2002.
16. TRIMIS, D., WAWRZINEK, K., KRIEGER, R. AND SCHNEIDER, H.: A Highly Efficient Porous Radiant Burner for Industrial Applications, 6th European Conference on Furnaces and Boilers (INFUB), Lisbon, Portugal, 2002.
17. KENNEDY, L.A., FRIDMAN, A.A. AND SAVELIEV, A.V.: Superadiabatic combustion in porous media: Wave propagation, instabilities, new type of chemical reactor. *Fluid Mechanics Research*, **22**(2), (1995), 1-26.
18. BARENBLATT, G.I., ZELDOVICH, YA.B. AND ISTRATOV, A.G.: On the diffusion-thermal stability of a laminar flame, *Prikladnaya Mekhanika i Tekhnicheskaya Fizika*, **4**, (1962), 21-26. (In Russian)
19. SMITH, G.P., GOLDEN, D.M., FRENKLACH, M., MORIARTY, N.W., EITENEER, B., GOLDENBERG, M., BOWMAN, C.T., HANSON, R.K., SONG, S., GARDINER, W.C., JR., LISSIANSKI, V.V. AND QIN, Z.: GRI Mech. 3.0, 1999.
http://www.me.berkeley.edu/gri_mech/
20. EGOLFOPOULOS, F.N., ZHU, D.L. AND LAW, C.K.: Experimental Determination of Laminar Flame Speeds: Mixtures of C2-Hydrocarbons with Oxygen and Nitrogen, 23rd Int. Symp. on Combustion, The Combustion Institute, 1990, 471-478.
21. VAGELOPOULOS, C.M., EGOLFOPOULOS, F.N. AND LAW, C.K.: Further Consideration on the Determination of Laminar Flame Speeds with Counterflow Twin-Flame Technique, 25th Int. Symp. on Combustion, The Combustion Institute, 1994, 1341-1347.
22. AUNG, K.T., HASSAN, M.I. AND FAETH, G.M.: Flame stretch interactions of laminar premixed hydrogen/air flames at normal temperature and pressure. *Combustion and Flame*, **109**, (1997), 1-24.
23. BAULCH, D.L., DUXBURY, J., GRANT, S.J. AND MONTAGUE, D.C.: Evaluated kinetic data for high temperature reactions, Volume 4, "homogeneous" gas phase reactions of halogen- and cyanide-containing species. *Journal of Physical Reference Data*, **10**(1), (1981) p. 721.

EFFECTS OF SWEEP AND SPANWISE CHANGING CIRCULATION APPLIED TO AIRFOILS: A CASE STUDY

JÁNOS VAD

Department of Fluid Mechanics, Budapest University of Technology and Economics
H-1111 Budapest, Hungary
vad@simba.ara.bme.hu

[Received: February 11, 2004]

Abstract. Isolated stationary airfoils of simple geometry were tested in incompressible flow in order to study the combined aerodynamic effects of sweep, spanwise changing circulation, and their combination. Endwall effects were excluded from the studies. The tool of study was computational fluid dynamics, supplemented with wind tunnel experiments involving laser Doppler anemometry and flow visualisation. The computational results suggested unloading effects due to leading and trailing edge sweep. A model has been proposed for the description of such effects. It has been rendered probable that harmonization of the sweep with the spanwise circulation gradient results in reduction of the fluid pathline length on the suction side, giving a potential for reduction of profile losses.

Keywords: airfoil, axial flow turbomachinery, computational fluid dynamics, controlled vortex design, spanwise changing circulation, sweep

Nomenclature

b	$[m]$	projection of airfoil at midspan
c	$[-]$	force coefficient
c_p	$[-]$	static pressure coefficient
f	$[m]$	camber height
F	$[N]$	force
ℓ	$[m]$	blade chord
LR	$[-]$	lift coefficient ratio
p	$[Pa]$	static pressure
p_t	$[Pa]$	total pressure
s	$[m]$	span
v	$[m/s]$	velocity
y	$[m]$	transverse coordinate
α	$[^\circ]$	geometric angle of incidence
λ	$[^\circ]$	sweep angle of the stacking line
λ_{EQ}	$[^\circ]$	equivalent sweep (equation 5.3)
λ_{LE}	$[^\circ]$	leading edge sweep
λ_{TE}	$[^\circ]$	trailing edge sweep
ρ	$[kg/m^3]$	air density

ξ	$[-]$	total pressure loss coefficient (equation 5.5)
Γ	$[m^2/s]$	circulation ¹

Subscripts and superscript

<i>inlet</i>	at the inlet of the test section
<i>L, D</i>	lift, drag
<i>mid</i>	at 50 percent span (midspan)
<i>PS, SS</i>	pressure side, suction side
<i>SW, USW</i>	swept, unswept
<i>ref</i>	reference
<i>x, y, s</i>	orthogonal coordinates ²
$\hat{}$	chordwise averaged

1. Introduction

An axial flow turbomachinery blade is swept when each blade section of a datum blade with a radial stacking line is displaced parallel to its chord line in a prescribed manner. Backward or forward sweep occurs if a blade section at a given radius is downstream or upstream of the adjacent blade section at lower radius, respectively.

Blade sweep, often combined with dihedral, offers a potential for improvement of turbomachinery stage performance and efficiency, increase of pressure peak, shift of stall margin towards lower flow rate [1], [2], reduction of shock losses [3]; and noise reduction [4]. No general concept exists for prescribing the optimum spanwise blade sweep distribution for best stage efficiency. Only a qualitative guideline – regarding the direction of optimum sweep – can be given, and even the applicability of this guideline is restricted to the near-endwall region. The loss-reducing effects of ‘positive sweep’ (for which the blade section under consideration is upstream of the adjacent inboard section) are widely acknowledged for the near-endwall blade sections in low-speed rectilinear cascades [5]–[7], in transonic propfan rotors [8], in stators of low-speed compressors [9] and in transonic compressors [10]. This suggests the trend that a high-efficiency blading should have backward sweep near the hub and forward sweep near the tip, as appears in [8], [11], [12].

However, even such a qualitative guideline has not yet been found in the literature regarding optimum sweep for sections further away from the endwalls, as concluded in the CMFF’03 workshop organized in this topic [13]. For parts of blades of large aspect ratio where the flow is less affected by the endwalls, optimization of sweep could be an important issue in efficiency improvement. With the lack of a general concept yielding optimum sweep (design output), designs consider spanwise sweep distribution as input (arbitrarily prescribed) data. Optimum sweep is sought even

¹integral of velocity on a closed curve surrounding an airfoil section and fitting to a plane normal to the spanwise direction

²axial (along the wind tunnel axis), transverse, spanwise (Figure 3)

in the most recent research programs on a trial-and-error basis, by means of testing bladings of various sweep or skew prescribed in an arbitrary manner.

The lack of a general sweep optimization concept manifests itself in apparently contradictory results in the technical literature. Disregarding the advantages of backward sweep near the hub, the studies by most researchers suggest the benefits of forward sweep along the entire span. Such benefits are: higher energy transfer, lower wake losses and better blade element flow [1], better fit to design flow conditions along the entire span [2], reduced shock/boundary layer interaction [3], and generally improved fan performance [4], [11]. In contrast to the concept of leading edge (LE) sweep benefit near the endwalls, it has been reported in [14] that a forward-swept rotor with unswept LE is favorable for obtaining good hydraulic efficiency. There are a few reports opposing the view that forward sweep is advantageous in general. In [8], it has been pointed out that sweep results in a longer path of the fluid particles over the suction surface near midspan, thus increasing the thickness of the suction side boundary layer compared to the case of no sweep. This suggests that, although sweep diminishes shock losses, both forward and backward sweep may result in increased profile losses and reduced efficiency. Studies in [15] and [16] show that both backward and forward sweep reduce the total pressure rise and efficiency, however, the swept-back blading had more regular wake along the entire span and demonstrated better overall characteristics than the forward-swept one.

It is a generally widespread view in the turbomachinery community that the sweep angle and blade circulation distribution along the span are independent design variables. However, a correlation appears to exist between the aerodynamic optimum sweep and the spanwise circulation gradient. Favorable tendencies due to forward sweep have been reported usually in the case of rotors for which a positive spanwise blade circulation gradient was present. This was either due to the controlled vortex design (i.e. total pressure rise increasing along the dominant part of span) [2], [3], [11], [17]; or due to a flow rate lower than design [1], [4]. Unswept blades were proven to be most beneficial for rotors of free vortex operation (negligible spanwise circulation gradient by design) [8], [16]. Measurements in [15], [18] showed that both performance and efficiency were reduced for a swept-forward bladed rotor compared to a swept-back blading. In this case, a slight negative spanwise circulation gradient was present in the swept-forward bladed rotor, due to the only approximate realization of the free vortex design concept.

Similar tendency can be observed in the case of glider or bird wings. Figure 1 shows a lifelike example of presumable aerodynamic optimum combination of sweep and spanwise circulation gradient. The seagull wing has evolved over millions of years to realize a high lift-to-drag ratio, making effective gliding possible. In this paper, the classic sign convention and interpretation in [19] applies, i.e. the sweep angle λ (the angle between the stacking line and the spanwise direction) is positive for backward sweep and is negative for forward sweep. Starting from the body of the bird (nearly zero circulation) up to midspan, increasing circulation dominates ($d\Gamma/ds > 0$). Accordingly, the wing is swept forward ($\lambda < 0$) in this region. Above

midspan, the circulation must decrease along the span ($d\Gamma/ds < 0$) to zero (wing tip). During evolution, backward sweep ($\lambda > 0$) has been developed for this wing section.

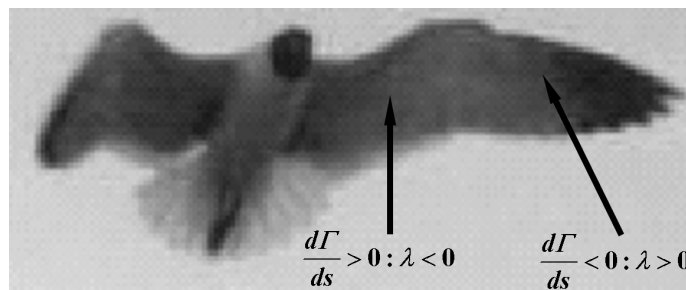


Figure 1. Seagull wing

As a step towards a concept for aerodynamic optimum harmonization of sweep and spanwise changing circulation in turbomachine design, this paper presents a case study for exploration of fluid mechanical effects due to sweep, spanwise changing circulation, and their combination applied to airfoils, with exclusion of endwall and compressibility effects. The case study has been carried out by means of Computational Fluid Dynamics (CFD) supplemented by wind tunnel experiments involving laser Doppler anemometry (LDA) and flow visualization. Preliminary studies have been reported in [20]. Isolated stationary airfoils of simple geometry are studied herein and similar qualitative behavior is assumed for rotating cascade arrangements, as in [5]. The former studies presented in the literature on swept airfoils and cascades usually aimed at the investigation of endwall effects. Furthermore, the loading [19] or camber geometry [6], [7] was constant with span, i.e. no attention was paid to the combined effects of sweep and spanwise changing circulation farther from the endwalls.

2. Test airfoils

The subjects of the present investigation are four airfoils, either unswept (US) or backward-swept (BS), and either of spanwise nearly constant circulation (CC) or spanwise decreasing circulation (DC) at midspan. The airfoils have been labelled accordingly, as shown in Figure 2. In Figure 2, the vertical upward direction is considered to be spanwise direction. During the experiments, each airfoil was placed in a single airfoil configuration in a wind tunnel section of rectangular cross-section $430\text{ mm} \times 520\text{ mm}$ in such a way that the airfoil root and tip extended to the tunnel walls ($s = 430\text{ mm}$) and the airfoil was located in the tunnel mid-plane. The coordinate system is indicated in Figure 3a.

Each airfoil consists of geometrically similar circular arc plate sections parallel to the xy plane. The data of such airfoil sections are presented in Table 1. The leading and trailing edges (LE, TE) have been rounded. US/CC was used as a reference. The

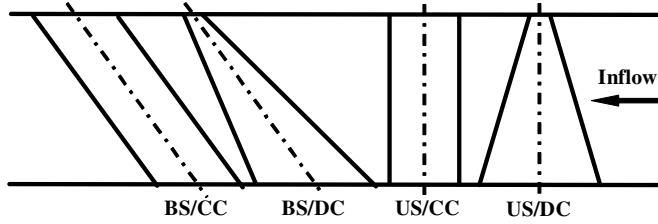


Figure 2. Scheme of airfoils

camber geometry and the geometrical angle of incidence (angle between the far-field upstream velocity and the chord) result in a lift coefficient of 0.740 and a maximum lift-to-drag ratio of approximately 40 for US/CC in two-dimensional (2D) tests [21]. BS/CC and BS/DC are swept backward, i.e. the consecutive blade sections along the span have been shifted toward the relative downstream direction, parallel to their chord. The capabilities of the wind tunnel limited the mean axial velocity set in the test to 10.0 m/s , and this value was used as reference velocity v_{ref} . The chord decreases linearly along the span in the cases of US/DC and BS/DC. The Reynolds number calculated with midspan chord, reference velocity, and kinematical viscosity of air at 20°C was $1.13 \cdot 10^5$ during the tests. This relatively low value may raise the question of whether laminar separation occurs on the airfoils. The experiments and, consistently, the CFD runs showed no evidence for separation, supported also by the fact that the airfoil sections were adjusted to the angle providing maximum lift-to-drag ratio for the 2D airfoil test case [21]. The Mach number computed with reference velocity and speed of sound in air at 20°C was 0.03 and therefore, the flow was considered truly incompressible. It is not an objective of this paper to report on problems related to compressibility or on shock loss reduction by means of appropriate sweep. The midspan chord length, lift coefficient, and sweep angle of the stacking line (the line passing through the airfoil section centers of gravity) were set to values equal to those valid for the case study in [22].

This paper reports studies on the behavior of the airfoils at 50 percent span only, where the endwall effects were found negligible. As is known, the shed vorticity due to the presence of endwalls induces downwash/upwash and thus effective spanwise changes of bound circulation. Computations on the endwall effects have been carried out for US/CC and BS/CC using the method proposed in [19]. These computations showed that the modification of incidence due to downwash perturbation fell below 1 percent of the geometrical angle of incidence 60 percent chord length farther from the endwalls. Considering the aspect ratio $s/\ell_{mid} = 2.53$, this implies that endwall effects are negligible near midspan in the cases studied. Computed pressure distributions on the suction and pressure surfaces and LDA wake measurements at different spanwise locations also showed that near-endwall fluid mechanical effects, for example due to LE and TE inclined to the spanwise direction [27], practically do not affect the flow field near midspan.

Table 1. Airfoil data

Airfoil	US/DC	US/CC	BS/DC	BS/CC
λ	0°	0°	35°	35°
$d\ell/ds$	-0.572	0	-0,572	0
Common data				
Rel. curvature (camber height-to-chord ratio): $f/\ell = 0.04$				
Camber angle: 18.28°				
Plate thickness: 2.0 mm				
Span: $s = 430.0\text{ mm}$				
Midspan chord: $\ell_{mid} = 170.0\text{ mm}$				
Aspect ratio: $s/\ell_{mid} = 2.53$				
Geometrical angle of incidence: $\alpha = 3.3^\circ$				
Lift coefficient (2D airfoil): $c_L = 0.740$				
Axial inlet velocity (reference velocity): $v_{ref} = 10.0\text{ m/s}$				

The force coefficient for either lift or drag force acting on an elementary airfoil section parallel to the xy plane and having spanwise height ds is defined as follows:

$$c_{L,D} = \frac{dF_{L,D}}{ds \ell (\rho/2) v_{ref}^2}, \quad (2.1)$$

where L and D represent lift and drag, respectively.

The circulation around such an airfoil section, in accordance with the Kutta-Joukowski theorem, can be approached as follows:

$$\Gamma = \frac{dF_L}{ds \rho v_{ref}} = \frac{c_L ds \ell \rho v_{ref}^2 / 2}{ds \rho v_{ref}} = \frac{c_L \ell v_{ref}}{2}. \quad (2.2)$$

Near midspan, the endwall effects and the downwash/upwash due to trailing shed vorticity were found negligible for US/DC and BS/DC, resulting in a constant incidence (practically equal to the geometrical angle of incidence). This, together with the constant camber relative curvature, yields a spanwise constant lift coefficient in the midspan region. Since the reference velocity is also constant along the span, the spanwise decreasing circulation has been represented by spanwise decreasing chord near midspan for US/DC and BS/DC, quantified by $d\ell/ds$, as indicated in Table 1.

3. CFD technique

The wind tunnel tests have been simulated by means of the commercial finite-volume CFD code FLUENT 6 [23]. Figure 3 shows the structured computational mesh for BS/DC as an example, together with an enlarged view of the mesh near the LE. The mesh structure is similar for the TE. The computational domain extends to 3 and 8 ℓ_{mid} upstream and downstream of the airfoil section at midspan, respectively. The total number of nodes is 50 in the spanwise direction. There are 34 nodes in the transverse direction farther from the airfoils, and 30 refined additional nodes have been

applied in the vicinity of the airfoil, both on the suction side (SS) and the pressure side (PS). In the axial direction, 30 nodes are applied upstream of the wing, 8 refined nodes are in the vicinity of both the LE and TE, 20 nodes are along the chord, and 100 nodes are in the downstream section. This amounts to a total number of cells of approximately 800 000, being a compromise with the limited computational infrastructure. When elaborating the grid structure, with special regard to the near-blade region, the guidelines obtained in international collaboration on carefully optimized turbomachinery CFD tools [14], [17], [18], [24] have been followed.

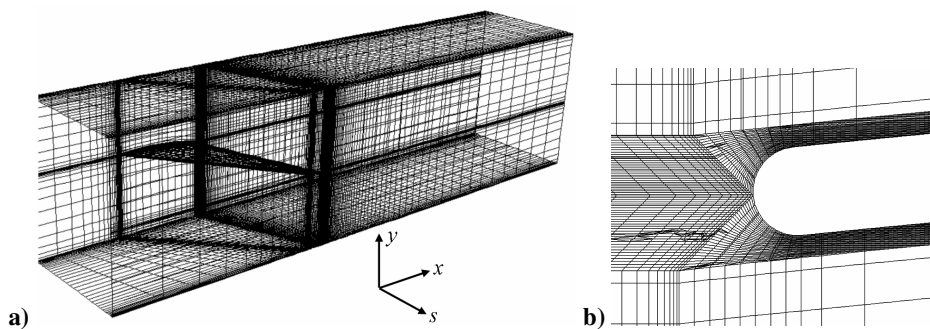


Figure 3. **a)** Computational mesh for airfoil BS/DC, **b)** Enlarged view of near-LE region

The turbulence model elaborated by Spalart and Allmaras [25] has been used because it is acknowledged to give good results for wall-bounded flows and boundary layers subjected to adverse pressure gradients. It has been successfully applied in advanced design systems of swept-bladed turbomachinery [26].

As the LDA measurements revealed, the inlet velocity was practically axial and uniform in the wind tunnel (nearly equal to v_{ref}), and the inlet turbulence intensity was 0.5 percent. These data have been applied as inlet conditions in the CFD studies. A fixed static pressure has been used as the outlet condition.

4. Experiments

The wind tunnel experiments were carried out in the National Physics Laboratory (NPL) type wind tunnel at the Department of Fluid Mechanics, Budapest University of Technology and Economics. An inlet contraction with honeycombs and static pressure taps for flow rate measurements, followed by a 1.3 m-long straight duct, precedes the test section. The 0.8 m-long test section is equipped with glass endwalls for optical access during LDA measurements. The airflow is induced by an axial fan of variable speed 2 m downstream of the test section. An ILA flowPOINT fp50-fus LDA system was connected to the test section. The diameter and the length of the LDA probe volume are 0.3 and 3.3 mm, respectively. The flow was seeded with oil

droplets of mean diameter $1.5\ \mu\text{m}$ by means of a DANTEC Fog 2005 Loop seeding generator.

LDA measurements were carried out upstream and downstream of the airfoils in order to obtain inlet data for CFD and to check the airfoil wake structure. Five hundred pieces of data were collected for each measuring point. The capability of the CFD technique can be critically evaluated by means of comparison of the CFD and LDA results obtained in the wake. The computed and measured transverse distributions of axial velocity v_x in the wake regions at midspan, 6 percent midspan chord downstream of the TEs, non-dimensionalized by the axial reference velocity v_{ref} , viewed from the downstream direction, are presented in Figure 4. The estimated experimental uncertainty of the LDA measurements is 0.5 percent. The transversal coordinate y has been non-dimensionalized by the b width of projection of the airfoils onto the ys plane at midspan. The velocity profiles are arranged in such a way that the minimum axial velocity appears at $y/b = 0$. The PS and SS wake regions can be seen at $y/b < 0$ and $y/b > 0$, respectively (also for Figure 8). As the Figure shows, the width of the wakes is approximately equal to b , behaving as expected in absence of separation, and the SS wake region is wider, in accordance with the thickened SS boundary layer near the TE. The wake velocity structure is practically identical for each airfoil, within the uncertainty range dedicated to geometrical and alignment uncertainties. The agreement between CFD and LDA data is satisfactory in the middle of the wake. More significant discrepancy can be observed farther away, which could have probably been reduced with repeated attempts on further optimization of the grid. Thus, the computation was considered to be an acceptable basis for only a qualitative comparison of loss behavior.

The flow in the boundary layers of BS/DC has been visualized by emission of a white tracer liquid at midspan near the LE, similarly to the technique applied in [6]. The experimental results, compared to computed pathlines, are shown in Figure 5. The experimental and CFD results are in satisfactory agreement, representing the upward and weak downward flow on the PS and SS, respectively, developing in accordance with the trailing shed vorticity due to spanwise decreasing circulation.

5. Computational results and discussion

In the following, the discussion is based on the computed results. Figure 6 shows the computed static pressure distribution on the surface of the airfoils at 50 percent span, represented by the static pressure coefficient

$$c_p = \frac{p - p_{ref}}{(\rho/2) v_{ref}^2}, \quad (5.1)$$

where p_{ref} is a reference pressure. Data points of larger absolute value near the LE are not shown.

Considering that $c_L \approx \hat{c}_{p\ PS} - \hat{c}_{p\ SS}$, the lift coefficients were calculated on the basis of the data in Figure 6 and are presented in Table 2. In the case of US/CC, the computed lift coefficient is in satisfactory agreement with the nominal value of

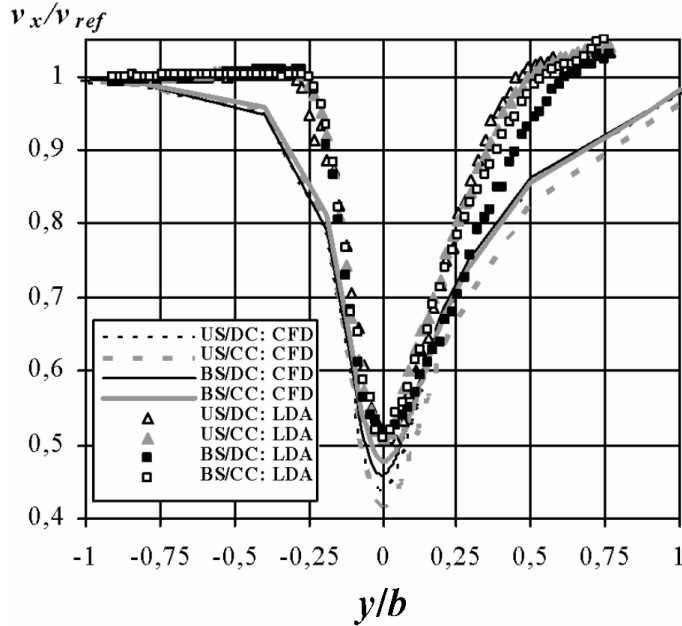


Figure 4. Axial velocity in the wake region

0.740 obtained for the 2D test case (see Table 1). The departure is probably due to the approximations in CFD modelling, as well as numerical integral-averaging of the pressure coefficients along the chord and computation of the lift coefficient from pressure coefficients. The satisfactory agreement confirms the applicability of the CFD tool at the present state of research and also that neglect of endwall effects – also regarding the sidewalls – is reasonable in the region under investigation. Such confirmation can also be made on the basis of the fact that the ratio between the lift coefficients BS/CC and US/CC is 0.81. This value approaches $\cos \lambda = 0.82$ with high accuracy, fitting to the theory stating that, if uncorrected, sweep tends to reduce the lift by the factor of $\cos \lambda$ for airfoils of infinitely large aspect ratio (no endwall effects) [1], [11], [19]. This theory, termed herein ‘classic $\cos \lambda$ law’, can be easily explained by resolving the incoming flow into components parallel to and perpendicular to the stacking line, parallel to both the LE and TE in the case of BS/CC.

Table 2. Geometrical and computed aerodynamic characteristics

Airfoil	US/DC	US/CC	BS/DC	BS/CC
c_L	0.736	0.797	0.657	0.643
λ_{LE}	16.0°	0°	44.6°	35°
λ_{TE}	-16.0°	0°	22.4°	35°
λ_{EQ}	16.0°	0°	33.5°	35°

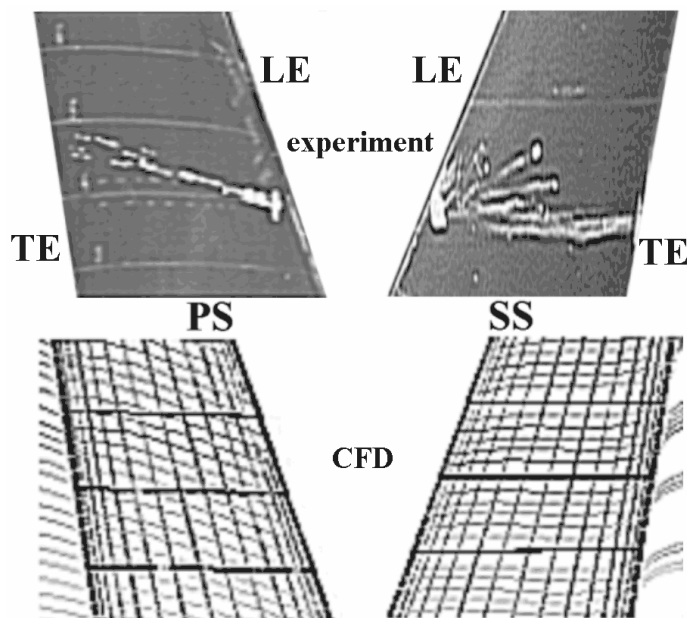


Figure 5. Experimentally and computationally visualized pathlines past airfoil BS/DC

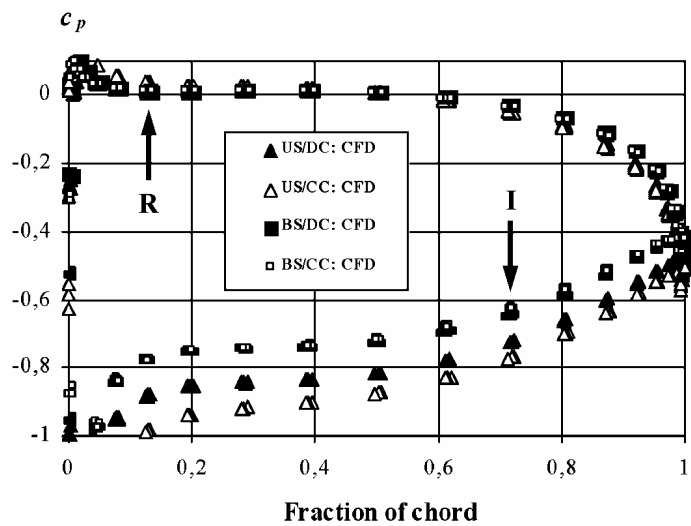


Figure 6. Computed pressure coefficient distribution

It can be observed in Figure 6 and in Table 2 that, although no sweep of stacking line has been applied, US/DC also produces reduced lift compared to US/CC. Furthermore, a slight increase of load can be observed for BS/DC compared to BS/CC on the SS after mid-chord. This effect manifests itself in reduced c_p values on the SS between mid-chord and the TE (indicated by arrow and label 'I' in Figure 6), whereas the pressure is practically equal on the PS. In contrast, the load between the LE and mid-chord of BS/DC is slightly reduced compared to that of BS/CC (slightly reduced pressure on the PS, indicated by arrow and label 'R' in Figure 6; and equal pressures on the SS). The dominance of increased load after mid-chord results in a slightly increased lift for BS/DC vs. BS/CC.

For explanation of these phenomena, the angles between the airfoil edges and the spanwise direction have been calculated and presented in Table 2 as leading edge sweep (λ_{LE}) and trailing edge sweep (λ_{TE}). The sign convention (positive and negative angles for backward and forward sweep, respectively) has consequently been applied.

Based on the above observations, it can be concluded that regardless of the sweep of the stacking line, the sweep of both airfoil edges originating from their inclination to the spanwise direction may cause local unloading of the airfoil. The local unloading can be interpreted similarly to the classic $\cos \lambda$ law: resolving the flow into components parallel to and perpendicular to the LE or TE, only the perpendicular component contributes to the lift. The larger the sweep, the higher the unloading (e.g. LE sweep in sequence for US/CC, US/DC, BS/CC and BS/DC), and reduced sweep causes increased loading (e.g. TE sweep for BS/DC vs. BS/CC). Deliberate use of sweep for unloading the blade LE near the endwalls has been discussed in [27]. However, such effects away from the endwalls have been disregarded, and no TE sweep phenomena have been reported. As the observations presented herein suggest, LE and TE sweep may also be used deliberately farther from the endwalls in order to realize a more favorable load distribution along the chord.

The above suggests that the $\cos \lambda$ law may be extended to airfoil or blade geometries for which both the LE and TE may have sweep, although the stacking line is not necessarily swept.

The lift coefficient ratio LR is introduced as the ratio between lift coefficient $c_{L\ SW}$ of a swept airfoil section (with LE and/or TE sweep) and that of an unswept 2D airfoil $c_{L\ USW}$ (no LE and/or TE sweep, US/CC in the case investigated). Unloading effects of LE and/or TE sweep are expressed in the present case study by means of LR. The following relationships are proposed for LR in order to make a comparison possible with the classic $\cos \lambda$ law:

$$LR = \frac{c_{L\ SW}}{c_{L\ USW}} = \cos \lambda_{EQ}, \quad (5.2)$$

where the equivalent sweep is defined as

$$\lambda_{EQ} = \frac{|\lambda_{LE}| + |\lambda_{TE}|}{2}. \quad (5.3)$$

The diagram corresponding to equation (5.2), compared with the LR results computed for the presently investigated airfoils of various λ_{EQ} (summarized in Table 2), is presented in Figure 7a. For comparison, Figure 7b presents the correlation between the computed data and the classic $\cos \lambda$ law stating that

$$LR = \frac{c_{L\ SW}}{c_{L\ USW}} = \cos \lambda. \quad (5.4)$$

The sparseness of data points must be acknowledged; the present discussion is to be supported by further tests in the future. Still, the following observations can be made. Both diagrams show the linear trendlines fitted to the data points with use of the least squares method, together with the coefficient of determination R^2 . Despite the simple model in equation (5.2), it appears to represent the test results better than the classic $\cos \lambda$ law: in Figure 7a, no inclination and only moderate shift of trendline is observed compared to the plot of equation (5.2); and R^2 is closer to unity. Better agreement could be achieved by: i) considering the streamline inclination modifying the effective angles of sweep; ii) considering that fluid particles along the inclined streamlines pass regions of various local lift in the case of US/DC and BS/DC, due to the spanwise changing geometry.

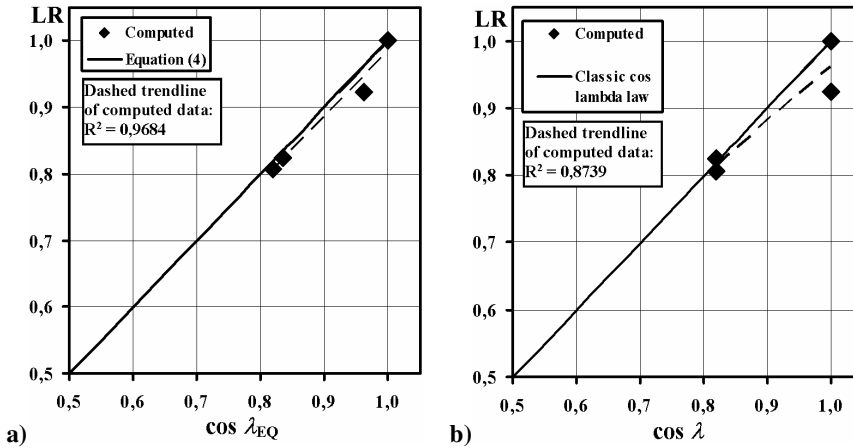


Figure 7. Comparison of a) equation (4), b) the classic $\cos \lambda$ law with computed data

The ratio between the lift coefficients for BS/DC and US/DC is 0.89. If intending to correct the lift reduction of BS/DC due to sweep using the classic $\cos \lambda$ law (on the basis of stacking line sweep angle $\lambda = 35^\circ$), one would realize that a correction by $\cos \lambda = 0.82$ would overshoot the required lift. Instead, $(\cos \lambda)^{0.58} = 0.89$ would give an appropriate correction. This is in agreement with the results in [11]. Based on several computations, the authors found that fans designed with a sweep correction of $(\cos \lambda)^{0.62}$ instead of $\cos \lambda$ achieved the prescribed pressure rise more accurately.

Beside the effects of finite aspect ratio, the model in equation (5.2) may contribute to the explanation of this observation. Based on [28], it can be established that the rotors studied in [11] had blades with chord decreasing along the span, resulting in LE and TE sweep and thus, in non-zero λ_{EQ} even if the stacking line was unswept ($\lambda = 0$). Therefore, a lift reduction was present even in the reference bladings of unswept stacking line (equation 5.2), and sweep correction moderate compared to $\cos \lambda$ was found sufficient to retain this reduced lift.

Figure 8 shows the distribution of total pressure loss coefficient at midspan, 6 percent midspan chord downstream of the TEs. This characteristic was calculated as follows:

$$\xi = \frac{p_{t\,inlet} - p_t}{(\rho/2) v_{ref}^2} . \quad (5.5)$$

US/CC appears to generate the highest losses, implying that the drag is the largest for this airfoil. However, it must also be noted that the lift of US/CC is also the largest, probably resulting in reasonably high lift-to-drag ratio. Regarding the airfoil series of US/CC, US/DC and BS/CC, a reduction of total pressure loss can be observed.

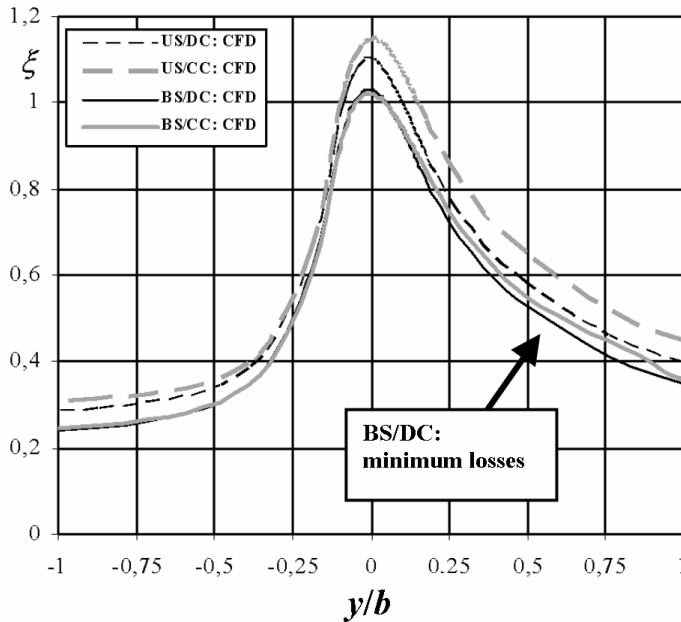


Figure 8. Computed total pressure loss distribution in the wake region

Further reduction of total pressure loss appears on the SS of BS/DC, compared to BS/CC (indicated by an arrow in Figure 8). In the following, causes of this favourable effect are investigated. For qualitative evaluation, Figure 9 presents the

map of computed ξ distributions for BS/CC and BS/DC, including the airfoil part of 75 percent to 100 percent chord. The black regions represent the airfoil. The light grey zones in the SS boundary layer and in the wake correspond to increased losses. The losses are moderate on the SS along the entire represented zone of BS/DC, suggesting that a favourable phenomenon is in effect for this airfoil after mid-chord. As Figure 6 suggests, the chordwise pressure gradient is moderate on the SS from 50 to 80 percent chord for BS/DC compared to BS/CC. This is due to the increased load of BS/DC after mid-chord since its TE is less swept (see Table 2). Such reduction of the adverse pressure gradient appears to reduce the losses. However, one would expect increased losses in the zone of 80 to 100 percent chord where the chordwise pressure gradient is higher in the case of BS/DC. Since Figure 9 shows moderate losses of BS/DC also near the TE, another beneficial effect must be presumed. A possible explanation follows.

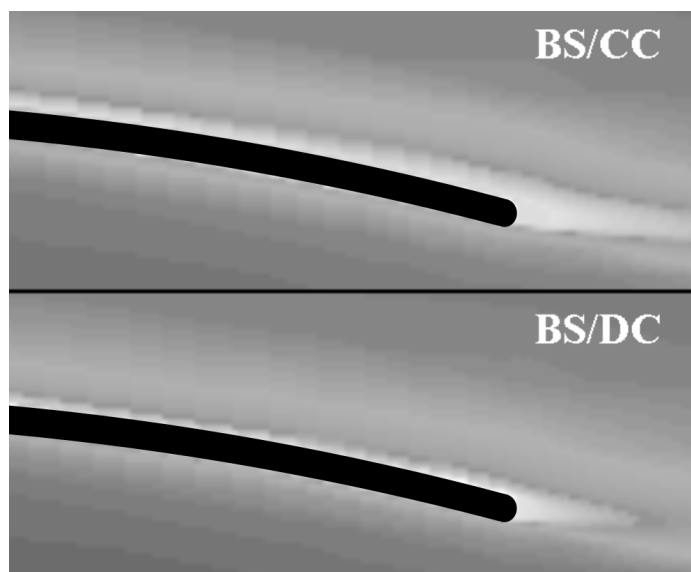


Figure 9. Computed total pressure loss map near the trailing edges

As suggested by the results in [8], the longer path of the fluid particles on the suction surface results in increased losses since the wall friction is more effective along the longer path. Figure 10a shows computed pathlines at the edge of SS boundary layers of BS/CC and BS/DC at midspan, in the region of 75 percent to 100 percent chord. In order to make the inclination of pathlines more visible, the sketches have been compressed to 25 percent in the chordwise direction. The arrows indicate the direction of pathlines at the TE. Due to spanwise constant circulation, no trailing vortices are shed from the TE of BS/CC. This results in SS pathlines parallel to the inflow near the TE of BS/CC. In contrast, trailing shed vorticity is present in the case

of BS/DC due to spanwise decreasing circulation, manifesting itself in SS pathlines inclined downward. (Spanwise increasing circulation would result in upward flow on the SS, as experienced, for example, in [29].) Due to the swept-back TE and downward inclined streamlines for BS/DC, the particles reach the TE along a shorter path. This is a possible explanation of reduced losses also near the TE. Spanwise increasing circulation would elongate the pathlines in the case of a swept-back TE, potentially leading to increased losses. The simplified sketch in Figure 10b illustrates these effects in the vicinity of the TE in a lifelike manner. The case of swept-forward TE could be interpreted in an ‘upside down’ configuration.

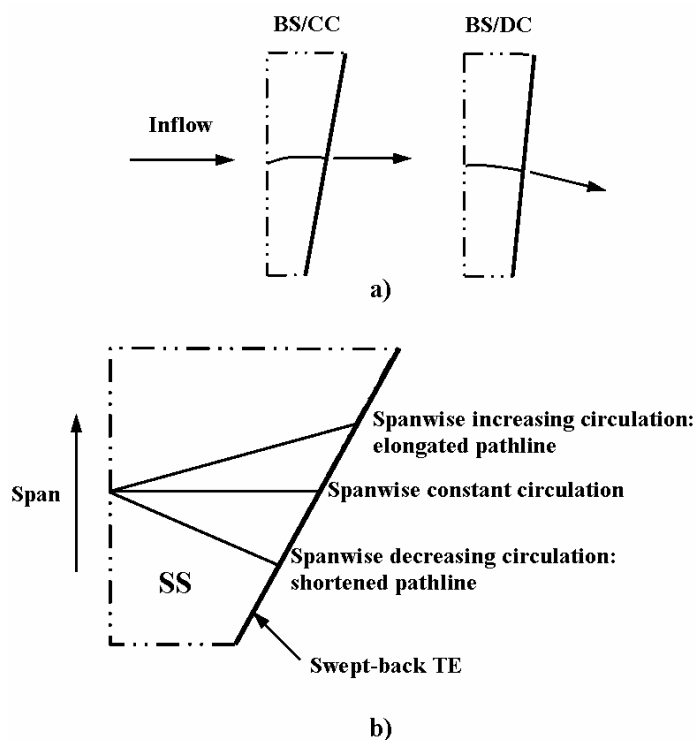


Figure 10. **a)** Computed suction side pathlines near the trailing edges, **b)** Sketch of suction side pathlines for different spanwise circulation gradients

The above suggests that tuning TE sweep and spanwise circulation gradient together can be an aspect for reducing profile losses via reduction of pathline length on the SS near the TE. In the case of swept-forward/swept-back TEs, trailing vorticity according to spanwise increasing/decreasing circulation of appropriate gradient contributes to such pathline reduction, whereas an unswept TE requires spanwise

constant circulation from this aspect. Flow field details reported in [3], [8], [15], and [30] appear to support this pre-concept, already mentioned in the Introduction.

Sweep is often applied in axial flow turbomachines e.g. for noise reduction and improved near-stall behavior. On the other hand, spanwise circulation gradient appears deliberately in blade rows of controlled vortex design. Therefore, both sweep and spanwise circulation gradient are present in certain bladings. Their appropriate tuning may give a potential for efficiency improvement.

6. Summary

The results of the case study presented herein are summarized as follows:

1. The studies suggested that regardless of the sweep of the stacking line in itself, the sweep of LE and/or TE causes local unloading of the airfoil. This may enable aerodynamically favorable tuning of chordwise distribution of load.
2. With introduction of equivalent sweep, a model has been proposed to calculate the reduced lift compared to a 2D infinite airfoil in the case of airfoil or blade geometries for which both LE and TE may have sweep, although the stacking line is not necessarily swept. This model represents the results of the present case study better than the classic $\cos \lambda$ law.
3. A possible aspect in reduction of profile losses is reduction of the fluid particle pathline length on the SS. This can be realized via appropriate prescription of forward sweep / no sweep / backward sweep for spanwise increasing / constant / decreasing circulation, respectively, and vice versa.

Acknowledgement. This work has been supported by the Hungarian National Fund for Science and Research under contract No. OTKA T 043493, and by the Széchenyi István Fellowship under contract No. SZÖ 271/2003. Gratitude is expressed to G. Constandinides and T. Réger for the computations, as well as to F. Peretti and M. Gutermuth, who performed the experiments.

References

1. MOHAMMED, K. P. AND PRITHVI RAJ, D.: Investigations on axial flow fan impellers with forward swept blades. *ASME J. Fluids Engineering*, (1977), 543-547.
2. YAMAGUCHI, N., TOMINAGA, T., HATTORI, S. AND MITSUHASHI, T.: Secondary-loss reduction by forward-skewing of axial compressor rotor blading, ASME J. Proc. Yokohama International Gas Turbine Congress, Yokohama, Japan, 1991, II.61-II.68.
3. WADIA, A. R., SZUCS, P. N. AND CRALL, D. W.: Inner workings of aerodynamic sweep. *ASME J. Turbomachinery*, **120**, (1998), 671-682.
4. WRIGHT, T. AND SIMMONS, W. E.: Blade sweep for low-speed axial fans. *ASME J. Turbomachinery*, **112**, (1991), 151-158.
5. CLEMEN, C. AND STARK, U.: Compressor blades with sweep and dihedral: a parameter study, Proc. 5th European Conference Turbomachinery Fluid Dynamics and Thermodynamics, Prague, Czech Republic, 2003, 151-161.

6. SHANG, E., WANG, Z. Q. AND SU, J. X.: The experimental investigations on the compressor cascades with leaned and curved blade, ASME paper No. 93-GT-50, 1993.
7. SASAKI, T. AND BREUGELMANS, F.: Comparison of sweep and dihedral effects on compressor cascade performance. *ASME J. Turbomachinery*, **120**, (1998), 454-464.
8. HELMING, K.: Numerical analysis of sweep effects in shrouded propfan rotors. *J. Propulsion Power*, **12**, (1996), 139-145.
9. FRIEDRICHS, J., BAUMGARTEN, S., KOSYNA, G. AND STARK, U.: Effect of stator design on stator boundary layer flow in a highly loaded single-stage axial-flow low-speed compressor. *ASME J. Turbomachinery*, **123**, (2001), 483-489.
10. GÜMMER, V., WENGER, U. AND KAU, H.-P.: Using sweep and dihedral to control three-dimensional flow in transonic stators of axial compressors. *ASME J. Turbomachinery*, **123**, (2001), 40-48.
11. BEILER, M.G. AND CAROLUS T.H.: Computation and measurement of the flow in axial flow fans with skewed blades, *ASME J. Turbomachinery*, **121**, (1999), 59-66.
12. UNITED STATES PATENT: High efficiency and low weight axial flow fan, Patent No.: US 6, 368, 061 B1, 2002.
13. BRAEMBUSSCHE R. A. AND VAD J.: Challenges in optimisation of axial flow turbomachinery blades for 3D flow, including sweep and dihedral effects, Summary of workshop organised at the Conference on Modelling Fluid Flow (CMFF'03), 3 to 6 September 2003, Budapest, Hungary. Accepted for publication in Modeling Fluid Flow - State of the Art, Springer Verlag Heidelberg (published in 2004).
14. GLAS, W. AND JABERG, H.: Multi-objective evolutionary algorithm for the optimization of swept pump impellers, Proc. 4th European Conference Turbomachinery Fluid Dynamics Thermodynamics, Florence, Italy, 2001, 469-479.
15. KUHN, K.: Experimentelle Untersuchung einer Axialpumpe und Rohrturbine mit gepfeilten Schaufeln, Dissertation Technische Universität Graz, Institut für Hydraulische Strömungsmaschinen, 2000.
16. FORSTNER, M., KUHN, K., GLAS, W. AND JABERG, H.: The flow field of pump impellers with forward and backward sweep, Proc. 4th European Conference Turbomachinery Fluid Dynamics Thermodynamics, Florence, Italy, 2001, 577-587.
17. VAD, J. AND CORSINI, A.: Comparative investigation on axial flow industrial fans of high specific performance with unswept and forward swept blades at design and off-design conditions, Proc. 9th International Symposium Transport Phenomena Dynamics Rotating Machinery, Honolulu, Hawaii, USA. Log. No. FD-ABS-016. CD-ROM, 2002.
18. VAD J., KWEDIKHA A. R. A. AND JABERG H.: Influence of blade sweep on the energetic behaviour of axial flow turbomachinery rotors at design flow rate, Accepted for 2004 ASME TURBO EXPO. ASME Paper GT2004-53544., 2004.
19. SMITH, L. M. AND YEH, H.: Sweep and dihedral effects in axial-flow turbomachinery. *ASME J. Basic Engineering*, **85**, (1963), 401-416.
20. VAD, J., CONSTANDINIDES, G., PERETTI, F., GUTERMUTH, M. AND RÉGERT, T.: Investigation on combined effects of sweep and spanwise changing design circulation on airfoil aerodynamics, Proc. Conference on Modelling Fluid Flow, CMFF'03, Budapest, Hungary, 2003, 145-152.
21. WALLIS, R. A.: Wind tunnel tests on a series of circular arc plate airfoils, A.R.L. Aero Note 74., 1946.

22. CORSINI, A., RISPOLI, F. AND VAD, J.: Iterative development of axial flow fans of high specific performance with swept blades, Proc. 5th European Conference Turbomachinery Fluid Dynamics and Thermodynamics, Prague, Czech Republic, 2003, 245-256.
23. FLUENT 6 USER'S GUIDE. Fluent Inc., Lebanon, NH, USA, 2001.
24. BORELLO, D., CORSINI, A. AND RISPOLI, F.: A finite element overlapping scheme for turbomachinery flows on parallel platforms. *Computers & Fluids*, **32**, (2003), 1017-1047.
25. SPALART, P. AND ALLMARAS, S.: *A One-Equation Turbulence Model for Aerodynamic Flows*. AIAA Technical Report AIAA-92-0439, 1992.
26. GALLIMORE, S. J., BOLGER, J. J., CUMPSTY, N. A., TAYLOR, M. J., WRIGHT, P. I. AND PLACE, J. M. M.: The use of sweep and dihedral in multistage axial flow compressor blading - Parts I and II. *ASME J. Turbomachinery*, **124**, (2002), 521-541.
27. DENTON, J. D. AND XU, L.: The exploitation of 3D flow in turbomachinery design, In Turbomachinery Design Systems, Von Karman Institute for Fluid Dynamics, Belgium, Lecture Series 1999-02, 1999.
28. BEILER, M. G.: Untersuchung der dreidimensionalen Strömung durch Axialventilatoren mit gekrümmten Schaufeln, Dissertation Universität Siegen. VDI-Verlag, Reihe 7, No. 298, Düsseldorf, 1996.
29. VAD, J. AND BENCZE, F.: Three-dimensional flow in axial flow fans of non-free vortex design. *Int. J. Heat Fluid Flow*, **19**, (1998), 601-607.
30. CORSINI, A., RISPOLI, F., VAD, J. AND BENCZE, F.: Effects of Blade Sweep in a High Performance Axial Flow Rotor, ATI-CST paper 005/01, Proc. 5th European Conference Turbomachinery Fluid Dynamics and Thermodynamics, Italy, 2001, 63-76.

Notes for Contributors

to the Journal of Computational and Applied Mechanics

Aims and scope. The aim of the journal is to publish research papers on theoretical and applied mechanics. Special emphasis is given to articles on computational mechanics, continuum mechanics (mechanics of solid bodies, fluid mechanics, heat and mass transfer) and dynamics. Review papers on a research field and materials effective for teaching can also be accepted and are published as review papers or classroom notes. Papers devoted to mathematical problems relevant to mechanics will also be considered.

Frequency of the journal. Two issues a year (approximately 80 pages per issue).

Submission of Manuscripts. Submission of a manuscript implies that the paper has not been published, nor is being considered for publication elsewhere. Papers should be written in standard grammatical English. Two copies of the manuscript should be submitted on pages of A4 size. The text is to be 130 mm wide and 190 mm long and the main text should be typeset in 10pt CMR fonts. Though the length of a paper is not prescribed, authors are encouraged to write concisely. However, short communications or discussions on papers published in the journal must not be longer than 2 pages. Each manuscript should be provided with an English Abstract of about 50–70 words, reporting concisely on the objective and results of the paper. The Abstract is followed by the Mathematical Subject Classification – in case the author (or authors) give the classification codes – then the keywords (no more than five). References should be grouped at the end of the paper in numerical order of appearance. Author's name(s) and initials, paper titles, journal name, volume, issue, year and page numbers should be given for all journals referenced.

The journal prefers the submission of manuscripts in \LaTeX . Authors should prefer the $\mathcal{AMS}\text{-}\text{\LaTeX}$ article class and are not recommended to define their own \LaTeX commands. Visit our home page for further details concerning the issue how to edit your paper.

For the purpose of refereeing, two copies of the manuscripts should initially be submitted in hardcopy to an editor of the journal. The eventual supply of an accepted-for-publication paper in its final camera-ready form (together with the corresponding files on an MS-DOS diskette) will ensure more rapid publication. Format requirements are provided by the home page of the journal from which sample \LaTeX files can be downloaded:

<http://www.uni-miskolc.hu/home/web/pumns/mechanics>

These sample files can also be obtained directly (via e-mail) from a member of the Editorial Board, Gy. Szeidl (Gyorgy.SZEIDL@uni-miskolc.hu), upon request.

Twenty offprints of each paper will be provided free of charge and mailed to the correspondent author.

The Journal of Computational and Applied Mechanics is abstracted in Zentralblatt für Mathematik and in the Russian Referativnij Zhurnal.

Responsible for publication: Rector of the Miskolc University

Published by the Miskolc University Press under the leadership of Dr. József PÉTER

Responsible for duplication: works manager Mária KOVÁCS

Number of copies printed: 200

Put to the Press on September 30, 2004

Number of permission: TU 2004-820-ME

HU ISSN 1586–2070

A Short History of the Publications of the University of Miskolc

The University of Miskolc (Hungary) is an important center of research in Central Europe. Its parent university was founded by the Empress Maria Teresia in Selmezbánya (today Banská Štiavnica, Slovakia) in 1735. After the first World War the legal predecessor of the University of Miskolc moved to Sopron (Hungary) where, in 1929, it started the series of university publications with the title *Publications of the Mining and Metallurgical Division of the Hungarian Academy of Mining and Forestry Engineering* (Volumes I.-VI.). From 1934 to 1947 the Institution had the name Faculty of Mining, Metallurgical and Forestry Engineering of the József Nádor University of Technology and Economic Sciences at Sopron. Accordingly, the publications were given the title *Publications of the Mining and Metallurgical Engineering Division* (Volumes VII.-XVI.). For the last volume before 1950 – due to a further change in the name of the Institution – *Technical University, Faculties of Mining, Metallurgical and Forestry Engineering, Publications of the Mining and Metallurgical Divisions* was the title.

For some years after 1950 the Publications were temporarily suspended.

After the foundation of the Mechanical Engineering Faculty in Miskolc in 1949 and the movement of the Sopron Mining and Metallurgical Faculties to Miskolc, the Publications restarted with the general title *Publications of the Technical University of Heavy Industry* in 1955. Four new series - Series A (Mining), Series B (Metallurgy), Series C (Machinery) and Series D (Natural Sciences) - were founded in 1976. These came out both in foreign languages (English, German and Russian) and in Hungarian.

In 1990, right after the foundation of some new faculties, the university was renamed to University of Miskolc. At the same time the structure of the Publications was reorganized so that it could follow the faculty structure. Accordingly three new series were established: Series E (Legal Sciences), Series F (Economic Sciences) and Series G (Humanities and Social Sciences). The latest series, i.e., the series H (European Integration Studies) was founded in 2001. The eight series are formed by some periodicals and such publications which come out with various frequencies.

Papers on computational and applied mechanics were published in the

Publications of the University of Miskolc, Series D, Natural Sciences.

This series was given the name Natural Sciences, Mathematics in 1995. The name change reflects the fact that most of the papers published in the journal are of mathematical nature though papers on mechanics also come out.

The series

Publications of the University of Miskolc, Series C, Fundamental Engineering Sciences

founded in 1995 also published papers on mechanical issues. The present journal, which is published with the support of the Faculty of Mechanical Engineering as a member of the Series C (Machinery), is the legal successor of the above journal.



Journal of Computational and Applied Mechanics

Volume 5, Number 2 (2004)

Contents

Preface 207–208

Contributed Papers

- László BARANYI: Numerical simulation of flow past a cylinder in orbital motion 209–222
- Edward CANEPA, Andrea CATTANEI, Marina UBALDI and Pietro ZUNINO: An experimental investigation of the unsteady flow in a two-stage low-pressure research turbine 223–236
- Alessandro CORSINI, Franco RISPOLI and Andrea SANTORIELLO: A quadratic Petrov-Galerkin formulation for advection-diffusion-reaction problems in turbulence modelling 237–249
- Martin GABI and Toni KLEMM: Numerical and experimental investigations of cross flow fans 251–261
- Akbar Khodaparast HAGHI: Relations for water-vapor transport through fibers 263–274
- Peter HERGT, Stephan MESCHKAT and Bernd STOFFEL: The flow and head distribution within the volute of a centrifugal pump in comparison with the characteristics of the impeller without casing 275–285
- Károly JÁRMAI: Optimum design of a uniplanar CHS truss for fatigue 287–296
- Mizuyasu KOIDE, Tsutomu TAKAHASHI, Masataka SHIRAKASHI: Influence of cross-sectional configuration on Kármán vortex excitation 297–310
- Piotr LAMPART: Numerical optimization of a high pressure steam turbine stage 311–321
- R. Ivan LEWIS: Study of blade to blade flows and circumferential stall propagation in radial diffusers and radial fans by vortex cloud analysis 323–335
- Petr A. NIKRITYUK, Kerstin ECKERT and Roger GRUNDMANN: Electromagnetically forced swirling flow during solidification of a binary metal alloy 337–352
- Daniel RUSCH, Axel PFAU, Joël SCHLIENGER, Anestis I. KALFAS and Reza S. ABHARI: Deterministic unsteady vorticity field in a driven axisymmetric cavity flow 353–365
- Dimosthenis TRIMIS and Klemens WAWRZINEK: Flame stabilization of highly diffusive gas mixtures in porous inert media 367–381
- János VAD: Effects of sweep and spanwise changing circulation applied to airfoils: A case study 383–400